Modeling of ultrasound transducers

Bæk, David

Publication date:
2010

Document Version
Publisher's PDF, also known as Version of record

Technical University
of Denmark

Modeling of ultrasound transducers

David Bæk

July 2010

DTU Electrical Engineering
Department of Electrical Engineering

Technical University of Denmark
Department of Electrical Engineering
Center for Fast Ultrasound Imaging
DK-2800 Kgs. Lyngby
Denmark

Submitted in partial fulfillment of the requirements for the degree of Doctor of Philosophy at the Technical University of Denmark.

Preface

This Ph.D. dissertation has been submitted to the Technical University of Denmark in partial fulfillment of the requirements for the degree of Doctor of Philosophy.

The work presented in this dissertation is based on the work carried out from August 1st, 2007 to July 31th, 2010 at the Center for Fast Ultrasound Imaging, Department of Electrical Engineering, Technical University of Denmark. It includes four journal papers, three conference papers, and two accepted abstracts for conference proceedings 2010.

The preparation of this Ph.D. dissertation has been conducted through three years of research. It has taken my skills within mathematical modeling to a whole new level and taught me the physics and science within medical ultrasound transducers and modeling of ultrasound wave propagation. The project has given me the opportunity to travel around the world to attend conferences in New York, Santiago de Chile, Beijing, Stockholm, and Rome. A privilege I have valued very much and which has expanded my knowledge within ultrasound. Yet another valuable asset of my study was given to me through my time abroad at the Stanford University, where I worked with a research group from which I learned many professional engineering skills as an engineer and which helped me grow personally.

During my study period I have had the great opportunity to teach students in signal processing and to share my knowledge within mathematical modeling with professors, colleagues and students. A valuable asset of the Ph.D. education that I am going to miss.

David Bæk
Kgs. Lyngby, July 2010

Acknowledgments

First of all, I would like to thank my supervisors, Professor Jørgen Arendt Jensen from the Technical University of Denmark and Professor Morten Willatzen from the University of Southern Denmark, for giving me the opportunity to study the mathematics behind modeling medical ultrasound transducers and for teaching me the scientific disciplines expected at Ph.D. level. They have both exhibited great enthusiasm in driving my results forward and got me to accomplish further than I thought possible. It has been an honor to learn from these two well recognized researchers.

I would also like to thank the Khuri-Yakub ultrasonics group at Stanford University and Professor B.T. Khuri-Yakub for inviting me to a 5 month study at their facilities in Stanford, California.

Furthermore, I would like to thank BK-Medical Aps, Sound Technology Inc., and Ferroperm Aps, for their help in discussions and supply of information that made some of this project's simulations possible.

I would like to thankfully mention my current and former colleagues for numerous discussions, inputs, talks and pleasant travels; amongst others Martin Hemmsen, Henrik Andresen, Svetoslav Nikolov, Jacob Kortbek, Jesper Udesen, Fredrik Gran, Niels Oddershede, Borislav Tomov, Iben Kraglund Holfort, Yigang Du, Michael Pihl, Ye Li, An Pahm, Joachim Rasmussen, Matthias Stuart, Jens Munk, Kristoffer Lindskov Hansen and Mads Møller Pedersen. Furthermore Henrik Laursen and Elna Sørensen for their always very kind help.

Last, but definitely not least, I would like to thank my beloved spouse, and wife-*to-be* Anna Kirstin Böttcher for her always kind help in correcting my written texts, for listening, supporting, helping, and always being there when I needed her during the project.

Thanks to you all

Abstract

This Ph.D. dissertation addresses ultrasound transducer modeling for medical ultrasound imaging and combines the modeling with the ultrasound simulation program Field II. The project firstly presents two new models for spatial impulse responses (SIR)s to a rectangular elevation focused transducer (REFT) and to a convex rectangular elevation focused transducer (CREFT). These models are solvable on an analog time scale and give exact smooth solutions to the Rayleigh integral. The REFT model exhibits a root mean square (RMS) error relative to Field II predictions of 0.41 % at 3400 MHz, and 1.37 % at 100 MHz. The CREFT model exhibits a RMS deviation of 0.01 % relative to the exact numerical solution on a CREFT transducer. A convex non-elevation focused, a REFT, and a linear flat transducer are shown to be covered with the CREFT model as well. Pressure pulses calculated with a one-dimensional transducer model in combination with Field II are calculated on a circular piezoceramic transducer and a convex 128 element commercial transducer. The pulses are shown to be predictable within ± 2 dB of the amplitude which is excellent for this modeling. Intensity profiles are shown to be predicted with a RMS deviation of 5.5 % to 11.0 %. Finite element modeling of piezoceramics in combination with Field II is addressed and reveals the influence of restricting the modeling of transducers to the one-dimensional case. An investigation on modeling capacitive micromachined ultrasonic transducers (CMUT)s with Field II is addressed. It is shown how a single circular CMUT cell can be well approximated with a simple square transducer encapsulating the cell, and how this influence the modeling of full array elements. An optimal cell discretization with Field II's mathematical elements is addressed as well. The error in modeling CMUT cells as squares or flat circular plates instead of curved circular cells is also addressed.

Abbreviations

SIR	Spatial impulse response
RMS	Root mean square
CMUT	Capacitive Micromachined Ultrasonic Transducers
REFT	Rectangular elevation focused transducer
CREFT	Convex rectangular elevation focused transducer
FEM	Finite element model

x

Contents

CHAPTER

ONE

Introduction

The fundamental purpose of this research project has been to investigate ultrasound transducer modeling techniques that can improve the simulation software Field II [1, 2]. Field II is a widely known and well recognized simulation software. It is capable of simulating the pressure field and the pulse-echo response from an inhomogeneous medium such as the human body, and its main application areas are within ultrasound imaging and blood flow estimation. Typically the program is used to simulate RF-data as it would be received by a real medical ultrasound scanner. The program has, due to its high flexibility, been accepted by the ultrasound community as one of the leading simulation programs within ultrasound research. The flexibility of the program makes it possible to simulate any transducer geometry, excitation wave form, focusing, and attenuation, and as simulation output the program can return beam-formed RF-lines, spatial impulse responses, pressure fields, pulse-echo responses, and received RF-data of a transducer in a variety of combinations. Field II is therefore, amongst others, capable of doing very complex simulations for standard ultrasound imaging, synthetic aperture, adaptive beam-forming, compound imaging, diverse flow simulations, and pressure field simulations. It can handle these for both homogeneous and inhomogeneous mediums of theoretically any size and any transducer geometry.

The implementation and the calculation principle performed inside the kernel of Field II are the main keys to its fast computational ability and success. Fundamentally speaking the program predicts wave propagation in the field in front of the transducer by calculating a unique impulse response that relates a scatter point in front of the transducer (an inhomogeneity in the medium) to the transducer's surface geometry. This relation is called the spatial impulse response (SIR). The SIR is then convolved with the transducer's

electromechanical impulse response and the excitation waveform to yield the actual pressure at the point's location. Both of the wave forms are to be supplied by the user and are not pre-calculated by the program. If a pulse-echo response from a scatter point is to be calculated then also the SIR in receive and the mechanical to electrical impulse response of the transducer are convolved onto the result [3]. This is performed in the time domain, and it is therefore essential for the program to have a fast evaluation of the SIR and also a fast convolution algorithm. The solvers for finding the SIR currently rely on subdividing the transducer surface into smaller piston transducer elements (mathematical elements (ME)) in the shape of either rectangles [1] or triangles [4]. The superposition principle is then utilized to add the response from each ME to yield the overall SIR. This is a very fast calculation principle and can approximate the SIR from any transducer geometry. Clearly the drawback of this method arises when too coarse a subdivision is applied whereby an inaccurate summation will be present. This is especially the case for curved surfaces. It is therefore a trade off between accuracy and computation time with this method.

A valuable asset to improve on the theory of the SIR calculation method and Field II for the special group of transducers with either a convex unfocused, a rectangular elevation focused, or a convex rectangular elevation focused geometry would be to calculate the SIR from a closed form mathematical expression that can be analytically or semi-analytically solved without subdividing the surface into ME. These transducers are of special interest because they can be found in medical ultrasound imaging applications.

A part of this research project has been concerned with finding such mathematical expressions for rectangular elevation focused elements and convex rectangular elevation focused elements that are analytically and semi-analytically solvable. The development has been considered novel and has been submitted for publication. These works are found in the appended chapters titled: Paper I and Paper II (see table of contents) which fully document this work. A single abstract on this topic, which has been accepted for a conference publication ultimo 2010, has also been written. It can be found in the appended chapter titled: Abstract I. A supplying discussion of the theory of SIRs and the findings in the publications are the topics of **Chapter 2**.

Chapter 3 summarizes and addresses the work published in the journal paper appended in the chapter: Paper III. This work focuses on combining Field II with a one-dimensional piezoelectrical transducer modeling principle originally suggested by Willatzen [5], and it fully documents this part of the Ph.D. work. The purpose of the work was to get an estimation of the accuracy in

predicting pressure pulses with Field II and this kind of transducer modeling. Two transducers were modeled, a single element circular pz27 ceramic and a 128 element convex commercial medical transducer. The reason for this choice was that it was possible to achieve a set of valuable simulation parameters and construction drawings from the manufacturer to the transducer handle. Usually these information are protected property of the manufacturers of commercial transducers, and to respect this for the manufacturer the name and version number of the given transducer is not mentioned in this publication. Two conference papers used as initial studies, and of which the results have been improved in Paper III are attached in Paper VI and Paper VII. These studies were pre-studies of the main journal paper.

An interesting parameter sensitivity study is addressed in the conference contribution in the chapter titled Paper V. This paper addresses the validity of the input simulation parameters applied in Paper III, and it discusses the piezoceramic model's sensitivity to its input parameters.

Finally, the chapter discusses the findings in the journal paper in the chapter Paper IV. This journal paper investigates a finite element model in combination with Field II. It emphasizes the influence of restricting the modeling of the impulse responses to a one-dimensional model as is assumed in Paper III.

Chapter 4 addresses the feasibility of simulating capacitive micromachined ultrasonic transducers (CMUTs) with Field II. The project was conducted in collaboration with the Ginzton Laboratory at the Stanford University, California, and its purpose was to investigate simulation of the SIR for CMUTs with the current Field II modeling capacity. The importance of this project can be realized by studying the extent of publications within medical imaging that is concerned with CMUTs. Field II is currently not supporting build-in predefined transducer models for CMUT transducers. The current version only supports the geometry of the classical piezoceramic transducers, and developers with the need to simulate CMUT devices have to create their own models using the Field II's manual transducer setup. An abstract Abstract II has been accepted for a conference proceeding on this work.

For the reading of this dissertation it is recommended to read the journals Paper I and Paper II as well as Abstract I prior to entering Section 2.2 of Chapter 2. Prior to entering Chapter 3 is it recommended to read journal papers Paper III and Paper IV as well as conference paper Paper V. Chapter 4 can be read as it is and followed by Abstract II.

CHAPTER

TWO

Spatial impulse responses for rectangular elevation focused and convex elevation focused transducers

As described in the introduction, the spatial impulse response (SIR) for double curved transducers is currently calculated by subdividing the surface into smaller elements. An interest to find an algorithm which without surface discretization can solve the SIR for these types of transducers efficiently and exactly has originated. In order to complement the currently available solution methods, this part of the research project has been concerned with finding a closed form analytical and semi-analytical solution for SIRs of the problem.

This chapter firstly gives an overview of the relevant literature for SIRs that was applied in the inspiration process of the development. Afterwards a discussion on the derivation and the nature of the SIR for simple flat transducer elements is presented. This is intended to give the reader an overview of the topic and to clarify associated problems with the technique. A presentation and a discussion follow. They are based on two new developed algorithms for SIRs which are presented in the journal papers by the author and inserted into the chapters: Paper I and Paper II. Paper I presents an exact semi-analytical solution for the elevation focused rectangular transducer, and Paper II presents an exact solution for the rectangular convex elevation focused transducers (double curved transducers) through an approximation can be solved analytically. Finally a conclusion and a discussion of future development is presented.

2.1 Literature and state of the art within spatial impulse responses

A literature study within the field of acoustic wave radiation from acoustic transducers reveals a research field that has been studied thoroughly through history and is well understood by the acoustic research community. Some of the earliest publications with relevance to SIR date back to Lord Rayleigh [6] in 1945 on the theory of sound, the work on concave cylindrical transducers by O'Neil [7] in 1949, or e.g. Oberhettinger [8] from 1961 on transient solutions of baffled pistons. These references direct the attention to several other works that have been written in between these years which cannot all be mentioned and often only touch the issue of SIRs tangentially. A literature review on the theory of sound radiation from acoustic transducers will therefore only consider references that have a direct relevance to the study of SIRs of which the work presented in this chapter is concerned with. It should, however, be mentioned that for the interested reader Freedman [9] has published a literature summary in 1969 containing many of the works known at that time. A similarly excellent study has been conducted by Harris in 1981 [10].

A good starting point for the review is the work by Tupholme [11] in 1969. In this work he describes how the velocity potential for circular pistons, strip pistons, and wedge formed pistons can be easily formulated using Green's function on Helmholtz's equation. He applied a formulation with step functions from which the velocity profile can be evaluated as a dependence of a field points' location relative to the transducer.

Later Stephanishen [12–14] has in a series of papers described the velocity potential or the pressure prediction from circular and rectangular pistons as a time convolution between the surface velocity and a surface integral. The integrand of the surface integral was formulated by using the well known Green's function. This principle applied the assumption that the radiating surface moves uniformly, and it is valid in both near- and far-field for a piston mounted in an infinite planar baffle. The principle formulates a simple method for evaluating time-dependent calculations of the pressure field. A time convolution between a surface velocity and a spatial integral was formulated as:

$$\phi(\vec{x},t) = v(t) \overset{*}{_t} h(\vec{x},t), \tag{2.1}$$

where

$$h(\vec{x},t) = \frac{1}{2\pi}\int_S \frac{\delta(t-|\vec{x}-\vec{x_0}|/c)}{|\vec{x}-\vec{x_0}|}dS. \tag{2.2}$$

The velocity profile $v(t)$ of the transducer surface is assumed to be spatial independent, and the impulse integral of the expression is entirely depending on the observing point's location relative to the transducer surface, S.

Lockwood and Willette [15] presented a high speed calculation method for calculating the pressure in the near-field of a harmonic excitated piston by representing the surface integral of the pressure integral with a single integral. They showed how the impulse response for a rectangular flat transducer could be formulated in a closed form with numerical integration and represented it with a proper choice of Dirac delta functions.

Following the publications by Tupholme, Stephanishen, and Lockwood and Willette several works have been presented with main focus on finding analytical solutions to the integral in (2.2) on simple geometries such as rectangles, triangles, circles, and concave annular pistons. Among these is the work by Jensen and Svendsen in [1], where Tupholme's and Stephanishen's methods were adapted for the development of a far-field approach. This method subdivides the surface into smaller rectangular elements and can be used to formulate any transducer geometry. Jensen also adapted the SIR method to formulate the response from triangular flat transducer elements [4] and for arbitrary shaped flat apertures in a bounding line method [2]. A similar approach was applied in 2004 by Neild et. al. in [16]. Penttinen and Luukkala presented a solution for the concave focused annular pistons in [17] in 1976. They did this by geometrically formulating the small integration segment, dS, in (2.2) and showed that their algorithm was in consistency with the SIR for flat circular pistons. Arditti, Foster, and Hunt later formulated analytical expression for the SIR of concave annular pistons following the same principle, and they also commented on concave annular concentric rings in [18] in 1981.

O'Neil [7] commented on applying the Rayleigh surface integral method for slightly curved transducers. The problem associated with the integral is its limited validity for curved transducers. The integral does not account for the fact that a slightly curved transducer will introduce reflections and diffraction. However, O'Neil assumed that this secondary diffraction effect is negligible as long as the transducer curvature is small compared to the wavelength. The same assumptions are defended by Penttinen and Luukkala [17] and Arditti et. al [18].

Tjotta et al. [19] considered the situation in which the surface velocity for planar radiators is non-uniform. This resulted in a somewhat more complicated mathematical description if the velocity distribution takes on a form that is not directly solvable with their method. Furthermore, they presented a study

on non-planar radiators, in which they applied Green's formula instead of the Rayleigh integral.

Literature addressing rectangular focused transducer elements includes among others Piwakowski and Sbai [20] who present a method to solve an arbitrary geometry by reformulating the classical Rayleigh integral into a weighted sum and by discretization of the surface into smaller elements. This method is found in the DREAM software [21, 22]. Another interesting investigation was presented by Faure et. al [23] for a curved strip, i.e. a part of a sphere cut out with four lines. This work showed reasonable consistency between simulated results and measurements. The authors commented on the slight error as being caused by the measurement setup. Their work indicates that the secondary diffraction effect has little significance as O'Neil, Penttinen, Luukkala, and Arditti also assumed in their works. A cylindrical transducer was considered by Theumann et. al [24]. They formulated the radiation using the SIR method and solved (2.2) in cylindrical coordinates. They achieved reasonably good results with experiments which support the conclusion made by Faure et. al [23]. They found an analytical expression for a point located at the center of the cylinder and for points anywhere else a numerical solver was needed. In 1999 Wu and Stepinski [25] presented a method to calculate a SIR from a linear array with concave surface. They formulated the SIR by subdividing the surface into thin rectangular strips with the same length as the height of the aperture/element, and they then utilized that each rectangular strip has a well known analytical response. Comparison with measurements validated their model and showed good consistency.

The thorough interest in calculating the pressure field from arbitrary transducer geometries has especially been motivated by medical ultrasound research. Modern medical transducers can consist of several array elements arranged linearly, curved, or in matrix form. Their applications are typical for pulse-echo measurements in inhomogeneous mediums, which complicate the simulation of the response significantly. To cope with this development several simulation programs for simulating such complicated environments have been developed. These programs utilize many of the references mentioned above and are either based on the SIR principle or on an advanced numerical integration. Among these programs one can find Ultrasim [26], DREAM [22], DELFI [27], and Field II [1, 2].

2.1.1 The nature of the spatial impulse response

The SIR concept can easily be derived from the Rayleigh integral. The pressure field from an aperture can be defined as

$$p(\vec{r_1},t) = \frac{\rho}{2\pi}\int_S \frac{\frac{\partial v(\vec{r_0},t-\frac{|\vec{r_1}-\vec{r_0}|}{c})}{\partial t}}{|\vec{r_1}-\vec{r_0}|}dS, \tag{2.3}$$

where v is the normal velocity of the aperture, $\vec{r_0}$ is a vector describing a location on the aperture surface, $\vec{r_1}$ is the location vector of a given point, P, at which the pressure is to be predicted, c is the speed of sound of the medium in front of the aperture, and ρ is the corresponding density. This integral is only exact for the situation where the transducer surface is flat, and it is required that no reflection from one part of the surface affects another part of the surface. It is furthermore derived with the assumption that the medium is homogeneous, and that the wave propagation is linear. Linear wave propagation is necessary because the integral follows Huygen's principle by adding contributions from many small surface elements, dS, which requires linear assumptions. Figure 2.1 shows the geometrical definition of the vectors $\vec{r_0}$ and $\vec{r_1}$ for a flat rectangular piston placed in an infinite baffle as well as the definition of the Cartesian coordinate system.

A velocity potential, ϕ, can be introduced and related to the pressure as [28]:

$$v(\vec{r_0},t) = -\nabla\phi(\vec{r_0},t), \tag{2.4}$$

$$p(\vec{r_1},t) = \rho\frac{\partial\phi(\vec{r_0},t)}{\partial t}. \tag{2.5}$$

This makes it possible to formulate the velocity potential as

$$\phi(\vec{r_0},t) = \int_S \frac{v(\vec{r_0},t-\frac{|\vec{r_1}-\vec{r_0}|}{c})}{2\pi|\vec{r_1}-\vec{r_0}|}dS. \tag{2.6}$$

Since the wave propagation is assumed to be linear it is possible to separate the surface movement from the spatial wave propagation by introducing a delta function and a time convolution:

$$\phi(\vec{r_0},t) = \int_S\int_T \frac{v(\vec{r_0},t_1)\delta(t-t_1-\frac{|\vec{r_1}-\vec{r_0}|}{c})}{2\pi|\vec{r_1}-\vec{r_0}|}dt_1 dS. \tag{2.7}$$

This integral can be separated if it is assumed that the surface movement of

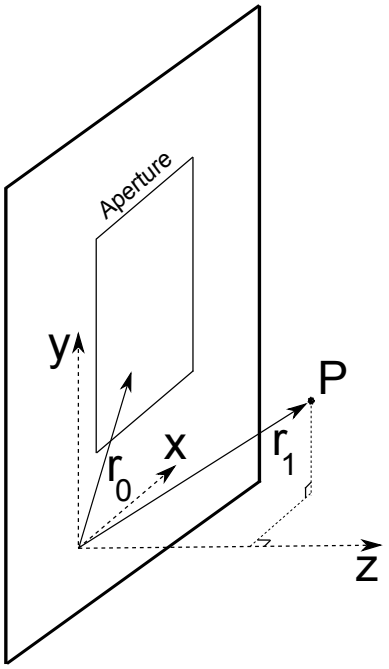

Figure 2.1: Figure showing the definition of an aperture placed in an infinite baffle and the vectors $\vec{r_0}$ and $\vec{r_1}$ as well as the point P.

the transducer is uniform, i.e. spatial independent

$$\begin{aligned} \phi(\vec{r_0}, t) &= \int_T v(t_1) \int_S \frac{\delta(t - t_1 - \frac{|\vec{r_1} - \vec{r_0}|}{c})}{2\pi|\vec{r_1} - \vec{r_0}|} dS dt_1 \\ &= v(t) \overset{\star}{}_t \int_S \frac{\delta(t - \frac{|\vec{r_1} - \vec{r_0}|}{c})}{2\pi|\vec{r_1} - \vec{r_0}|} dS, \end{aligned} \tag{2.8}$$

where $\overset{\star}{}_t$ is the time convolution.

Recall from (2.2) that

$$h(\vec{r_1}, t) = \int_S \frac{\delta(t - \frac{|\vec{r_1} - \vec{r_0}|}{c})}{2\pi|\vec{r_1} - \vec{r_0}|} dS. \tag{2.9}$$

This is the spatial impulse response.

The simplest way to analyze the nature of this integral is to consider a rectangular flat transducer and a point, P, located somewhere in front of the transducer. A wave emanating from such given point, which is possible due to acoustical reciprocity, will eventually intersect the transducer, and the

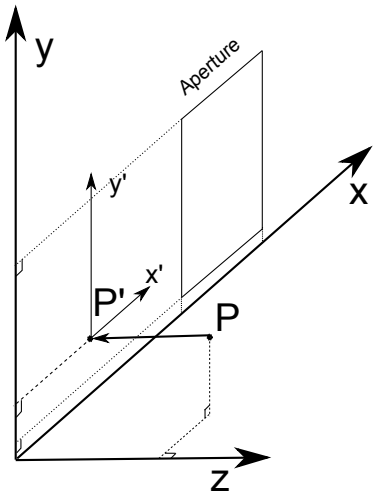

Figure 2.2: Figure showing how a point is projected onto the plane of the piston.

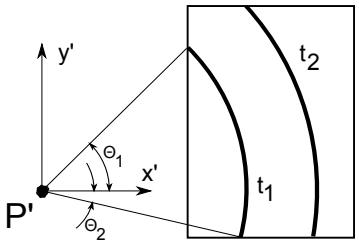

Figure 2.3: Figure showing how the crossing between the sphere and the aperture is defined with two angles and a projected circle. Two time instances are depicted.

intersection will form a circular arc. By projecting P onto the plane of the transducer as depicted in Fig. 2.2 a new one-dimensional manifold with the projected point P' defining the coordinate center is formed. This projection makes it beneficial to transform the integral (2.9) into polar coordinates as suggested by Jensen [2]. Working with polar coordinates in the plane of the transducer yields a very simple solution to the complicated integral in (2.9)

$$h(\vec{r_1}, t) = \frac{c}{2\pi}[\Theta_2(t) - \Theta_1(t)]. \tag{2.10}$$

The SIR for this simple situation is therefore found by identifying the angles $\Theta_1(t)$ and $\Theta_2(t)$ in radians, which can be geometrically found as illustrated in Fig 2.3.

In the solution form (2.10), c will be the speed of sound and the angles $\Theta_2(t)$ and $\Theta_1(t)$ define the angle difference created to a given time instance t, as shown in Fig. 2.3. The unit for the SIR is therefore the one of velocity, m/s. Furthermore, from (2.10) it can be identified that for a closed arc segment the response takes on the value for the speed of sound, and in this simple form it can easily be verified that the SIR is related to the arc length of the intersection.

It can therefore be proven that the pressure can be expressed by

$$p(\vec{r_1}, t) = \rho \frac{\partial v(t)}{\partial t} \overset{\star}{_t} h(\vec{r_0}, t), \tag{2.11}$$

Examples of SIRs with a simple flat rectangular transducer and six points located in the xz-plane as depicted on Fig. 2.4 can be seen in Fig. 2.5. All points are placed in the same y-plane, i.e. $y = 0$. The figures clearly show that the pulse shapes are different, which is due to the points' geometrical dependency to the transducer. Points close to and in front of the transducer are initially constant (c). The flat constant section is shortened as the point gets further away from the transducer. Points very far away from the transducer give responses that take on the shape of a sharp spike. Theoretically, there will always be a flat constant section as long as no focusing occurs. However, to resolve a flat section smaller time steps need to be considered in the plotting and in the simulation. Figure 2.6 depicts the corresponding normalized pressure calculations of the points as described with (2.11). For illustration purposes a two cycle Hanning weighted excitation pulse has been applied here. In consistency with the definition (2.10) and the illustration in Fig. 2.3 discontinuities are seen on the responses in Fig. 2.5. These correspond to wave crossings of the aperture edges.

Practically speaking the SIR itself is of no interest in actual measurement situations. Recall that the actual measured pressure can be found as a time convolution between the excitation waveform of the transducer and the impulse response wherefore the SIR is hidden in the measured response, and it is to be considered a mathematical operator.

2.1.2 Spatial impulse responses in medical imaging and Field II

In medical imaging the propagating medium, the tissue, is highly inhomogeneous. A reformulation of the wave equation to include a scattering term has therefore been presented in [3]. This reformulation has shown that a pulse-echo response can be approximated with the SIR principle. For reference purposes the developed expression is mentioned here in its original form

$$p_r(\vec{r_5}, t) = v_{pe}(t) \overset{\star}{_t} f_m(\vec{r_1}) \overset{\star}{_t} h_{pe}(\vec{r_1}, \vec{r_5}, t). \tag{2.12}$$

The term $v_{pe}(t)$ is the transducer's two way impulse response and excitation wave form. $f_m(\vec{r_1})$ is a scattering term that was introduced accounting for a weak scattering assumption, and $h_{pe}(\vec{r_1}, \vec{r_5}, t)$ is a pulse echo SIR. The latter corresponds to a convolution between SIRs in transmission with the SIRs in reception. For array transducers these are different, but for single element transducers the terms become identical. The vectors $\vec{r_1}$ and $\vec{r_5}$ are vectors defining the transducer location and the point location similar to what was

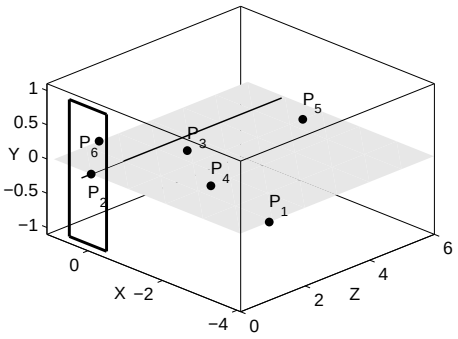

Figure 2.4: Six different locations of a point, P, placed in relation to a flat rectangular transducer. The points are placed in the xz-plane. The y-coordinate of the points is fixed at zero or center plane of the transducer.

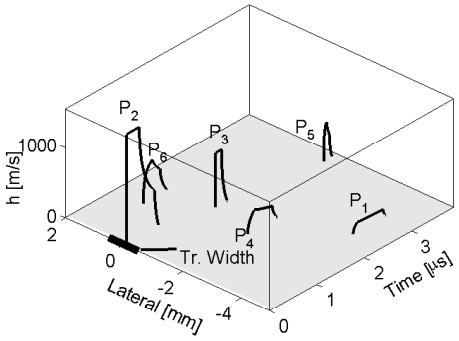

Figure 2.5: SIR for the six points.

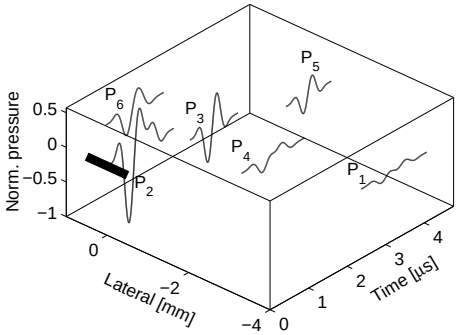

Figure 2.6: Pressure corresponding to the impulses in Fig. 2.5. A two cycle Hanning weighted excitation pulse is applied.

shown in Fig. 2.1. For image simulation within medical imaging a computationally heavy part in generating RF-data is found in h_{pe} which has to be performed as efficiently as possible.

To simulate RF-data for imaging with Field II one has to know on forehand the pulse form of v_{pe}, and an assumption of the scattering tissue has to be represented with a scatterer map. The scatterer map is related to f_m and can consist of thousands of scatterers (reflecting Ps). Field II calculates the SIR for each scatter point, and it does this for all transmit and all receive elements. This can include a fair amount of calculations for typical medical transducers

with e.g. 192 transmit and receive elements and e.g. 1 million scatter points. Beam-forming and image processing are to be performed afterwards. A discussion of the exact influence of the different terms in (2.12) can be found in [3].

Curved transducers can be represented in Field II by building the surface of many smaller flat elements, so called mathematical elements. The SIR is calculated by summing the response from each smaller element at the correct time instances. This method is very efficient in terms of calculation speed on computers with large memory since very simple solutions for the subresponse are known, e.g. (2.10). The drawback is, however, the accuracy of the phase summation. Smooth curves and energy conservation of the SIR pulse require very exact phase summation, which is a challenge if the sampling frequency is relatively low, and the subdivision is too coarse. However, such one is an important factor for a simulation program utilizing the SIR method. High sampling frequency yields an exact summation, but is on the cost of longer convolution times in e.g. (2.12).

2.2 A new model for a rectangular elevation focused transducer

A journal paper describing the development of the SIR for an elevation focused rectangular transducer can be found in the chapter: Paper I. It fully documents the development and the work that this part of the Ph.D. project has been concerned with. The presented model solves the problems on discretizing the transducer surface as described in the previous sections. The current section is an addendum and a summary to the journal in Paper I. It presents and discusses the developed algorithm for the SIR.

The development was initially inspired by the closed form analytical solution for the intersecting curves between a sphere and a cylinder where the center of the sphere is located on the boundary of the closed cylinder. The arising intersecting curves are called Viviani's curves. The preparations for Paper I investigated whether it was possible to adapt the equations for Viviani's curves to the problem of finding a common expression for the curve length when the center of the sphere is located arbitrarily in front of the cylinder. The curve length is interesting since it has been shown for flat transducer elements that the SIR is proportional to the curve length e.g. (2.10). The investigations, however, showed that algorithms for the curve length took on an extensive mathematical formula that required a numerical solver. The approach was therefore abandoned and a method inspired by Theumann et.

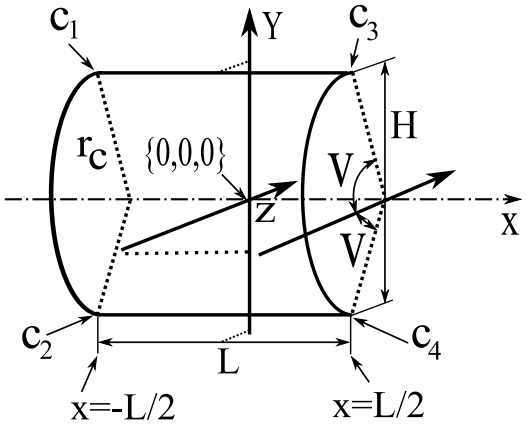

Figure 2.7: Figure defining the geometry and the coordinate system of a considered cylinder section. Figure taken from Paper I.

al [24] was adapted.

The geometry of an elevation focused rectangular transducer element corresponds to an open cylinder and is in Paper I geometrically defined as depicted in Fig. 2.7. The center of the curvature is located at the x-axis along which the element width, L, is defined. The height, H, of the element is defined along the y-axis, and the depth of the field is defined along the z-axis, i.e. into the page. An opening angle, V, and a radius, r_c, define a height, H, and the element's corners are defined as c_1, c_2, c_3, and c_4.

In the paper it is shown that the surface integral (2.9) can be represented with an elliptical line integral

$$H(\theta_{min}, \theta_{max}) = \int_{\theta_{min}}^{\theta_{max}} \frac{r_c c}{2\pi\sqrt{\zeta\cos[\theta+\gamma] - f(\tau)}}\, d\theta. \tag{2.13}$$

The different terms are given by: $f(\tau) = r_c^2 + l^2 - (c\tau)^2$, $l^2 = |OQ|$, and $\zeta = 2r_c l$, where τ represents a given time instance, and $|OQ|$ is a line segment dependent on a point's location relatively to the transducer (see Paper I). The integration angles, θ_{max} and θ_{min}, are found by properly analyzing a projection of the intersection onto circles as illustrated in Fig. 2.8. The intersection between the cylinder section and a sphere is illustrated with the curved arc in the figure. Notice that the actual transducer is illustrated by I. Two imaginary transducers are drawn as II and III, represented with dashed lines in Fig 2.8. The intersecting arc is divided into a left (superscript L) and a right (superscript R), and projections of the intersection onto a left and a right circle are also shown in the figure. As time proceeds in the simulation the angles change due to changes to the intersections.

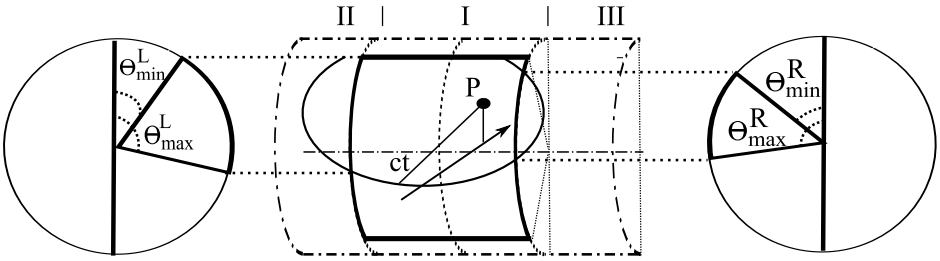

Figure 2.8: Figure showing the projection of the intersection onto two circles. (I) is the actual transducer. (II) and (III) are imaginary transducers. Figure taken from Paper I.

As described in Paper I the equations for the SIR are highly dependent on the point P's location relative to the transducer. The development showed that the propagation medium in front of the transducer can be divided into five different zones in which a point can be located.

No fully analytical solution was found for the integral (2.13) or the SIR in general, however, a semi-analytical solution was found by utilizing the elliptical integral function of the first kind.

Discussion of the results and the validity of the model

Simulations with the developed algorithm are made with Field II as reference in the journal paper.

The simulations are conducted on 2500 randomly distributed points on a transducer with a height, H, of 30 mm and a length, L, of 30 mm. The elevation radius, r_c, is 28 mm. Simulations at sampling frequencies of 3400 MHz and 100 MHz are conducted. The errors are calculated as the root mean square (RMS) of the difference between Field II and a MATLAB implementation of the developed algorithm relative to the RMS of the Field II prediction. This is chosen because an error calculation like this is very sensitive to differences, and it is therefore very important that the same time instances are subtracted. A slight shift in times or differences will hereby immediately be revealed.

The chosen transducer size is relatively large seen in the perspective of medical ultrasound imaging. However, the work is conducted as a validation of the model, and a transducer as chosen is sufficient for this task. A smaller transducer would reveal the same results on another time scale, but would

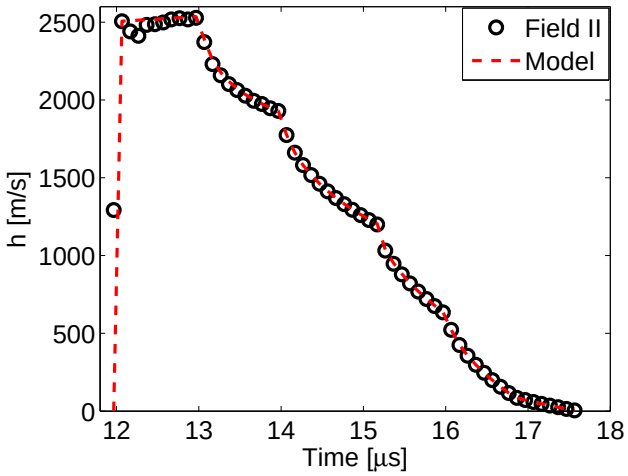

Figure 2.9: SIR at $\{x_p, y_p, z_p\} = \{1, 1, -10\}$ mm. Circles are Field II. Solid line is the presented model. Figure taken from Paper I.

also require considerations of energy conservation of the pulses at lower sampling frequencies. This is, however, a topic concerning the implementation and is for instance to be considered in an actual Field II implementation. By simulating on a large transducer this is partially avoided with the given sampling frequency.

Figure 2.9 shows SIR pulses calculated with the model and Field II at a sampling frequency of 3400 MHz. Circles represent the Field II solution, and the dashed line represents the model. Clearly a good consistency is found. However, it should be noticed that a small inconsistency at the horizontal line segment at around 12.1 μs is found. This is a consequence of the summation principle applied in Field II, and it shows the advantage of the developed algorithm to give a smooth accurate response.

Figure 2.10a is suggested in Paper I. It shows the deviation errors from 2500 random point simulations. The errors are projected down to the xy-plane for visualization. The errors are calculated for each of the 2500 points and simulated at 3400 MHz. The color intensity corresponds to the error and the white square indicates the bounding lines of the transducer when it is projected onto the xy-plane as well. A maximum error of 3.5 % is found. The highest concentration of errors is located inside the square (directly in front of the transducer), and Fig. 2.10b shows the distribution of the errors and indicates that a significant part of the errors is below 1 %. The average deviation is calculated to 0.41 %. The same study applied with a 100 MHz

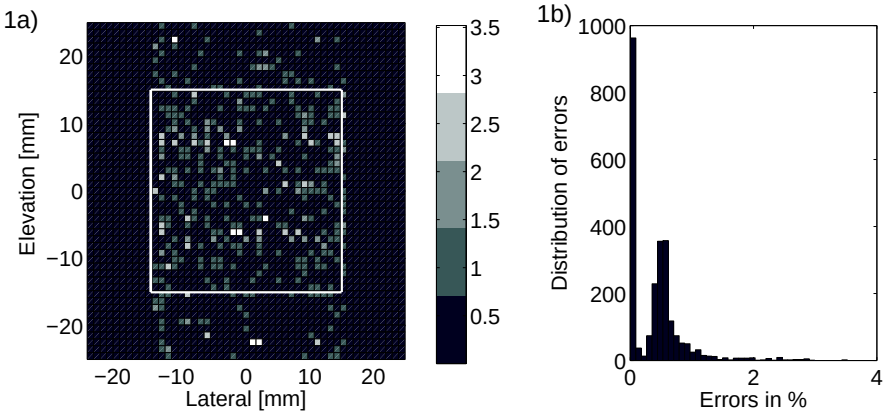

Figure 2.10: 1a) The RMS error for 2500 points, projected down onto the xy-plane. The white square indicates the outer boundary of the transducer. 1b) Distribution of the errors. Figure taken from Paper I.

sampling frequency revealed a mean deviation of $1.37\ \%$, and a maximum error of $24.7\ \%$ was found for a response with a very sharp spike.

A strong validation of the integral in (2.13) can be found if the limit function is applied to the integrand in its full form:

$$Real\left[\lim_{r_c\to\infty}\left[\frac{1}{2\pi}\frac{r_c c}{\sqrt{c^2\tau^2+2lr_c\cos\left[\theta+\gamma\right]-l^2-r_c^2}}\right]\right] = \frac{c}{2\pi}. \qquad (2.14)$$

This yields exactly the same constant $\frac{c}{2\pi}$ that was encountered in (2.10) for flat transducer elements. The algorithm can therefore be used to approximate the response from a purely flat transducer. Calculation of θ will, however, be a numerical unstable task because the angle differences in the integration will be very small when $r_c \to \infty$.

2.3 A new algorithm for a rectangular convex elevation focused transducer

This section is an addendum to and a summary of the work in the journal paper inserted into the chapter Paper II. This paper describes in detail the development and the results of an algorithm for a rectangular convex elevation focused aperture, which was developed in this Ph.D. project.

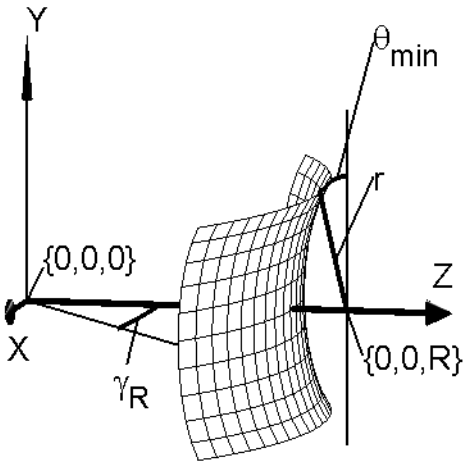

Figure 2.11: Figure showing the geometry definition of a double curved transducer. Figure taken from Paper II.

A rectangular convex elevation focused transducer (double curved transducer) is in this context represented by a section of a torus. It is defined with both an elevation focused and a convex rotation radius. The latter will give a spreading radiation, and the former will concentrate the energy. The geometry is depicted in Fig. 2.11. The transducer is defined in torus coordinates placed in the Cartesian coordinate system. It is represented with a convex opening angle γ_R, which is measured relatively to the z-axis. The z-axis goes directly through the center of the transducer and defines a symmetry. The convex radius, R, is measured from the zero reference to the center of the outer circle, and an inner radius is defined as r. A limiting minimum opening angle is defined as θ_{min} and a similar maximum opening angle is defined as $\theta_{max} = \pi - \theta_{min}$.

The surface integral (2.9) is shown to be representable with a line integral as it also is the case for the rectangular elevation focused transducer:

$$h(t_i) = \frac{1}{2\pi} \int_{\theta_{min}(t_i)}^{\theta_{max}(t_i)} \frac{cr}{|OP^*|\sqrt{1 - \frac{(-k+c^2t^2+2ry_p\cos\theta+2rR\sin\theta)^2}{(2|OP^*|R-2|OP^*|r\sin\theta)^2}}} d\theta, \qquad (2.15)$$

where $k = |OP^*|^2 + r^2 + R^2 + y_p^2$ when a point is defined as $P = \{x_p, y_p, z_p\}$, and $|OP^*|$ is the direct horizontal distance to a point.

The angles θ_{min} and θ_{max} in (2.15) are to be evaluated at each time step as it was for the rectangular elevation focused model. The propagation medium

in front of the transducer is divided into ten different zones at which a point can be located. Each zone has its unique definition of the integration angles in (2.15).

It was not possible to find a direct analytical expression for the elliptical integral (2.15). Instead a suitable approximation is possible because of the integrand's nature. It is shown that an approximation of the term

$$\frac{(-k + c^2t^2 + 2ry_p \cos\theta + 2rR\sin\theta)^2}{(2|OP^*|R - 2|OP^*|r\sin\theta)^2} \tag{2.16}$$

in (2.15) can be achieved by performing a Taylor expansion to second order around either one or three points or by a direct second order polynomial fitting. The three-point Taylor approximation divides the integral into three sub integrations. The approximations result in the expression (2.16) to be representable by $A\theta^2 + B\theta + C$ + higher order terms, whereby the integral becomes analytically integrable.

$$\begin{aligned} I(\theta) &= \frac{1}{2\pi}\int \frac{cr}{|OP^*|\sqrt{1-(A\theta^2+B\theta+C)}}d\theta \\ &= \frac{1}{2\pi}\frac{i\,cr\log\left[2\sqrt{-A\theta^2-B\theta-C+1}-\frac{i\,(2A\theta+B)}{\sqrt{A}}\right]}{\sqrt{A}|OP^*|}, \end{aligned} \tag{2.17}$$

where $i = \sqrt{-1}$. For a programing environment (2.17) is very suitable and can be rapidly calculated.

Each of the polynomial fittings is performed by using three points for finding the unknown coefficients A, B, and C. These three points are located at the upper integration value θ_{max}, the lower integration value θ_{min}, and the mean integration value $(\theta_{max} + \theta_{min})/2$.

Discussion of the results and the validity of the model

Several transducer configurations are tested for this algorithm. Firstly, a double curved transducer with a width, a height, an outer radius R, and an inner radius r of 20 mm, 30 mm, 60 mm, and 90 mm, respectively, is investigated with a 5 GHz sampling frequency. The exact model is solved using a numerical integration, and it is compared to Field II, the one-point Taylor approximation (1T), the three-point Taylor approximation (3T), and the second order polynomial fitting (2p).

Setup: /Solver:	G-K	Field II	1T	3T	2p
Double curved: $\{0, 0, 10\}$ mm	x	0.40	0.80	0.03	0.18
Double curved: $\{0, 0, 105\}$ mm	x	0.49	3.58	0.01	0.83
Double curved: 200 points	x	0.45	1.78	0.01	0.45
Convex no elev.: $\{0, 0, 40\}$ mm	x	6.90	5.90	0.01	0.03
Convex no elev.: 200 points		x	3.80	2.50	2.50
Linear flat: 200 points		x	3.56	3.56	34.86
Linear elev. focused: 200 points		x	4.43	3.46	33.30

Table 2.1: Table showing the different relative deviations of the model and the solvers found in Paper II. The x indicates which solver was applied as reference, and all numbers are in percent. G-k is the Gauss-Konrod numerical solver of MATLAB.

Figure 2.12a shows a comparison between all the solvers as a full pulse view. The results are from a point located directly in front of the transducer in a distance of 10 mm. The difference between the pulses are negligible, and a zoom as shown in Fig. 2.12b is made to reveal the difference. On the zoom it can be identified that the Numerical solver, Field II, and the 3T give consistent results, whereas the 2p and the 1T have difficulties in capturing all the energy of the pulse. The reasons for failure of the 2p and the 1T are different. The 2p method is based on calculating the exact values at the outer integration values, θ_{min} and θ_{max}, as well as at the mean angle value of these two, $(\theta_{min} + \theta_{max})/2$. This results in a polynomial fitting that captures most of the energy stored at the edges and at the mean integration angle, but not necessarily in between these intervals. The 1T method fails, because it approximates the function from the mean integration angle, whereby in this case an inadequate polynomial fit is made at the minimum and the maximum integration angles.

Table 2.1 summarizes the relative root mean square errors for the different simulation cases. The error/deviation is calculated as the RMS of the difference between a prediction by a reference solver and a prediction by one of the other solvers relative to the RMS of the reference prediction. The reference solver for the different setups is in Table 2.1 indicated with an x. The first three rows of the table presents results for a double curved transducer setup with single point comparisons $\{0, 0, 10\}$ mm, $\{0, 0, 105\}$ mm, and 200 points comparison. A 200 points comparison is based on distributing points across all zones in front of the transducer and then calculating the mean relative error from the relative error of all the points. The table also represents simulation studies where a convex non-elevation focused transducer is mimicked. This is done by increasing the value of r to 6 meter. Furthermore, it presents results for mimicking a flat linear transducer element and a linear

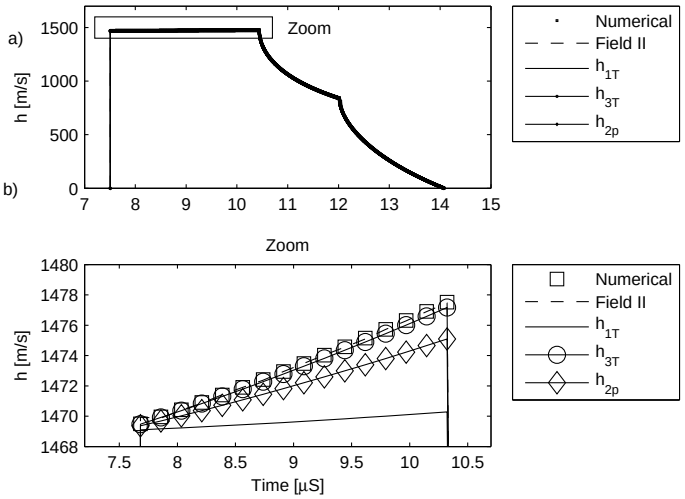

Figure 2.12: Figure showing the comparison between the different solvers. a) Full pulse. b) Zoom onto (a). Figure taken from Paper II.

elevation focused transducer element.

For the double curved simulation the table reveals that all solvers exhibit almost the same error, and it is seen that the situation depicted in Fig. 2.12b, corresponding to the first row in the table, is of no significant influence to the overall error. The 1T solver is seen to give an error of $0.80\ \%$, which is relatively small compared to what the other solvers exhibit. In contrary, it is seen that for steep spike simulations (points far away from the transducer) as represented by the second row in the table both the 1T and the 2p solver are relatively more challenged. With the 200 points simulation both Field II and the 3T stay almost constant in their performance, whereas the 2p has improved its performance.

When simulating a setup mimicking a convex non-elevation focused transducer Field II had to be applied as reference because the numerical solver was unstable for some point calculations. However, the analytical approximations exhibit a much more stable behavior. The error calculations show that the model is still in consistency with what Field II predicts. For linear flat transducers and linear elevation focused transducers it is seen that the 2p solver fails completely. It becomes very unstable for some points and is therefore disqualified for these types of setup.

A consideration of the integrand in (2.15) with the limit theory is useful for validating the model mathematically. Consider the case where the distance

$|OP^*|$ (see paper) is defined with $|OP^*| = R - L$, where L is the horizontal distance from the point to the center of the concave curvature. This will yield

$$Integrand = \frac{1}{2\pi} \frac{cr}{(R-L)\sqrt{1 - \frac{(-k+c^2t^2+2ry_p\cos\theta+2rR\sin\theta)^2}{(2(R-L)R-2(R-L)r\sin\theta)^2}}} d\theta, \tag{2.18}$$

The limit for $R \to \infty$ is

$$\lim_{R\to\infty}[Integrand] = \frac{1}{2\pi} \frac{cr}{\sqrt{-L^2 - r^2 + c^2t^2 - y_p^2 + 2ry_p\cos[\theta] + 2Lr\sin[\theta]}} \tag{2.19}$$

This limit operation changes the double curved transducer to the rectangular elevation focused one. The limit expression in (2.19) is very similar to the integrand of (2.13).

Consider next the case where the limit $r \to \infty$ on the latter limit is performed

$$Real\left[\lim_{r\to\infty}\left[\frac{1}{2\pi}\frac{cr}{\sqrt{-L^2 - r^2 + c^2t^2 - y_p^2 + 2ry_p\cos[\theta] + 2Lr\sin[\theta]}}\right]\right] = \frac{c}{2\pi}. \tag{2.20}$$

This reveals the constant factor $\frac{c}{2\pi}$, which was found for the planar transducers in (2.10) and in (2.14). This makes the model consistent with the literature findings.

2.4 Conclusion

The study presented in Paper I reveals that a semi-analytical model can be formulated to calculate the SIR in consistency with Field II. This model is the exact solution to the complicated surface integral of the single curved transducer. It was, however, not possible to find an exact simple analytical solution to this model. The model avoids discretizing the transducer surface and can therefore give smooth curves on an analog time scale. The RMS deviations for 2500 random points are ranging from 0 % to 3.5 %, and the mean error was found to be 0.41 %. This is valid for a sampling frequency of 3400 MHz and with Field II as reference. When the sampling frequency is lowered to 100 MHz the mean error was found to be 1.37 %, and the maximum error was 24.7 %, which is for spiky pulse responses.

The model presented in Paper II shows that an elliptical line integral can be formulated for the complicated surface integral of the double curved transducer. This elliptical integral is an exact model to the SIR, but no direct analytical solution was found to it. The integral can, however, be solved with a second order polynomial approximation to a part of the integral's integrand. When the integrand is approximated like this it gets possible to integrate the elliptical integral and find an analytical solution. The accuracy of the approximation is therefore dependent on the accuracy of the polynomial fitting. Best results are achieved by dividing the integral into three parts. A Taylor expansion of each interval exhibits best accuracy and stability for finding the polynomial fit. A mean RMS accuracy of 0.01 % can be found when comparing the prediction from 200 random points solved with the three-point Taylor approximation and with a numerical integration of the exact integral as reference. Field II exhibited in comparison and RMS deviation of 0.45 % for the same comparison. A convex non-elevation focused transducer can be mimicked with the model. This yields a RMS deviation of 2.5 % when compared to Field II and 200 random points predictions. A linear flat transducer can be mimicked with a mean RMS of 3.56 % compared to Field II predictions on 200 random points. Finally a linear elevation focused transducer can be simulated with a mean RMS of 3.46 % relative to the Field II prediction.

A given implementation into the Field II software of this model is recommended to be done by dividing the integration interval into three parts. More Taylor point approximations can also be performed in the predictions. This will, however, not lower the RMS error significantly, since the three point approximation exhibits a very low error on its predictions. Instead, more subdivision of the integral will increase the computation time.

2.5 Future development

A calculation speed comparison between Field II and a C-implementation of the models presented in Paper I and Paper II would be the next step in qualifying the models for a practical implementation into a program such as Field II. This process has been initiated. In principle a stable implementation of the model in Paper II would make the elevation focused rectangular model superfluous. It should, however, be investigated more in depth if this is always the case for all configurations of R, r, height, and width.

The degree of curvature that can be accepted for the models should also be addressed in a future study. It was indicated in the literature review that the

Rayleigh integral could be accepted for slightly curved transducers. This is, however, a weak definition, and an exact definition of this term would be a natural follow-up on the presented study.

It should also be remembered that the presented SIRs assume that the transducer surface moves uniformly and as a piston. This approximation may be valid for many transducers, but a natural question that arises is how much curvature can be allowed before interfering surface waves, traveling across the surface, becomes of noticeable influence for the piston movement and how much does the roughness of the surface influence the solution? This should also be addressed in future investigations. Both of the above aspects may be best solved through a finite element study of such a model.

A conference paper on the double curved transducer model, which is accepted on Abstract I, is in preparation.

CHAPTER

THREE

Combining Field II with piezoceramic transducer models

A calculation of the emitted pressure from medical ultrasound transducers by utilizing Field II requires knowledge of the transducer surface's exact geometry, the input terminal's excitation wave form, and the electrical to mechanical impulse response of the transducer. The geometry of the transducer mainly determines the spatial impulse response (SIR) as described in Section 2.1.1, and is, for certain transducer geometries, easily set up with the Field II software. The wavelets have to be calculated externally or measured. The actual pressure pulse as measured in an experiment will be dependent on the SIR convolved with the excitation pulse and the transducer's surface acceleration, which is mathematically described in equation (2.11) in Section 2.1.1.

The importance of knowing the volt-to-surface acceleration for a transducer in connection to the simulation software Field II can be realized when in-vivo experiments in medical imaging research are to be performed. Such experiments are only allowed if a limited amount of ultrasound energy is transmitted into the human tissue. Intensity measurements are therefore to be conducted prior to a new measurement setup, where the emitted amount of energy is unknown. A hydrophone measurement is a reliable way of ensuring a satisfactory intensity level, however, it is also a cumbersome procedure if the experimental waveform is often changed. Prediction of the intensity level through simulation would lighten this procedure.

The motivation for the work presented in this chapter is to investigate a hybrid modeling of pressure fields with piezoelectric transducer models and the Field II simulation software.

The chapter is organized in five major sections. The first section gives a brief review of literatures utilized in the investigations. The second section comments on the author's work presented in the journal paper found in the chapter: Paper III. This paper presents a one-dimensional model in combination with Field II, and it compares one-dimensional simulations with measurement on both a circular piezoceramic disc and a more complex convex medical transducer. The section following discusses the simulation parameters' influence on the one-dimensional model as documented in the author's conference paper found in the chapter: Paper V. The third section discusses the results found in the author's journal paper found in the chapter: Paper IV. This journal paper compares the one-dimensional modeling principle with a full three-dimensional axissymetrical model, where both models are combined with Field II. A discussion and a conclusion then follows. Finally the chapter is ended with comments on future developments.

3.1 Inspiring literatures for the development

The literature addressing piezoelectric transducer modeling is very exhaustive. Piezoelectric modeling is a well established knowledge, and it would be overwhelming to comment on all the relevant references that has been published since the works by Mason [29], Redwood [30], or Krimholtz et al. [31] became sort of the golden standard for equivalence diagram transducer modeling of piezoceramic transducers. Instead, this section briefly emphasize some of the works that have given inspiration to the publications discussed in this chapter. More references can also be found in the author's works inserted in the chapters: Paper III, Paper IV, Paper VI, Paper V, and Paper VII.

First of all the work "Acoustic Fields and Waves in Solids" by B. A Auld [32] should be mentioned. This book is a comprehensive work on acoustic wave fields and waves in solids. It describes and derives the basic principles behind the acoustics and electrostatic behavior of solids. The reference is an ideal starting point for understanding the acoustic vibrations in solids due to the piezoelectric effect and wave propagation in solids. It considers vibrations mainly in three-dimensional coordinates when dealing with theory, and it gives examples mostly in one-dimensional form. Furthermore, it presents some basic one-dimensional models for transducers based on the transmission line models in perspective of the KLM [31] modeling principle. The theories and examples presented are suitable for composite transducer simulation.

"Piezoelectric Transducers and Applications" [33] is also a work that needs to be mentioned here. It is a good preview into the piezoelectric transducers and presents several transducer principles by means of the transmission line model. The models are based on simple analytical models, by using the analogy to standard electronic components. Furthermore, the book describes electronic systems for driving the different transducers. It gives a nice overview of the piezoelectric transducers.

The journal paper [5] by Willatzen 2001 is deriving the piezoelectric constitutive equations from a thermodynamic perspective. These equations are limited to the one-dimensional case, in which plane harmonic waves are considered. By applying one-dimensional assumptions the article models and derives a reciprocal transducer system with backing layer, piezo layer, and two matching layers to a given fluid. The model has the advantage that it can model both mechanical and electrical losses and damping in the different mediums by considering the physics of the ultrasound's interaction with the medium. Furthermore, it can be coupled to any electronic driving network when knowing the impedance of these networks. The method is a good starting point for modeling since the model contains a potential for being expanded into two- or three-dimensional coordinates as well as cylindrical coordinates. An earlier paper by the same author concerns the same model [34]. The journal is furthermore a good addendum to the work by Auld [32].

An interesting paper by Maréchal et al. [35] shows that rather accurate results can be achieved with the KLM model for focused and axisymmetric transducers. This article is using an expanded form of the KLM model to model a one-dimensional axisymmetric transducer with a lens in front. It uses the reflection and transmission coefficient principles between each single layer. The extension to the KLM model is a curved lens which is divided into circular rings, and it applies Snell's law to find the refraction of the elements. The response is then integrated up across the front to model the acoustic field at the focal point. The model is validated against experimental and FEM results which exhibit good similarity. From this journal it can be learned that focused transducers can be modeled accurately with simple models.

P. Schnabel [36] presented an interesting modeling principle with piezoelectric transducers in cylindrical coordinates. It was shown how the different vibration modes and their dispersion could be studied. It was also shown how the coupling between a surrounding non-piezoelectric rim could be considered in relation to the piezoceramic.

Algueró et al. [37] published a set of material parameters for the Pz27 piezoceramic with a variety of shapes. These parameters they achieved by mea-

surements. Their intention was to predict these parameters from a few measurement. These parameters has an imaginary and a real part and can be used to simulate the loss mechanism of the the piezoceramic.

A good discussion on the implementation of finite element equations with boundary conditions and several simulation examples can be found in the master thesis by Amby [38] 2005.

The interested reader can find a derivation of the full three-dimensional equation set in Cartesian coordinates for the piezoelectric effect in solids and from a thermodynamical point of view in Appendix A.

3.2 Field II combined with a one-dimensional transducer model

Despite the many modeling principles that can be found in the literature the modeling principle by Willatzen [5] was elected for initial investigation in combination with Field II. The results of this is found in the journal paper Paper III, which fully documents this work.

The modeling principle was chosen due to several reasons. Firstly, the model can reveal the displacement, velocity, acceleration, and electrical conditions of an arbitrary number of solid layers, piezoelectric as well as non-piezoelectric. This is true for the case, where the transducer is assumed to move one-dimensional. An implementation of the modeling principle can be easily performed into a MATLAB or a C-environment when continuity of velocity and tension are preserved at the boundaries as described in Paper III. Yet another advantage of the model is its avoidance of calculating equivalent model parameters. This qualifies the model for a simple intuitive implementation. Secondly, the model is capable of modeling attenuation of the wave propagation inside the solids. Similar abilities are also applicable for the classical electrical equivalent models e.g the KLM model, but by comparing the literature on these transducers the simple one-dimensional model [5] was found more suitable and interesting in combination with Field II. The reason is its simplicity and its potential for revealing information on the transducer's behavior.

The results presented in Paper III on both a simple Pz27 piezoceramic and a commercial convex array show that good consistency between prediction and measurements is achieved. The amplitude on pressure pulses is found to be calculated within ± 2 dB. The root mean square (RMS) errors calculated as the RMS of the difference between pressure pulse prediction and measure-

ments and divided with the RMS of the measurement are found in the range between $11\ \%$ and $36\ \%$. Measurements of the current through the Pz27 samples are found to exhibit a deviation of $8 - 36\ \%$. As commented on in the journal paper, these errors may seem large. However, the RMS comparison is very efficient to reveal differences, and by considering the plot comparisons it becomes clear that the pulses are very closely related. Worst responses are found for short pulses.

Intensity profiles for the commercial transducer is found to be predicted within $5.9\ \%$ to $20\ \%$, and the profile shapes indicate that the geometry of the transducer element is well captured.

A tendency for the pressure pulses is the drifting of the pulse tails. It is seen that a pressure pulse can be nearly $\pi/2$ out of phase, which indicates that the free oscillating behavior of the model has a resonance frequency that is slightly different from the measured. This is commented on in the journal paper, and it is concluded that to improve on this error a better attenuation algorithm is required and a better control of the input parameters is needed. This also helps explaining that worst RMS results are found for short pulses.

The attenuation assumptions applied are not frequency dependent and are restricted to a mechanical quality factor or measurements published by Algueró et al. [37]. Modeling a frequency dependent attenuation would improve the results.

Despite the transducer model's simplicity it is capable of predicting rapid changes of the current pulse shape of the Pz27, which e.g. is seen in the current plot of Fig. 3.1. In the figure a measurement (M) is compared with the simulation results where an attenuation based on a real valued parameter set [5] and a complex valued parameter set [37] is used as characteristic input parameters. It is seen how the tail of the measured current pulse rapidly changes direction and how well the model captures this change. Such changes are in principle difficult to capture for a simple model like the one applied here. It is therefore a strong ability of the model that the rapid change in the tail oscillation of the current pulse is captured. The figure also reveals that the model works well with both sets of simulation parameters.

The modeling of the commercial transducer is a rather difficult task. It consists of a complicated structure which consists of five material layers. Many years of electronic design by the manufacturer have developed a complicated driving circuit, which is not fully accounted for in the modeling. An exact model of the electronic will therefore affect the amplitude deviation in the positive direction.

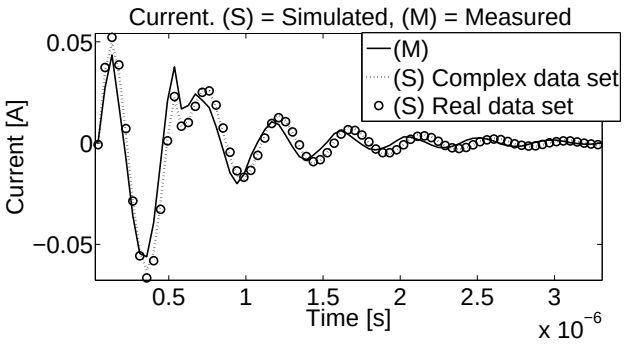

Figure 3.1: Current comparison between measured (sold) and simulated current through the electronic circuit. Two simulation parameter sets were applied. One complex-valued (dotted line). One real-valued (circle). Figure taken from Paper III.

An array transducer as the one considered is fabricated to behave as an ideal piston. This is attempted by dicing a single transducer element into smaller rectangular elements. The small elements are then intended to operate as one-dimensional pistons. The overall response is therefore a summation of all the contributions, which is why it is assumed that it is possible for a simple one-dimensional simulation model and the measurements to be closely correlated.

Considerations about both acoustic and electronic cross talks are neglected in the modeling. These phenomena are not possible to model with the one-dimensional model and Field II, but should ideally be considered as well.

The modeling is performed in a hybrid modeling environment between a piezoceramic model and Field II, which sets these natural limitations. It therefore must be argued that it is very satisfactory results that has been achieved with the modeling in the journal. The model is therefore a good candidate as an permanent model implemented into Field II, and it can be used for fast prediction of the pressure pulses.

3.3 An investigation of simulation parameters' influence on the one-dimensional modeling

The chapter Paper V includes a conference publication by the author, which is a follow-up on Paper III. On the basis of the findings presented in Paper III it was necessary to investigate how sensitive the transducer model is to inaccu-

racies and changes in the characteristic simulation parameters. The validity of the input parameters to simulations should always be questioned in a simulation study. In a transducer modeling study where results are compared with measurements on a commercial transducer as complex as the one used in Paper III is it even more critical to consider the results in relation to the input parameters. The conference contribution described in Paper V addresses this topic for the commercial transducer investigated in Paper III.

The study is conducted with the measurements from Paper III as reference. Each input simulation parameter, that is not concerned with the Field II simulation domain, is altered ± 20 % in steps of 2 % while all other parameters are kept at the intial value. Two comparisons are made. One where the RMS deviation between predicted pressure pulse shapes and measured pulse is considered and one where the difference between intensity measurement and prediction is compared. These two comparison each reveal their valuable information. The pressure pulse comparison reveals how the given parameter affects the pulse shape and phase of the pulse. The intensity comparison reveals how the given parameter affects the overall energy of the pulse. Both comparison are valuable dependent on the perspective of the study. An investigation interested in the pulse form comparison is a very phase sensitive study. An investigation with focus on the intensity error may be considering FDA regulations.

The study reveals that the pressure pulse comparisons are mainly sensitive to changes in the density, the stiffness, and the thickness of the piezoceramic and the lens material. The lens material shows out to affect the model the most. It is amongst others shown that a -4 % change in the lens stiffness yields a 6 % change in relative RMS error, and a -4 % change in the piezoceramic stiffness yields a -1.2 % change. The latter implies that the error is being improved on. The influence of the matching layers is of relatively less influence compared to the ceramic and the lens. For the intensity predictions is it shown that the pulse errors are mainly sensitive to the piezoceramic and the loading electronic.

The study indicates that the source for errors can be found in all of the simulation parameters. Focus should, however, mainly be on optimizing the stiffness, the density and the length of the piezoceramic and the lens if better results on the given transducer is to be achieved.

3.4 Combining Field II with an axisymmetric finite element model

This section discusses the findings in the journal paper by the author and found in the chapter: Paper IV. This journal paper presents the mathematics of a finite element model (FEM) for an axisymmetric piezoceramic transducer, and it compares the FEM with the one-dimensional modeling principle described in Paper III. The axisymmetric model is inspired by the publication by Schnabel [36] and was implemented in an extended form into the finite element software from Comsol [39].

The axisymmetrical model in Paper IV is interesting as a model because it benefits from expressing a complicated interaction between particle movement in the thickness direction and movement in the radial direction under the assumption of linearity, no rotation, or torque. This is performed through a set of partial differential equations in cylindrical coordinates, and it can reveal exactly the same information as the one-dimensional model in Paper III and more to it. The model therefore has a great potential for revealing the exact behavior of a crystal's thickness and radial movement with an arbitrary number of adjacent material layers, and it is easily combinable with Field II if the surface response is integrated and averaged.

The journal paper models a Pz27 piezoceramic circular disc with silver electrodes mounted on both sides. This piezoceramic is identical with the discs found in Paper III. The FEM model is furthermore modeling a plastic rim placed along the perimeter of the discs. This is done to mimic a transducer fixture and to create an isotropic domain in which the radial waves can propagate. As an extension to the FEM model the paper is also concerned with showing how the impulse response of the transducer impedance can be used to load the ceramic with an arbitrary electronic loading. This is shown to be possible outside the FEM modeling domain. The motivation for the paper is therefore clearly to further validate the modeling principle in Paper III, to study the influence of the coupled modes, the frequency response, the pressure, and the hybrid modeling with Field II.

Note, however, that the FEM is significantly more complicated and cumbersome to implement than the one-dimensional model. It is therefore a trade-off between complexity and relevant information needed in the context of a Field II simulation that should determine the relevance of applying this model in ultrasound imaging context.

The results show that an exact comparison between pressure pulses can be

made between the one-dimensional model and the FEM when radial movement of the outer boundaries of the ceramic is prevented. This is valid both when a loading electronic network is applied and not. If the radial movement is allowed, then a decrease of 2 dB in pressure amplitude is found on the FEM model compared to the one-dimensional one. A similar decrease of 1.5 dB is found when an electronic network is accounted for. Small resonance spikes below the main resonance frequency is revealed as a consequence of the free radial movement. These resonance spikes cannot be captured with the one-dimensional model. It is therefore expected that the amplitude for the FEM should be smaller than for the one-dimensional one. The shape of the pressure pulse predicted with the FEM model is seen to have a slightly more bulky pulse tail, which is due to the allowance of radial movements of the boundary.

3.5 Conclusion

Modeling of pressure pulses with a one-dimensional modeling principle as suggested by Willatzen [5] can be made within ± 2 dB with a circular pz27 piezoceramic and a convex commercial transducer. This is with the assumption that manufacturer information on the simulation parameters are exact and with an approximation of the electronic loading network. Pressure pulse shapes can be predicted with an RMS deviation of $11 - 36\ \%$ and a deviation of $8 - 36\ \%$ on current pulse measurements. Intenity profiles can be predicted with an RMS of $5.8 - 19.8\ \%$.

For better prediction is it needed to consult the input simulation parameters more accurately. Especially the stiffness, the density, and the length of the piezoceramic and the lens material of the commercial transducer.

The one-dimensional model was found to give exactly the same pressure prediction in combination with Field II as a circular axisymmetric model where the outer radial boundary is constrained to no movement. If the boundary is free and only restricted by a plastic ring will the one-dimensional model overshoots on the amplitude.

3.6 Future development

A more exact prediction with the hybrid modeling attempts can be found if the input parameters are measured for each transducer element. This is

therefore an obvious topic for future investigation which users of this work should be concerned with.

It would also be beneficial to pursue if a backward prediction of the actual simulation parameters that are needed to simulate complicated medical transducers could be made. As implied earlier, simulation parameters for medical transducers are somewhat bound by confidentiality by the manufacturers. General users of Field II and the mathematical models presented here may therefore be left to a guessing or estimation of the needed input parameters. This clearly has the drawback that it can have an infinite number of combinations, and as a consequence it would be easier simply to measure the impulse response. It is therefore suggested that future development is concerned with a backward estimation procedure that can reveal the simulation parameters accurately.

Surface measurements of the vibrating surfaces for both the circular piston and the medical transducer would also be interesting projects as a follow-up to conduct. These would reveal the actual behavior of the non-ideal surface and give an idea of how well the planar approximation is valid. Attempts to measure the surface movements with an interferometer of the convex medical transducer has been attempted in the project. However, it showed out to be a rather difficult task since the surface is dark, curved, and very rough. The experiment therefore gave no valid and stable information. Acoustical holography experiments conducted by Sapozhnikov et al. [40], however, indicated that the axisymmetric assumption of a circular piston is very well valid. A holography investigation of the convex transducer could therefore also be attempted with the model suggested in Sapozhnikov et al. [41].

A comparison with measurements is in Paper IV not investigated. It could, however, be interesting with a follow-up on this in a future development to see if the FEM pressure prediction can get closer to the measured.

CHAPTER

FOUR

Capacitive micromachined ultrasonic transducer simulations with Field II

Field II was originally developed with the classical piezoelectric transducers in mind. As consequence, all of its currently predefined transducer geometries are based on flat, curved, or double curved transducers with rectangular elements as the ones which are often found in medical imaging applications. The improvement of Field II's support of other transducer geometries has to date not been of major concern since the piezoceramic transducers have been dominating within the field of ultrasound imaging.

The Capacitive Micromachined Ultrasonic Transducer (CMUT), however, has become a fast developing transducer which has caught significant attention from the medical imaging community. A CMUT transducer for medical imaging can in principle take on any transducer geometry. It is build up of smaller capacitive units, which typically have a circular, a rectangular, or a hexagonal shape. Field II does currently not have predefined models for these kinds of transducers.

This chapter describes an investigation of these new transducers in relation to Field II and ultrasound imaging. Consequently, this chapter is dealing with a technology study of the CMUT and a feasibility study on what it takes to combine Field II with these new transducers. The chapter is structured as follows: First a review of the technology and the relevant literature is done. Then a discussion on combining Field II with CMUTs follows. Finally different studies are presented and commented on.

4.1 A description of the CMUT technology

This section describes the principle of operation of a CMUT.

A classical CMUT transducer is based on the capacitor principle. It is a transducer that consists of a bottom electrode, an insulation layer, a vacuum sealed air gap, a top plate/membrane, and an electrode as shown in Fig. 4.1.

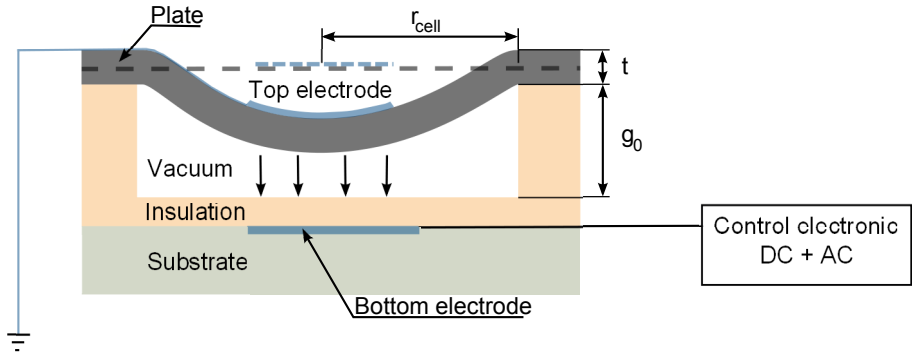

Figure 4.1: A typical cross section of a circular axissymetric CMUT membrane.

The two electrodes are defining the capacitor. By applying a DC bias across the electrodes an electrostatic force will displace the electrodes toward each other. This force results in a deflection of the top plate and of the top electrode whereby the capacitance of the CMUT changes and exhibits a spatial dependency. The deflection makes the plate pre-stressed and the transducer therefore becomes highly sensitive to any disturbances such as an incoming pressure wave or an applied AC excitation. Any vibration forced by an incoming pressure wave will result in a measurable change in the capacitance.

The amount of static deflection is highly dependent on the DC bias. If the voltage is relatively small, only a slight deflection will occur, and the CMUT will be less sensitive to disturbances. However, if the DC bias is increased until a certain value at which the electrostatic force becomes greater than the upward directed forces of the top plate, a collapse or a so called pull-in will occur. The DC value at which this occurs is called the pull-in voltage. At pull-in the bottom of the top plate collapses and sticks to the bottom insulation layer. At this configuration the plate displacement becomes highly non-linear, but the transmission and the receive sensitivity can be improved by changing the state between pull-in and snap-back, which is the term for a plate leaving the collapsed mode [42,43]. The drawback of a collapsed CMUT is the stressing of the plate which may become unreliable over time. Conventionally the CMUTs are driven at a DC bias around $80 - 90$ % of the pull-in

voltage.

Because the pull-in is a highly non-linear operation, calculations become difficult. To date exact calculations on the non-linear operation require FEM tools, and it is usually desired to operate in the approximately linear domain when analytical calculations are to be made.

The geometry of a CMUT can vary. Typical geometries are circles, hexagons, squares, or rectangles, but in principle no limitation is made to this. An array transducer for medical ultrasound applications will have each element build up of many smaller CMUT units. In conventional CMUT terminology each unit is called a cell. All cells on an array element are excitated at the same time and with the same pulse. The cells thereby operate as one unit.

A piston type CMUT transducer can also been found in the literature [44]. This reference presents fabrication and measurements off a piston CMUT. A piston CMUT is a classical CMUT but with an extra mass at the center of the top plate. The width of the mass can be as the width of the electrode. The benefits of this method are a more uniform electrical field and a more ideal-piston shaped movement. This gives better transmission and receiving efficiency compared to the classical CMUTs with uniform thick top plate. Several references reporting on this transducer type can be found in [44].

The CMUT technology has some advantages and disadvantages compared to classical piezoceramic transducers [45]:

- + CMUTs have a much poorer ringing effect than piezo. As a result CMUT impulses are very short and broad banded (typically $> 100\ \%$ when submerged)
- + Because the CMUT has a much lower acoustic impedance than piezo then matching layers are less critical for efficient transmission of the waves
- + Opposite piezoceramic transducers then CMUTs do not need backing layers. CMUTs transmit most of the energy into the medium
- + The couplings coefficient can in principle be $100\ \%$ for CMUTs
- -/+ It is possible to transmit at a pressure level identical to piezo. However, this brings the current technology to its maximum level (2005)
- -/+ CMUTs are operating in the non-linear domain compared to piezo

A basic description of the fabrication process of the CMUT is very helpful in understanding the CMUT structure and operation. For this Fig. 4.2 is convenient. The following description is based on the wafer bonding technique. This technique requires a conductive silicon wafer as illustrated in (a). This wafer is exposed to thermal oxidation whereby an oxide layer is grown on top of the wafer (b). A fine mask is then put on to the oxide layer, and a pattern is etched into the oxide using e.g. lithography and etching fluid (c). A second oxide layer is then grown to create an insulation layer (d). A second silicon wafer, that is to be used as the top plate, is bounded to a carrier wafer(e). These are separated with an oxide layer, and the construction is called a silicon-on-insulation. The carrier wafer is necessary because the silicon that is to be used as plate, is very thin and may brake when the bonding is performed. Flipping the construction in (e) upside down and bonding it with the construction in (d) creates the construction in (f). The carrier wafer and the oxide are then removed by grinding and etching. Electrodes can afterwards be deployed to the top and the bottom to create the electrical connections. The fabrication is applying standard processes found in the semi conductor industry which makes the CMUTs attractive for mass production.

More advanced manufacturing processes where e.g. electrode connections from top to bottom, flip-chip bonding, or piston shaped CMUTs are described can be studied in detail in other works such as [44,46–49]. These works again reference several publications on the topic.

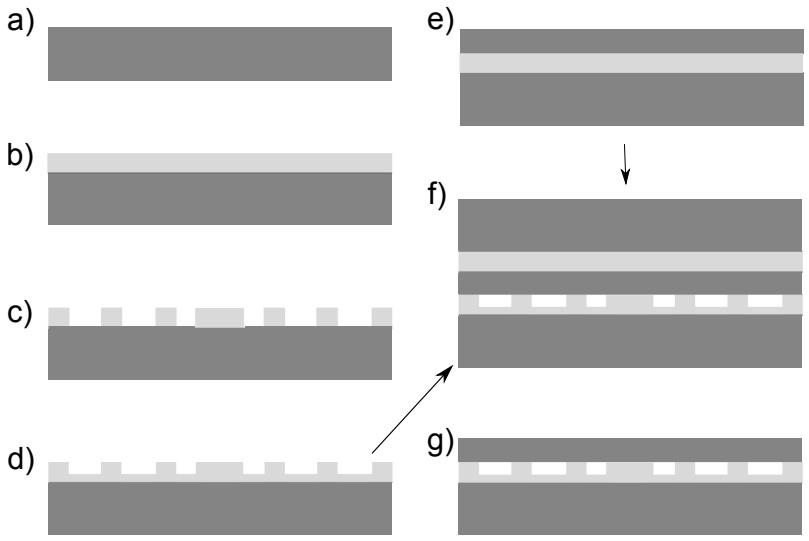

Figure 4.2: A typical process layout for CMUT fabrication using wafer bonding.

Modeling plate deflection of CMUTs

A model that can calculate a realistic deflection of a cell's top plate is needed to conduct the intended investigation. A literature review reveals that there are several attempts to model the deflection behavior of CMUT transducers and their transient and dynamical behavior as well. Some of the modeling principles can be found in [50–53] which again reference several other works. The literature review reveals, however, that due to the complexity in the non-linear behavior of the top plate displacement, certain approximations have to be made. Most of the analytical expressions are only applicable for the static situation and are usually calculated on the basis of an equivalent piston model.

In this context two authors' works should be mentioned. The first work is the publication by Lohfink [54]. She presents a one-dimensional model that relies on finding an equivalent resonance frequency, an equivalent area, and a mass of the deflected plate from which the CMUT can be modeled as a one-dimensional mass-spring-damper system. These equivalents are, however, found from a static and a harmonic FEM simulation. She validates the model against ANSYS FEM simulations, and a very good consistency between a simple one-dimensional model and FEM is seen.

The second work that is to be mentioned is the dissertation by Wygant [55] and his paper [56] based on [55]. This literature present a one-dimensional equivalent model that calculates the deflection based on an average deflection of the plate. Simple expressions are given for the pull-in voltage, and equations that account for slight non-linear effects are presented as well. This model does not require pre-calculated FEM parameters and can therefore be used for a fast initial estimation of the pull-in voltage and the degree of deflection. It is, however, only valid for calculations on circular cells and with weak non-linearities. Because of the model's simplicity is it chosen for calculating the plate deflection in the following investigations. A short review of the theory and the mathematics for this model can be found in Appendix B.

4.2 Assumptions in combining Field II with CMUTs

As mentioned in chapter 2 Field II calculates the pressure or the pulse-echo response by calculating the SIR. The same technique is also possible with CMUT transducers. A single CMUT cell can take on several geometries such as the ones of circular, rectangular, hexagonal etc. Only for the special case, in

which the cells are circular and the plate is deflected uniformly with the curvature of a sphere, analytical solutions for the SIR can be found as shown by Arditi et al. [18]. The calculations for a whole element in this special case are easily performed through a coordinate translation of each cell. A summing of each cell's response would yield a full transducer element's response as a linear approximation and with no cross talk consideration.

To cover CMUT geometries with the Field II program a surface discretization with small flat mathematical elements as the ones Field II currently utilizes for all other transducer geometries is necessary. This approach would avoid the process of developing new algorithms for the SIR of all the known geometries that a CMUT currently is seen to be manufactured with.

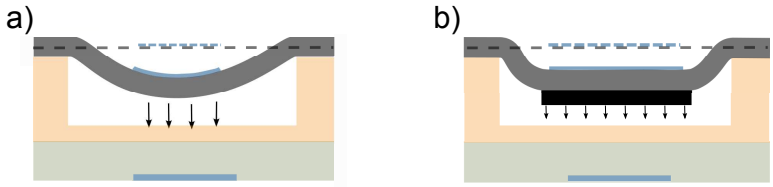

Figure 4.3: Figure showing the cross section of two types of CMUT cells. a) Classical CMUT. b) Piston CMUT with an extra mass added at the center.

Figure 4.3 shows the deflection situations for two types of cells. One for regular classical cells and one for piston type cells. Plate material in the middle of the cell will for the case in Fig. 4.3a be moving a longer vertical distance than plate material at the edges. The movement of the edge material will, however, not be entirely normal to the surface as required for the SIR to be valid. It is therefore necessary to assume that when a cell is excitated with a small AC waveform, then the movement of the plate is approximately similar to that of a piston moving in the normal direction of the deflected plate surface. This approximation is very similar to what is required in the case of curved transducers developed in the journal papers in Paper I and Paper II. For piston type cells as depicted in Fig 4.3b this approximation becomes even more valid. This is because a large fraction of the plate is moving as a real piston, and the side material will have a relatively little contribution to both the pressure field and the electrical field.

For large AC waveforms these approaches will most likely fail because of the non-linear stretching of the plate, and collapsed mode studies may also break down in the near-field. Furthermore, these considerations are only of significant influence for the case where the wave length of the transmission is much smaller than the curvature and the radius of the cell it self. For cells placed in a pattern of cells on a large transducer element, these possible errors

become of small influence far from the element. Hence, it is expected that for medical imaging applications the influence of the non-ideal radiation pattern from each cell will be very small far from the transducer element.

If the above assumptions can be accepted in a simulation, a Field II simulation, where each cell is subdivided into smaller mathematical elements and where an external program calculates the cell's deflection profile, will be possible.

4.3 Study cases and results

A program that defines CMUTs in Field II terminology was crated. This program sets a user defined number of cells on each transducer element in a linear one-dimensional or two-dimensional array. These cells can be set with a deflection that is dictated by the solution to the static deflection model presented in [55] and described in Appendix B. This model is solved by setting the effective cell radius, r_{cell}, and proper material properties. The distribution of the cells can be performed in an evenly spaced grid with a NxM number of cells along the lateral direction and the elevation direction, respectively. The cells are placed with a cell-to-cell pitch which is the same in both directions. A minimum pitch corresponding to a cell's diameter is allowed. The excitations of all the cells are set identical to the excitation of the corresponding element.

The number of mathematical elements needed to resolve a single cell is controlled with a resolution factor, n. This factor is an integer number and corresponds to the number of mathematical elements that fits across a cell's radius. It therefore scales the number of elements with the radius of the cells.

Figure 4.4 to Fig. 4.6 show examples of how the current CMUT program works. The plots show all mathematical elements as defined in Field II.

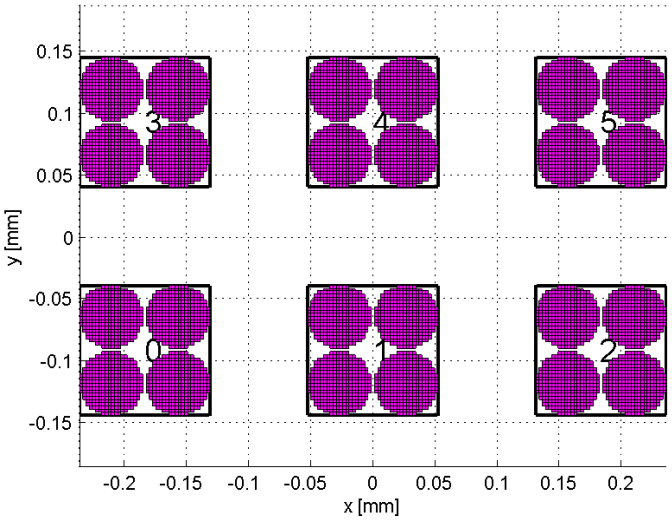

Figure 4.4: Example of a 2x3 multi row transducer. Each element has 4 cells.

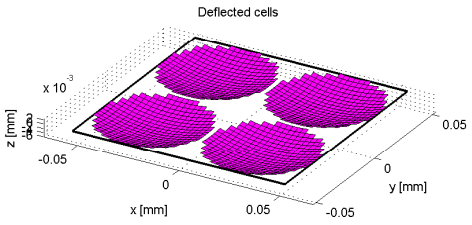

Figure 4.5: Example of an element with four cells having a shape function. Notice that the deflection is amplified with 100 for easier visualization.

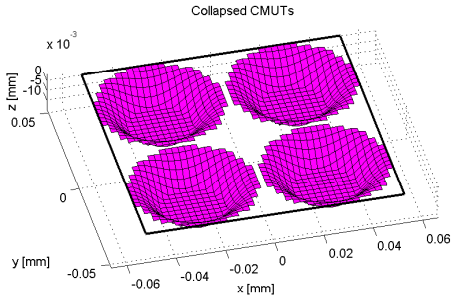

Figure 4.6: Example of a collapsed cell. Notice that the deflection is amplified with 100 for easier visualization.

4.3.1 Approximating the spatial impulse response of a single cell

If it is assumed that the cell deflections are infinitely small, whereby each cell is considered a plane piston, the only physical difference between a full transducer element with each cell modeled (ECM) or as a single square model (SSM), where no cells are considered, is the active area. Clearly the active area

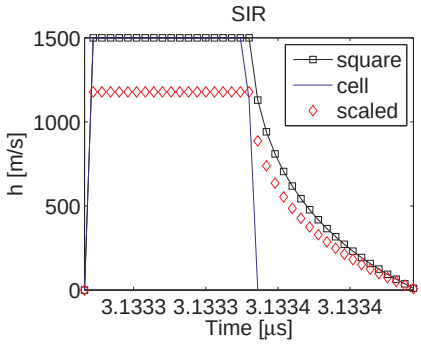

Figure 4.7: Spatial impulse responses for a square element, $square$, a flat circular cell with no deflection, $cell$, and a scaled version of $square$, $scaled$. Sampling frequency 10^4 GHz. Only each 12th point is shown.

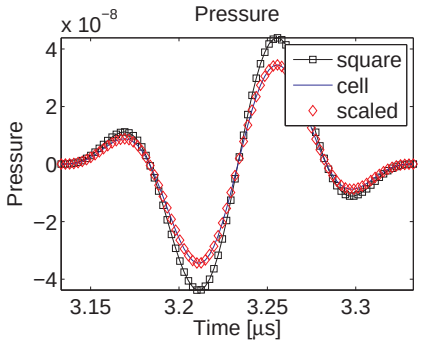

Figure 4.8: The pressure corresponding to the spatial impulse responses in Fig. 4.7 when a two cycle Hanning weighted tone burst at 10 MHz is applied. Sampling frequency 10^4 GHz. Only each 24000th point is shown.

for a SSM is bigger than the one for an ECM. If it is furthermore assumed that the cells are distributed with a pitch corresponding to twice the cell radius, i.e. the boundary rims being in contact, the fraction between the active areas will be

$$f = \frac{A_{square}}{A_{cell}} = \frac{2r_c 2r_c}{\pi r_c^2} = \frac{4}{\pi}, \tag{4.1}$$

where A_{square} is the active area of the SSM, and A_{cell} is the active area of an ECM.

Consider a single cell with a radius of $18\ \mu m$. If the SIR is calculated at a point $\{x_p, y_p, z_p\} = \{0, 0, 4.7\}$ mm for this cell with no deflection and a corresponding cell approximated with a rectangular transducer element with the height and the width of twice the cell radius, then the SIRs become as shown in Fig. 4.7. The simulation is conducted at a high sampling frequency of 10^4 GHz and with Field II set to the bounding lines solver. In the figure $cell$, $square$, and $scaled$ are the responses from the circular cell, the square element, and the square element scaled with $1/f$, respectively.

As seen in Fig. 4.7 the response from the square element is spread along a longer time interval, which is also to be expected. However, if the pulses, h_{cell} and h_{scaled} are integrated and the difference in percentage relative to h_{cell} is found, the error amounts to $0.02\ \%$. Fig. 4.8 shows the pressure pulses of the same setup when a 10 MHz two cycle Hanning weighted excitation pulse is applied. The RMS difference relative to the RMS of the cell response

	Points	Solver	Deviation
Area deviation	$\{0, 0, 4.7\}$ mm	Lines	$0.02\ \%$
Pressure deviation	$\{0, 0, 4.7\}$ mm	Lines	$0.032\ \%$
Pulse-echo deviation	$\{0, 0, 4.7\}$ mm	Lines	$0.064\ \%$
Mean area deviation	20 points	Lines	$0.021\ \%$
Mean pressure deviation	20 points	Lines	$0.05\ \%$
Mean pulse-echo deviation	20 points	Lines	$0.10\ \%$
Mean area deviation	20 points	Rect	$0.022\ \%$
Mean pressure deviation	20 points	Rect	$0.051\ \%$
Mean pulse-echo deviation	20 points	Rect	$0.103\ \%$

Table 4.1: Table showing the deviation between the area of spatial impulse responses, pressure pulses, and pulse-echo pulses between a flat circular CMUT cell and a scaled version of the response from a square transducer element. Two different Field II solvers were applied.

is calculated to be $0.032\ \%$. Clearly the slightly longer time interval of the SIR presented by the $square$ does not have much influence on the pressure and the pulse-echo at this 10 MHz pulse. Calculation of the pulse-echo deviation reveals a $0.064\ \%$ deviation, which is twice the deviation for the pressure. This indicates an accumulation of the error proportional to the number of convolutions.

The same study with 20 points randomly distributed within a space of $10 \cdot r_{cell}$ x $10 \cdot r_{cell}$ x 0.01 m in front of the cell was performed. A rectangular solver, which is a far-field solver in Field II, and a similar line solver, which is a very exact solver in Field II, were applied. The mean error of the three simulations is listed in Table 4.1, where also the given solver is indicated. Area integration comparison is stated in the table as "Area deviation".

The pulse start times in Fig. 4.7 are identical because the shortest distances between the cell and the point are identical for the two models. It should, however, be noticed that in some cases, for points outside the transducer perimeter, the shortest distance to the $square$ is shorter than for the $cell$, which will introduce a start time error. The end time will always have a larger value for the $square$ model.

If the cell is deflected as calculated with the model in section 4.1, then a focus point is introduced. A 36 volt DC bias for a cell with the material parameters listed in Table 4.2 yields a deflection of 33.4 nm. Calculating the mean error for 20 points as above yields the mean deviations shown in Table 4.3. Notice that the deviations are significantly different for the two solvers, "Lines" and

Young's module	169	GPa
Poison ratio ν	0.29	[]
Gap height g_0	150	nm
Plate thickness t	1.125	μm
c_v	0.43	
r_{cell}	18	μm
Exterior pressure	101.3	kPa

Table 4.2: Simulation parameters used for calculating the cell deflection.

	Points	Solver	Deviation
Mean area deviation	20 points	Lines	$1.85\ \%$
Mean pressure deviation	20 points	Lines	$5.62\ \%$
Mean pulse-echo deviation	20 points	Lines	$11.12\ \%$
Mean area deviation	20 points	Rect	$1.87\ \%$
Mean pressure deviation	20 points	Rect	$3.99\ \%$
Mean pulse-echo deviation	20 points	Rect	$7.92\ \%$

Table 4.3: Table showing the deviation between the area of spatial impulse responses, pressure pulses, and pulse-echo pulses between a deflecting circular CMUT cell and a scaled version of the response from a square transducer element. Two different Field II solvers were applied.

"Rect", compared to the case in Table 4.1.

In Table 4.3 a higher deviation is found compared to the flat cell simulation. This is also to be expected, since the cell has a focus point, and for this high resolution simulation such focus point becomes influential to the phase and the concentration of the energy of the pressure pulses and the pulse-echo pulses. Figure 4.9 shows the difference in the SIRs for the $square$ and the $scaled$ rectangular responses together with the deflected $cell$ response. Clearly the pulses are different but the area of the curves are close to being identical, in average $1.85\ \%$ as Table 4.3 reveals. Figure 4.10 shows the pulse echo response as calculated with the solver, "Lines", for one of the 20 points. A 10 MHz excitation was applied. From this figure the deviation can be identified as a slight phase difference in the pulses.

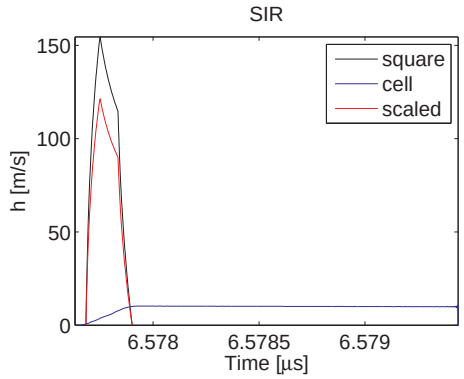

Figure 4.9: An example of the difference between the spatial impulse responses when the cell deflects.

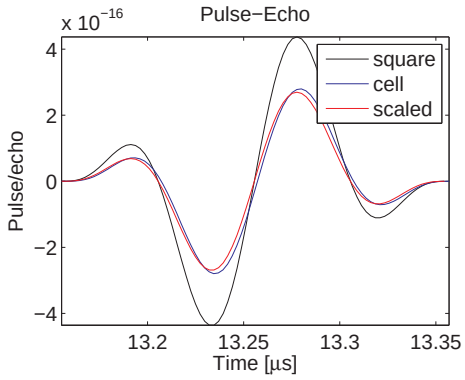

Figure 4.10: The pulse echo response when a 10 MHz excitation pulse is applied.

4.3.2 Resolution of a CMUT cell

The above study was conducted with a very high number of mathematical elements to form the geometry of the cell very exactly, and it was performed at an undesired high sampling frequency. In practical simulations with Field II a sampling frequency around 200-400 MHz is more suitable, which is possible because of Field II's energy preservation of the pulses. Furthermore, as few mathematical elements as possible are preferred. The following section describes a study in which the sampling frequency is lowered to 200 MHz and 400 MHz, and the radius of the cell is varied from 18 μm to 30 μm. The resolution of a single cell is controlled by adjusting the integer resolution number, n, as described in section 4.3 and the responses are solved using the rectangular solver. The times for solving the SIR and for solving the pressure for 20 random points each solved a 1000 times, are measured when varying n in the interval 1 to 30 and the sampling frequency. The RMS of the difference between a high resolution solution solved at 10^4 GHz and $n = 30$, and the solutions found at the lower sampling frequencies are calculated for pressure pulse predictions with a 10 MHz excitation waveform. The area difference of the SIR is calculated as well.

The mean computation times for the SIR are found in Fig. 4.11. This time is found to be exponentially increasing for an increasing resolution number. The same observation can be made for the pressure prediction in Fig. 4.12. Figure 4.13 shows the mean RMS deviation between pressure pulses at the high sampling frequency and pressure pulses at the lower sampling frequencies. The figure reveals the interesting fact that the responses have stabilized

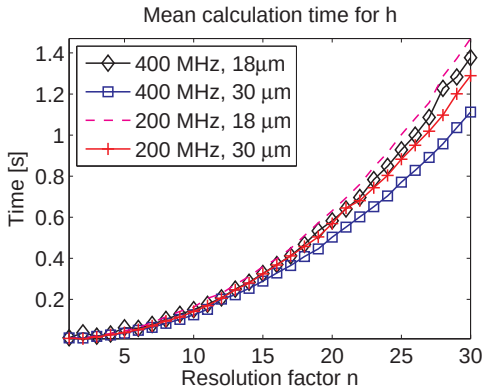

Figure 4.11: Mean calculation time for spatial impulse responses of 20 random points, each solved a 1000 times.

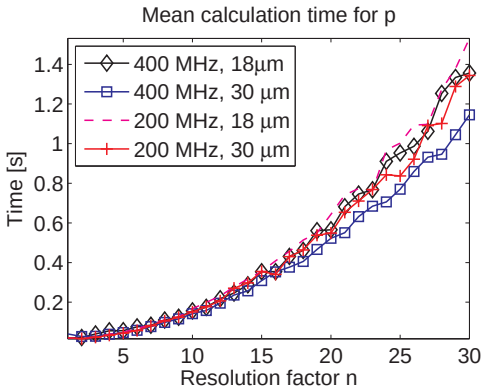

Figure 4.12: Mean calculation time for pressure pulses of 20 random points, each solved a 1000 times.

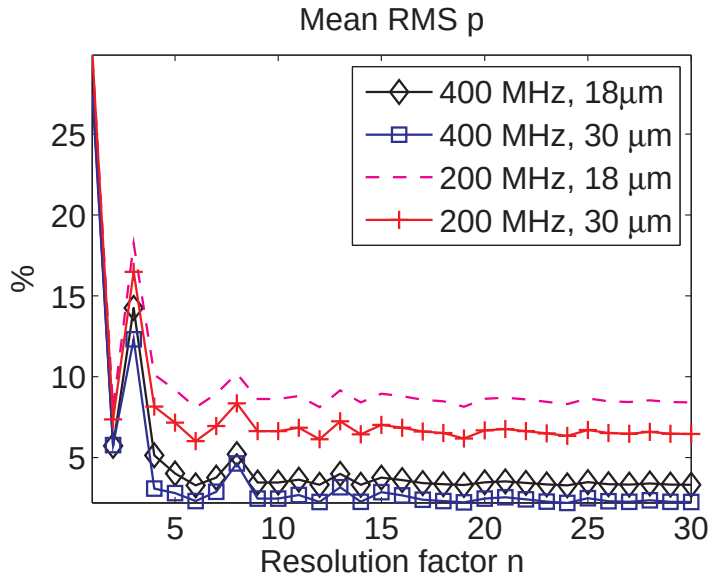

Figure 4.13: The mean RMS of the pressure pulses for 20 random points , each solved 1000 times calculated relatively to a high resolution solution at 10^4 GHz and $n = 30$.

after $n = 5$. It can furthermore be identified that the errors are decreasing for higher sampling frequencies, and the relative size between mathematical element size and sampling frequency is important for the amount of error. It can also be identified that the 200 MHz sampling frequency yields a relatively large deviation compared to the 400 MHz sampling frequency.

	Points	Solver	Sampling	Deviation
Mean area deviation	200 points	Rect	5 GHz	$1.78\ \%$
Mean pulse-echo deviation	200 points	Rect	5 GHz	$3.19\ \%$
Mean area deviation	200 points	Rect	400 MHz	$3.89\ \%$
Mean pulse-echo deviation	200 points	Rect	400 MHz	$5.29\ \%$
Mean area deviation	200 points	Rect	200 MHz	$4.07\ \%$
Mean pulse-echo deviation	200 points	Rect	200 MHz	$4.83\ \%$

Table 4.4: Table showing the deviations calculated for 200 random points with an element populated with 5x150 cells.

4.3.3 Approximation of a populated transducer element

An investigation with a transducer element fully populated with cells is required for ultrasound imaging simulation. Consider a single CMUT element populated with 5x150 cells in the lateral and the elevation plane. Each cell has a radius of $r_{cell} = 18$ μm, and the cell to cell pitch is $cell_p = 38$ μm. A corresponding rectangular element is assumed to have the dimensions $5 \cdot cell_p$ x $150 \cdot cell_p$.

The study for a single cell simulation showed that the response from the rectangular element could be scaled with the area fraction (4.1). It must therefore be assumed that within certain limitations this will be applicable for a whole element, where the cell to cell spacing prevents the cell boundaries from touching each other. However, the scaling factor is no longer $\pi/4$ but instead the fraction between active areas.

A setup of Field II to model a single element with and without cells was performed. The cells were assumed to deflect 33.4 nm as in all the other studies. 200 random points were used to calculate the pulse-echo response. An integration of the SIRs was performed and a RMS deviation between pulse-echo responses was calculated. The cell resolution was set to $n = 6$, which is based on the results in Fig. 4.13, and sampling frequencies of 5 GHz, 400 MHz, and 200 MHz were investigated. The results are presented in Table 4.4.

Table 4.4 reveals that a deviation ranging from $1.7\ \%$ to $5.29\ \%$ can be found between the two modeling principles. It also reveals that the increase in deviation is relatively little by lowering the sampling frequency from 5 Ghz to 400 MHz. A plot of the response from one of the 200 points investigated reveals the difference in pulse shape as shown in Fig. 4.14.

Figure 4.14a shows the pulse shapes of the three calculation methods, and

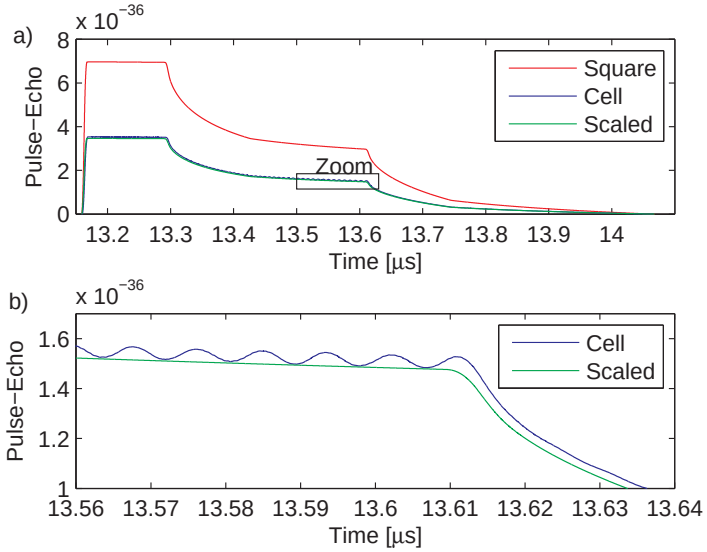

Figure 4.14: Pulse-echo response for a single point calculated with the rectangular transducer, $Square$, CMUT cells, $Cell$, and a scaling of the rectangular response, $Scale$ a) Full pulse shapes. b) Zoom onto (a).

Fig. 4.14b shows a zoom onto (a). Fig. 4.14b reveals that the response for the CMUT yields a ripple shape which is due to the summing of many small responses from circular cells.

4.4 Comparing envelope data of point spread functions for different CMUT configurations

This section compares point spread functions calculated using a standard linear array, equivalent CMUT model with flat elements, and an equivalent CMUT model with deflecting cells.

The simulation setup uses a 15 element array with the height and element width of 6 mm x 198 μm. Each major element is assumed to have 5x150 cells populated systematically in the lateral and the elevation plane. Each cell has $r_{cell} = 18$ μm, and the cell to cell pitch is 40 μm. The equivalent rectangular model has an element height and a width of 6 mm x 196 μm with a kerf of 2 μm. The model parameters for calculating the deflection are as found in Table 4.2, and a deflection of 33.4 nm with a DC bias of 36 volt is used.

Two point spread functions are simulated. One at 1 mm distance from the

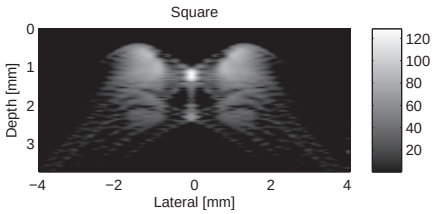

Figure 4.15: Point spread function of a point at 1 mm modeled with rectangular elements in a linear array, i.e. no cells.

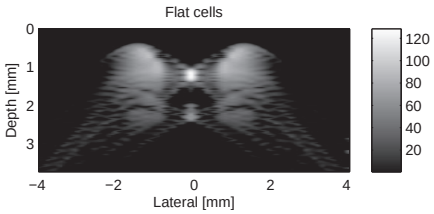

Figure 4.16: Point spread function of a point at 1 mm modeled with CMUT model and flat cells.

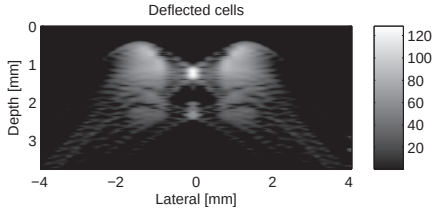

Figure 4.17: Point spread function of a point at 1 mm modeled with CMUT model and shaped cells.

transducer and one at 15 mm from the transducer. Both points are located in the middle image plane. The elements are assumed excited with a 2 cycle 10 MHz pulse, and the impulse response of the transducer is a 2 cycle Hanning weighted pulse. This is a plausible situation in imaging. The sampling frequency was set to 400 MHz and the cell resolution to $n = 5$. The solver applied was the rectangular solver in Field II.

The images in Fig. 4.15 to Fig. 4.17 are representing the point spread function at 1mm, when the RF-data is compressed to a dynamic range of 60 dB. The difference is found to be very small and is mainly located behind the point as a small tail.

The same study for a point located at 15 mm is depicted in Fig. 4.15 to Fig. 4.17. From these figures all the differences are found even smaller than for the 1 mm point.

All grouped figures are plotted to the same scale for comparison.

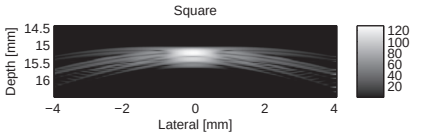

Figure 4.18: Point spread function of a point at 15 mm modeled with rectangular elements in a linear array, i.e. no cells.

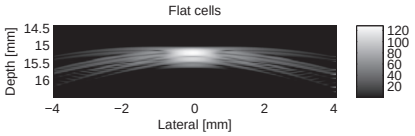

Figure 4.19: Point spread function of a point at 15 mm modeled with CMUT model and flat cells.

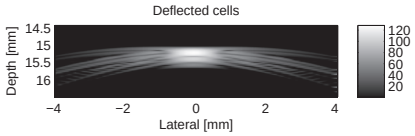

Figure 4.20: Point spread function of a point at 15 mm modeled with CMUT model and shaped cells.

4.5 Discussion

Computationally it will be faster to model the transducer without the cells and then scale the response to get a good approximation. This approach will only require a minor change in the Field II source code. This method, however, is only beneficial when the far-field is utilized.

Yet another remark on Field II combined with CMUTs has to be made. Simulations very close to the aperture will require near-field considerations, which also can imply cross talk considerations. This phenomenon is indeed difficult to capture with Field II and would probably be better solved with a finite element program.

4.6 Conclusion

The SIR from a single circular transducer cell can be approximated by a square element enclosing the circle. The square element response will, however, always have a longer time interval. The area of the SIR curves can be approximated by scaling the response from a fraction between active cell area and full element area. The RMS deviation of this principle is around $0.02\ \%$ for flat unfocused cells and $1.85\ \%$ for deflecting cells. Scaling can be applied

for pressure pulses and pulse-echo responses as well. For flat cells the pressure deviation is around 0.05 %, and the pulse-echo response is 0.10 %. For deflecting cells the pressure RMS deviation is ranging from 3.99 % to 5.62 % depending on the Field II solver applied. The pulse-echo RMS deviation is ranging from 7.92 % to 11.12 %. The RMS deviation has a factor of two in difference between pressure and pulse-echo responses. A full element with 5x150 cells can be similar approximated with scaling of the area.

The response from a single cell can be resolved with a resolution factor of $n = 5$. Higher resolution factors were seen to give almost identical RMS deviations on the pressure pulses. Increasing the resolution factor increases the calculation time exponentially.

The influence of approximating a CMUT element with a flat square element or with all cells and no deflection can hardly be identified on the imaging of point spread functions. Exact simulation close to the transducer, however, requires full modeling of the cells which also requires high sampling frequency. As a consequence imaging with CMUTs in Field II can be well performed using the standard rectangular transducer models that currently are implemented into the program. This is in line with the assumption that the pulse wavelength has to be large compared to the cell.

4.7 Future development

A disadvantage of not modeling all the cells is the missing ability to study the exact effect of a mis-functioning cell or the missing ability to retrieve the response from each single cell. This can, however, be a valuable information to have in a beam-forming context. Currently only models are considered where all cells on a given element are excitated and received with in parallel. This should be improved on.

The Field II modeling is dependent on the piston movement of the cell's plate. For high precision simulation the validity of this approximation should be addressed and compared with finite element simulations. This is a topic for future investigation.

A conference paper based on the accepted abstract Abstract II is in preparation and addresses the results in the chapter.

CHAPTER

FIVE

Project conclusion

This project was divided into three research topics. 1) Modeling of a spatial impulse response (SIR) for a convex rectangular elevation focused transducer (CREFT) and a rectangular elevation focused transducer (REFT). 2) Hybrid modeling between transducer impulse response models and Field II. 3) Investigation of combining CMUTs with Field II.

1) The research on SIRs resulted in two new and exact models for SIRs. One model for the REFT and one for the CREFT. A semi-analytical solution for the SIR of the REFT was found. This solution is best solved with an elliptical integral of the first kind. It can exhibit a root mean square (RMS) deviation, relatively to the Field II prediction, below 3.5 %. This is applicable for simulations on 2500 randomly distributed points at a sampling frequency of 3400 MHz. The mean error can be caclulated to 0.41 % precision. The largest errors are located in front of the transducer. At a 100 MHz sampling frequency the mean error was found to be 1.37 %. The SIR model for the CREFT has no direct analytical solution but can be approximated to give an analytical solution. A mean error calculated on 200 random points and solved by dividing the integrand into three parts yields an error of 0.01 %. The CREFT model can predict the SIR from a rectangular elevation focused element, a convex non-elevation focused element, and a linear planar element. Each transducer approximation is represented with a RMS deviation relative to the Field II prediction of 3.46 %, 2.5 %, and 3.56 %, respectively. It is therefore proven that the model can approximate general rectangular and symmetric transducer geometries.

2) The work on combining the Field II program with a one-dimensional transducer model revealed that the pressure amplitude can be predicted within ± 2 dB. This was shown by simulating the pressure response from a circu-

lar piezoceramic transducer of Pz27 material and by simulating a commercial 128 element transducer. The RMS deviations of the pressure waveforms range from 11 % to 36 %. It was also shown that combining Field II with an axisymmetric finite element model (FEM) of the Pz27 ceramic can give identical results with the one-dimensional transducer model applied above. This is when the radial movement of the radial perimeter is prevented. The amplitude difference is 2 dB with the assumption that the radial movement of the transducer perimeter is free in the FEM. A parameter sensitivity study reveals that the stiffness, the density, and the length of firstly the lens material and secondly the piezoceramic affect the model of the commercial transducer the most.

3) Responses from circular CMUT cells can be approximated with a scaling of the response from a flat rectangular transducer. The scaling is performed with the ratio between the active areas of a transducer element that neglects the presence of all the cells and a transducer element that accounts for all the cells. Simulation of the response from a cell with a deflecting surface is only beneficial close to the cell and at high frequencies, as long as the cell size is small compared to the simulation distance. At a typical sampling frequency for Field II of 400 MHz the point spread functions are only slightly affected by the modeling of the cell deflections close to the transducer. No visual difference is to be observed far away from the transducer.

Paper I

Spatial impulse response of a rectangular elevation focused transducer

David Bæk, Morten Willatzen, and Jørgen Arendt Jensen

IEEE Transactions on Ultrasonics, Ferroelectrics, and Frequency Control

In review 2010

Spatial impulse response of a rectangular elevation focused transducer

David Bæk, Morten Willatzen, and Jørgen Arendt Jensen

***Abstract*—The spatial impulse response for a concave cylindrical rectangle is solved using the Rayleigh integral. A concave cylindrical rectangle forms a typical medical ultrasound transducer element and the spatial impulse response is often represented by a far field approximation. This work presents, to first order in diffraction effects, an exact solution to the Rayleigh integral on such transducer elements. The expressions are derived such that simple line integrals are to be solved. Comparison is made with the Field II simulation software, and root mean square errors are calculated as the difference between pulse shapes of the exact solution to the Rayleigh integral and Field II relative to the root mean square of the Field II pulse forms. The errors range from 0 % to 3.5 % when 2500 simulation points are compared.**

I. Introduction

CAlculation of a time dependent pressure field in front of a transducer can be performed efficiently by applying the well-known method of the spatial impulse response as suggested by Tupholme and Stepanishen [1], [2]. With this method the time dependent acoustic pressure is found by multiplying the fluid density of the medium-of-propagation with the convolution between a transducer's surface acceleration and the source's spatial impulse response. The spatial impulse response is dependent on the aperture geometry as well as the source location relative to the aperture. Several works have investigated the pressure fields from baffled planar pistons of circular, annular, and planar square geometries by using this computational efficient method. In the case of simple geometries, a tractable analytical representation of their spatial impulse responses exists which is preferable for pressure field calculations. Some of the interesting works that investigate these transducers are found in a series of references [3], [4], [5], [6], [7], [8], [9]. More complicated expressions for concave annular transducers have also been developed [10], [11] which made it possible to calculate the pressure field from focused piston transducers efficiently by assuming a uniform velocity distribution on the surface of the transducer. Additionally work as the ones by Tjøtta et al. [12] or Verhoef et al. [13] discuss these focused transducers with emphasis to nonuniform velocity distributions. However, the latter simple transducer geometries are not adequate in describing the geometries of modern medical ultrasonic array transducers that often consist of linear arrays with concave elements or arrays with concave and/or convex geometries. The spatial impulse response for such more complex transducers are typically found by sub dividing the elements into either strips or small rectangles of which a exact known or approximate solution can be found [14], [15], [16]. Other interesting methods for arbitrary surfaces rely on solving the Rayleigh's surface integral numerically by applying advanced approximations [17]. Most of the solutions rely on Huygen's principle as well as the far-field approximation. A practical example of the use of these methods can be found in the Field II software package [18], [19] where the methods described in the references by Jensen [20], [8] are some of the few that are practically applied in pressure predictions for complex medical transducers. Other examples are the DELFI [21], DREAM [22], and Ultrasim [23] simulation programs that utilize the spatial impulse response method.

Only little focus has been on finding exact expressions for the spatial impulse response of rectangular elevation focused transducers in part due to the fact that a simple analytical solution is not available. The motivation of this paper is to find the exact solution of the spatial impulse response represented by the Rayleigh integral to a such concave rectangular transducer by means of a semi-analytical expression. The long-term motivation is to incorporate the obtained solution into the Field II software package as an alternative to the current far-field approximation.

In the work by Theumann et al. [24], a related approach was taken in obtaining exact impulse responses. The authors validated their model by measurements on a closed cylindrical transducer and found good agreement. Their solution may also be extended to consider cylindrical shells as well. However, the expressions found were limited to account for field points within the radius of the concave cylinder. In addition, solutions for points of axis in front of cylindrical shells are cumbersome to find due to their method of integration limits.

This work applies a similar method for developing expressions but the focus is on cylindrical shells accounting for field points located both inside and outside the concave radius of the shell. The latter is desirable in connection with the Field II software where such points may occur.

II. Theory

The integral form of the spatial impulse response is well known from the literature [2]:

$$h(\bar{r},t) = \frac{1}{2\pi}\int_S \frac{\delta[t-\frac{r'}{c}]}{r'}dS, \tag{1}$$

where $\bar{r}$ is the spatial coordinate of a given point in front of the transducer, t is the time, c is the speed of sound, and r' is the distance from $\bar{r}$ to the transducer surface element dS. The integration surface, S, is a cylindrical shell as shown in Fig. 1. Since this work is concentrated on a curved transducer geometry it should also be noted that the Rayleigh integral (1) is only exact for plane transducers. However, for transducers where the wavelength is much smaller than the curvature as well as the extent of the transducer all distortion from the secondary diffraction effects will be insignificantly small [25], [10]. This situation is usually the case in medical ultrasonic applications. Therefore, (1) is a good approximation.

The shell will be described by the cylindrical variables x, r_c, and θ being the axial, radial, and azimuthal coordinates, respectively. The Cartesian coordinate system is chosen so that a point P in front of the transducer has the coordinates $\{x_p, y_p, z_p\}$. The geometrical focus defines the zero reference for the y and the z coordinate, and the transducer half width $L/2$ defines the zero reference for the x coordinate. The shell has a full length restricted to L, and a height H as depicted in Fig. 1. The height H is defined by an opening angle V given by $H = 2r_c\sin(V)$. The transducer corners are defined as c_1, c_2, c_3, and c_4. In the following, these are paired such that c_1 and c_2 belong to the transducer arc at $x = -L/2$. Accordingly, the corners c_3 and c_4 are associated with the arc at $x = L/2$.

A surface element, dS, in cylindrical coordinates is defined as

$$dS = r_c dx d\theta, \tag{2}$$

where θ is the azimuthal angle, r_c is the cylindrical radius, and dx is the lateral span of the element. To find an expression for this surface element, a geometrical consideration as shown in Fig. 2 may be used.

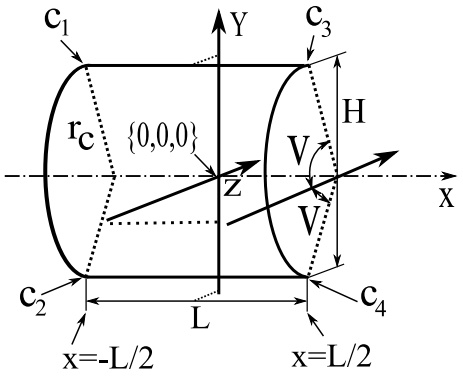

Fig. 1. Figure showing the geometrical definition of the cylindrical shell.

From this figure the distance $|NQ|$ may be given by the cosine relation

$$|NQ|^2 = r_c^2 + |OQ|^2 - 2r_c|OQ|\cos[\theta+\gamma], \tag{3}$$

where $|OQ| = l = \sqrt{z_p^2 + y_p^2}$ and $\gamma = \sin^{-1}[\frac{z_p}{l}]$. Using the Phytagorean theorem on the triangle NPQ to get the time-dependent distance $|PQ|$ yields

$$|PQ|^2 = \xi^2 = (ct)^2 - |NQ|^2, \tag{4}$$

where it has been used that the distance $|NP| = ct$. Note that the distance $|PQ|$ is always parallel to the x-axis such that a single surface element dS at any given time instance can be found as

$$\begin{aligned} dS &= r_c\frac{\partial\xi}{\partial t}dt\,d\theta \\ &= \frac{r_c c^2 t\ dt\ d\theta}{\sqrt{(ct)^2 - r_c^2 - l^2 + 2r_c l\cos[\theta+\gamma]}}. \end{aligned} \tag{5}$$

If one substitutes the latter expression for dS into the integral expression in (1), the integral will be transformed into a line integral along an intersecting curve created by the crossing between the cylindrical shell and a sphere emanating from the point P. Again, this result applies at any given time interval. Consequently, the integration variable will then effectively be the azimuthal coordinate θ. If one also considers the intersection as consisting of two domains, one to the left side (i.e. $x <= x_p$) and one to the right side (i.e $x > x_p$) of the point P then at any given time instance $t = \tau$, (1) becomes

$$\begin{aligned} h &= \int_{\theta_{min}^L}^{\theta_{max}^L} \frac{r_c c}{2\pi\sqrt{\zeta\cos[\theta+\gamma] - f(\tau)}}d\theta + \\ &\quad \int_{\theta_{min}^R}^{\theta_{max}^R} \frac{r_c c}{2\pi\sqrt{\zeta\cos[\theta+\gamma] - f(\tau)}}d\theta, \end{aligned} \tag{6}$$

where it has been used that $r' = ct$, $f(\tau) = r_c^2 + l^2 - (c\tau)^2$, and $\zeta = 2r_c l$.

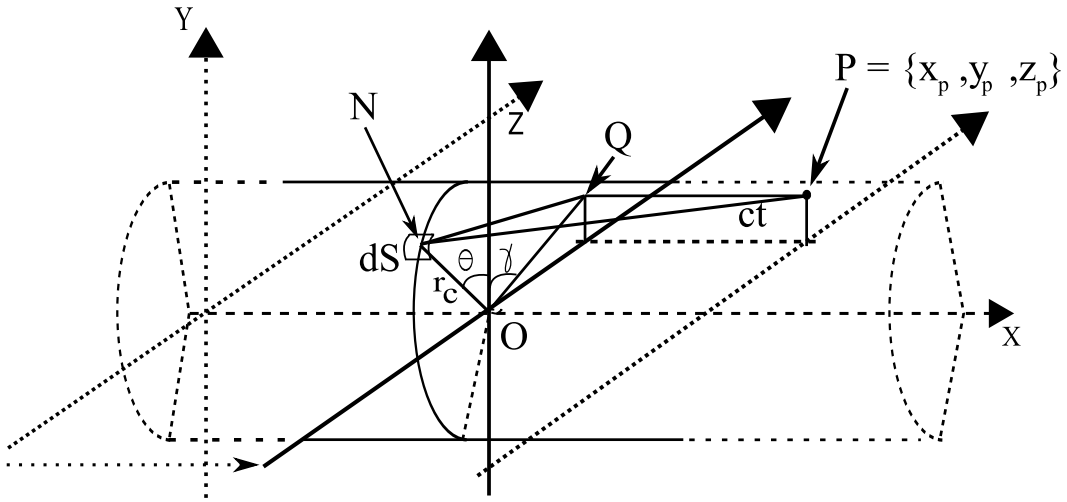

Fig. 2. Figure showing the cylinder shell and the distances applied in the derivation of the response at a point P.

For values of $P = \{x, y, 0\}$, and closing the shell to form a cylinder, ($V = \pi$), the above expression becomes identical with the expressions suggested by Theumann et al. [24] for a closed cylinder. However, (6) has the advantage that it describes the spatial impulse response from any spatial point in front of a cylindrical shell transducer an extension not accounted for by Theumann et al. [24].

Since the integrands of the integrals in (6) are identical it is convenient to define the following general integral function

$$H = \int_{\theta_{min}}^{\theta_{max}} \frac{r_c c}{2\pi\sqrt{\zeta cos[\theta+\gamma] - f(\tau)}} d\theta, \qquad (7)$$

where the integration boundaries are point and time dependent.

A. Integration boundary conditions

The integration limits are time dependent and may be found as the horizontal projections of the intersecting lines onto two circular arcs with radius r_c as shown in Fig. 3. The θ angles on each circle reveal the integration limits. Fig. 3 shows the actual transducer surface as the middle domain indicated with (I) and two imaginary neighboring surface domains (II) and (III). The arcs contributing to the spatial impulse response are only the arcs in (I). However, as will be apparent in the following sections, the arc contributions from (II) and (III) are subtracted again. The different angles are given by isolating θ in (4) yielding

$$\begin{aligned} \theta &= \cos^{-1}\left[\frac{\xi^2 - (ct)^2 + r_c^2 + l^2}{2r_c l}\right] - \gamma, \\ &= \cos^{-1}\left[\frac{\xi^2 + f(t)}{\zeta}\right] - \gamma. \end{aligned} \qquad (8)$$

Any integration limit is found by choosing an appropriate value for ξ in (8). Such values are determined in the following.

B. Integration limits in different domains

The integration limits consists of a maximum angle and a minimum angle. One set of integration limits is given at the vertical aperture boundary arc at $x = -L/2$. These angles are here defined as ϕ_{max}^L and ϕ_{min}^L. Another set of integration limits are defined at the vertical aperture boundary at $x = L/2$. These are defined as ϕ_{max}^R and ϕ_{min}^R. Finally, an integration limit set is found at $x = x_p$ denoted by ϕ_{max} and ϕ_{min}.

Independent of the point P's location, the angles will be dependent on the absolute distance from x_p to the aperture's vertical boundaries at $x = \pm L/2$ as is clear from (8). Hence, the following functions are conveniently defined

$$\sigma_1[x_p] = \begin{cases} |L/2 + xp| & x_p \leq L/2 \\ |L/2 - xp| & x_p > L/2, \end{cases} \qquad (9)$$

$$\sigma_2[x_p] = \begin{cases} |L/2 - xp| & x_p \leq L/2 \\ L/2 + xp & x_p > L/2. \end{cases} \qquad (10)$$

A set of general angle definitions is hereby:

$$\phi_{max} = \begin{cases} \cos^{-1}\left[\frac{f[t]}{\zeta}\right] - \gamma & -1 \leq \frac{f(t)}{\zeta} \leq 1 \\ \phi_{maximum} & \textit{else,} \end{cases} \qquad (11)$$

$$\phi_{min} = \begin{cases} -\cos^{-1}\left[\frac{f[t]}{\zeta}\right] - \gamma & -1 \leq \frac{f(t)}{\zeta} \leq 1 \\ \phi_{minimum} & \textit{else,} \end{cases} \qquad (12)$$

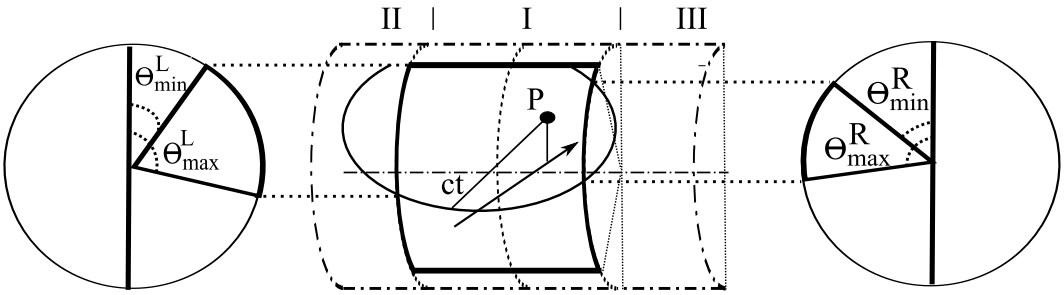

Fig. 3. Figure showing the left and right integration boundaries for the point P at a given time instance as projections onto circles of radius r_c. The actual transducer is the middle transducer (I). (II) and (III) are imaginary transducers.

$$\phi^R_{min} = \begin{cases} -\cos^{-1}\left[\frac{\sigma_2[x_p]^2+f[t]}{\zeta}\right]-\gamma & -1 \le \frac{\sigma_2[x_p]^2+f(t)}{\zeta} \le 1 \\ \phi_{minimum} & \textit{else,} \end{cases} \tag{13}$$

$$\phi^R_{max} = \begin{cases} \cos^{-1}\left[\frac{\sigma_2[x_p]^2+f[t]}{\zeta}\right]-\gamma & -1 \le \frac{\sigma_2[x_p]^2+f(t)}{\zeta} \le 1 \\ \phi_{maximum} & \textit{else,} \end{cases} \tag{14}$$

$$\phi^L_{min} = \begin{cases} -\cos^{-1}\left[\frac{\sigma_1[x_p]^2+f[t]}{\zeta}\right]-\gamma & -1 \le \frac{\sigma_1[x_p]^2+f(t)}{\zeta} \le 1 \\ \phi_{minimum} & \textit{else,} \end{cases} \tag{15}$$

$$\phi^L_{max} = \begin{cases} \cos^{-1}\left[\frac{\sigma_1[x_p]^2+f[t]}{\zeta}\right]-\gamma & -1 \le \frac{\sigma_1[x_p]^2+f(t)}{\zeta} \le 1 \\ \phi_{maximum} & \textit{else.} \end{cases} \tag{16}$$

The different angle definitions are constrained to be purely real valued as is ensured by the limits ± 1 on the conditions. If a constraint is violated, it must be set to an angle $\phi_{maximum}$ or $\phi_{minimum}$ dependent on the location of the point P in front of the aperture. These angles may be set to the maximum and minimum allowable angles for the given point location. This will be defined for each zone in the following.

III. Time of flight to the transducer corners

The time of flight from the point P to the transducer corners can advantageously be defined as $t1, t2, t3, t4$ and are found as

$$t_1 = \begin{cases} \bar{t}_1 & y_p \ge 0 \\ \bar{t}_2 & y_p < 0 \end{cases}, \quad t_2 = \begin{cases} \bar{t}_2 & y_p \ge 0 \\ \bar{t}_1 & y_p < 0 \end{cases}, \quad t_3 = \begin{cases} \bar{t}_3 & y_p \ge 0 \\ \bar{t}_4 & y_p < 0 \end{cases}, \quad t_4 = \begin{cases} \bar{t}_4 & y_p \ge 0 \\ \bar{t}_3 & y_p < 0 \end{cases}, \tag{17}$$

where the intermediate times $\bar{t}_1$, $\bar{t}_2$, $\bar{t}_3, \bar{t}_4$ are given by

$$\bar{t}_1 = \begin{cases} t_{c1} & x_p \le L/2 \\ t_{c3} & x_p > L/2 \end{cases}, \quad \bar{t}_2 = \begin{cases} t_{c2} & x_p \le L/2 \\ t_{c4} & x_p > L/2 \end{cases}, \quad \bar{t}_3 = \begin{cases} t_{c3} & x_p \le L/2 \\ t_{c1} & x_p > L/2 \end{cases}, \quad \bar{t}_4 = \begin{cases} t_{c4} & x_p \le L/2 \\ t_{c2} & x_p > L/2 \end{cases}. \tag{18}$$

In this way the point P can be placed anywhere in front of the transducer. The nearest corners are defined as corner 1 (c1) and corner 2 (c2), and these have the same x-value but opposite signs on their y-values. Similar relations are valid for corner 3 (c3) and corner 4 (c4) of the transducer. This way one can exploit the symmetry of the transducer to simplify the number of cases.

The following sections will describe the spatial impulse responses to be calculated from different point locations by using the above angle definitions.

Fig. 4 is useful in defining the different zones where the point P can be located. These zones have different representations of the spatial impulse responses and are therefore to be considered independently. Notice in Fig. 4b that the zones 3 and 4 are only drawn on the left and the right side, respectively. A mirror image of both zones is clearly also found on the right and the left side of the aperture. The drawing of this has been left out to simplify the picture.

IV. Spatial impulse response for points in zone 1

This zone is defined as

$$-L/2 \le x_p \le L/2, \;\; z_p < 0, \;\; |y_p| < |z_p| \tan[V]. \tag{19}$$

The determination of the different integration limits depends on the time of flight from the emitting point to the aperture corners, edges, and the shortest distance to the aperture. Fig. 5 illustrates some time steps of the integration limits for this zone. Two time instances of intersection are shown in the figure, and the transducer

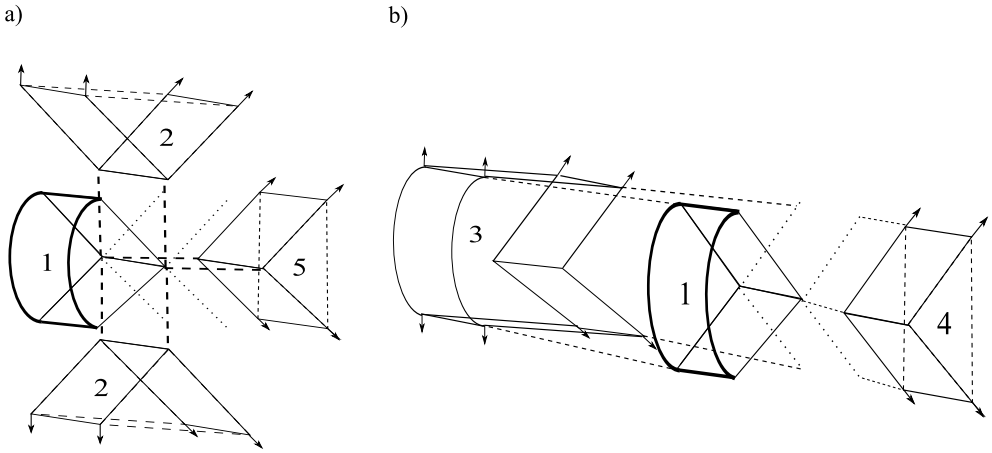

Fig. 4. a) An assembly split of the different zones within the aperture width, i.e. $-L/2 \leq x_p \leq L/2$. b) An assembly split of the zones 3, and 4 outside the aperture width. Notice that a duplicate of zone 3 is also to be found on the right side of zone 1, and that accordingly a duplicate of zone 4 is on the left side of zone 1.

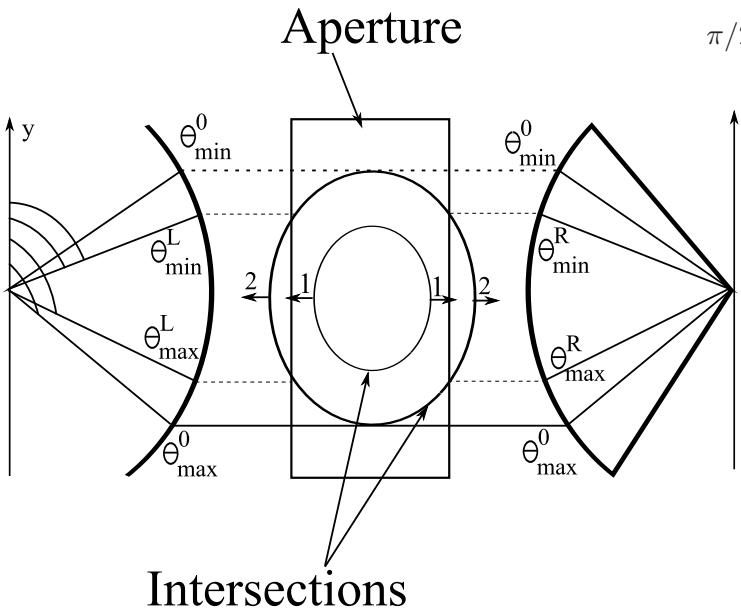

Fig. 5. Picture showing the integration angles for zone 1. The transducer is seen as a back view in the $x-y$ plane perpendicular to the z-axis. The intersections at two time instances are plotted starting with the arc (1) and then the arc (2). The direction of the propagation is indicated with arrows.

is plotted as seen from the back side and forward along the positive z-direction.

The boundary angles for this zone are therefore given as follows when $\phi_{maximum} = \pi/2+V$ and $\phi_{minimum} = \pi/2-V$ are choosen

$$\theta^0_{max} = \begin{cases} \phi_{max} & \phi_{max} < \phi_{maximum} \\ \phi_{maximum} & \textit{else}, \end{cases} \quad (20)$$

$$\theta^0_{min} = \begin{cases} \phi_{min} & \phi_{min} > \phi_{minimum} \\ \phi_{minimum} & \textit{else}, \end{cases} \quad (21)$$

$$\theta^R_{max} = \begin{cases} \phi^R_{max} & \phi^R_{max} < \phi_{maximum} \\ \phi_{maximum} & \textit{else}, \end{cases} \quad (22)$$

$$\theta^R_{min} = \begin{cases} \phi^R_{min} & \phi^R_{min} > \phi_{minimum} \\ \phi_{minimum} & \textit{else}, \end{cases} \quad (23)$$

$$\theta^L_{max} = \begin{cases} \phi^L_{max} & \phi^L_{max} < \phi_{maximum} \\ \phi_{maximum} & \textit{else}, \end{cases} \quad (24)$$

$$\theta^L_{min} = \begin{cases} \phi^L_{min} & \phi^L_{min} > \phi_{minimum} \\ \phi_{minimum} & \textit{else}. \end{cases} \quad (25)$$

The significant time of flights for a wave to arrive at the aperture is formulated as follows

$$t_0 = (r_c - l)/c, \quad (26)$$

$$t^L = \sqrt{(r_c - l)^2 + \sigma_1[x_p]^2}/c, \quad (27)$$

$$t^R = \sqrt{(r_c - l)^2 + \sigma_2[x_p]^2}/c, \quad (28)$$

$$t_{max} = max\{t_1, t_2, t_3, t_4\}. \quad (29)$$

Here t_0 is the smallest time always being the direct distance from a point P to the aperture on a line going through the transducer focus. The two flight times t^L and t^R are the shortest distances to the nearest edge at $x = \pm L/2$. The end time t_{max} is the maximum time of flight to the different transducer corners.

This gives the following definition of the spatial

impulse response, h

$$h(t) = \begin{cases} 0 & t < t_0 \\ \Lambda & t^L \geq t \leq t^R \\ \Lambda - H[\theta^R_{min}, \theta^R_{max}] & t^L \geq t > t^R \\ \Lambda - H[\theta^L_{min}, \theta^L_{max}] & t^L < t \leq t^R \\ \Lambda - H[\theta^R_{min}, \theta^R_{max}] - H[\theta^L_{min}, \theta^L_{max}] & t^L < t > t^R \\ 0 & t > t_{max}, \end{cases} \tag{30}$$

were

$$\Lambda = 2H[\theta^0_{min}, \theta^0_{max}]. \tag{31}$$

The definition used for Λ calculates the full contribution on the intersection of the domains I, II, and III (see Fig. 2). The arc contributions outside the aperture are to be subtracted from the full arc contribution, i.e., the imaginary arcs on II and III are to be subtracted by solving $H[\theta^L_{min}, \theta^L_{max}]$ and $H[\theta^R_{min}, \theta^R_{max}]$ as seen in (30). Notice that the same result to $h(t)$, can be achieved by finding the arc contributions on I alone.

V. Spatial impulse response for points in zone 2

This zone is defined as

$$-L/2 \leq x_p \leq L/2, \ |y_p| > |z_p| \tan[V]. \tag{32}$$

The angle definitions of this zone are identical with the ones from zone 1 (20)-(25), however, the important time of flights are defined slightly differently:

$$t_0 = \min \begin{cases} \sqrt{(H/2 - y_p)^2 + Z^2}/c, \\ \sqrt{(H/2 + y_p)^2 + Z^2}/c, \end{cases} \tag{33}$$

$$t^L = t_1, \tag{34}$$

$$t^R = t_3, \tag{35}$$

$$t_{max} = \max\{t_2, t_4\}. \tag{36}$$

where $Z = z_p + r_c \cos[V]$. The times t^L and t^R are the times of flight to the closest transducer corner at $x = -L/2$ and $x = L/2$, respectively. They are dependent on the coordinate y_p to exploit the symmetry around $y = 0$. The time t_0 is the shortest distance to the point P. The definition of h is identical to the one used in (30).

VI. Spatial impulse response for zone 3

This zone is defined by the constraints

$$-L/2 > x_p > L/2, \quad y_p = y, \quad z_p \leq 0.$$

or

$$-L/2 > x_p > L/2, \quad |y_p| > |z_p| \tan[V], \quad z_p > 0.$$

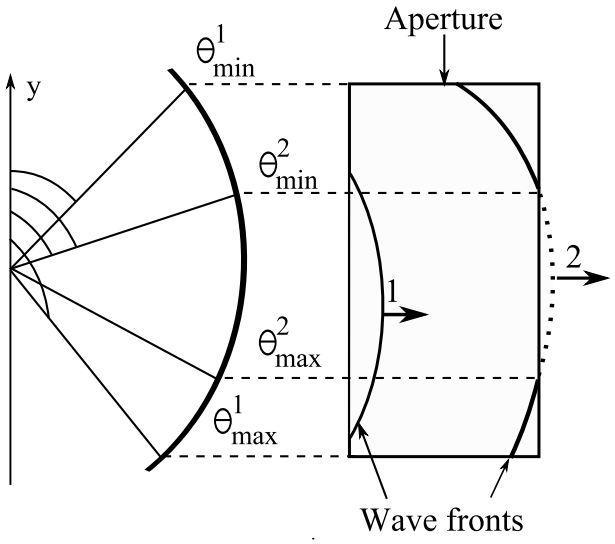

Fig. 6. Picture showing the integration angles for zone 3. The transducer is seen from a back view in the $x - y$ plane. The intersections at two time instances are plotted starting with the arc (1) and ending with the arc (2). The direction of the propagation is indicated with arrows. The dotted arc length outside the aperture is to be subtracted in h.

Fig. 6 shows how to define the integration boundaries for this zone. A point located outside the aperture width will generate a wave that travels from one aperture side to the opposite aperture side. This is shown by the intersecting arcs 1 and 2 where 1 is the intersection for an earlier time instance. One integration boundary set is denoted θ^1_{min} and θ^1_{max}. Another is denoted θ^2_{min} and θ^2_{max}. Notice, that the latter is relevant only when the waves cross the boundary furthest away.

The boundary angles for this zone are defined as

$$\theta^1_{max} = \begin{cases} \phi^L_{max} & \phi^L_{max} < \phi_{maximum} \\ \phi_{maximum} & \textit{else}, \end{cases} \tag{37}$$

$$\theta^1_{min} = \begin{cases} \phi^L_{min} & \phi^L_{min} > \phi_{minimum} \\ \phi_{minimum} & \textit{else}, \end{cases} \tag{38}$$

$$\theta^2_{max} = \begin{cases} \phi^R_{max} & \phi^R_{max} < \phi_{maximum} \\ \phi_{maximum} & \textit{else}, \end{cases} \tag{39}$$

$$\theta^2_{min} = \begin{cases} \phi^R_{min} & \phi^R_{min} > \phi_{minimum} \\ \phi_{minimum} & \textit{else}. \end{cases} \tag{40}$$

Here $\phi_{maximum} = \pi/2 + V$ and $\phi_{minimum} = \pi/2 - V$.

Some special time of flights for this zone are defined as

$$t_0 = \begin{cases} t_{s1} & |y_p| \leq |z_p| \tan[V] \\ t_1 & |y_p| > |z_p| \tan[V], \end{cases} \tag{41}$$

$$t_5 = \begin{cases} t_{s2} & |y_p| \leq |z_p| \tan[V] \\ t_3 & |y_p| > |z_p| \tan[V]. \end{cases} \tag{42}$$

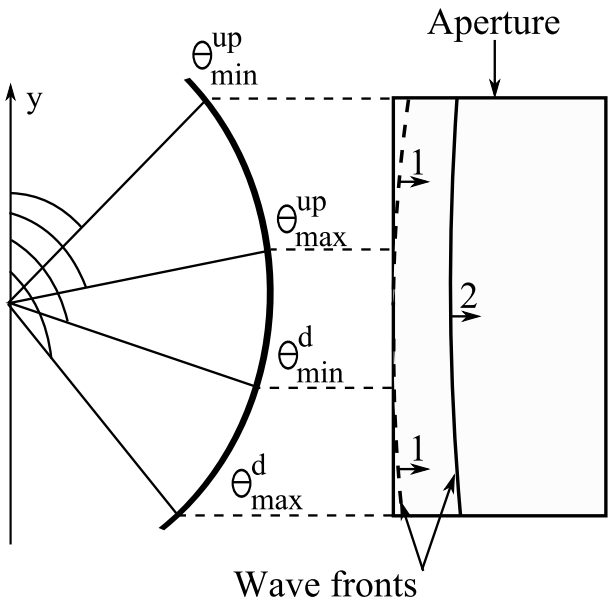

Fig. 7. Picture showing the integration angles for zone 4. The transducer is seen as a back view in the $x-y$ plane. The intersections at two time instances are plotted starting with the dashed arcs (1) and ending with the solid arc (2). The direction of the propagation is indicated with arrows.

The above times t_{s1} and t_{s2} are given by

$$t_{s1} = \sqrt{(|x_p| - L/2)^2 + (r_c - l)^2}/c, \quad (43)$$

$$t_{s2} = \sqrt{(|x_p| + L/2)^2 + (r_c - l)^2}/c. \quad (44)$$

The time t_5 is the time of flight for the wave front to reach the furthest away boundary relative to the point P. Also recall that t_1 and t_3 are adequate to define the time of flights to the appropriate corners. This is because symmetry is exploited in (17).

The maximum time is calculated as

$$t_{max} = t_4. \quad (45)$$

The spatial impulse response then becomes

$$h = \quad (46)$$
$$\begin{cases} H[\theta^1_{min}, \theta^1_{max}] & t_0 \le t < t_5 \\ H[\theta^1_{min}, \theta^1_{max}] - H[\theta^2_{min}, \theta^2_{max}] & t_5 \le t \le t_{max} \\ 0 & \text{else.} \end{cases}$$

VII. Spatial impulse response for zone 4

This zone is defined as

$$-L/2 > x_p > L/2, \quad |y_p| \le |z_p| \tan[V], \quad z_p > 0.$$

Fig. 7 shows how waves emanating from this zone cross the aperture. The crossing between the aperture and the propagating wave generates a crossing line bending away from the source point. As a result, one must divide the integration boundaries into an upper set θ^{up}_{min} and θ^{up}_{max} and a lower set θ^{d}_{min} and θ^{d}_{max}. Here $\phi_{maximum} = \pi - \gamma$.

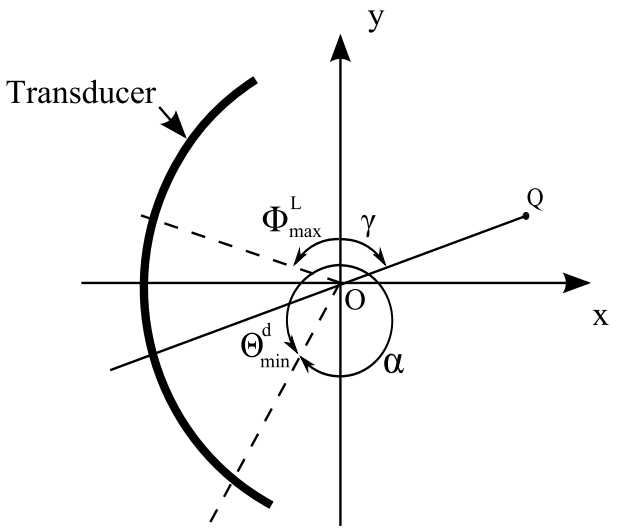

Fig. 8. Figure showing how to define the θ^d_{min} angle for this zone.

These angles may therefore be written as

$$\theta^{up}_{max} = \begin{cases} \phi^L_{max} & \phi^L_{max} \le \phi_{maximum} \\ \phi_{maximum} & \textit{else}, \end{cases} \quad (47)$$

$$\theta^{up}_{min} = \begin{cases} \pi/2 - V & t_1 \le t \le t_3 \\ \phi^R_{max} & \textit{else}, \end{cases} \quad (48)$$

$$\theta^{d}_{max} = \begin{cases} \pi/2 + V & t_2 \le t \le t_4 \\ 2\pi - 2\gamma - \phi^R_{max} & \textit{else}, \end{cases} \quad (49)$$

$$\theta^{d}_{min} = \begin{cases} 2\pi - 2\gamma - \phi^L_{max} & \eta \\ \phi_{maximum} & \textit{else}. \end{cases} \quad (50)$$

where $\eta = ((2\pi - 2\gamma - \phi^L_{max}) \ge (\phi_{maximum}))$ & $(t \ge t_2)$. The angle definitions $2\pi - 2\gamma - \phi^{R,L}_{max}$ are given by considering Fig. 8. The α angle is given by $2\gamma + \phi^L_{max}$ and is dependent on the γ angle. Recall that the zero reference for these angles are defined along the y-axis. The definition for θ^d_{max} can be derived similarly.

The spatial impulse response becomes

$$h = \begin{cases} H[\theta^{up}_{min}, \theta^{up}_{max}] & t_0 \le t \le t_2 \\ H[\theta^{up}_{min}, \theta^{up}_{max}] - H[\theta^{d}_{min}, \theta^{d}_{max}] & t_2 < t \le t_{max} \\ 0 & \textit{else}, \end{cases} \quad (51)$$

where

$$t_0 = \sqrt{(|x_p| - L/2)^2 + (r_c + l)^2}/c, \quad (52)$$

and $t_{max} = \sqrt{(|x_p| + L/2)^2 + (r_c + l)^2}/c$.

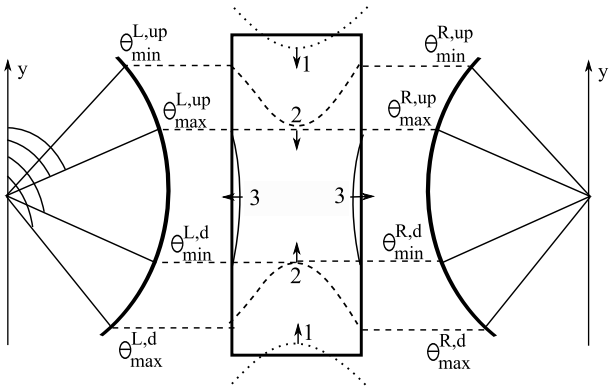

Fig. 9. Picture showing the integration angles for zone 5. The transducer is seen as a back view in the $x-y$ plane. The intersections at three time instances are plotted starting with the dashed arcs (1) and ending with the solid arcs (3). The direction of the propagation is indicated with arrows.

VIII. Spatial impulse response for zone 5

This zone is defined as

$$-L/2 \leq x_p \leq L/2,\ |y_p| \leq |z_p| \tan[V],\ z_p > 0.$$

It is different from the previous zones as Fig. 9 reveals. In this zone, arcs are split apart (dashed arcs 1) and as time exceeds the arcs will combine and create two new arcs (solid arcs 3). The angles are therefore divided into upper and lower angles on both sides of the transducer as shown in Fig. 9. For the upper arcs the following angle definitions are valid

$$\begin{aligned}
\theta^{up}_{max} &= \phi_{max}, && (53)\\
\theta^{up}_{min} &= \pi/2 - V, && (54)\\
\theta^{R,up}_{max} &= \phi^{R}_{max}, && (55)\\
\theta^{up}_{min} &= \pi/2 - V, && (56)\\
\theta^{L,up}_{max} &= \phi^{L}_{max}, && (57)\\
\theta^{L,up}_{min} &= \pi/2 - V. && (58)
\end{aligned}$$

Here $\phi_{maximum} = \pi - \gamma$. The spatial impulse response for these angles then becomes

$$h_{up} = \begin{cases}
0 & t < t_{start}\\
\Lambda^{up} & t_1 \geq t \leq t_3\\
\Lambda^{up} - H[\theta^{R,up}_{min}, \theta^{R,up}_{max}] & t_3 < t \leq t_1\\
\Lambda^{up} - H[\theta^{L,up}_{min}, \theta^{L,up}_{max}] & t_3 \geq t > t_1\\
\Lambda^{up} - H[\theta^{L,up}_{min}, \theta^{L,up}_{max}] - H[\theta^{R,up}_{min}, \theta^{R,up}_{max}] & t_3 < t > t_1\\
0 & t > t_{max},
\end{cases} \quad (59)$$

where $\Lambda^{up} = 2H[\theta^{up}_{min}, \theta^{up}_{max}]$. The start time and the end time are found as

$$t_{start} = \min \begin{cases} \sqrt{(H/2 - y_p)^2 + (z_p + r_c cos[V])^2}/c \\ \sqrt{(H/2 + y_p)^2 + (z_p + r_c cos[V])^2}/c, \end{cases} \quad (60)$$

$$t_{max} = \max \begin{cases} \sqrt{(L/2 - x_p)^2 + (r_c + l)^2}/c \\ \sqrt{(L/2 + x_p)^2 + (r_c + l)^2}/c. \end{cases} \quad (61)$$

For the lower arcs the following angles are to be defined

$$\begin{aligned}
\theta^{d}_{max} &= 2\pi - 2\gamma - \phi_{max}, && (62)\\
\theta^{d}_{min} &= \pi/2 + V, && (63)\\
\theta^{R,d}_{max} &= 2\pi - 2\gamma - \phi^{R}_{max}, && (64)\\
\theta^{R,d}_{min} &= \pi/2 + V, && (65)\\
\theta^{L,d}_{max} &= 2\pi - 2\gamma - \phi^{L}_{max}, && (66)\\
\theta^{L,d}_{min} &= \pi/2 + V. && (67)
\end{aligned}$$

The spatial impulse response then becomes

$$h_d = \begin{cases}
0 & t < t_{start}\\
\Lambda^{d} & t_4 \geq t \leq t_2\\
\Lambda^{d} - H[\theta^{R,d}_{min}, \theta^{R,d}_{max}] & t_4 < t \leq t_2\\
\Lambda^{d} - H[\theta^{L,d}_{min}, \theta^{L,d}_{max}] & t_4 > t \geq t_2\\
\Lambda^{d} - H[\theta^{L,d}_{min}, \theta^{L,d}_{max}] - H[\theta^{R,d}_{min}, \theta^{R,d}_{max}] & t_4 < t > t_2\\
0 & t > t_{max},
\end{cases} \quad (68)$$

where $\Lambda^{d} = 2H[\theta^{d}_{min}, \theta^{d}_{max}]$.

The final spatial impulse response is therefore

$$h = h_{up} - h_d. \quad (69)$$

Notice the minus sign in the latter. This is necessary since the integrals for h_d becomes negative.

IX. Spatial impulse response for $z_p = 0$ and $y_p = 0$

Points located along the center axis of curvature of the transducer are characterized by a special expression of the spatial impulse response. For such points (7) becomes

$$\begin{aligned}
H &= \frac{1}{2\pi} \int_{\theta_{min}}^{\theta_{max}} \frac{r_c c}{\sqrt{c^2 t^2 - r_c^2}} d\theta,\\
&= \frac{c r_c (\theta_{max} - \theta_{min})}{2\pi \sqrt{c^2 t^2 - r_c^2}}. && (70)
\end{aligned}$$

The boundary angles will, at any time, be the maximum and minimum allowable angles for θ_{max} and θ_{min}. Since the point is located in the focus point a spherical wave intersecting the cylinder shell will intersect in a line parallel to the $y-z$ plane because the x coordinate of the intersection will be constant and dependent on time

only. This is proved in the appendix A. The integration angles are therefore given by

$$\theta_{max} = \frac{\pi}{2} + V, \tag{71}$$

$$\theta_{min} = \frac{\pi}{2} - V. \tag{72}$$

The times of significance in this zone are the start time and the time of flight to the right and the left vertical boundaries. These times are given by

$$t_R = \frac{\sqrt{r_c^2 + \sigma_2[x_p]^2}}{c}, \tag{73}$$

$$t_L = \frac{\sqrt{r_c^2 + \sigma_1[x_p]^2}}{c}. \tag{74}$$

$$t_{start} = \begin{cases} \frac{r_c}{c} & -L/2 \geq x_p \leq L/2 \\ t_R & x_p > L/2 \\ t_L & x_p < -L/2. \end{cases} \tag{75}$$

The spatial impulse response yields

$$h = \begin{cases} 2H[\theta_{min}, \theta_{max}] & t_0 < t \leq min\{t_R, t_L\} \\ H[\theta_{min}, \theta_{max}] & min\{t_R, t_L\} < t \leq max\{t_R, t_L\} \\ 0 & \text{else.} \end{cases} \tag{76}$$

X. Solving the integrals

Clearly the above angle definitions and time definitions are rapidly calculated using a computer. The time consuming part of the suggested algorithm is unarguably the integral calculation of H in (7). This integral is of an elliptical type which generally has no analytical solution. It can, however, always be directly evaluated using a numerical integration scheme. Yet another way of solving the integral is by considering the indefinite integral form

$$\int \frac{q}{\sqrt{f(\tau) + \zeta cos[\theta + \gamma]}} d\theta = \\ = \frac{2q\sqrt{\frac{f[\tau] + \zeta cos[\theta+\gamma]}{f[\tau]+\zeta}}}{\sqrt{f[\tau] + \zeta cos[\theta + \gamma]}} F\left[\alpha, \rho\right], \tag{77}$$

where

$$q = \frac{r_c c}{2\pi}, \ \alpha = \frac{\theta + \gamma}{2}, \ \rho = \frac{2\zeta}{f[\tau] + \zeta}. \tag{78}$$

The function $F\left[\alpha, \rho\right]$ is the elliptical integral function of the first kind

$$F\left[\alpha, \rho\right] = \int_0^{\alpha} \frac{1}{\sqrt{1 - \rho \sin^2[\xi]}} d\xi, \tag{79}$$

where α is the upper integration boundary. The latter integral can be evaluated using infinite series expressions [26], by numerical integration, or using the method suggested by Carlson [27]. The latter is computationally very efficient and a c/Fortran implementation increases the simulation speed significantly.

XI. Simulation case

As a reliable reference for validating the above spatial impulse responses the Field II simulation program is used. This software is capable of simulating spatial impulse responses from any given point in front of a concave rectangular transducer.

A simulation case with a concave rectangular transducer having a concave radius $r_c = 28$ mm, a height $H = 30$ mm, and a length $L = 30$ mm is chosen. Points in all zones are analyzed by generating 2500 random simulation points covering all zones. The corresponding spatial impulse response from each point is calculated and compared with the Field II predictions. Sampling frequencies of 3400 MHz and 100 MHz are applied. The highest sampling frequency of 3400 MHz is applied to ensure sufficient accuracy on short impulse responses. This especially applies to focus zones. The 100 MHz sampling frequency is chosen because it is the usually applied sampling frequency applied in Field II.

XII. Results

Fig. 10 is a comparison between a Field II simulation and a simulation using this work. The result is for a point P in zone 1 located at $\{x_p, y_p, z_p\} = \{1, 1, -10\}$ mm.

The solid line is the prediction of this work, and the circles are the prediction of Field II. Clearly, the comparison verifies excellent agreement. The simulation was performed with a sampling frequency, f_s, of 100 MHz corresponding to a root mean square error (RMS) of 3.2 % relative to the Field II prediction. Notice that only each tenth sample is plotted in the figure thus circles are seen spread apart at some of the arc lengths. Figure 11 is a simulation at the point $\{x_p, y_p, z_p\} = \{8.7, 7.7, 40.9\}$ mm. This simulation yielded an RMS error of 24.7 % which is due to the sharp peak that is not captured with Field II as shown in the figure.

To quantify the models accuracy at several points in front of the transducer a three dimensional simulation domain with the dimensions $50x50x100$ mm for the x, y, z coordinates, respectively, were defined. The simulation space was set to start at $z = -27.9$ mm and placed symmetrically around $\{x, y\} = \{0, 0\}$. It was furthermore ensured that no points were located behind the transducer. The x and y coordinates were linearly spaced and the z coordinates were randomly distributed with a Gaussian distribution. This yields 2500 simulation points covering all the zones in front of the transducer.

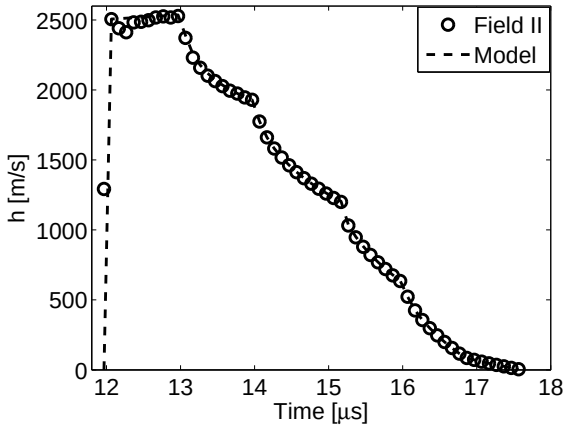

Fig. 10. Spatial impulse response at $\{x_p, y_p, z_p\} = \{1, 1, -10\}$ mm. Circles are Field II. Solid line is the presented model.

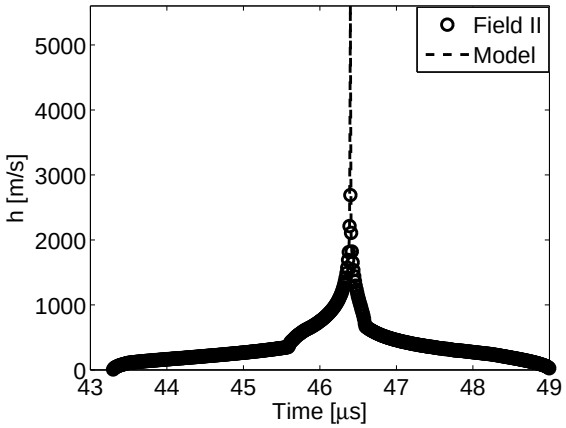

Fig. 11. Spatial impulse response for a point $\{x_p, y_p, z_p\} = \{8.7, 7.7, 40.9\}$ mm. The error is 24.7 % with a samplings frequency of 100 MHz.

The sampling frequency was significantly increased to 3400 MHz which decreases errors due to inconsistency in eventually sharp edges.

Figure 12a shows a projection of all the errors onto the x-y plane as a gray scale plot. The solid white square in the figure shows the contour of the transducer when projected onto the x-y plane. A given pixel color corresponds to the relative deviation and deviations ranging from approximately 0 % to 3.5 % are found. The mean deviation was calcualted to 0.41 %. Also it should be identified that points located outside the transducer's lateral width has the highest agreement. Figure 12b shows the distribution of the errors. Clearly it is seen that the deviations are clustered below 1 %, revealing that the consistency in general is very high. Simulations using the exact same point locations but with a samplings frequency of 100 MHz were also made. A mean deviation of 1.37 % and a maximum deviation of 24.7 % corresponding to the results seen in Fig. 11 were then found.

XIII. Discussion

As seen on Fig. 10 and Fig. 11 the algorithm benefits from giving smooth curve segments as compared to Field II. This is because the algorithm is not sensitive to discretization errors in summing the responses from many smaller surface elements. Smooth line segments in the context of simulating pulse-echo spatial impulse responses and convolving responses with excitation pulses may be of minor influence. This is because of the filtering effect these convolutions will exhibit. However, calculating the spatial impulse response by using a parameterized representation of the transducer has some advantages. Firstly less computation for each point may have to be performed. The calculations are in contrary more exhausting but can be performed efficiently within the cache of the cpu and may require less memory allocation and accessing. Secondly, the whole spatial impulse response can be represented on an analog time scale for the whole transducer element. This limits the numerical round-off error in the energy conservation when summing the spatial impulse responses from more transducer elements. This is, e.g., an important topic when delay time simulation is performed in medical imaging.

Implementation of the algorithm into a medical imaging program such as Field II requires consideration of energy conservation. Field II is capable of simulating the spatial impulse response for small elements at a relatively low sampling frequency (100 MHz). The program is capable of this because it integrates the area of an spatial impulse response within two samples. This means that if edge times of a spatial impulse response are within the desired sampling times, then the energy is conserved in this interval by sub-integration. This requirement is also needed for the algorithm presented in this paper if it is to work as an alternative solver for a program as Field II. Yet another advantage of the new algorithm is, however, that it does not have to sub-integrate for all discretized surface elements, and the conservation of energy calculation is not dependent on near- or far-fields.

The model presented in this work is not entirely analytical because of the elliptical integral of the first kind that has to be evaluated in (79). However, the elliptical integral is very efficiently evaluated and the function is in mathematics often used as an analytical manipulator. Therefore one could argue that the spatial impulse response can be found by a semi-analytical

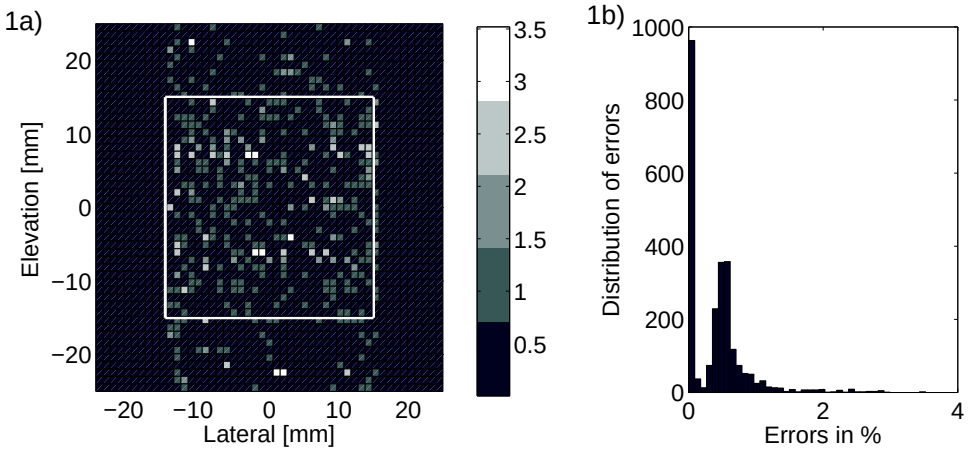

Fig. 12. a) Projection of the errors in percentage onto the x-y plane. The white square indicates the contours of the transducer. b) Distribution of the errors.

expression.

XIV. Conclusion

Exact expressions for the Rayleigh integral on a concave cylindrical shell transducer have been derived and compared to the Field II software simulation program. The spatial impulse response had to be represented in six different ways corresponding to six zones defined in front of the transducer. In order to solve for the impulse response an elliptical integral was evaluated. Evaluation of this integral is the most time consuming part in the algorithm, and thus has to be solved as efficiently as possible if the algorithms are to compete with far-field approximations on prediction time. The root mean square errors for the different zones are ranging from 0 % to 3.5 % where the error is calculated in percent relative to the Field II prediction for a 3400 MHz samplings frequency. An average error for 2500 simulation points spread across all the domains was found to be 0.41 %.

Appendix

To prove that for points satisfying $z_p = 0$ and $y_p = 0$ the intersection curve of a sphere and a cylinder is parallel to the $y - z$ plane one considers the general expression of a sphere

$$(x - x_0)^2 + (y - y_0)^2 + (z - z_0)^2 = R_s^2, \qquad (80)$$

and a cylinder with its length along the x direction

$$y^2 + z^2 = r_c^2, \qquad (81)$$

where R_s and r_c are the radius of the sphere and the cylinder shell, respectively. The coordinates x_0, y_0, and z_0 are the center of the sphere.

Combining (80) and (81) yields

$$x = \pm\sqrt{R_s^2 - r_c^2} + x_0, \qquad (82)$$
$$z = \pm\sqrt{r_c^2 - y^2}. \qquad (83)$$

Therefore the parametric representation of the intersection becomes

$$\{x, y, z\} = \{\pm\sqrt{R_s^2 - r_c^2} + x_0, y, \pm\sqrt{r_c^2 - y^2}\}. \qquad (84)$$

It is hereby proved that the intersection will be a circular arc in the $y - z$ plane. This plane is located at x but dependent on time as $R_s = ct$.

References

[1] G. E. Tupholme, "Generation of acoustic pulses by baffled plane pistons," *Mathematika*, vol. 16, pp. 209–224, 1969.

[2] P. R. Stepanishen, "Transient radiation from pistons in an infinite planar baffle," *J. Acoust. Soc. Am.*, vol. 49, pp. 1629–1638, 1971.

[3] ——, "The time-dependent force and radiation impedance on a piston in a rigid infinite planar baffle," *J. Acoust. Soc. Am.*, vol. 49, pp. 841–849, 1971.

[4] ——, "An approach to compute time-dependent interaction forces and mutual radiation impedances between pistons in a rigid planar baffle," *J. Acoust. Soc. Am.*, vol. 49, pp. 283–292, 1971.

[5] J. C. Lockwood and J. G. Willette, "High-speed method for computing the exact solution for the pressure variations in the nearfield of a baffled piston," *J. Acoust. Soc. Am.*, vol. 53, pp. 735–741, 1973.

[6] P. R. Stepanishen, "Wide bandwidth near and far field transients from baffled pistons," in *Proc. IEEE Ultrason. Symp.*, 1977, pp. 113–118.

[7] G. R. Harris, "Review of transient field theory for a baffled planar piston," *J. Acoust. Soc. Am.*, vol. 70-1, pp. 10–20, 1981.

[8] J. A. Jensen, "A new calculation procedure for spatial impulse responses in ultrasound," *J. Acoust. Soc. Am.*, vol. 105, no. 6, pp. 3266–3274, 1999.

[9] C.-C. Sung, H.-I. Yang, and J.-H. Jeng, "Calculation of spatial impulse response for array transducer," *Jap. J. Appl. Phys.*, vol. 44-10, pp. 7680–7689, 2005.

[10] A. Penttinen and M. Luukkala, “The impulse response and nearfield of a curved ultrasonic radiator,” *J. Phys. D: Appl. Phys.*, vol. 9, pp. 1547–1557, 1976.
[11] M. Arditi, F. S. Forster, and J. Hunt, “Transient fields of concave annular arrays,” *Ultrason. Imaging*, vol. 3, pp. 37–61, 1981.
[12] J. N. Tjøtta and S-Tjøtta, “Nearfield and farfield of pulsed radiators,” *J. Acoust. Soc. Am.*, vol. 71-4, pp. 824–834, 1982.
[13] W. A. Verhoef, M. J. T. M. Cloostermans, and J. M. Thijssen, “The impulse response of a focused source with an arbitrary axisymmetric surface velocity distribution,” *J. Acoust. Soc. Am.*, vol. 75-6, pp. 1716–1721, 1984.
[14] R. Reibold and R. Kažys, “Radiation of a rectangular strip-like focussing transducer. part1: harmonic excitation.” *Ultrasonics*, vol. 30, pp. 49–55, 1992.
[15] ——, “Radiation of a rectangular strip-like focussing transducer. part2: transient excitation.” *Ultrasonics*, vol. 30, pp. 49–55, 1992.
[16] P. Wu and T. Stepinski, “Spatial impulse response method for predicting pulse-echo fields from a linear array with cylindrically concave surface,” *IEEE Trans. Ultrason., Ferroelec., Freq. Contr.*, vol. 46-5, pp. 1283–1297, 1999.
[17] B. Piwakowski and K. Sbai, “A new approach to calculate the field radiated from arbitrarily structured transducer arrays.” *IEEE Trans. Ultrason., Ferroelec., Freq. Contr.*, vol. 46-2, pp. 422–440, 1999.
[18] J. A. Jensen, “Field: A program for simulating ultrasound systems,” *Med. Biol. Eng. Comp.*, vol. 10th Nordic-Baltic Conference on Biomedical Imaging, Vol. 4, Supplement 1, Part 1, pp. 351–353, 1996b.
[19] ——, “Users’ guide for the Field II program, version 2.70 of may 26, 1999,” Department of Information Technology, DTU, Tech. Rep., 1999.
[20] J. A. Jensen and N. B. Svendsen, “Calculation of pressure fields from arbitrarily shaped, apodized, and excited ultrasound transducers,” *IEEE Trans. Ultrason., Ferroelec., Freq. Contr.*, vol. 39, pp. 262–267, 1992.
[21] M. A. Ellis, D. Guenther, and W. F. Walker, “Spline-based approach for computing spatial impulse responses,” *IEEE Trans. Ultrason., Ferroelec., Freq. Contr.*, vol. 54-5, pp. 1045–1054, 2007.
[22] F. Lingvall, “User manual for the DREAM toolbox- an ultrasound simulation software for use with MATLAB and GNU OCTAVE,” 2009.
[23] S. Holm, “Ultrasim - a toolbox for ultrasound field simulation,” *University of Oslo*, 2001.
[24] J. F. Theumann, M. Arditi, J. J. Meister, and E. Jaques, “Acoustic fields of concave cylindrical transducers,” *J. Acoust. Soc. Am.*, vol. 88-2, pp. 1160–1169, 1990.
[25] H. T. O’Neil, “Theory of focusing radiators,” *J. Acoust. Soc. Am.*, vol. 21-5, pp. 516–526, 1949.
[26] M. Abramowitz and I. A. Stegun, *Handbook of Mathematical Functions with Formulas, Graphs, and Mathematical Tables*, ninth dover printing, tenth gpo printing ed. New York: Dover, 1964.
[27] B. C. Carlson, “Computing elliptic integrals by duplication,” *Numerische Math.*, vol. 33, pp. 1–16, 1979.

Paper II

Spatial impulse response of a rectangular double curved transducer

David Bæk, Morten Willatzen, and Jørgen Arendt Jensen

Journal of the Acoustical Society of America, In review

Spatial impulse response of a rectangular double curved transducer

David Bæk[a)] and Jørgen Arendt Jensen
Center for Fast Ultrasound Imaging, Department of Electrical Engineering, Technical University of Denmark

Morten Willatzen
Mads Clausen Institute for Product Innovation,University of Southern Denmark

(Dated: July 30, 2010)

Calculation of the pressure field from transducers with both a convex and a concave geometry is a complicated assignment that often is solved by subdividing the transducer surface into smaller flat elements of which the spatial impulse response is well known. This method is often seen applied to curved transducers because an analytical solution is not known. In this work a semi-analytical algorithm for the exact solution to a first order in diffraction effect of the spatial impulse response of rectangular shaped double curved transducers is presented. The algorithm and an approximation of it are investigated. The approximation reformulates the algorithm to an analytical integrable expression which is computationally efficient to solve. Simulation results are compared with the simulation software Field II. By calculating the response from 200 different points yields a mean error for the different approximations ranging from 0.03 % to 0.8 % relative to a numerical solution for the spatial impulse response. It is shown that the presented algorithm gives consistent results with Field II for both a linear flat, a linear focused, and a convex non-focused element. Best solution was found to be 0.01 % with a three-point Taylor expansion.

PACS numbers: 43.38.Hz,43.20.Px,43.40.Rj

I. INTRODUCTION

Calculation of spatial impulse responses for pressure calculations and pulse-echo responses has been a well known technique for decades. Some of the first works within this field were by Tupholme and Stepanishen[1,2] and several analytical expressions for rectangular, plane circular, concave circular, and array transducer have been reported since then[3–11]. Also expressions for transducers with a slightly in-homogenous surface movement have been introduced[12,13]. Most of these works represent simple transducer geometries, which are not the types often used in medical imaging. The simple solutions can be used to calculate the spatial impulse response of more complicated geometries such as annular arrays, linear elevation focused transducers, convex transducers, and double curved transducers, i.e., rectangular transducers with a convex geometry and an elevation focused geometry. Typically this is done by subdividing the surface into smaller simpler elements such as triangles or rectangles. The final response is then calculated by applying superposition of all the responses. An example where this principle is practically applied is the Field II simulation software package[14,15]. This package utilizes the algorithms described by Jensen[8,16,17]. Only a minor part of the literature within spatial impulse responses addresses the problem of finding analytical expressions of curved rectangular transducers. Within these literatures the works[18–20] show that subdivision of the elements into small stripes or rectangles are possible. The motivation for applying these assumptions is that no analytical solution this far has been found. Theumann et al.[21] formulated a semi-analytical expression for points inside a closed cylinder. To model the response from slightly curved transducer elements, that often are found in medical imaging, simulation tools such as Ultrasim[22], DREAM[23], DELFI[24], and Field II typically apply a discretization of the surface into smaller elements and they then solve for the spatial impulse response by summing up contributions from smaller planar elements or they utilize a special integration technique that efficiently solves the Rayleigh integral.

This paper presents an exact expression for the spatial impulse response of a rectangular convex elevation focused transducer (or double curved transducer) in the form of an elliptical integral. This integral is shown to be solvable by applying either a Taylor expansion or fitting a second order polynomial to a part of the elliptical integral. Both the elliptical integral and the different approximations are the topic of this paper.

[a)] Electronic address: db@elektro.dtu.dk

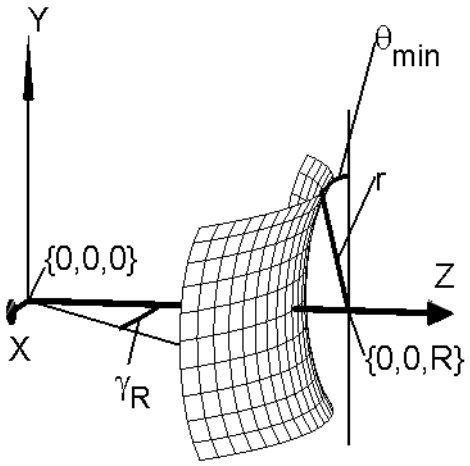

FIG. 1. Figure showing the geometrical definition of the double curved transducer.

II. THEORY

The spatial impulse response is assumed by the Rayleigh integral[1,2]:

$$h(\vec{r},t) = \frac{1}{2\pi}\int_S \frac{\delta(t-\frac{|\vec{r}|}{c})}{|\vec{r}|}dS \tag{1}$$

For this equation to hold it is assumed that the wavelength is much smaller than the curvature of the transducer. It is thereby assumed that the secondary diffraction effects are negligible[10,25] and it is furthermore assumed that the surface movement is uniform.

A torus can be formed by an outer revolution angle γ and an inner revolution angle θ describing a circle that rides on the outer circle. The angles are limited within $0-2\pi$ for γ and $0-\pi$ for θ.

A double curved transducer as considered in this work is defined by the torus coordinates

$$x = (R - r\sin\theta)\sin\gamma \tag{2}$$
$$z = (R - r\sin\theta)\cos\gamma, \tag{3}$$
$$y = r\cos\theta, \tag{4}$$

where the angles γ and θ are the revolving angles and R and r define the outer and the inner circle radius, respectively. Figure 1 depicts the boundary limiting angles and the geometry. The maximum and minimum opening angles for the concave curvature are defined as θ_{min} and θ_{max}, where $\theta_{max} = \pi - \theta_{min}$. Similarly do γ_L and γ_R define the limiting angles of the convex curvature and due to the transducer symmetry: $\gamma_R = -\gamma_L$. It should be noted that in this work the positive angle definition for γ is calculated CCW around the y-axis and relative to the z-axis. The angle γ_R is therefore negative. Furthermore, the θ angle definition has its zero reference from the vertical line going through the point $\{0,0,R\}$ parallel to the y-axis, hence $0 \le \theta \le \pi$. All Cartesian coordinates are relative to the $\{0,0,0\}$ coordinate. A point, $P = \{x_p, y_p, z_p\}$, can be placed at any location in front of the transducer, to the left and to the right, below or above the transducer. The only requirement for the point's location is that a spherical wave emitted from the location does not meet the backside of the concave transducer before meeting the front side.

To perform the integration in (1) a definition of the surface element, dS, on the torus surface S is needed

$$dS = r(R - r\sin\theta)d\gamma d\theta, \tag{5}$$

which is valid when the torus is parametric defined as $T(\gamma,\theta) = z\vec{i} + x\vec{j} + y\vec{k}$.

By considering Fig. 2 and by applying cosine relations one can obtain an expression for the angle β as

$$\begin{aligned}\beta &= \cos^{-1}\left[\frac{|OP^*|^2 + (R - r\sin[\theta])^2 - ((ct)^2 - (y_p - r\cos[\theta])^2)}{2(R - r\sin[\theta])|OP^*|}\right] \\ &= \cos^{-1}\left[\frac{k - c^2t^2 - 2ry_p\cos[\theta] - 2rR\sin[\theta]}{2|OP^*|R - 2|OP^*|r\sin[\theta]}\right],\end{aligned} \tag{6}$$

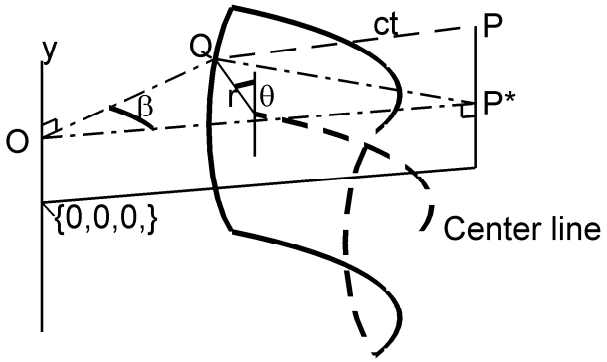

FIG. 2. Figure showing the geometrical definition of the angle β.

where t is the time and c is the speed of sound and $k = |OP^*|^2 + r^2 + R^2 + y_p^2$.

At any time instance the surface element, dS, can be found as

$$\begin{aligned} dS &= r(R - r\sin\theta)\frac{\partial\beta}{\partial t}dtd\theta \\ &= r(R - r\sin\theta)\frac{2c^2t}{(2|OP^*|R - 2|OP^*|r\sin\theta)\sqrt{1 - \frac{(-k+c^2t^2+2ry_p\cos\theta+2rR\sin\theta)^2}{(2|OP^*|R-2|OP^*|r\sin\theta)^2}}}dtd\theta. \end{aligned} \tag{7}$$

By substituting (7) into (1) the integral for the spatial impulse response becomes:

$$h(t_i) = \frac{1}{2\pi}\int_{\theta_{min}(t_i)}^{\theta_{max}(t_i)} \frac{cr}{|OP^*|\sqrt{1 - \frac{(-k+c^2t^2+2ry_p\cos\theta+2rR\sin\theta)^2}{(2|OP^*|R-2|OP^*|r\sin\theta)^2}}}d\theta. \tag{8}$$

Notice that β is another definition of γ but with a zero reference to the point P's location. The surface integral in (1) has hereby been transformed into a line integral of elliptical form that integrates along the intersection between a crossing sphere and the transducer.

The integration boundaries θ_{min} and θ_{max} are to be found from (6). A general expression for the angle θ is found by isolating it in (6) for a given angle of β. This will due to the $\cos^{-1}()$ yield four solutions of which two are valid for the integration domain defined for this type of transducer. The two remaining angles are to be used if $\pi \leq \theta \leq 2\pi$.

$$\theta = \cos^{-1}\left[\frac{f_1 \pm f_2}{f_3}\right], \tag{9}$$

where

$$f_1 = 2ry_p(k - c^2t^2 - 2|OP^*|R\cos(\beta))), \tag{10}$$

$$\begin{aligned} f_2 = [&(2rR - 2|OP^*|r\cos(\beta))^2(-(k - c^2\ t^2)^2 + (2r)^2(R^2 + y_p^2) + ... \\ &+ (2|OP^*|\cos(\beta)(2R(k - 2\ r^2 - c^2t^2) + 2|OP^*|(r^2 - R^2)\cos(\beta))))]^{1/2}, \end{aligned} \tag{11}$$

$$f_3 = 4r^2\left[R^2 + y_p^2 + |OP^*|\cos(\beta)\left(|OP^*|\cos(\beta) - 2R\right)\right]. \tag{12}$$

There are three values of β to which the integration boundaries occur. These are for the angles at which the intersecting curve crosses the vertical side edges, and for the angle at which the intersecting curve can be split into two arcs by a vertical plane through P and the y-axis. The values are $\beta_l = (\gamma_L - \gamma_p)$, $\beta_r = (\gamma_R - \gamma_p)$, and $\beta_0 = 0$, where

$$\gamma_p = \tan^{-1}\left[\frac{x_p}{z_p}\right]. \tag{13}$$

The angle γ_p is the angle to which the point P is located relative to the z-axis in the xz-plane.

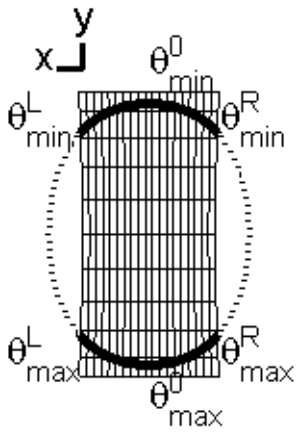

FIG. 3. Figure showing the definition of the integration angles θ^L_{min}, θ^L_{max}, θ^R_{min}, and θ^R_{max}, which occur when the spherical wave has passed the boundaries of the transducer. The transducer is seen from the back side toward the positive z-axis.

Each value of β corresponds to a wave crossing that have passed a transducer edge (γ_L and γ_R) or not yet passed an edge (γ_p). This is illustrated by Fig. 3, where a transducer is seen from the back side in the xy-plane and towards the positive z-axis. The solid arcs are defining the intersection between a sphere emanating from a point P and the dotted lines are the sphere's crossing with a fictive extension of the transducer depicted. The integration angles associated with β_l are θ^L_{min} and θ^L_{max}. The corresponding angles for β_r are θ^R_{min} and θ^R_{max} while for β_0 the associated angles are θ^0_{min} and θ^0_{max}. The angles θ^L_{min}, θ^L_{max}, θ^R_{min}, and θ^R_{max} found in Fig. 3 are illustrated as being defined at the transition from solid to dotted wave line. The angles θ^0_{min} and θ^0_{max} split the solid arcs into a left and a right arc line. For the depicted situation in Fig. 3 the spatial impulse response found from (8) is calculated by organizing the integration angles as

$$h = 2\frac{1}{2\pi}\int_{\theta^0_{min}}^{\theta^0_{max}} I(\theta)d\theta - \frac{1}{2\pi}\int_{\theta^L_{min}}^{\theta^L_{max}} I(\theta)d\theta - \frac{1}{2\pi}\int_{\theta^R_{min}}^{\theta^R_{max}} I(\theta)d\theta, \tag{14}$$

where $I(\theta)$ is the integrand found in (8).

It is beneficial to define two functions for the integration angles as:

$$\theta[t,\chi,t_s,\theta_s,t_e,\theta_e,\beta] = \begin{cases} \theta_s & t \le t_s \\ \cos^{-1}\left[\frac{f_1(\beta,t)+\chi f_2(\beta,t)}{f_3(\beta,t)}\right] & t_s < t < t_e \\ \theta_e & t \ge t_e, \end{cases} \tag{15}$$

$$\theta_{single}[t,\chi,\beta]) = \cos^{-1}\left[\frac{f_1(\beta,t)+\chi f_2(\beta,t)}{f_3(\beta,t)}\right]. \tag{16}$$

Here t_s defines a lower time at which the integration angle is a constant. Similarly, t_e defines an upper time at which the angle is constant. In between these times the angle θ takes on a time dependent value. The constant χ takes on the values 1 or -1 and determines the sign in front of the function f_2. The function θ_{single} is useful for calculating single angle values, which is necessary in some of the follow definitions of the spatial impulse response. By defining the integration angles as having a value at all time instances the number of time branching needed to define the spatial impulse response is limited. By this it is meant that the pulse will have a starting time, which corresponds to the time at which the sphere touches the aperture the first time, similarly the pulse has an end time. In between these two times many crossings between the edges of the aperture and the sphere will occur. By properly subtracting and adding line contributions each time the sphere crosses a boundary, one can achieve much fewer expressions that accounts for all point locations in front of the transducer. This is shown in the following.

III. TIME OF FLIGHT DEFINITIONS

To fully describe all possible locations of a point in front of the transducer one needs to define nine time of flight values. These times are given by the distance from the point, P, to each transducer corner, shortest distance to the

side edges at γ_L and γ_R, the shortest distances to the upper and the lower horizontal edges at θ_{max} and θ_{min}, and the shortest distance to the transducer. The transducer corners are defined as c_1, c_2, c_3, and c_4. Corner coordinates em are defined as $c_i = \{x, y, z\}$:

$$c_1 = \{(R - r\sin[\theta_{min}])\sin[\gamma_L],\ r\cos[\theta_{min}],\ (R - r\sin[\theta_{min}])\cos[\gamma_L]\}, \tag{17}$$
$$c_2 = \{(R - r\sin[\theta_{max}])\sin[\gamma_L],\ r\cos[\theta_{max}],\ (R - r\sin[\theta_{max}])\cos[\gamma_L]\}, \tag{18}$$
$$c_3 = \{(R - r\sin[\theta_{min}])\sin[\gamma_R],\ r\cos[\theta_{min}],\ (R - r\sin[\theta_{min}])\cos[\gamma_R]\}, \tag{19}$$
$$c_4 = \{(R - r\sin[\theta_{max}])\sin[\gamma_R],\ r\cos[\theta_{max}],\ (R - r\sin[\theta_{max}])\cos[\gamma_R]\}, \tag{20}$$

Coordinates for the shortest distances to the vertical edges at γ_L and γ_R are geometrically differently defined according to the location of the point, P, and is in this work referred to as c_L, and c_R, respectively. Similar situations occur for coordinates defining the shortest distance to the upper and the lower horizontal transducer edges. The location of these horizontal edges are defined by θ_{min} and θ_{max} as shown in Fig. 1. The coordinates to the shortest distance at these locations are here defined as c_5 and c_6 for the edges associated with θ_{min} and θ_{max}, respectively. The location of the coordinate for the shortest distance to the transducer is denoted c_0.

The time of flight associated with the different coordinates are hereafter defined as t_{c_0}, t_{c_1}, t_{c_2}, t_{c_3}, t_{c_4}, t_{c_5}, t_{c_6}, t_{c_L}, and t_{c_R}.

IV. THE DIFFERENT ZONES

The final integral expression in (1) takes on different forms depending on where the point, P, is located relative to the transducer. It is beneficial to define different zones at which the point can be located at relative to the transducer. In this work it is chosen to define ten zones in total as mathematically described in the following. These definitions will cover all possible zones that a point P can be found in. See the multimedia file for an animation of the zones.

Zone 1: $\theta_{min} \le \theta_p \le \theta_{max}\ ,\ |OP^*| < R\ ,\ \gamma_R \le \gamma_p \le \gamma_L,$
Zone 2: $\theta_{min} \ge \theta_p \le \theta_{max}\ ,\ |OP^*| < R\ ,\ \gamma_L \le \gamma_p \le \gamma_R,$
Zone 3: $(|\theta_p| > \theta_{max}\ ||\ |\theta_p| < \theta_{min})\ , \gamma_R \le\ \gamma_p \le \gamma_L\ ,\ y_p! = 0\ ,\ |OP^*| \ge R,$
Zone 4: $((\gamma_p < \gamma_R)\ ||\ (\gamma_p > \gamma_L))\ ,\ |OP^*| > R\ ,\ \theta_{min} < |\theta_p| < \theta_{max},$
Zone 5: $\theta_{min} < |\theta_p| < \theta_{max}\ ,\ \gamma_L \ge \gamma_p \ge \gamma_R\ ,\ |OP^*| > R,$
Zone 6: $((\theta_{max} < \theta_p)\ ||\ (\theta_{min} > \theta_p))\ ,\ ((\gamma_p < \gamma_R)\ ||\ (\gamma_p > \gamma_L))\ ,\ y_p! = 0\ ,\ |OP^*| < R,$
Zone 7: $((|\theta_p| > \theta_{max})||(|\theta_p| < \theta_{min}))\ ,\ \gamma_R \le \gamma_p \le \gamma_L\ ,\ y_p! = 0\ ,\ |OP^*| < R,$
Zone 8: $((\theta_{max} < |\theta_p|)\ ||\ (\theta_{min} > |\theta_p|))\ ,\ ((\gamma_p < \gamma_R)\ ||\ (\gamma_p > \gamma_L))\ ,\ y_p! = 0\ ,\ |OP^*| \ge R,$
Zone 9: $y_p = 0\ ,\ |OP^*| = R$
Zone 10: $|OP^*| = R\ ,\ \gamma_L \le \gamma_p \le \gamma_R\ ,\ y_p = 0,$
See an illustration of the zones in the video: "ZoneVideo" found on attached CD.

A. Spatial impulse response for Zone 1

This zone is located directly in front of the transducer and before the elevation focus. A sphere emanating from within this zone may intersect the transducer as shown in Fig. 4a and Fig. 4b. Initially the crossing will be a closed arc with upper and lower integration boundaries θ^0_{min} and θ^0_{max} as seen in Fig. 4a. The angle θ^0_{min} gets equal to θ_{min} when the crossing exceeds the upper horizontal edge of the transducer. A similar situation occurs for the θ^0_{max} that equals θ_{max} when the crossing exceeds the lower horizontal edge of the transducer. For the time instances, at which the intersections have not yet exceeded the vertical side of the transducer, the spatial impulse response is calculated as

$$h = 2\frac{1}{2\pi}\int_{\theta^0_{min}}^{\theta^0_{max}} I(\theta)d\theta, \tag{21}$$

where $I(\theta)$ is the integrand found in (8). The factor of two is because the integration only integrates along one of the two line segments. Due to the symmetry of the segments the integral must be multiplied with a factor of two.

For the time instances where the intersections crosses the vertical sides of the transducer, i.e γ_R and γ_L, two new set of integration limits occur: θ^R_{max} and θ^R_{min} for γ_R and θ^L_{max} and θ^L_{min} for γ_L as seen in Fig. 4b. The spatial impulse response can then be calculated following one of two principles. The first principle relies on integrating along arcs that actually intersect the transducer (See solid lines on Fig. 4). The spatial impulse response is then formulated as

$$h = \frac{1}{2\pi}\int_{\theta^0_{min}}^{\theta^R_{min}} I(\theta)d\theta + \frac{1}{2\pi}\int_{\theta^0_{min}}^{\theta^L_{min}} I(\theta)d\theta + \frac{1}{2\pi}\int_{\theta^R_{max}}^{\theta^0_{max}} I(\theta)d\theta + \frac{1}{2\pi}\int_{\theta^L_{max}}^{\theta^0_{max}} I(\theta)d\theta. \tag{22}$$

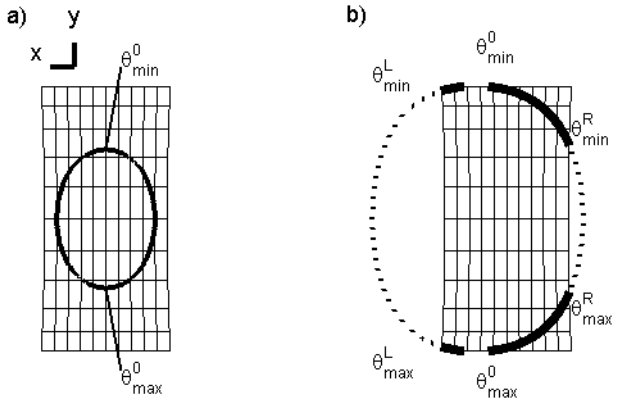

FIG. 4. Figure showing a sphere's crossing with a transducer (solid) and virtual crossings (dotted). View seen from the transducer back side in direction of the z-axis. a) The sphere has not yet crossed the side edges. The point is centered at $x_p = 0$, which gives symmetry. b) The sphere has crossed the edges. Dotted lines indicate the virtual arc crossings. The point is offset to the left, which makes the left virtual arc significant bigger than the right virtual arc. *See an illustration of the angles being created by the crossing in the video: "AngleVideo" found on the attached CD.*

This yields four integrations.

The second method relies on calculating contributions from arc lengths located outside the transducer geometry as if the transducer was violating the limitations by $\gamma_L \leq \gamma \leq \gamma_R$. One should then subtract contributions from these virtual arcs from the total response. A mathematical formulation of this can be found as

$$h = 2\frac{1}{2\pi}\int_{\theta^0_{min}}^{\theta^0_{max}} I(\theta)d\theta - \frac{1}{2\pi}\int_{\theta^L_{min}}^{\theta^L_{max}} I(\theta)d\theta - \frac{1}{2\pi}\int_{\theta^R_{min}}^{\theta^R_{max}} I(\theta)d\theta. \tag{23}$$

The latter principle requires three integrations and may be considered more stable than the first principle because it has fewer small arc contributions. Throughout this work the second principle is utilized for formulating the spatial impulse response in all zones. Note, however, that the first integration principle will give exactly the same result and could just as well have been used.

The complete spatial impulse response for the current zone using the latter principle is formulated as

$$\begin{aligned} h_{zone1}(t) = {} & 2h[\theta[t,1,t_0,\theta_0,t_{c_5},\theta_{min},\beta_0],\theta[t,-1,t_0,\theta_0,t_{c_6},\theta_{max},\beta_0]]- \\ & h[\theta[t,1,t_0,\theta_R,t_{c_3},\theta_{min},\beta_r],\theta[t,-1,t_0,\theta_R,t_{c_4},\theta_{max},\beta_r]]- \\ & h[\theta[t,1,t_0,\theta_L,t_{c_1},\theta_{min},\beta_l],\theta[t,-1,t_0,\theta_L,t_{c_2},\theta_{max},\beta_l]]. \end{aligned} \tag{24}$$

This pulse is therefore defined from the minimum time instance, t_0, to the maximum time instance, which is one of the times t_{c1}, t_{c2}, t_{c3}, t_{c4}, t_{c5}, or t_{c6}. Note that (24) accounts for the different edge times and angle limitations through the formulation of the analytical function θ in (15).

A short analysis of the integration angles represented in (24) can be performed for a given case by plotting the different θ angles as shown in Fig. 5. The considered situation is shown for a point located at $\{x_p, y_p, z_p\} = \{5, 0, 45\}$ mm on a transducer with a height of 30 mm, outer radius, R, of 60 mm, inner radius, r, of 90 mm and a $\gamma_L = 0.26$. The point is therefore placed in the xz-plane wherefore $t_{c_5} == t_{c_6}$. Furthermore, the point is placed to the left ($x_p > 0$) of the z-axis, which results in $t_{c_L} < t_{c_R}$ and $t_{c_1} == t_{c_2} < t_{c_3} == t_{c_4}$. The contribution from the virtual arc to the left of the transducer is therefore only nonzero in the time interval $t_{c_L} \leq t \leq t_{c_3}$ and for the right virtual arc it is the time interval $t_{c_R} \leq t \leq t_{c_3}$. Notice also that the function (15) introduces a cut off at t_{c_1} and t_{c_2}, which are the time instances at which the virtual arc length to the left of the transducer exceeds the minimum and maximum opening angles θ_{min} and θ_{max}.

B. Spatial impulse response for Zone 2 to Zone 10

The same analysis principle as applied for Zone 1 can be applied for all other zones.

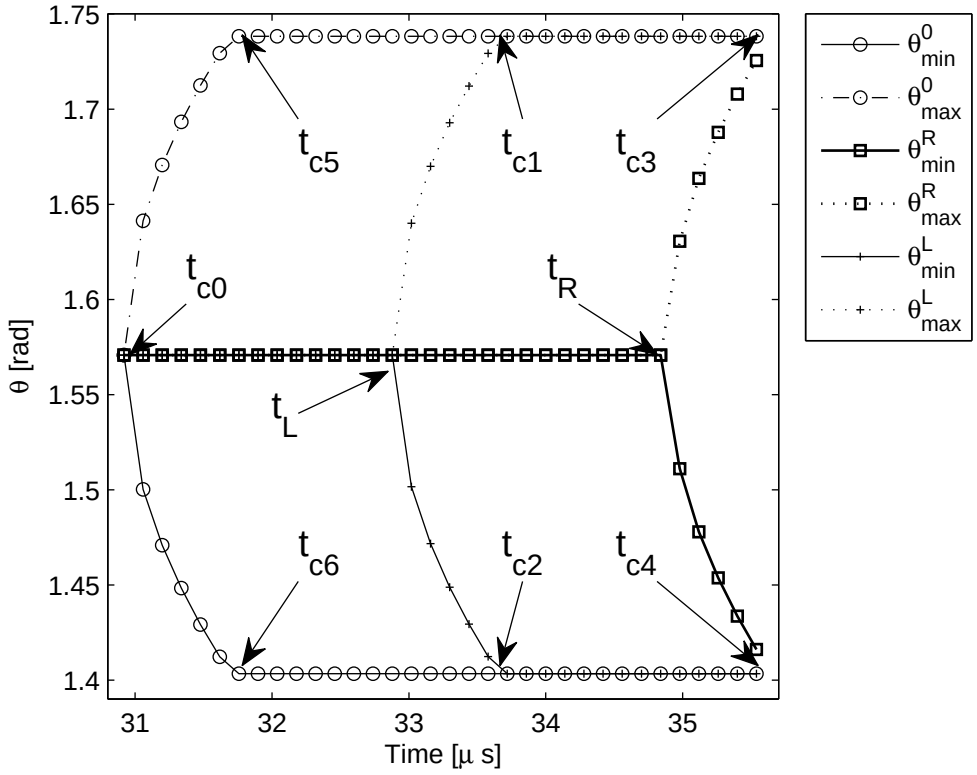

FIG. 5. Figure showing the integration angles plotted for a point located in Zone 1 of a transducer. The angles show that the wave crosses the left edge before it crosses the right. Start and end times are t_{c_0} and t_{c_3}, respectively.

1. Zone 2

For Zone 2 the spatial impulse response formulation is dependent on the point being to the right or to the left of the transducer. The responses are formulated as follows:

For $\gamma_p < \gamma_R$

$$h_{zone2}(t) = h[\theta[t, 1, t_{c_R}, \theta_{c_R}, t_{c_3}, \theta_{min}, \beta_r], \theta[t, -1, t_{c_R}, \theta_{c_R}, t_{c_4}, \theta_{max}, \beta_r]] - h[\theta[t, 1, t_{c_L}, \theta_{c_L}, t_{c_1}, \theta_{min}, \beta_l], \theta[t, -1, t_{c_L}, \theta_{c_L}, t_{c_2}, \theta_{max}, \beta_l]]. \quad (25)$$

For $\gamma_p > \gamma_L$

$$h_{zone2}(t) = h[\theta[t, 1, t_{c_L}, \theta_{c_L}, t_{c_1}, \theta_{min}, \beta_l], \theta[t, -1, t_{c_L}, \theta_{c_L}, t_{c_2}, \theta_{max}, \beta_l]] - h[\theta[t, 1, t_{c_R}, \theta_{c_R}, t_{c_3}, \theta_{min}, \beta_r], \theta[t, -1, t_{c_R}, \theta_{c_R}, t_{c_4}, \theta_{max}, \beta_r]]. \quad (26)$$

2. Zone 3

For Zone 3 the spatial impulse response is formulated as follows:

If $y_p > 0$

$$\chi_r = \begin{cases} 1, & \theta_{single}[t_{c_3}, 1, \beta_r] == \theta_{min} \\ -1, & else \end{cases} \quad (27)$$

$$\chi_l = \begin{cases} 1, & \theta_{single}[t_{c_1}, 1, \beta_l] == \theta_{min} \\ -1, & else \end{cases} \quad (28)$$

$$h_{zone3}(t) = 2h[\theta[t,1,t_{c_5},\theta_{min},t_{c_5},\theta_{min},\beta_o],\theta[t,1,t_{c_5},\theta_{min},t_{c_6},\theta_{max},\beta_o]]+ h[\theta[t,\chi_r,t_{c_3},\theta_{min},t_{c_3},\theta_{min},\beta_r],\theta[t,\chi_r,t_{c_3},\theta_{min},t_{c_4},\theta_{max},\beta_r]]- h[\theta[t,\chi_l,t_{c_1},\theta_{min},t_{c_1},\theta_{min},\beta_l],\theta[t,\chi_l,t_{c_1},\theta_{min},t_{c_2},\theta_{max},\beta_l]], \quad (29)$$

and for $y_p < 0$

$$\chi_r = \begin{cases} -1, & \theta_{single}[t_{c_4},-1,\beta_r] == \theta_{max} \\ 1, & else \end{cases} \quad (30)$$

$$\chi_l = \begin{cases} -1, & \theta_{single}[t_{c_2},1,\beta_l] == \theta_{max} \\ 1, & else \end{cases} \quad (31)$$

$$h_{zone3}(t) = 2h[\theta[t,-1,t_{c_6},\theta_{max},t_{c_5},\theta_{min},\beta_o],\theta[t,-1,t_{c_6},\theta_{max},t_{c_6},\theta_{max},\beta_o]]+ h[\theta[t,\chi_r,t_{c_4},\theta_{max},t_{c_3},\theta_{min},\beta_r],\theta[t,\chi_r,t_{c_4},\theta_{max},t_{c_4},\theta_{max},\beta_r]]- h[\theta[t,\chi_l,t_{c_2},\theta_{max},t_{c_1},\theta_{min},\beta_l],\theta[t,\chi_l,t_{c_2},\theta_{max},t_{c_2},\theta_{max},\beta_l]], \quad (32)$$

The determination of the sign for $\chi_{l,r}$ is needed because the nature of the angles at the side edges of the transducer is dependent on the point being before or after the elevation focus for a translated and rotated coordinate system to these edges. This means that if the location of the z-coordinate of the point, P, is before or after the elevation focus at the edge when the coordinates x_p, y_p, z_p are transformed to a coordinate system located at the given edge, it alters the sign of $\chi_{r,l}$. A reformulation of the zone definitions may avoid this problem, but for the zone definitions applied in this work it is valid.

3. Zone 4

For Zone 4 the equations are dependent on $\gamma_L \leq \gamma_p \leq \gamma_R$. For $\gamma_L \leq \gamma_p$ the formulation becomes

$$h_{zone4}(t) = h[\theta[t,-1,t_{c_2},\theta_{max},t_{c_L},\theta_{c_L},\beta_l],\theta[t,-1,t_{c_2},\theta_{max},t_{c_2},\theta_{max},\beta_l]]+ h[\theta[t,1,t_{c_1},\theta_{min},t_{c_1},\theta_{min},\beta_l],\theta[t,1,t_{c_1},\theta_{min},t_{c_L},\theta_{c_L},\beta_l]]- h[\theta[t,-1,t_{c_4},\theta_{max},t_{c_R},\theta_{c_R},\beta_r],\theta[t,-1,t_{c_4},\theta_{max},t_{c_4},\theta_{max},\beta_r]]- h[\theta[t,1,t_{c_3},\theta_{min},t_{c_3},\theta_{min},\beta_r],\theta[t,1,t_{c_3},\theta_{min},t_{c_R},\theta_{c_R},\beta_r]], \quad (33)$$

and for $\gamma_p \leq \gamma_R$ the formulation becomes

$$h_{zone4}(t) = h[\theta[t,-1,t_{c_4},\theta_{max},t_{c_R},\theta_{c_R},\beta_r],\theta[t,-1,t_{c_4},\theta_{max},t_{c_4},\theta_{max},\beta_r]]+ h[\theta[t,1,t_{c_3},\theta_{min},t_{c_3},\theta_{min},\beta_r],\theta[t,1,t_{c_3},\theta_{min},t_{c_R},\theta_{c_R},\beta_r]]- h[\theta[t,-1,t_{c_2},\theta_{max},t_{c_L},\theta_{c_L},\beta_l],\theta[t,-1,t_{c_2},\theta_{max},t_{c_2},\theta_{max},\beta_l]]- h[\theta[t,1,t_{c_1},\theta_{min},t_{c_1},\theta_{min},\beta_l],\theta[t,1,t_{c_1},\theta_{min},t_{c_L},\theta_{c_L},\beta_l]], \quad (34)$$

4. Zone 5

For Zone 5 only one expression is needed for describing the spatial impulse response

$$h_{zone5}(t) = 2h[\theta[t,1,t_{c_5},\theta_{min},t_{c_5},\theta_{min},\beta_0],\theta[t,1,t_{c_5},\theta_{min},t_{c_0},\theta_0,\beta_0]]+ 2h[\theta[t,-1,t_{c_6},\theta_{max},t_{c_0},\theta_0,\beta_0],\theta[t,-1,t_{c_6},\theta_{max},t_{c_6},\theta_{max},\beta_0]]- h[\theta[t,1,t_{c_3},\theta_{min},t_{c_3},\theta_{min},\beta_r],\theta[t,1,t_{c_3},\theta_{min},t_{c_R},\theta_R,\beta_r]]- h[\theta[t,-1,t_{c_4},\theta_{max},t_{c_R},\theta_R,\beta_r],\theta[t,-1,t_{c_4},\theta_{max},t_{c_4},\theta_{max},\beta_r]]- h[\theta[t,1,t_{c_1},\theta_{min},t_{c_1},\theta_{min},\beta_l],\theta[t,1,t_{c_1},\theta_{min},t_{c_L},\theta_L,\beta_l]]- h[\theta[t,-1,t_{c_2},\theta_{max},t_{c_L},\theta_L,\beta_l],\theta[t,-1,t_{c_2},\theta_{max},t_{c_2},\theta_{max},\beta_l]]. \quad (35)$$

5. Zone 6

In Zone 6 four different cases are defined. Zone 6 is located to the left and to the right of the transducer and the sign of χ is dependent on the point P being below or above the z-axis for this zone.

For $y_p < 0$ and $\gamma_p < \gamma_R$ the spatial impulse response is formulated as

$$\begin{aligned} h_{zone6}(t) = h[\theta[t, 1, t_{c_4}, \theta_{max}, t_{c_3}, \theta_{min}, \beta_r], \theta[t, 1, t_{c_4}, \theta_{max}, t_{c_4}, \theta_{max}, \beta_r]] - \\ h[\theta[t, 1, t_{c_2}, \theta_{max}, t_{c_1}, \theta_{min}, \beta_l], \theta[t, 1, t_{c_2}, \theta_{max}, t_{c_2}, \theta_{max}, \beta_l]]. \end{aligned} \tag{36}$$

For $y_p > 0$ and $\gamma_p < \gamma_R$ the spatial impulse response is formulated as

$$\begin{aligned} h_{zone6}(t) = h[\theta[t, -1, t_{c_3}, \theta_{min}, t_{c_3}, \theta_{min}, \beta_r], \theta[t, -1, t_{c_3}, \theta_{min}, t_{c_4}, \theta_{max}, \beta_r]] - \\ h[\theta[t, -1, t_{c_1}, \theta_{min}, t_{c_1}, \theta_{min}, \beta_l], \theta[t, -1, t_{c_1}, \theta_{min}, t_{c_2}, \theta_{max}, \beta_l]]. \end{aligned} \tag{37}$$

For $y_p < 0$ and $\gamma_p > \gamma_R$ the spatial impulse response is formulated as

$$\begin{aligned} h_{zone6}(t) = h[\theta[t, 1, t_{c_2}, \theta_{max}, t_{c_1}, \theta_{min}, \beta_l], \theta[t, 1, t_{c_2}, \theta_{max}, t_{c_2}, \theta_{max}, \beta_l]] - \\ h[\theta[t, 1, t_{c_4}, \theta_{max}, t_{c_3}, \theta_{min}, \beta_r], \theta[t, 1, t_{c_4}, \theta_{max}, t_{c_4}, \theta_{max}, \beta_r]]. \end{aligned} \tag{38}$$

For $y_p > 0$ and $\gamma_p > \gamma_R$ the spatial impulse response is formulated as

$$\begin{aligned} h_{zone6}(t) = h[\theta[t, -1, t_{c_1}, \theta_{min}, t_{c_1}, \theta_{min}, \beta_l], \theta[t, -1, t_{c_1}, \theta_{min}, t_{c_2}, \theta_{max}, \beta_l]] - \\ h[\theta[t, -1, t_{c_3}, \theta_{min}, t_{c_3}, \theta_{min}, \beta_r], \theta[t, -1, t_{c_3}, \theta_{min}, t_{c_4}, \theta_{max}, \beta_r]]. \end{aligned} \tag{39}$$

6. Zone 7

This zone is dependent on the sign of y_p. For $y_p > 0$ the spatial impulse response becomes

$$\begin{aligned} h_{zone7}(t) = 2h[\theta[t, -1, t_{c_0}, \theta_{min}, t_{c_0}, \theta_{min}, \beta_0], \theta[t, -1, t_{c_0}, \theta_{min}, t_{c_6}, \theta_{max}, \beta_0]] - \\ h[\theta[t, -1, t_{c_3}, \theta_{min}, t_{c_3}, \theta_{min}, \beta_r], \theta[t, -1, t_{c_3}, \theta_{min}, t_{c_4}, \theta_{max}, \beta_r]] - \\ h[\theta[t, -1, t_{c_1}, \theta_{min}, t_{c_1}, \theta_{min}, \beta_l], \theta[t, -1, t_{c_1}, \theta_{min}, t_{c_2}, \theta_{max}, \beta_l]]. \end{aligned} \tag{40}$$

For $y_p < 0$ the spatial impulse response becomes

$$\begin{aligned} h_{zone7}(t) = 2h[\theta[t, 1, t_{c_0}, \theta_{max}, t_{c_5}, \theta_{min}, \beta_0], \theta[t, 1, t_{c_0}, \theta_{max}, t_{c_0}, \theta_{max}, \beta_0]] - \\ h[\theta[t, 1, t_{c_4}, \theta_{max}, t_{c_3}, \theta_{min}, \beta_r], \theta[t, 1, t_{c_4}, \theta_{max}, t_{c_4}, \theta_{max}, \beta_r]] - \\ h[\theta[t, 1, t_{c_2}, \theta_{max}, t_{c_1}, \theta_{min}, \beta_l], \theta[t, 1, t_{c_2}, \theta_{max}, t_{c_2}, \theta_{max}, \beta_l]]. \end{aligned} \tag{41}$$

7. Zone 8

Zone 8 is very similar to Zone 6, where four conditions were found and it relies on finding the sign of χ as it was seen in Zone 3. For $y_p < 0$ and $\gamma_p < \gamma_R$ the spatial impulse response is formulated as

$$\chi_r = \begin{cases} -1, & \theta_{single}[t_{c_4}, -1, \beta_r] == \theta_{max} \\ 1, & else \end{cases} \tag{42}$$

$$\chi_l = \begin{cases} -1, & \theta_{single}[t_{c_2}, -1, \beta_l] == \theta_{max} \\ 1, & else \end{cases} \tag{43}$$

$$\begin{aligned} h_{zone8}(t) = h[\theta[t, \chi_r, t_{c_4}, \theta_{max}, t_{c_3}, \theta_{min}, \beta_r], \theta[t, \chi_r, t_{c_4}, \theta_{max}, t_{c_4}, \theta_{max}, \beta_r]] - \\ h[\theta[t, \chi_l, t_{c_2}, \theta_{max}, t_{c_1}, \theta_{min}, \beta_l], \theta[t, \chi_l, t_{c_2}, \theta_{max}, t_{c_2}, \theta_{max}, \beta_l]]. \end{aligned} \tag{44}$$

For $y_p > 0$ and $\gamma_p < \gamma_R$ the spatial impulse response is formulated as

$$\chi_r = \begin{cases} 1, & \theta_{single}[t_{c_3}, 1, \beta_r] == \theta_{min} \\ -1, & else \end{cases} \tag{45}$$

$$\chi_l = \begin{cases} -1, & \theta_{single}[t_{c_1}, -1, \beta_l] == \theta_{min} \\ 1, & else \end{cases} \tag{46}$$

$$\begin{aligned} h_{zone8}(t) = h[\theta[t, \chi_r, t_{c_3}, \theta_{min}, t_{c_3}, \theta_{min}, \beta_r], \theta[t, \chi_r, t_{c_3}, \theta_{min}, t_{c_4}, \theta_{max}, \beta_r]] - \\ h[\theta[t, \chi_l, t_{c_1}, \theta_{min}, t_{c_1}, \theta_{min}, \beta_l], \theta[t, \chi_l, t_{c_1}, \theta_{min}, t_{c_2}, \theta_{max}, \beta_l]]. \end{aligned} \tag{47}$$

For $y_p < 0$ and $\gamma_p > \gamma_L$ the spatial impulse response is formulated as

$$\chi_l = \begin{cases} -1, & \theta_{single}[t_{c_2}, -1, \beta_l] == \theta_{max} \\ 1, & else \end{cases} \tag{48}$$

$$\chi_r = \begin{cases} -1, & \theta_{single}[t_{c_4}, -1, \beta_r] == \theta_{max} \\ 1, & else \end{cases} \tag{49}$$

$$\begin{aligned} h_{zone8}(t) = h[\theta[t, \chi_l, t_{c_2}, \theta_{max}, t_{c_1}, \theta_{min}, \beta_l], \theta[t, \chi_l, t_{c_2}, \theta_{max}, t_{c_2}, \theta_{max}, \beta_l]] - \\ h[\theta[t, \chi_r, t_{c_4}, \theta_{max}, t_{c_3}, \theta_{min}, \beta_r], \theta[t, \chi_r, t_{c_4}, \theta_{max}, t_{c_4}, \theta_{max}, \beta_r]]. \end{aligned} \tag{50}$$

For $y_p > 0$ and $\gamma_p > \gamma_L$ the spatial impulse response is formulated as

$$\chi_l = \begin{cases} 1, & \theta_{single}[t_{c_1}, 1, \beta_l] == \theta_{min} \\ -1, & else \end{cases} \tag{51}$$

$$\chi_r = \begin{cases} 1, & \theta_{single}[t_{c_3}, 1, \beta_r] == \theta_{max} \\ -1, & else \end{cases} \tag{52}$$

$$\begin{aligned} h_{zone8}(t) = h[\theta[t, \chi_l, t_{c_1}, \theta_{min}, t_{c_1}, \theta_{min}, \beta_l], \theta[t, \chi_l, t_{c_1}, \theta_{min}, t_{c_2}, \theta_{max}, \beta_l]] - \\ h[\theta[t, \chi_r, t_{c_3}, \theta_{min}, t_{c_3}, \theta_{min}, \beta_r], \theta[t, \chi_r, t_{c_3}, \theta_{min}, t_{c_4}, \theta_{max}, \beta_r]]. \end{aligned} \tag{53}$$

8. Zone 9

This zone is located at the elevation focus of the transducer. Considering (8) and setting $R = |OP^*|$ and $y_p = 0$ yields

$$h_f(t_i) = \frac{1}{2\pi} \int_{\theta_{min}(t_i)}^{\theta_{max}(t_i)} \frac{c\ r}{R\sqrt{1 - \left(1 + \frac{r^2\ -c^2\ t_i^2}{2\ R^2 - 2\ r\ R\ \sin\theta}\right)^2}} d\theta. \tag{54}$$

For the initial time step, where $r^2\ -c^2\ t_i^2 = 0$, the integral is infinite, which is both a numerical problem and physically not appropriate. This has to be accounted for in a given implementation by either finding an asymptotic value using the gradient of the integration values from time $t > t_{minimum}$ and the following time steps, or by finding the initial step from a point located just before the elevation focus as well as one located just after the elevation focus. These initial values may give an approximate mean value of the initial samples at the elevation focus. The mean energy between these two samples may then be distributed across the samples.

The spatial impulse response takes on the following form

$$\begin{aligned} h_{zone9}(t) = 2h_f[\theta[t, 1, t_{c_0}, \theta_{min}, t_{c_0}, \theta_{min}, \beta_0], \theta[t, 1, t_{c_0}, \theta_{max}, t_{c_0}, \theta_{max}, \beta_0]] - \ ... \\ h_f[\theta[t, 1, t_{c_L}, \theta_L, t_{c_1}, \theta_{min}, \beta_l], \theta[t, -1, t_{c_L}, \theta_L, t_{c_2}, \theta_{max}, \beta_l]] - \ ... \\ h_f[\theta[t, 1, t_{c_R}, \theta_R, t_{c_3}, \theta_{min}, \beta_r], \theta[t, -1, t_{c_R}, \theta_R, t_{c_4}, \theta_{max}, \beta_r]]. \end{aligned} \tag{55}$$

Notice that the $\theta[t, 1, t_{c_0}, \theta_{min}, t_{c_0}, \theta_{min}, \beta_0]$ for the first integration equals θ_{min} and $\theta[t, 1, t_{c_0}, \theta_{max}, t_{c_0}, \theta_{max}, \beta_0]$ equals θ_{max} for all time instances.

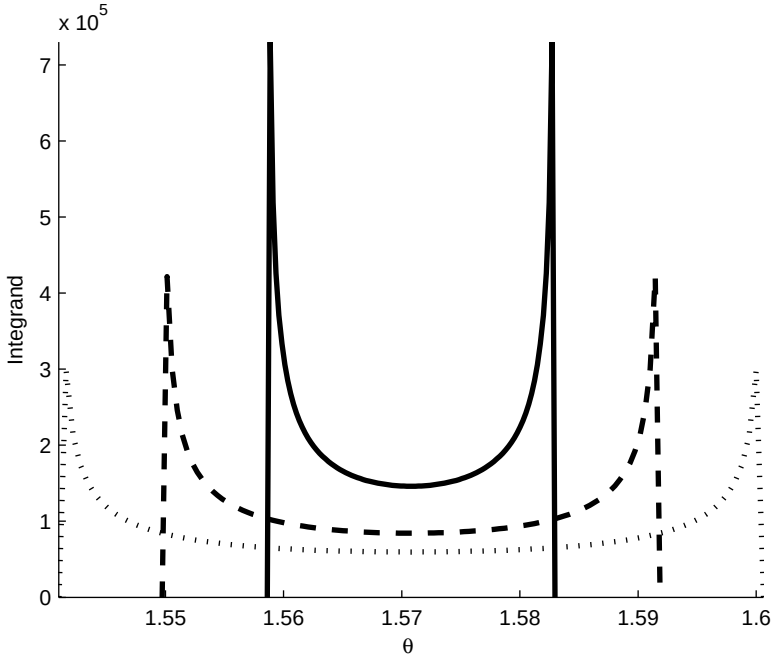

FIG. 6. Figure showing the curve shape of the integrand in (56) at different time steps. It is clearly seen how the curve increases asymptotic forward infinity at ϕ_{min} and ϕ_{max}. Notice that a full symmetric case is shown for the plot. Symmetry is always the case, however, depending on the value of ϕ_{min} and ϕ_{max} one or both spikes at the start and end of the integration domain may not be present.

9. Zone 10

This zone is similar to Zone 2 and only differ at $y_p = 0$. All time of flight calculations are the same. Also the spatial impulse response is given by (25) and (26) as for Zone 2.

V. APPROXIMATING THE INTEGRAL EXPRESSION

The integral in (8) is of elliptical type and requires a numerical solver to find the result. However, the following analysis of the integral will show that an approximation of the integrand makes the spatial impulse response analytically integrable.

Consider (8) in the following form

$$h = \frac{1}{2\pi} \int_{\phi_{min}}^{\phi_{max}} \frac{cr}{|OP^*|\sqrt{1 - P[\theta]}} d\theta, \tag{56}$$

where

$$P[\theta] = \frac{(-k + c^2t^2 + 2ry_p \cos\theta + 2rR\sin\theta)^2}{(2|OP^*|R - 2|OP^*|r\sin\theta)^2}. \tag{57}$$

Example plots for the integrand at several time instance are seen in Fig. 6. The vertical lines indicate the location of the ϕ_{min} and ϕ_{max} at different time steps and as indicated by the form of (57) the integrand approaches infinity for $P[\theta] \to 1$.

Because of the integrand's nature it gets difficult, (but not impossible), to perform a series expansion that can replace the integrand and reveal an analytical integrable integrand without introducing a significant error in energy conservation close to the maximum integration angles. As a consequence this method may not be the most effective one to apply.

It may be more beneficial to consider the expression in (57) and apply a second order Taylor expansion to this polynomial and achieve a second order polynomial, $T[\theta, \theta_0]$, around a local integration angle θ_0.

$$T[\theta, \theta_0] = A[\theta_0]\theta^2 + B[\theta_0]\theta + C[\theta_0], \tag{58}$$

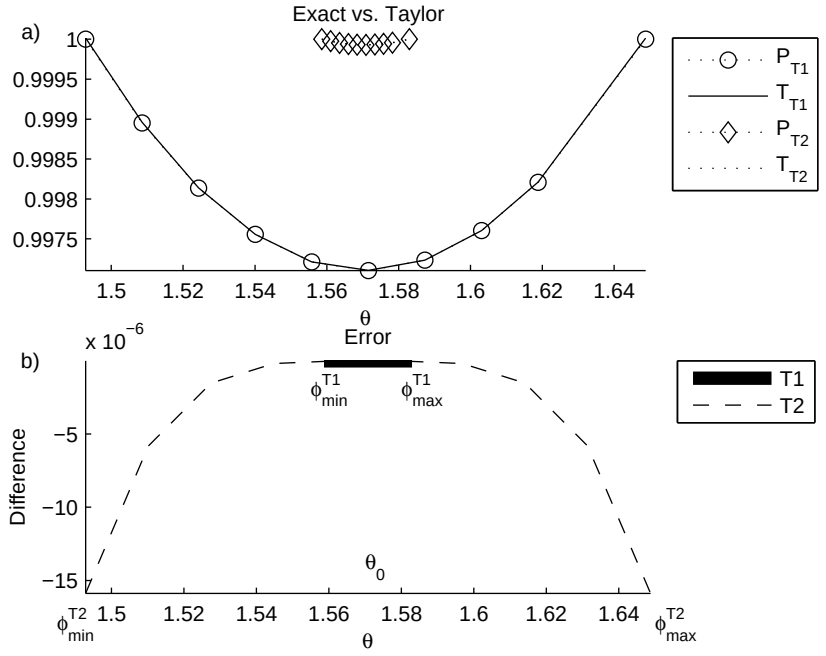

FIG. 7. Figure showing: a) a comparison between $P[\theta]$ and $T[\theta]$ at two time instances, T1 and T2, where T1 < T2. b) the difference between $P[\theta]$ and $T[\theta]$ at the two time instances. Notice how ϕ_{min} and ϕ_{max} includes a wider angle difference for $T2$ and how the error has increased significantly.

where $A[\theta_0]$, $B[\theta_0]$, and $C[\theta_0]$ are the coefficients found by ordering the Taylor series.

Expanding the polynomial into only a second order is in this work beneficial, contrary higher order expansions, since the indefinite integral of the spatial impulse response becomes analytically integrable

$$Int = \frac{1}{2\pi}\int \frac{cr}{|OP^*|\sqrt{1-(A\theta^2+B\theta+C)}}d\theta \tag{59}$$

$$= \frac{1}{2\pi}\frac{c\,r\tan^{-1}\left[\frac{B+2A\theta}{2\sqrt{A}\sqrt{1-C-B\theta-A\theta^2}}\right]}{|OP^*|\sqrt{A}} \tag{60}$$

$$= \frac{1}{2\pi}\frac{i\,c\,r\log\left[2\sqrt{-A\theta^2-B\theta-C+1}-\frac{i\,(2A\theta+B)}{\sqrt{A}}\right]}{\sqrt{A}|OP^*|}, \tag{61}$$

where $i=\sqrt{-1}$.

An integration of (56) can be found by performing the second order Taylor expansion around a sufficient number of θ_0 angles within the interval of ϕ_{min} and ϕ_{max} and then make the corresponding sub integrations. This will, however, compromise the desired benefit of a fast computational expression in the analytical expression.

Consider Fig. 7a. This figure shows how the second order polynomial, $T[\theta,\theta_0]$, fits (57) for $\theta_0 = \frac{\phi_{min}+\phi_{max}}{2}$ at different time steps. It is seen that when a small angle interval $\Delta\phi = \phi_{max}-\phi_{min}$ is considered, as for the T_1 example, a very close curve fit is possible. However, Fig. 7b. shows that for bigger $\Delta\phi$, as for the T_2 example, the residual of the expansion becomes of more and more influence at the outer integration boundaries, which is a natural consequence of the Taylor expansion. This is an undesirable consequence that becomes very important for calculations on large transducers, since a significant amount of energy is located in the neighborhood of ϕ_{min} and ϕ_{max} as shown in Fig. 6

A strategy for capturing the energy at the outer integration boundaries could therefore be to perform Taylor expansions at ϕ_{min}, ϕ_{max}, and $\frac{\phi_{min}+\phi_{max}}{2}$ and then subdivide the integration into three intervals:

$$\left(\phi_{min}\rightarrow\frac{\phi_{min}+\phi_0}{2}\right),\qquad \left(\frac{\phi_{min}+\phi_0}{2}\rightarrow\frac{\phi_{max}+\phi_0}{2}\right),\qquad \left(\frac{\phi_{max}+\phi_0}{2}\rightarrow\phi_{max}\right). \tag{62}$$

This method ensures better conservation of the energy near the outer integration angles than a single expansion around the mean integration value does. Furthermore, it captures the centered curvature. The cost of this method is however, three times more calculation time for small angles.

VI. SIMULATIONS

To test the developed algorithms an adaptive Gauss-Kronrod quadrature numerical integrator from MATLAB is applied for solving the exact form of the integral in (8). As reference to validate the pulse shape of the exact solution a high resolution transducer model in Field II is used. Furthermore, to approximate the integral of the spatial impulse response simulations with a three-point Taylor expansion, as described above, a single-point Taylor expansion at the mean integration angle, and a direct second order polynomial fit are implemented. The latter implementation uses three points to find the coefficients of a second order polynomial. These three points are $P[\phi_{min}]$, $P[(\phi_{min}+\phi_{max})/2]$, and $P[\phi_{max}]$. The latter method differs from the three-point Taylor approximation, because it finds a best polynomial fit through the three points and not a local fit as the Taylor expansion does.

The error is calculated as

$$E_i = 100\frac{\sqrt{\frac{1}{N}\sum_N (h_i - h_{numerical})^2}}{\sqrt{\frac{1}{N}\sum_N h_{numerical}^2}}, \tag{63}$$

where $h_{numerical}$ is the exact solution to the spatial impulse response as represented by (8) and solved using the numerical integrator. h_i is the spatial impulse response calculated with either Field II, h_F, the three-point Taylor expansion, h_{3T}, the single-point Taylor expansion, h_{1T}, or the second order polynomial fit, h_{2p}. N is the number of samples in the response. To get sample times aligned a simple spline interpolation between the points are performed. This is necessary since start times for the pulses may be calculated slightly differently in Field II than in the MATLAB implementation applied in this work.

A double curved transducer with a width of 20 mm and a 30 mm height is simulated. The outer radius, R, is 60 mm and the inner radius, r, is 90 mm. Initially a single response from a point located in Zone 1 at $\{x_p, y_p, z_p\} = \{0, 0, 10\}$ mm is calculated. The coordinates are defined using the coordinate definition of Field II. The zero reference for the z-coordinate is located at the outer most z-coordinates for the transducer defined in the torus coordinates. The sampling frequency is set to 5 GHz. A second simulation case investigates 200 points randomly distributed in front of the transducer and covering all zones.

A third simulation investigates the error for the situation where $R = 90$ mm and $r = 6$ m by comparing h_{3T} and h_{1T} with Field II as reference. The mean error is calculated for 200 points randomly distributed across the zones. This simulation will due to the transducers' large inner radius, r, mimic a convex transducer with no elevation focus. Yet a fourth simulation investigates $R = 6$ m and $r = 6$ m which corresponds to a plane transducer and the mean error of simulating 200 points are calculated. Finally a study case where $R = 6$ m and $r = 60$ mm is performed. This type of transducer corresponds to a elevation focused linear rectangular transducer. The transducer dimensions for simulation case three, four, and five are changed to a more realistic size with a width of 1 mm and a height of 10 mm. The sampling frequency is fixed at 5 GHz.

VII. RESULTS

Figure 8a shows the results of simulating the double curved transducer i.e. $R = 60$ mm and $r = 90$ mm at the point $\{x_p, y_p, z_p\} = \{0, 0, 10\}$ mm. Clearly all the solvers agree visually on the result from a full pulse perspective and a zoom as shown in Fig. 8b is needed to visually identify the difference. The relative errors were found to be: $E_{Field} = 0.40\%$, $E_{1T} = 0.80$ %, $E_{3T} = 0.03$ %, and $E_{2p} = 0.18$ %. A higher exactness for the $3T$ approximator was seen compared to the other solvers. Performing the same simulation for 200 points randomly distributed across all zones resulted in a mean error (ME) of: $\mathrm{ME}_{Field} = 0.45$ %, $\mathrm{ME}_{1T} = 1.78$ %, $\mathrm{ME}_{3T} = 0.01$ %, and $\mathrm{ME}_{2p} = 0.45$ %. Also calculating the mean of the solving time, T_i, for each solver yielded: $\mathrm{T}_{Numerical} = 73.0$ s, $\mathrm{T}_{1T} = 8.7$ s, $\mathrm{T}_{3T} = 9.4$ s, and $\mathrm{T}_{2p} = 7.0$ s. Clearly the numerical solver is by far the slowest, which was also expected, however, the mean times show that an improvement in the error from 1.78 % to 0.01 % can be achieved with a 8.1 % increase in simulation time by applying the three point approximator instead of the fast one point approximator or an improvement in the error from 0.45 % to 0.01 % with a 34.3 % increase in simulation time by changing the solver from the polynomial fitting to the three point expansion. Notice that the Field II calculation time has been left out since it cannot relate to the above times because Field II is implemented in C and the algorithm in this work is implemented in MATLAB.

Figure 9a shows a simulation for a point at $\{x_p, y_p, z_p\} = \{0, 0, 105\}$ mm. A point at this location introduces a sharp spike to the response. From Fig. 9a a zoom onto the spike in Fig. 9a is to be found. Clearly the one point solver h_{1T} is calculating the spike incorrectly. This may look like a wrong edge calculation for this solver, however, the implementation of edge calculation, zones etc. are identical with all the other zones, which are seen to calculate the response more correctly. The errors where found to be $E_{Field} = 0.49$ %, $E_{1T} = 3.58$ %, $E_{3T} = 0.006$ %, $E_{2p} = 0.83$ %.

Figure 10a shows the result of simulating a point at $\{x_p, y_p, z_p\} = \{0, 0, 40\}$ mm on a convex non-elevation focused transducer using the model presented in this work. Figure 10b shows a zoom from Fig. 10a of the horizontal line section. From the latter it can be seen that the h_{1T} curve is having difficulties in capturing the pulse shape. The

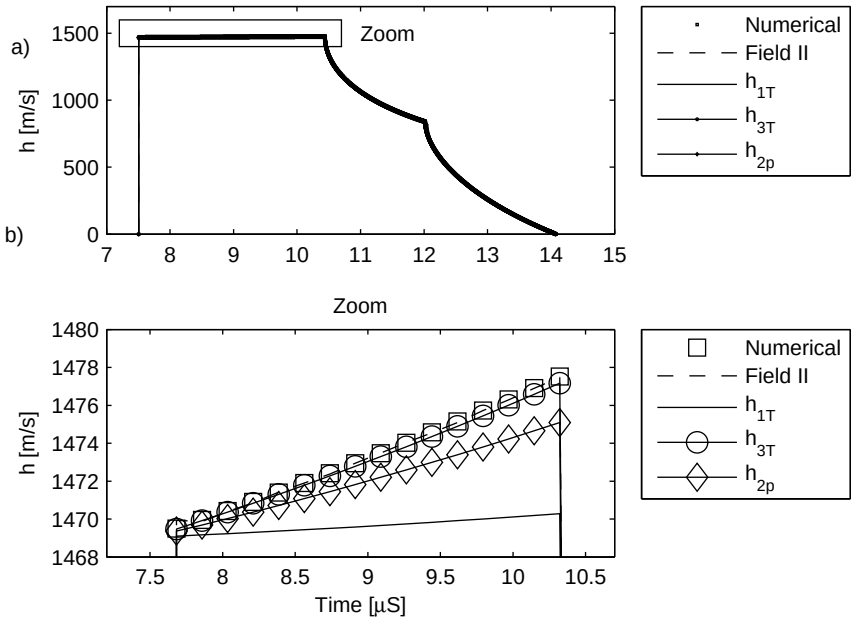

FIG. 8. Results of simulating a single point in front of a double curved transducer. a) Full pulse profile. b) Zoom onto (a) to magnify the difference.

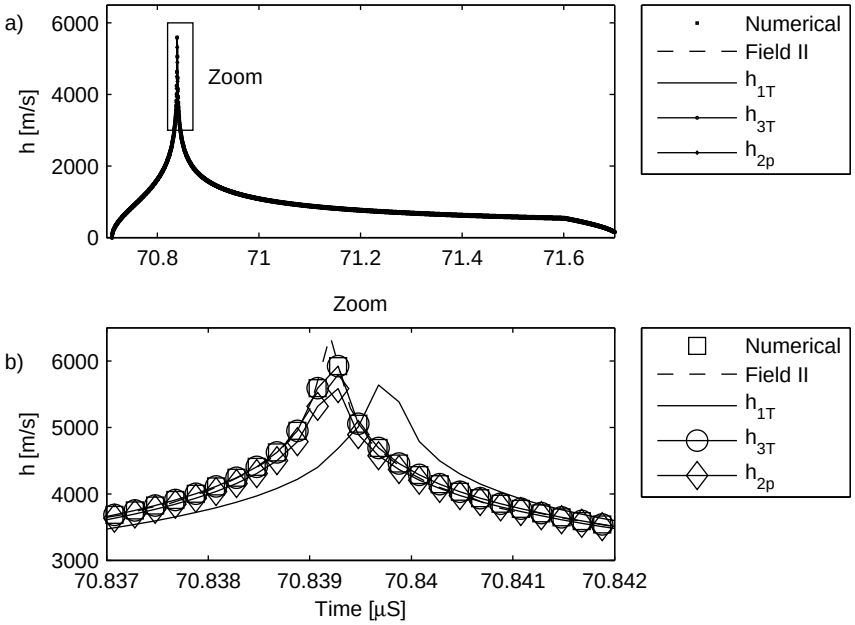

FIG. 9. Results of simulating a sharp spiking spatial impulse response from a double curved transducer. $E_{Field} = 0.49\%$, $E_{1T} = 3.580$ %, $E_{3T} = 0.006$ %, $E_{2p} = 0.83$ %. Only a few data points are shown from each curve a) Full pulse profile. b) Zoom onto (a) to magnify the difference.

error, E_i, relative to the numerical solution is $E_{Field} = 6.9$ %, $E_{1T} = 5.9$ %, $E_{3T} = 0.01$ %, $E_{2p} = 0.0283$ %. This shows that the 3T and the 2p are good solvers for convex arrays, and the error E_{Field} shows that the algorithm has consistency with what Field II predicts. Further experiments with simulations at points close to the convex transducer e.g. $\{x_p, y_p, z_p\} = \{0, 0, 1\}$ mm have shown that the numerical integrator breaks down. However, the approximating models are still stable. Field II is therefore applied as the reference to get a measure of the error for simulations in all zones of a convex transducer. 200 points were investigated and the mean error for each solver was found to be $\mathrm{ME}_{1T} = 3.8$ %, $\mathrm{ME}_{3T} = 2.5$ %, $\mathrm{ME}_{2p} = 2.5$ %, which indicate a rather identical performance of the solvers.

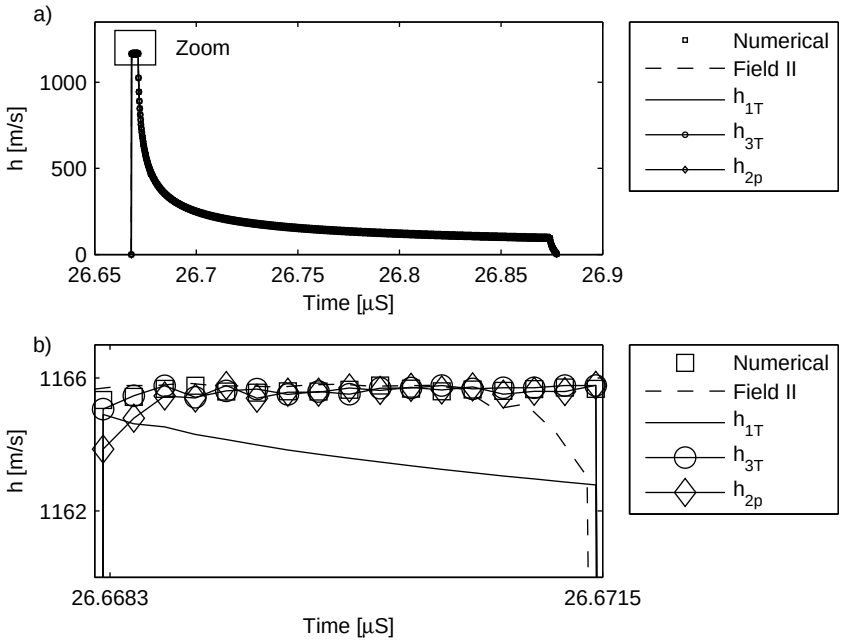

FIG. 10. Results of simulating a convex non-elevation focused array.

Changing the transducer geometry to a linear flat transducer $R = 6$ m and $r = 6$ m for the model presented here and for Field II yields a mean error of $\mathrm{ME}_{1T} = 3.56$ %, $\mathrm{ME}_{3T} = 3.56$ %, $\mathrm{ME}_{2p} = 34.86$ % for 200 points and with Field II as the reference. The errors show that the model can capture the response from plane transducers as well. It also indicates that the polynomial fitting, $2p$, fails to predict the response in contrary to the $1T$ and the $3T$ analytical solvers.

Finally a linear elevation focused array was considered. This transducer is mimicked by, $R = 6$ m, $r = 60$ mm, height $= 10$ mm, and $\gamma_L = 83\mu$rad, which corresponds to a width of approximately 1 mm. The mean error relative to Field II was found to be $\mathrm{ME}_{1T} = 4.43$ %, $\mathrm{ME}_{3T} = 3.46$ %, and $\mathrm{ME}_{2p} = 33.30$ % for a simulation with 200 points. The mean solving time for the three approximating methods was found to be $\mathrm{T}_{1T} = 0.49$ s, $\mathrm{T}_{3T} = 0.57$ s, and $\mathrm{T}_{2p} = 0.33$ s. This implies an error improvement of 21.9 % with a 15.4 % increase in the simulation time when using the 3T instead of the 1T and a 89 % improvement in the error when applying the 3T instead of the 2p solver. The latter improvement costs 72.7 % more calculation time.

VIII. DISCUSSION

The results showed that a very accurate prediction of the exact solution to (8) could be achieved by using the three-point Taylor expansion, 3T, for all transducer configurations. However, also good results were achieved by calculating the second order polynomial and the one point Taylor expansion for the double curved transducer. As it could be seen on Fig. 9 the 1T calculations fails for steep spikes. This is because the main energy that represent the spike is found at the outer integration values ϕ_{min} and ϕ_{max} when approximating (57) around the given time instances. The 1T solver in contrary seems to be more stable for linear arrays which the 2p showed not to be. This shows that the solvers 1T and 2p are sensitive to the curvatures of the transducer. Choosing which solver that operates the best is therefore application dependent. Clearly the 3T exhibits the best performance, but for the cost of a slight increase in the solution time relative to the other solvers. It should also be mentioned that the influence of miscalculating a spike as seen in Fig. 9 is significant when the pure shape of the spatial impulse responses are to be compared. However, it should be recalled that the spatial impulse response are typically convolved with a band-limited pulse representing the transducer in emission or in pulse-echo. Therefore, when the spatial impulse response is used in a convolution an error, as the ones typical for the 1T, becomes of less influence. If the convolved pulse is sufficiently band-limited for the given application, then it may be beneficial to calculate the responses with the slightly faster approximation of 1T and 2p. It should, however, be noted that the 8.1 % percent increase in simulation time that the 3T approximation offers relatively to the 1T or 34.3 % relatively to the 2p are relatively small compared to the high accuracy and stability it represents for the double curved transducer.

From the results it is also noticeable that the algorithm is a fairly good approximation as a model for linear arrays, elevation focused linear arrays, and convex arrays with no elevation focus. The model therefore represents an all-round

formulation of the spatial impulse response of general rectangular arrays. Further development should therefore focus on a fast and competitive implementation into a C/Fortran environment from which a simulation time comparison between recognized programs such as Ultrasim, Dream, DELFI, and Field II could be made.

Yet another aspect that should be commented on in context of an practical implementation is the sampling frequency. The sampling frequency applied in this work is relatively large, 5 GHz, which was chosen to validate the algorithm directly. A much lower sampling frequency should be applied if the algorithm and the solver should be implemented into a simulation program such as Field II, which is usually operated at a 100 MHz and with small elements. The combination between small elements and low sampling frequency is only possible if the implementation preserves conservation of energy in the spatial impulse response. This may be achieved by performing an area integration of the pulse within the samples. This area integration is then spread out onto the different global samples. In other words a sub-integration procedure is to be performed and is a trivial task to perform.

IX. CONCLUSION

An exact mathematical formulation for the spatial impulse response to a double curved transducer has been presented. The response can be represented with an integral of elliptical type. For this integral to be solved it requires a numerical integrator. It has been shown that a good approximation of the integral can be achieved by applying a three-point Taylor expansion to a part of the integral. The Taylor expansion yields an analytical integrable expression. A single-point Taylor expansion and a second order polynomial fit was also shown to give good results for simulations of a double curved transducer. The presented algorithm exhibited consistent results with Field II for both a double curved transducer, a linear flat transducer, a linear elevation focused transducer, and a convex non-elevation focused transducer. The three-point Taylor approximation showed to be the most stable approximation, of the cost of a slightly higher simulation time.

[1] G. E. Tupholme, "Generation of acoustic pulses by baffled plane pistons", Mathematika **16**, 209–224 (1969).

[2] P. R. Stepanishen, "Transient radiation from pistons in an infinite planar baffle", J. Acoust. Soc. Am. **49**, 1629–1638 (1971).

[3] P. R. Stepanishen, "The time-dependent force and radiation impedance on a piston in a rigid infinite planar baffle", J. Acoust. Soc. Am. **49**, 841–849 (1971).

[4] P. R. Stepanishen, "An approach to compute time-dependent interaction forces and mutual radiation impedances between pistons in a rigid planar baffle", J. Acoust. Soc. Am. **49**, 283–292 (1971).

[5] J. C. Lockwood and J. G. Willette, "High-speed method for computing the exact solution for the pressure variations in the nearfield of a baffled piston", J. Acoust. Soc. Am. **53**, 735–741 (1973).

[6] P. R. Stepanishen, "Wide bandwidth near and far field transients from baffled pistons", in *Proc. IEEE Ultrason. Symp.*, 113–118 (1977).

[7] G. R. Harris, "Review of transient field theory for a baffled planar piston", J. Acoust. Soc. Am. **70-1**, 10–20 (1981).

[8] J. A. Jensen, "A new calculation procedure for spatial impulse responses in ultrasound", J. Acoust. Soc. Am. **105**, 3266–3274 (1999).

[9] C.-C. Sung, H.-I. Yang, and J.-H. Jeng, "Calculation of spatial impulse response for array transducer", Jap. J. Appl. Phys. **44-10**, 7680–7689 (2005).

[10] A. Penttinen and M. Luukkala, "The impulse response and nearfield of a curved ultrasonic radiator", J. Phys. D: Appl. Phys. **9**, 1547–1557 (1976).

[11] M. Arditi, F. S. Forster, and J. Hunt, "Transient fields of concave annular arrays", Ultrason. Imaging **3**, 37–61 (1981).

[12] J. N. Tjøtta and S-Tjøtta, "Nearfield and farfield of pulsed radiators", J. Acoust. Soc. Am. **71-4**, 824–834 (1982).

[13] W. A. Verhoef, M. J. T. M. Cloostermans, and J. M. Thijssen, "The impulse response of a focused source with an arbitrary axisymmetric surface velocity distribution", J. Acoust. Soc. Am. **75-6**, 1716–1721 (1984).

[14] J. A. Jensen, "Field: A program for simulating ultrasound systems", Med. Biol. Eng. Comp. **10th Nordic-Baltic Conference on Biomedical Imaging, Vol. 4, Supplement 1, Part 1**, 351–353 (1996b).

[15] J. A. Jensen, "Users' guide for the Field II program, version 2.70 of may 26, 1999", Technical Report, Department of Information Technology, DTU (1999).

[16] J. A. Jensen and N. B. Svendsen, "Calculation of pressure fields from arbitrarily shaped, apodized, and excited ultrasound transducers", IEEE Trans. Ultrason., Ferroelec., Freq. Contr. **39**, 262–267 (1992).

[17] J. A. Jensen, "Ultrasound fields from triangular apertures", J. Acoust. Soc. Am. **100(4)**, 2049–2056 (1996a).

[18] R. Reibold and R. Kažys, "Radiation of a rectangular strip-like focussing transducer. part1: harmonic excitation.", Ultrasonics **30**, 49–55 (1992).

[19] R. Reibold and R. Kažys, "Radiation of a rectangular strip-like focussing transducer. part2: transient excitation.", Ultrasonics **30**, 49–55 (1992).

[20] P. Wu and T. Stepinski, "Spatial impulse response method for predicting pulse-echo fields from a linear array with cylindrically concave surface", IEEE Trans. Ultrason., Ferroelec., Freq. Contr. **46-5**, 1283–1297 (1999).

[21] J. F. Theumann, M. Arditi, J.-J. Meister, and E. Jaques, "Acoustic fields of concave cylindrical transducers", J. Acoust. Soc. Am. **88-2**, 1160–1169 (1990).

[22] S. Holm, "Ultrasim - a toolbox for ultrasound field simulation", University of Oslo (2001).

[23] F. Lingvall, "User manual for the DREAM toolbox- an ultrasound simulation software for use with MATLAB and GNU OCTAVE", (2009).

[24] M. A. Ellis, D. Guenther, and W. F. Walker, "Spline-based approach for computing spatial impulse responses", IEEE Trans. Ultrason., Ferroelec., Freq. Contr. **54-5**, 1045–1054 (2007).
[25] H. T. O'Neil, "Theory of focusing radiators", J. Acoust. Soc. Am. **21-5**, 516–526 (1949).

Paper III

Modeling transducer impulse responses for predicting calibrated pressure pulses with the ultrasound simulation program Field II

David Bæk, Morten Willatzen, and Jørgen Arendt Jensen

Journal of the Acoustical Society of America

Published

Modeling transducer impulse responses for predicting calibrated pressure pulses with the ultrasound simulation program Field II

David Bæk[a] and Jørgen Arendt Jensen
Department of Electrical Engineering, Center for Fast Ultrasound Imaging, Technical University of Denmark, 2800 Kgs. Lyngby, Denmark

Morten Willatzen
Mads Clausen Institute for Product Innovation, University of Southern Denmark, 6400 Sønderborg, Denmark

(Received 14 July 2009; revised 18 December 2009; accepted 24 February 2010)

FIELD II is a simulation software capable of predicting the field pressure in front of transducers having any complicated geometry. A calibrated prediction with this program is, however, dependent on an exact voltage-to-surface acceleration impulse response of the transducer. Such impulse response is not calculated by FIELD II. This work investigates the usability of combining a one-dimensional multilayer transducer modeling principle with the FIELD II software. Multilayer here refers to a transducer composed of several material layers. Measurements of pressure and current from Pz27 piezoceramic disks as well as pressure and intensity measurements in front of a 128 element commercial convex medical transducer are compared to the simulations. Results show that the models can predict the pressure from the piezoceramic disks with a root mean square (rms) error of 11.2% to 36.2% with a 2 dB amplitude decrease. The current through the external driving circuits are predicted within 8.6% to 36% rms error. Prediction errors of 30% and in the range of 5.8%–19.9% for the pressure and the intensity, respectively, are found when simulating the commercial transducer. It is concluded that the multilayer transducer model and the FIELD II software in combination give good agreement with measurements.
 [DOI: 10.1121/1.3365317]

PACS number(s): 43.38.Fx, 43.20.Px, 43.58.Vb [AJZ] Pages: 2825–2835

I. INTRODUCTION

The FIELD II program[1,2] is widely used within several ultrasound imaging research areas. It is suitable for simulating rf-data for signal processing and testing of several transducer geometries. However, Field II requires knowledge of each of the transducer elements' surface acceleration to perform calibrated pressure predictions. The acceleration is most often measured or approximated by a tapered tone burst. The tapered tone burst method may be found adequate for generating rf-data for signal processing as well as in studies of the transducer geometry where the transducers impulse response is mainly needed for, e.g., a proper matched filtering. Another useful area for the FIELD II software is for intensity simulation by calculating the pressure at a given point of interest. For such simulations to be useful in intensity validation processes, which have to fulfill Food and Drug Administration (FDA) requirements, it is no longer acceptable to have knowledge of an approximated impulse response. Direct measurement of the impulse response may then be needed. Measuring the impulse response is an expensive and cumbersome method, hence a direct simulation of the transducer and its driving circuits could be beneficial. Such an approach would also ease the development of new multilayered transducers and prediction of their pressure field responses.

To simulate the pressure response from transducers, a model which can predict the volt-to-surface acceleration conversion of multilayered transducers is needed. Methods for modeling piezoelectric transducers are well known in literature.[3–8] Most of these models are based on electrical equivalent circuits benefiting from transmission line theory to represent the electromechanical coupling and acoustic wave propagation, and others rely on deriving impedance matrices for describing the transducer behavior. All of these methods have their advantage and disadvantages depending on the application of use.

This paper, however, investigates the accuracy in combining a one-dimensional modeling principle as described by Willatzen[9,10] with the FIELD II simulation software. This hybrid modeling principle was briefly discussed in our previous works[11,12] and is in this work extended and investigated in detail. The model is based on Navier's equations, Maxwell–Poisson's law, and piezoelectric constitutive equations and can be easily solved in a closed form using, e.g., Gauss elimination. The modeling principle can account for both electrical and mechanical losses by using the mechanical quality factor and the dielectrical loss factor $\tan(\delta)$ or by using the transducers' characteristic parameters in a complex-valued form which accounts implicitly for attenuation.[13] Furthermore, by solving the closed form equa-

[a]Author to whom correspondence should be addressed. Electronic mail: db@elektro.dtu.dk

tions for a multilayered structure, it is possible to extract knowledge of particle displacement, velocity, acceleration, and dielectrical effects at any position inside a multilayer transducer assumed to operate in its longitudinal mode. The input parameters for the model are those directly found in the constitutive matrices such as the stiffness matrix, the piezoelectric stress constant matrix, and the permittivity matrix wherefore the influence of each constitutive parameter can be studied directly. All these matrices are most often directly available by the material manufacturers and are, thus, not hidden in an effective constant as is the case with electrical equivalent models. Furthermore, the volt-to-surface acceleration impulse response can easily be solved for using the method presented by Willatzen[10] to any bandwidth of interest. The bandwidth is only limited by the computer power available and may be restricted depending on the number of resonance frequencies needed. The modeling principle is therefore beneficial for both transducer designers and FIELD II users, especially since the modeling principle is mathematically very suitable for predicting this impulse response in a form that can be directly exported for use in the FIELD II software.

In this paper, the modeling principle is used for describing circular Pz27 piezoceramics from Ferroperm Piezoceramics A/S, Kvistgaard, Denmark. The ceramics are mounted with silver electrodes, immersed into water and driven with a function generator. Furthermore, a slightly more complicated transducer model describing a commercial 128 element convex medical ultrasound transducer from BK Medical Aps. (Herlev, Denmark) is presented with a simplified model description of a driving transmitter unit from BK Medical Aps. Pressure predictions along the center axis of the ceramic as well as pressure and intensity predictions in the elevation plane of the convex transducer are performed by combining the models with the FIELD II software. All simulations are compared with measurements to quantify the accuracy of the models.

II. THEORY

Section II A describes the basic equations needed to set up a consistent equation set for solving simple resistance loaded piezoceramics as well as more complicated electronic loaded commercial medical transducers. It shows how attenuation and boundary conditions can be included into the transducer model, and it discusses how to set up the FIELD II program for handling the piezoceramics and the convex transducer.

A. Acoustical wave propagation in solid layers

The time-dependent velocity and tension at any spatial position inside a one-dimensional transducer layer can be found based on monofrequency solutions for the particle velocity u and the tension T:[10]

$$u_{33}(z,t,\omega) = \frac{c_{33}^D S_A}{Z_a} e^{(-Jkz-J\omega t)} - \frac{c_{33}^D S_B}{Z_a} e^{(Jkz-J\omega t)}, \tag{1}$$

$$T_{33}(z,t,\omega) = c_{33}^D [S_A e^{(-Jkz-J\omega t)} + S_B e^{(Jkz-J\omega t)}] - h_{33} D, \tag{2}$$

where c_{33}^D and h_{33} are the stiffness constant in the longitudinal direction and the piezoelectric constant defined as e_{33}/ϵ_{33}^S, respectively. Here e_{33} and ϵ_{33}^S are the piezoelectrical coupling coefficient for stress-charge form and the electric permittivity, respectively. The propagation constant k is defined as ω/v_{33} where ω is the radial frequency, and v_{33} is the wave velocity defined by $\sqrt{c_{33}^D/\rho}$. Here ρ is the given layer's material density. The acoustical impedance Z_a is defined as $Z_a = v_{33}\rho$. The unknown coefficients S_A and S_B are frequency and boundary dependent constants, and D is the frequency-dependent electric displacement. In the following, any subscripts of 33 are discarded since the transducers are assumed to operate in the longitudinal thickness mode only.

For nonpiezoelectric layers the same solutions are valid. However, the piezoelectrical constant vanishes and the electrical displacement D can be neglected.

Tension and particle velocities must be continuous everywhere and, in particular, at interfaces

$$T_{\text{Layer}_1} = T_{\text{Layer}_2}, \tag{3}$$

$$u_{\text{Layer}_1} = u_{\text{Layer}_2}. \tag{4}$$

B. Modeling losses

Losses, which influence the transducer response, can mainly be divided into acoustical and electrical losses.[10,14–16]

The acoustical losses arise due to many physical mechanisms such as heating, viscosity, and cross-talks which are all relatively complicated mechanisms to model. Two ways of modeling losses are presented and tested with the modeling here. One method applies purely real-valued transducer parameters from which the attenuation can be approximated explicitly. Another method utilizes a complex-valued transducer parameter set which implicitly accounts for losses.[13]

The real-valued method accounts for losses by using a complex propagation constant $\bar{k}$ instead of a real-valued one in, e.g., Eqs. (1) and (2). A transformation of the real-valued propagation constant may therefore be performed as $k \rightarrow \bar{k} = k^r + J\alpha$, where $k^r = \omega/v^r$ and v^r is the phase velocity. The attenuation constant α is an approximation of mechanical losses and has the units [1/m]. It may be found using the mechanical quality factor, Q_m, as $\alpha = \pi/(Q_m \lambda)$, where λ is the wavelength. A complex phase velocity can therefore be found as

$$\bar{v} = \frac{\omega}{\bar{k}} = \frac{\omega}{k^r + J\alpha} = \frac{v^r}{1 + \frac{J\alpha v^r}{\omega}}, \tag{5}$$

and by substitution the complex propagation constant becomes

$$\bar{k} = \frac{\omega}{\bar{v}}. \tag{6}$$

Electrical losses may be defined in two categories: losses due to the electrical network and losses due to the transducer materials. Losses in the electrical network may be very cumbersome to account for since they highly depend on the

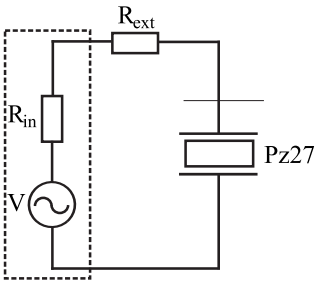

FIG. 1. Schematics of the electronic network loading the Pz27.

transmitter system, cables, element cross-talks, etc. Thorough knowledge of the electrical network design is therefore needed. The dielectrical losses in the transducer, however, can be modeled by defining the dielectrical loss factor as a complex-valued one $\epsilon' = \epsilon + J\epsilon \tan \delta$, where $\tan(\delta)$ is the dielectric loss factor.[10] This method is suitable if only real-valued material constants for the transducer are known.

The second suggested method for modeling both electrical and acoustical losses in the transducer is by applying complex-valued material coefficients for c^D, h, e, ϵ^S. This method may be theoretically more powerful than the method of using the mechanical quality factor and the dielectric loss factor, since it has been found that loss contributions in piezoelectric materials can be directly included into each material constant when defining them as complex valued.[13,17,18]

C. Electrical networks

The circular piezoceramic disks considered in this paper are assumed to be driven with a function generator in series with an internal and an external resistance, R_{in}, R_{ext}. The schematics is found in Fig. 1. The resistance R_{ext} seen in the figure is modeled as a series loading resistance. This resistance was used in the practical experiment to determine the current flow through the circuit.

This assumption makes the electrical constitutive equations identical with other works[10] where the resistance loading is modeled as a simple electrical impedance and gives the following electrical equation to be satisfied:

$$-J\omega V = -A(R_{\text{in}} + R_{\text{ext}})\omega^2 D - J\omega \frac{L_p}{\epsilon^S} D - h[u(L_p) - u(0)], \tag{7}$$

where L_p and A are the piezoelectric thickness and cross section, respectively.

A model for the exact electrical loading of a commercial medical transducer is more complicated to handle. It consists of a coaxial cable and the transmitter unit of the scanner driving the transducer. In this paper, a transmitter from BK Medical Aps. for driving the convex array transducer is applied. A simplified circuit diagram for the applied scanner and transducer is shown in Fig. 2, where the electronic components L_1 and L_2 are inductances. R_1, R_2, and R_{mux} are passive resistances.

The coaxial cable is modeled using lossless transmission line theory where forward and backward traveling voltage and current waves in the frequency domain are given by

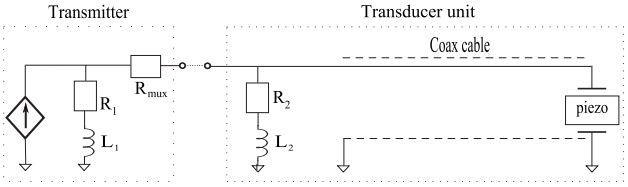

FIG. 2. Simplified electronic network loading the commercial transducer.

$$V_{\text{coax}} = V_+ e^{J\gamma z_{\text{coax}}} + V_- e^{-J\gamma z_{\text{coax}}}, \tag{8}$$

$$I_{\text{coax}} = \frac{V_+}{Z_0} e^{J\gamma z_{\text{coax}}} - \frac{V_-}{Z_0} e^{-J\gamma z_{\text{coax}}}. \tag{9}$$

Here Z_0 is the characteristic impedance of the cable, and γ is the propagation constant defined as $\sqrt{LC}$, where L and C are the cable series inductance per unit length and the shunt capacitance per unit length, respectively. The variable z_{coax} describes the distance along the coaxial cable.

The voltage, V_{pe}, across the piezoceramic is defined as

$$V_{pe} = -J\omega \frac{L_p}{\epsilon^S} D - h[u_p(L_p) - u_p(0)], \tag{10}$$

where L_p is the thickness of the piezoceramic.

The boundary conditions for the coaxial cable at the transducer end have to satisfy both current and voltage continuity. By recalling the relation between electrical displacement and displacement current: $I = A(\partial D/\partial t)$ while having $z_{\text{coax}} = 0$ at the transducer end of the cable, the following equations have to be satisfied:

$$V_+ + V_- = V_{pe}, \tag{11}$$

$$\frac{V_+}{Z_0} - \frac{V_-}{Z_0} = -J\omega A D. \tag{12}$$

At the other end of the cable, $z_{\text{coax}} = -L_{\text{coax}}$. Circuit analysis of the cable yields

$$V(\omega) = \left[\frac{Z_g}{R_2 - J\omega L_2} + 1\right] V_+ e^{-J\gamma L_{\text{coax}}} + \cdots + \left[\frac{Z_g}{R_2 - J\omega L_2} - 1\right] V_- e^{J\gamma L_{\text{coax}}}, \tag{13}$$

where $Z_g = R_1 + R_{mux} - J\omega L_1$ (see Fig. 2) and $V(\omega)$ is the Fourier transform of the driving pulse.

D. Transducer model for the circular piezoceramic disk

The piezoceramic disks used in testing our model are standard Pz27 piezoceramic samples produced by Ferroperm Piezoceramics A/S, Kvistgård, Denmark. The samples are circular in the cross section and coated with silver electrodes. Measurements were performed submerged into water which gives a setup as shown in Fig. 3. A function generator with an internal and an external series resistance was applied for driving. Therefore, modeling of

$$T_{\text{back}} = c_{Ag}^D (A_{Ag,1} + B_{Ag,1}), \tag{14}$$

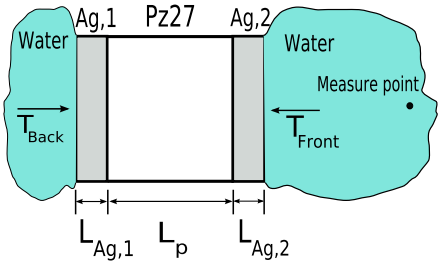

FIG. 3. (Color online) Illustration of the longitudinal cross section of a Pz27 ceramic layered with silver electrodes and submerged into water.

$$\frac{T_{\text{back}}}{Z_{\text{back}}} = \frac{c_{Ag}^D}{Z_{Ag}}(A_{Ag,1} - B_{Ag,1}), \tag{15}$$

$$c_p^D(A_p + B_p) - hD = c_{Ag}^D(A_{Ag,1}e^{-Jk_{Ag}L_{Ag}} + B_{Ag,1}e^{Jk_{Ag}L_{Ag}}), \tag{16}$$

$$\frac{c_p^D}{Z_p}(A_p - B_p) = \frac{c_{Ag}^D}{Z_{Ag}}(A_{Ag,1}e^{-Jk_{Ag}L_{Ag}} - B_{Ag,1}e^{Jk_{Ag}L_{Ag}}), \tag{17}$$

$$c_{Ag}^D(A_{Ag,2} + B_{Ag,2}) = c_p^D(A_p e^{-Jk_p L_p} + B_p e^{Jk_p L_p}) - hD, \tag{18}$$

$$\frac{c_{Ag}^D}{Z_{Ag}}(A_{Ag,2} - B_{Ag,2}) = \frac{c_p^D}{Z_p}(A_p e^{-Jk_p L_p} - B_p e^{Jk_p L_p}), \tag{19}$$

$$T_{\text{front}} = c_{Ag}^D(A_{Ag,2}e^{-Jk_{Ag}L_{Ag}} + B_{Ag,2}e^{Jk_{Ag}L_{Ag}}), \tag{20}$$

$$-\frac{T_{\text{front}}}{Z_{\text{front}}} = \frac{c_{Ag}^D}{Z_{Ag}}(A_{Ag,2}e^{-Jk_{Ag}L_{Ag}} - B_{Ag,2}e^{Jk_{Ag}L_{Ag}}), \tag{21}$$

$$-J\omega V(\omega) = -\left((R_{\text{in}} + R_{\text{ext}})\omega^2 A + J\omega\frac{L_p}{\epsilon^S}\right)D - h\frac{c_p^D}{Z_p} \times (A_p - B_p) + h\frac{c_{Ag}^D}{Z_{Ag}}(A_{Ag,2} - B_{Ag,2}), \tag{22}$$

this setup using the above described modeling method, yields a three layer solid transducer model, which is described by Eqs. (14)–(22). These equations model the electronics as resistances in series with a function generator having an internal resistance, R_{in}, and an external series resistance, R_{ext}.

The subscripts Ag_1, Ag_2, and p in Eqs. (14)–(22) are referring to the first silver layer, the second silver layer, and the piezoceramic layer, respectively, and they are used as subscripts for the unknown coefficients A and B. This model involves nine equations with nine unknowns to be solved in MATLAB.

E. Transducer model for a 128 element convex array

A medical convex array has a more complicated structure than regular circular disks as considered above. It consists of several matching layers, and the surface is geometrically more complicated. However, the modeling of each element's impulse response follows the same principle as discussed above. Each element of the convex transducer under consideration in this paper consists of a backing layer, a

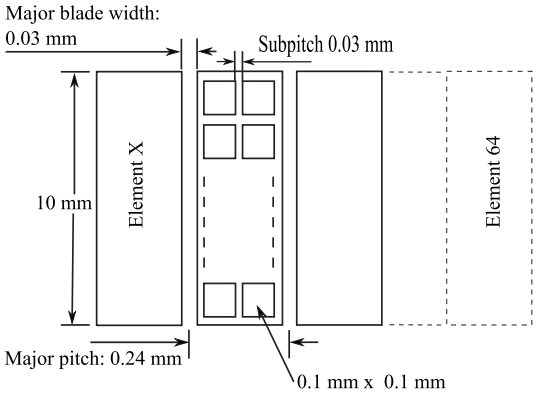

FIG. 4. Illustration of the subdivided elements of a convex ultrasound transducer under consideration.

piezoceramic layer, a first matching layer (ML1), a second matching layer (ML2), and a lens. Each of the 128 major elements consists of smaller subelements which are created as subdivided elements in two columns. Each subelement measures a rectangle of 0.1×0.1 mm^2 as shown in Fig. 4. Together all the subelements and subpitch measure 10 mm in height and define the major elements of which there are 128. The transducer has a convex radius of 29 mm and an elevation focus at 70 mm.

Considering the electronic network to be as shown in Fig. 2, and with parameter knowledge of the different layers for the different elements one can establish a consistent set of Eqs. (23)–(35) for this transducer.

$$T_{\text{back}} = c_p^D(A_p + B_p) - hD, \tag{23}$$

$$\frac{T_{\text{back}}}{Z_{\text{back}}} = \frac{c_p^D}{Z_p}(A_p - B_p), \tag{24}$$

$$c_{\text{ML1}}^D(A_{\text{ML1}} + B_{\text{ML1}}) = c_p^D(A_p e^{-Jk_p L_p} + B_p e^{Jk_p L_p}) - hD, \tag{25}$$

$$\frac{c_{\text{ML1}}^D}{Z_{\text{ML1}}}(A_{\text{ML1}} - B_{\text{ML1}}) = \frac{c_p^D}{Z_p}(A_p e^{-Jk_p L_p} - B_p e^{Jk_p L_p}), \tag{26}$$

$$c_{\text{ML2}}^D(A_{\text{ML2}} + B_{\text{ML2}}) = c_{\text{ML1}}^D(A_{\text{ML1}}e^{-Jk_{\text{ML1}}L_{\text{ML1}}} + B_{\text{ML1}}e^{Jk_{\text{ML1}}L_{\text{ML1}}}), \tag{27}$$

$$\frac{c_{\text{ML2}}^D}{Z_{\text{ML2}}}(A_{\text{ML2}} - B_{\text{ML2}}) = \frac{c_{\text{ML1}}^D}{Z_{\text{ML1}}}(A_{\text{ML1}}e^{-Jk_{\text{ML1}}L_{\text{ML1}}} - B_{\text{ML1}}e^{Jk_{\text{ML1}}L_{\text{ML1}}}), \tag{28}$$

$$c_{\text{lens}}^D(A_{\text{lens}} + B_{\text{lens}}) = c_{\text{ML2}}^D(A_{\text{ML2}}e^{-Jk_{\text{ML2}}L_{\text{ML2}}} + B_{\text{ML2}}e^{Jk_{\text{ML2}}L_{\text{ML2}}}), \tag{29}$$

$$\frac{c_{\text{lens}}^D}{Z_{\text{lens}}}(A_{\text{lens}} - B_{\text{lens}}) = \frac{c_{\text{ML2}}^D}{Z_{\text{ML2}}}(A_{\text{ML2}}e^{-Jk_{\text{ML2}}L_{\text{ML2}}} - B_{\text{ML2}}e^{Jk_{\text{ML2}}L_{\text{ML2}}}), \tag{30}$$

$$T_{\text{front}} = c_{\text{lens}}^D(A_{\text{lens}}e^{-Jk_{\text{lens}}L_{\text{lens}}} + B_{\text{lens}}e^{Jk_{\text{lens}}L_{\text{lens}}}), \tag{31}$$

TABLE I. Model parameters for Pz27.

	Real case	Complex case	
ρ	7 700	7 700	kg/m^3
c_p^D	1.44×10^{11}	$[(813.9+J0.113)\pm(0.7-J0.006)]\times10^{10}$	N/m^2
h	1.98×10^{9}	$[(21.0+J0.148)\pm(0.4-J0.004)]\times10^{8}$	V/m
ϵ^S	$914\epsilon_0$	$[(822-J10.3)\pm(12-J0.4)]\times\epsilon_0$	F/m
tan δ	0.017	0.017	
ρ_{Ag}	10 600	10 600	kg/m^3
c_{Ag}^D	1.13×10^{11}	1.13×10^{11}	N/m^2
ρ_w	1 000	1 000	kg/m^3
c_w^D	2.19×10^{9}	2.19×10^{9}	N/m^2

$$-\frac{T_{\text{front}}}{Z_{\text{front}}}=\frac{c_{\text{lens}}^D}{Z_{\text{lens}}}(A_{\text{lens}}e^{-Jk_{\text{lens}}L_{\text{lens}}}-B_{\text{lens}}e^{Jk_{\text{lens}}L_{\text{lens}}}), \tag{32}$$

$$-J\omega V_+ + -J\omega V_- = -J\omega\frac{L_p}{\epsilon^S}D-\left[h\frac{c_{\text{ML1}}^D}{Z_{\text{ML1}}}(A_{\text{ML1}}-B_{\text{ML1}})-h\frac{c_p^D}{Z_p}(A_p-B_p)\right], \tag{33}$$

$$-J\omega AD=\frac{1}{Z_0}V_+-\frac{1}{Z_0}V_-, \tag{34}$$

$$V(\omega)=\left(\frac{Z_g}{Z_0}+\frac{Z_g}{R_2-J\omega L_2}+1\right)V_+e^{J\gamma L_{\text{coax}}}+\left(-\frac{Z_g}{Z_0}+\frac{Z_g}{R_2-J\omega L_2}+1\right)V_-e^{-J\gamma L_{\text{coax}}}. \tag{35}$$

III. NUMERICAL SIMULATION

A. Solving the equations

The equation sets (14)–(35) are solved in MATLAB for each frequency component at a time for the bandwidth of interest. The surface acceleration is found from Eq. (1) evaluated at the interface between water and the front layer (the lens). It is then multiplied with $-J\omega$ to convert from velocity to acceleration, before the inverse Fourier transform

$$f(t)=\frac{1}{\sqrt{2\pi}}\int_{-\infty}^{\infty}F(\omega)e^{-J\omega t}dt. \tag{36}$$

is used for calculating the resulting impulse response.

1. Model data for Pz27 ceramics

The model input data set used for investigation with Pz27 materials is found in Table I. The table contains two sets of data. One set is a real-valued data set of material constants for testing of the model with attenuation based on the mechanical quality factor and the dielectrical loss factor. This set was manufacturer supplied. A second set consists of complex-valued data of material constants measured by Algueró *et al.*[13] These data are in their work supplied with a standard deviation which is the added/subtracted terms in the Table I. However, our analysis shows that best amplitude results are found by setting the deviation to zero for h and ϵ^S and $+(0.7-J0.006)\times10^{10}$ for the stiffness constant c_p^D which is the maximum allowable value according to Algueró *et al.*[13] The complex-valued data set is suitable for testing how well the model works with complex input data. The density of both the real-valued and the complex-valued data set is lowered with 2.5%, which is within the manufacturers tolerances. The small adjustments is made to create the best amplitude pulse shape for long pulses. This also gives the best shape for short pulses.

Two thicknesses of the piezoceramics were applied: 0.94 and 0.5 mm corresponding to a resonance frequency of 2.1 MHz and 4.0 MHz, respectively. Both types of ceramics were coated with silver with an estimated thickness of 9 μm. The ceramics were driven with a function generator having an internal resistance R_{in} of 50 Ω and an external resistance R_{ext} of 47.5 Ω. The radius of the ceramics was estimated to be 5.05 mm and the attenuation constants were calculated to $\alpha_{2.1\ \text{MHz}}=19\ \text{m}^{-1}$ and $\alpha_{4\ \text{MHz}}=36\ \text{m}^{-1}$ for the 2.1 MHz samples and the 4.0 MHz samples, respectively.

TABLE II. Simulation parameters for the convex ultrasound transducer.

	Value	Unit
ρ_p	7870	kg/m^3
ρ_{ML1}	2140	kg/m^3
ρ_{ML2}	1130	kg/m^3
ρ_{lens}	1260	kg/m^3
ρ_{back}	2160	kg/m^3
ρ_{front}	1000	kg/m^3
c_p^D	1.103×10^{11}	N/m^2
c_{ML1}^D	1.750×10^{10}	N/m^2
c_{ML2}^D	4.983×10^{9}	N/m^2
c_{lens}^D	1.235×10^{9}	N/m^2
c_{back}^D	1.017×10^{10}	N/m^2
c_{front}^D	2.372×10^{9}	N/m^2
ϵ^S	11.5×10^{-9}	F/m
h	1.713×10^{9}	V/m
tan(δ)	0.16	

2. Model data for the convex transducer

Table II lists the input parameters needed for predicting the impulse response of the convex ultrasound transducer. The thicknesses of the different layers L_p, L_{ML1}, L_{ML2}, and L_{lens} are set to 0.38, 0.17, 0.11, and 0.46 mm, respectively. The attenuation coefficients are calculated to be {1036,0,139,186,308,0.025} [1/m] for the backing layer, the piezoceramic layer, the ML1, the ML2, the lens, and water, respectively.

The electronic components R_1, R_2, R_{mux}, L_1, and L_2 found in Fig. 2 are set to 100 Ω, 20 Ω, 22 Ω, 3.9 μH, and 10 μH, respectively. The coaxial cable has a characteristic impedance of 75 Ω, a length L_{coax} of 2.2 m, an estimated inductance per unit length, L, of 0.387 μH/m, and an estimated capacitance per unit length, C, of 67 pF/m. The later estimations are taken from product descriptions of similar coaxial cables. This estimation is found acceptable through simulation investigations on the influence of these parameters for the final results. This was done by varying the parameters and identifying the effect on the pressure pulse.

This showed that an exact value does not have significant influence on the errors. To provide an estimate of the input waveform for the FIELD II model, the transmitter output was measured without the transducer being present.

B. Setting up FIELD II

For FIELD II to calculate the pressure, the surface acceleration and the transducer surface geometry must be defined. For the piezoceramic disks FIELD II was set up to calculate the point pressure field using square element sizes of 0.1 $\times 0.1$ mm^2 for the piston model.

For the convex array two possible surface models with which to set up FIELD II were investigated. One setup models each single subelement on the surface of the lens. In reality the lens material has a continuous smooth surface without any subdicing hence waves propagating from the underlying subdiced materials through the lens will propagate spherically forward toward the lens surface. These waves will superpose at the front surface according to Huygen's principle and give an approximate plane wave transmission. Modeling of each single element therefore assumes no superposition in the lens material.

The second setup also assumes one-dimensional operation of the lens surface. Here, however, the operation of each major element is modeled as vibrating in one dimension only and as if no dicing occurs on the underlying materials. This defines the area, A, in Eq. (34) to be the area of the total major element, whereas for the first setup A is the size of each subdivided element as shown in Fig. 4.

FIELD II supports two possible built-in functions for modeling the convex transducer, *xdc_convex_focused_multirow,* and *xdc_convex_focused_array.* The first function is suitable for setting up each subelement, and the second is suitable for modeling only the major elements.

The pressure at the points of interest along the centerline of an active element was calculated by simulation. At each measurement point in front of the convex transducer, the pressure at several points within the radius of the needle hydrophone was calculated. These point pressures were then used to account for the hydrophone area by averaging over the surface:

$$p_{\mathrm{hyd}} = \frac{1}{A_{\mathrm{hyd}}} \int_{A_{\mathrm{hyd}}} p(\bar{r},t)dS, \tag{37}$$

where p_{hyd} is the average pressure detected by the hydrophone, $p(\bar{r},t)$ is the spatial pressure calculation by FIELD II, and A_{hyd} is the area of the hydrophone. This integral is solved numerically as

$$p_{\mathrm{hyd}} = \frac{1}{\sum_{i=0}^{N} \Delta s_i} \sum_{i=0}^{N} p_i(\bar{r},t)\Delta s_i, \tag{38}$$

where N is the number of integration areas and p_i is the calculated pressure at the center of the area Δs_i.

The sampling frequency for the convex array modeling was set to 400 MHz. The pressure were calculated using 40 times 40 mathematical elements on the major elements.

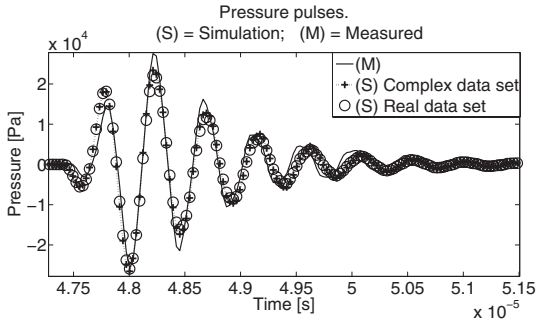

FIG. 5. Pressure comparison between measured (solid) and simulated pressure with a 2.1 MHz driving frequency. Two simulation parameter sets were applied. One complex-valued (dotted line+cross) and one real-valued (circles).

IV. MEASUREMENTS

A. The Pz27 ceramic disks

The ceramic disks were driven by an Agilent 33220A function generator that supplied a tone burst of 1, 4, and 10 cycles to the samples with a 20 Vpp from the internal source V in Fig. 1. The pressure pulses were captured with a needle hydrophone having a 250 μm radius and were sampled using a remote controlled Agilent MSO6014A oscilloscope. The oscilloscope was set up to average 128 times to lower the noise level, which was found relatively high for the samples. Measurements were performed on five different samples at 2.1 MHz and on five different samples at 4.0 MHz. Measurements were performed submerged into demineralized water, and the hydrophone was each time centered along the center axis of the elements to find the peak amplitude.

B. The convex array

Measurements with this transducer were performed on three center elements in three depths, 33, 72, and 112 mm along each of the element's centerlines. A shooting sequence was applied where only the considered element transmitted. Furthermore, at each of the three depths the pressures in the elevation plane were measured. The transducer was driven at 4.0 MHz using a BK Medical Aps. transmitter, delivering a 10 cycle tone burst with a limited peak amplitude of 31 V. The output voltage was limited to avoid too high nonlinear effects on the pressure pulses. All these setups were achieved by using our in house RASMUS (Ref. 19) system, which can be used to drive a transducer in transmit and receive with arbitrary configuration.

V. RESULTS

A. The results on the ceramic disks

Five transducer samples with a resonance frequency of 2.1 MHz and five transducer samples with a resonance frequency of 4.0 MHz have been measured. The average of these samples are used as a reference for comparison in the following. This has been done to minimize measurement uncertainties as well as differences in the samples.

Figure 5 shows a comparison between measured and

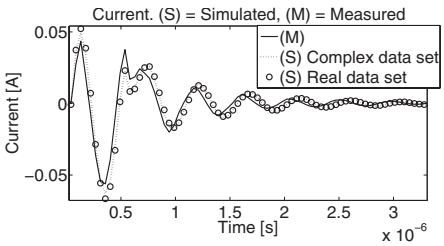

FIG. 6. Current comparison between measured (solid) and simulated pressure through the electronic circuit. Two simulation parameter sets were applied. One complex-valued (dotted line). One real-valued (circle).

simulated pressure pulses. The measured pulse is compared to simulations using the complex-valued and real-valued data sets. The comparison is made with an excitation pulse of 1 cycle at 2.1 MHz. Results indicate good agreement between measurement and model output which is a general characteristic for all combinations of pulses and samples that have been tested. A short pulse of 1 cycle has been chosen in Fig. 5 because a one-pulse excitation is the most difficult excitation situation to capture for the model. From the figure a slight overshoot is found as well as a slight tail drifting. From consecutive measurements it has been found that an amplitude decrease of the prediction of around 2 dB is needed to achieve the lowest error calculation. This amplitude adjustment has been used in the following results.

An example of current comparison between measured and simulated current flow through the driving circuit of the piezoceramic disk setup is shown in Fig. 6. This figure clearly exemplifies that the current is captured very well. A 1 cycle excitation of 2.1 MHz was applied here as well and it can be identified that the pulse tail exhibits the same drifting behavior as the above pressure pulse. Furthermore, it is noticeable that the model captures the rapid change in pulse behavior found in the beginning of the oscillating tail, indicating that the model has a certain capability to capture sudden changes in the pulse behavior.

Table III shows the results of a quantitative error calculation of the model's accuracy compared to the mean of the measurement as well as the deviation in the physical samples themselves. The sample deviations are calculated as the root mean square (rms) error relative to the rms of the mean of the measured pulses and is for a given measurement sequence defined as

$$\mathrm{rms}_m = 100 \cdot \frac{\sqrt{\frac{1}{N}\sum_{m=1}^{N}\frac{1}{N_s}\sum_{i=1}^{N_s}(\bar{P}(m)-P(m,i))^2}}{\sqrt{\frac{1}{N}\sum_{m=1}^{N}\bar{P}(m)^2}}. \quad (39)$$

Here $\bar{P}(m)$, $P(m,i)$, and N are the mean pressure of N_s piezoceramic samples, the measured pressure for the ith ceramic sample, and the number of time samples acquired, respectively.

The error of the simulation is calculated as the relative error with respect to the mean of the measurement. This is calculated as

$$\mathrm{rms}_s = 100 \cdot \frac{\sqrt{\frac{1}{N}\sum_{m=1}^{N}[(\bar{P}(m)-P_s(m))^2]}}{\sqrt{\frac{1}{N}\sum_{m=1}^{N}\bar{P}(m)^2}}, \quad (40)$$

where P_s is the pressure predicted by the model. From Table III it can be identified that the model has a significantly higher rms error in all predictions relative to the average of the measurements than each sample deviates from the average. This is a consequence of the drifting tail behavior and the slight overshoot on the transitions as is indicated on Fig. 5. The errors may seem high, however, it must be recalled that the rms error calculation is a very sensitive method of quantification. Therefore, a slight drift in phase results in a high error contribution.

From the table it becomes clear that the measured current standard deviation is ranging from 3.2% to 12.1% for short pulses and from 3.7% to 7.7% for long pulses, where best behavior is found for the 2.1 MHz pulses. For pressure measurements it is found that short pulses can be measured with a deviation error around 26% down to 8.5%, where best results are found for long pulses with a center frequency of 2.1 MHz. The error on the current simulation is found to be higher than the measurement deviation. The maximum simulated current error is found to be around 36.0% for short pulses while for long pulses the error is 17.9%. The best current result is found in the 4.0 MHz simulation, where a 8.6% error is found. Comparison of the current error calculated relative to simulations using either the real-valued data set or the complex-valued data set is seen to exhibit almost identical error prediction relative to the measured. This indi-

TABLE III. rms error in percentages for the model and measurements relative to the mean of the measurements using 1, 4, and 10 cycle excitations at 2.1 and 4.0 MHz resonance frequencies, respectively. Current (I) and pressure (P) errors are shown. Errors using either a real-valued data set (Re) or a complex-valued data set (C) in the simulation are shown. It is compared against deviations in the measurements (M).

	1 cycle excitation			4 cycle excitation			10 cycle excitation		
	Re	C	M	Re	C	M	Re	C	M
I: 2.1 MHz	36.0	35.5	3.2	24.9	25.4	4.8	17.1	17.9	3.7
I: 4 MHz	29.0	25.3	12.1	16.0	14.3	9.9	9.8	8.6	7.7
P: 2.1 MHz	36.2	36.0	10.0	21.6	24.4	8.5	14.3	20.0	8.5
P: 4 MHz	20.3	25.2	25.3	13.7	18.2	24.8	11.2	18.4	25.8

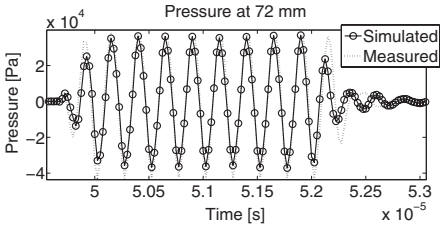

FIG. 7. Comparison between simulated and measured pressure pulses at a distance of 72 mm from a single element modeling each subdivided element.

cates that the model is capable of working with both types of data set and that the attenuation based on the mechanical quality factor is capturing the acoustic losses with a maximum difference of 3.7%. Prediction errors for the pressure pulses are found to range from 11.2% to 36.2% rms error with best results found with the 4.0 MHz center frequency. The 4.0 MHz predicted pulses are found to be closer to the mean measurement than each individual piezoceramic sample. This indicates the importance of using several samples for comparison, which gives the level of accuracy that one can expect.

B. Results for the convex transducer when modeling each single subelement

A comparison between the simulated and the measured pressure at a distance of 72 mm along the center axis of an active element is shown in Fig. 7. Several measurements and tests in different depths have shown that the simulations undershoot the amplitude by approximately 1.7 dB relative to the mean measurement, which is the value found to give the smallest rms error. The following rms results are therefore calculated with this adjustment in amplitude. From Fig. 7 it is furthermore found that the model captures the pulse behavior relatively well. Only a slight overshoot on the transition is found and some missing behavior on the pulse tail can be seen.

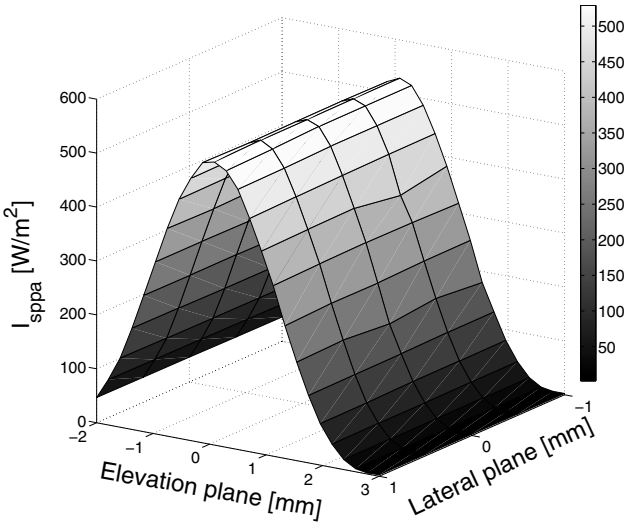

FIG. 8. Intensity profile measured at a 72 mm distance from an active element in the lateral plane and the elevation plane. The colors also indicate the intensity level.

TABLE IV. Intensity profiles' relative rms errors measured at three depths.

	rms % intensity		
Depth (mm)	33	72	112
Element 64	3.4	8.9	0.9
Element 65	1.0	0.6	1.5
Element 66	1.5	1.1	1.1

Figure 8 is an example of a measured intensity profile at a distance of 72 mm from an active element. The profile is measured in the elevation and the lateral direction and is calculated as the spatial peak pulse average intensity, which is chosen due to its suitability for pulse comparison. When comparing a simulated intensity profile in the elevation plane with measurements, it is very important that the proper lateral direction is found in the measurement. If this is not found one may compare with a wrong measurement profile. As is seen in Fig. 8 the deviation of the intensity profiles in the lateral direction can be seen to be small and may be quantified by an rms error calculated as

$$\mathrm{rms}_{\mathrm{prof}} = 100 \cdot \frac{\sqrt{\frac{1}{N}\sum_{m=1}^{N}\frac{1}{N_s}\sum_{i=1}^{N_s}(\bar{I}(m)-I(m,i))^2}}{\sqrt{\frac{1}{N}\sum_{m=1}^{N}\bar{I}(m)^2}}, \qquad (41)$$

where $\bar{I}(m)$, $I(m,i)$, N_s, and N are the mean intensity profile, the measured intensity profile at the ith lateral direction, the number of lateral profiles, and the number of elevation points measured, respectively. Table IV lists calculated rms errors for measurements of intensity profiles from three center elements at three different depths: 33, 72, and 112 mm.

Table IV shows that measurements on Element 65 and 66 are within a 1.5% deviation relative to the mean but increasing for Element 64 around the focus point. Therefore, a simulated intensity profile compared with an intensity profile for Element 65 and 66 for any of the lateral directions can be made with similar error predictions. However, Element 64 may give a highly different error prediction due to the high relative deviation of its measured lateral profiles. Therefore, in the following, all simulated intensity profiles along the elements' center axes are compared with the laterally average of measured intensity profiles.

Figure 9 shows an intensity comparison in the elevation plane between simulated and averaged intensity profiles at the three depths. From the results plotted in the figure, it is found that the tendency of the intensity level is captured

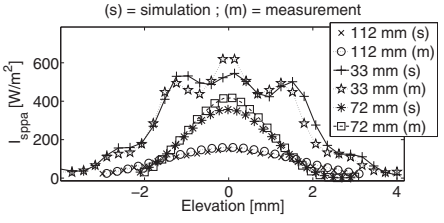

FIG. 9. Elevation intensity comparison between simulated and measured values at three depths.

TABLE V. rms error at three depths with 1.7 dB amplitude correction.

	rms % intensity			rms % pressure		
Depth (mm)	33	72	112	33	72	112
Element 64	11.5	14.2	5.9	26.2	26.3	27.2
Element 65	19.5	16.2	14.6	25.2	27.1	26.7
Element 66	15.2	7.1	5.8	26.0	26.2	26.1

through the whole elevation plane in the three depths 33, 72, and 112 mm. However, it is pointed out that the 1.7 dB amplitude adjustment on the pressure pulses is also used here.

The consistent tendency on the shape of the intensity curves is due to the setup of the FIELD II program and is not to be credited the impulse response calculated by the transducer model. This is because the shape of the intensity profile is entirely dependent on the spatial impulse response. It is therefore to be concluded that the FIELD II setup with the many subdivided elements is performed properly.

A quantitative comparison between the simulated and measured intensity and pressure is shown in Table V. The table shows the relative rms error between the simulated and the measured pressure in percent, which is calculated similarly as in Eq. (40). The calculation is made using the measured pressure in the three different measurement points along the element's center lines. The center lines are found by searching for the maximum amplitudes of the measurements along the lateral direction. Accordingly the intensity rms error is calculated for the intensity studies in the elevation plane using the lateral average. Both results are listed in Table V.

From Table V, it is found that the pressure prediction at the three depths in between differ by 2% rms error relative to the mean, which is a much better result than the one found for the piezoceramics in Table III. This indicates that the transducer is very homogeneous in its performance, and that the measurements along the center lines are performed uniformly. A comparison between simulated- and measured pressures corresponds to an rms error equal to 25.2% to 27.2%. The rms intensity errors of the three elements in between are found to differ by 5.1%–14.6% at 112 mm, 7.1%–16.2% at 72 mm, and 11.5%–19.5% at 33 mm. This increase in difference the closer the measurements are to the transducer is mainly due to the transducer's nonideal surface. Small deviations in the surface profile are of influence close to the transducer surface, since these are not accounted for in the FIELD II setup.

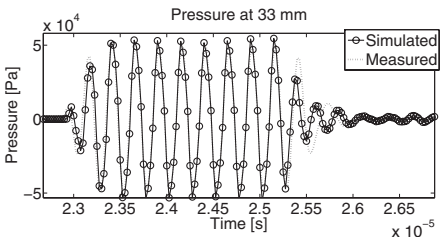

FIG. 10. Comparison between a simulated and a measured pressure pulse at a distance of 33 mm.

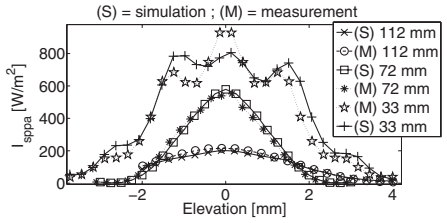

FIG. 11. Elevation intensity comparison between simulated and measured values at three depths using major elements only.

C. The results on the convex transducer modeling only the major elements

Figure 10 shows a comparison between simulated and measured pressures at a distance of approximately 33 mm from an emitting transducer element. The comparison does not involve an amplitude correction as seen in the previous results, which indicates that modeling of the major elements instead of each subelement predicts a better amplitude result. The same pulse behavior is, however, found with lacking information on pulse tails and slight overshoot on transitions.

Figure 11 is an intensity plot similar to Fig. 9. From the figure it can be identified that the amplitudes are well predicted and that the FIELD II surface model is predicting the intensity profile nicely in this configuration. The prediction is close to the one found in Fig. 9.

Table VI shows the quantitative rms errors for the intensity. As can be identified from the numerical errors on the pressure predictions only a small increase in the errors is found. Notice, that the data are given without amplitude correction which was not found necessary when using the given surface model of FIELD II. This indicates that the extra area contribution from the kerfs of the subdivided elements in between gives the extra small amplitude contribution needed for having a calibrated model. The intensity errors found in Table VI are found to be almost identical with those in Table V, which also implies that the two transducer models are working almost identically.

VI. DISCUSSION

Figure 5 shows that the free oscillating pulse tail may approach an almost $\pi/2$ phase shift. Such a phase drift is due to several consequences of the presented modeling. One consequence is the use of a one-dimensional model which restricts the impulse response to account for dispersion modes that are only valid in the thickness mode (vibrations and dependencies along the z coordinate only). The attenuation in this direction is, furthermore, modeled as being frequency independent. A more detailed model involves frequency-dependent attenuation algorithms and a multidimensional

TABLE VI. rms error at three depths with 0 dB amplitude correction.

	rms % intensity			rms % pressure		
Depth (mm)	33	72	112	33	72	112
Element 64	14.6	6.7	13.0	29.9	33.3	31.2
Element 65	19.9	9.6	5.76	29.4	34.0	30.7
Element 66	19.8	8.3	6.24	29.6	33.7	30.8

analysis. The amplitudes calculated in water may also be adjusted slightly since attenuation in water was not accounted for in FIELD II. This amounts to a maximum multiplication factor for the 112 mm 4 MHz pressure pulse of approximately 0.96 which will yield an amplitude difference of approximately 0.3 dB. Also inaccuracies of the input parameters are possible error sources.[20] The simulations in this work rely on the exactness of the input parameters obtained by consulting the manufacturers and the work by Algueró *et al.*[13] as wells as the simplified electronic circuit.[20] However, these parameters may be slightly different from those characterizing the samples used in the presented experiments. A correction of the free resonance frequency of the different transducers requires a fine tuning of especially the density ρ, the stiffness c^D, and the thickness L, by performing measurements on each individual transducer. For the pz27 samples also exact consideration of wire connections, soldering, and immersion medium would improve the errors, which to some extend is also applicable for the commercial transducer.

Despite the relatively high quantitative error found in this work it must also be argued that the model's simplicity makes it a qualified tool for fast hybrid modeling with FIELD II compared to hybrid modeling linked up against time-consuming finite-element programs. Impulse responses, nevertheless, calculated using the latter programs benefit in the level of detail from the full dimensionality, however, it is also more sensitive to the accuracy of input parameters.

VII. CONCLUSION

It has been shown that a one-dimensional model for ultrasound multilayer transducers can be implemented to predict the required volt-to-surface acceleration converted impulse response needed by the FIELD II software to calculate the field pressure in front of piezoceramic disk samples as well as from a more complicated 128 element convex ultrasound transducer. The implemented model predicts the current flow through simple electrical circuits driving piezoceramic disks within an rms error of 8.6%–36% for long and short pulses, respectively, and within 11.2% to 36.2% for pressure pulses, respectively. All pressure amplitudes were found to give an approximately 2 dB overshoot in prediction. Both the real-valued data set and the complex-valued data set were found to exhibit almost identical results, which implies that the model works well with both types of parameter sets. Furthermore, it implies that it is possible to model losses in the piezoceramic using the mechanical quality factor or complex material parameter sets.

Pressure measurements carried out on the medical convex transducer and compared to model predictions yield rms errors of 26%–30% depending on the surface model used. Generally, the different pressure measurements were found to differ within 2%. Comparison of measured and simulated intensities was found to give an error between 5.8% and 19.8%, where the largest errors were found close to the elements. The results also show that the simplified electronic circuit describing the transmitter unit and the coaxial cable models the voltage amplitude across the piezoelectric transducer elements properly. It has been shown that using a measurement of the transmitter output voltage as an input excitation waveform for the FIELD II model gives good agreement between simulated and measured results. It can also be concluded that modeling of each single subdivided element gives almost the same result for the pulse shape as modeling the entire element as a whole surface does. However, an undershoot of approximately 1.7 dB was found.

The FIELD II program combined with the one-dimensional modeling principle is therefore a good candidate for performing fast hybrid modeling of acoustic fields.

ACKNOWLEDGMENTS

The authors would like to thank Sound Technology, Inc. for supplying the transducer information as well as giving support in discussions. Also a great thank to BK Medical Aps for their assistance. Furthermore, the authors would like to thank Dr. Erling Ringgaard, Ferroperm Piezocermics A/S, Kvistgård, Denmark, for delivering the piezoceramic samples and supplying data sets as well as giving support in the discussions.

[1] J. A. Jensen, "Field: A program for simulating ultrasound systems," Med. Biol. Eng. Comput. **4**, 351–353 (1996).
[2] J. A. Jensen and N. B. Svendsen, "Calculation of pressure fields from arbitrarily shaped, apodized, and excited ultrasound transducers," IEEE Trans. Ultrason. Ferroelectr. Freq. Control **39**, 262–267 (1992).
[3] M. Redwood, "Transient performance of a piezoelectric transducer," J. Acoust. Soc. Am. **33**, 527–536 (1961).
[4] E. K. Sittig, "Transmission parameters of thickness-driven piezoelectric transducers arranged in multilayer configurations," IEEE Trans. Sonics Ultrason. **SU-14**, 167–174 (1967).
[5] R. Krimholtz, D. Leedom, and G. Matthaci, "New equivalent circuits for elementary piezoelectric transducers," Electron. Lett. **6**, 398–399 (1970).
[6] T. R. Meeker, "Thickness mode piezoelectric transducers," Ultrasonics **10**, 26–36 (1972).
[7] P. Marchal, F. Levarssort, L.-P. Tran-Huu-Hue, and M. Lethiecq, "Effects of acoustical properties of a lens on the pulse-echo response of a single element transducer," IEEE International Ultrasonics, Ferroelectrics, and Frequency Control Joint 50th Anniversary Conference, pp. 1651–1654 (2004).
[8] P. Maréchal, F. Levarssort, L.-P. Tran-Huu-Hue, and M. Lethiecq, "Lens-focused transducer modeling using an extended KLM model," Ultrasonics **46**, 155–167 (2007).
[9] M. Willatzen, "Ultrasound transducer modeling—Received voltage signals and the use of half-wavelength window layers with acoustic coupling layers," IEEE Trans. Ultrason. Ferroelectr. Freq. Control **46**, 1164–1174 (1999).
[10] M. Willatzen, "Ultrasound transducer modeling—General theory and applications to ultrasound reciprocal systems," IEEE Trans. Ultrason. Ferroelectr. Freq. Control **48**, 100–112 (2001).
[11] D. Bæk, J. A. Jensen, and M. Willatzen, "Testing of a one dimensional model for Field II calibration," Proc.-IEEE Ultrason. Symp. , 1417–1420 (2008).
[12] D. Bæk, J. A. Jensen, and M. Willatzen, "Calibration of Field II using a convex ultrasound transducer," in Proceedings of the International Congress on Ultrasonics, Vol. **3**, Issue 1 (2009).
[13] M. Algueró, C. Alemany, and L. Pardo, "Method for obtaining the full set of linear electric, mechanical and electromechanical coefficients and all related losses of a piezoelectric ceramic," J. Am. Ceram. Soc. **87**, 209–215 (2004).
[14] B. A. Auld, *Acoustic Fields and Waves in Solids*, 2nd ed. (Krieger, Malabar, FL, 1990), Vol. **1**.
[15] T. Tsurumi, H. Kakemoto, and S. Wada, "Dielectric, elastic and piezoelctric losses of PZT ceramics in resonate state," in Proceedings of the 13th IEEE International Symposium on Applications of Ferroelectrics, ISAF 2002 (2002), pp. 375–378.
[16] M. Castillo, P. Acevedo, and E. Moreno, "KLM model for lossy piezo-

electric transducers," Ultrasonics **41**, 671–679 (2003).
[17]J. G. Smits, "Iterative method for accurate determination of the real and imaginary parts of the materials coefficients of piezoelectric ceramics," IEEE Trans. Sonics Ultrason. **23-6**, 393–401 (1976).
[18]C. Alemany, L. Pardo, B. Jimnez, F. Carmona, and J. Mendiola, "Automatic iterative evaluation of complex material constants in piezoelectric ceramics," J. Phys. D: Appl. Phys. **27**, 148–155 (1994).
[19]J. A. Jensen, O. Holm, L. J. Jensen, H. Bendsen, H. M. Pedersen, K. Salomonsen, J. Hansen, and S. Nikolov, "Experimental ultrasound system for real-time synthetic imaging," Proc.-IEEE Ultrason. Symp. **2**, 1595–1599 (1999).
[20]D. Bæk, M. Willatzen, and J. A. Jensen, "Parameter sensitivity study of a Field II multilayer transducer model on a convex transducer," Proc.-IEEE Ultrason. Symp. In press.

Paper IV

Multilayer piezoelectric transducer models combined with Field II

David Bæk, Morten Willatzen, and Jørgen Arendt Jensen

Acta Acustica united with Acustica

In review

Multilayer piezoelectric transducer models combined with Field II

David Bæk, Morten Willatzen, and Jørgen Arendt Jensen

***Abstract*—A one-dimensional and a three-dimensional axisymmetric transducer model have been compared to determine their feasibility to predict the volt-to-surface impulse response of a circular Pz27 piezoceramic disc. The ceramic is assumed mounted with silver electrodes, bounded at the outer circular boundary with a polymer ring, and submerged into water. The transducer models are developed to account for any external electrical loading impedance in the driving circuit. The models are adapted to calculate the surface acceleration needed by the Field II software in predicting pressure pulses at any location in front of the transducer. Results show that both models predict the longitudinal resonances with consistency. The one-dimensional model is found to exhibit approximately 2.9 dB peak overshoot at the lowest longitudinal resonance frequencies prediction. These values are decreasing for higher longitudinal modes. If the three-dimensional model is restricted in its radial movement at the circular boundary both models exhibit identical results. The Field II predicted pressure pulses are found to have oscillating consistency with a 2.0 dB overshoot on the maximum amplitude using the one-dimensional compared to the three-dimensional model. This is with no electronic loading. With a 50 Ω loading an amplitude overshoot is found to be 1.5 dB.**

I. Introduction

It has previously been shown that a one-dimensional transducer model is bale to predict the surface acceleration needed for performing calibrated Field II [4], [5] simulations [1], [2], [3]. Good agreement has been found for circular piezo ceramic discs and with a 128 element commercial convex medical transducer. Field II is an ultrasound simulation program that is capable of simulating the acoustic scattering of tissue, and the program can be used to simulate the RF-data needed for ultrasound medical imaging or the field pressure. The program, however, only accounts for a simulation domain ranging from the transducer surface and into the tissue, and not for the actual waveform of the moving transducer surface. This waveform has to be provided externally by the user. The motivation for the works in [1], [2], [3] was to combine Field II with a transducer model, whereby a significant improvement of the program's applicability could be achieved. The investigations of the one-dimensional model should then be the foundation for determining whether such a model should be implemented permanently into the Field II program and available for the ultrasound simulation community. The one-dimensional modeling principle applied in the works was chosen for investigation due to its ability to reveal information such as displacement, velocity, acceleration, and electrical displacement to any position in a multilayer transducer and it was chosen for its simplicity. Such information is beneficial in a transducer development context and essential for Field II calibrated intensity simulations.

A one-dimensional model is particularly applicable when vibrations occur along one direction of the transducer only, albeit this is no strict requirement. There are, however, transducer applications where the transducer is not just operating in one direction. This could be transducers of ceramic discs with relative big radius compared to the thickness whereby radial modes may occur. In these situations it may be valuable to include the radial modes in the simulations.

Modeling transducer responses in one and more dimensions is well addressed in the literature [6], [7], [8], [9], [10], [11], [12]. However, a detailed comparison between a one-dimensional model [13] and a two-dimensional model, linked up with Field II, has not yet been investigated. This would, however, be a natural follow-up on the work with combining Field II with a one-dimensional model since a two-dimensional model could also be considered for implementation into the Field II source code.

In this work a two-dimensional axisymmetric transducer model originally suggested by Schnabel [14] is extended to include an electronic loading network as well as general acoustic impedance load conditions. This model is suitable for modeling ultrasonic transducers where radial modes are present and contribute to the surface movement. This axisymmetric model is compared with the one-dimensional modeling [13] to identify the strength and weaknesses between the two models in predicting the frequency response of a circular piezoceramic transducer. The transducer considered is submerged into water, enclosed in a polymer ring, and

coated with silver electrodes. Furthermore, combining Field II with each of the two models makes a comparison between model output pressure pulses possible. This will reveal information on the influence of the radial modes in a Field II simulation. Moreover, this analysis presents a feasibility study of the Field II software with a three-dimensional axisymmetric transducer model.

II. Theory

This work is concerned with an axisymmetric piezoceramic disc coated with silver electrodes and mounted in a polymer ring, where the outer boundaries are fixed as depicted in Fig. 1a. The transducer's longitudinal axis is chosen as the z-axis (with origo at the bottom plane of the transducer), and the r coordinate is the distance from the longitudinal axis. The electronic network consists of an impedance, Z_{load}, in series with a function generator, V_{drive}, (internal resistance Z_{in}) driving the piezoceramic disc. It is furthermore assumed that the whole transducer is submerged into water. Fig. 1b shows the cross section of the transducer. Similarly, Fig. 1c identifies the boundaries of the transducer. The materials of this transducer consist of a piezoelectric domain of a Pz27 material poled in the z-direction. This domain is to be modeled with a coupling between displacements and the electrical field generated by the vibration and the driving force. The silver electrodes and the polymer ring are modeled as isotropic materials where no coupling between electricity and displacement is present.

A. The governing equations for a axisymmetric transducer

The governing equations describing a $6mm$ two-dimensional axisymmetric piezoceramic are well known from the literature [14]. They are typically described using cylindrical coordinates r, z, θ, where r is the radial coordinate axis, z is the thickness axis coordinate, and θ is the azimuthal coordinate. If the disk is assumed to be axisymmetric, poled in its longitudinal direction, z, and driven with a potential across the faces perpendicular to the z-direction, then no torsional mode should occur and there is no dependence of the azimuthal angle. If the particle displacements associated with the different coordinates are defined as u_r, u_z, and u_θ the above assumptions can be formulated as:

$$u_\theta = 0, \qquad \frac{\partial}{\partial \theta} = 0, \qquad D_\theta = 0, \tag{1}$$

where D_θ is the electrical displacement in the θ direction and where $\frac{\partial}{\partial \theta}$ defines the derivative with respect to the θ coordinate.

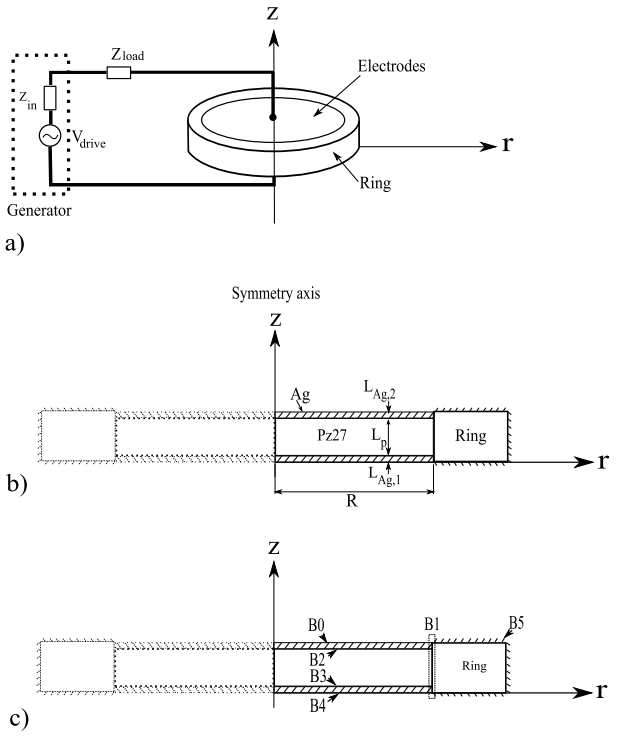

Fig. 1. Drawing of the transducer setup considered in this paper. a) A piezoceramic transducer with silver electrodes enclosed in a ring of plastic. A function generator with an internal resistance Z_{in} and an external impedance Z_{load} is loading the transducer. b) cross sectional cut of the transducer. c) boundary numbering of the cross section.

These statements follow as a consequence of full axisymmetric assumptions and no tangential movement or twisting of the cylinder.

The constitutive equations that obey the above assumptions in cylindrical coordinates can be written as [14], [15]

$$T_{rr} = c_{11}^E u_{r,r} + c_{12}^E \frac{u_r}{r} + c_{13}^E u_{z,z} + e_{31} V_{,z}, \tag{2}$$

$$T_{\theta\theta} = c_{12}^E u_{r,r} + c_{11}^E \frac{u_r}{r} + c_{13}^E u_{z,z} + e_{31} V_{,z}, \tag{3}$$

$$T_{zz} = c_{13}^E u_{r,r} + c_{13}^E \frac{u_r}{r} + c_{33}^E u_{z,z} + e_{33} V_{,z}, \tag{4}$$

$$T_{rz} = c_{44}^E u_{r,z} + c_{44}^E u_{z,r} + e_{15} V_{,r}, \tag{5}$$

$$T_{r\theta} = 0, \tag{6}$$

$$T_{\theta z} = 0, \tag{7}$$

$$D_r = e_{15} u_{r,z} + e_{15} u_{z,r} - \epsilon_{11}^S V_{,r}, \tag{8}$$

$$D_\theta = 0, \tag{9}$$

$$D_z = e_{31} \left(u_{r,r} + \frac{u_r}{r} \right) + e_{33} u_{z,z} - \epsilon_{33}^S V_{,z}, \tag{10}$$

where T and D are the tension and the electrical displacement, respectively. The electrical potential is defined as V, the electric field is then $E = -\nabla V$ where ∇ is the gradient operator. The constants c_{ij}^E, e_{ij}, and ϵ_{ij}^S

are respectively the stiffness coefficient under constant electrical field, the piezoelectric coupling coefficient for stress-charge form, and the electrical permitivity. Note the notation for the derivatives used in this work is: $\frac{\partial u}{\partial x_i} = u_{,x_i}$ and $\frac{\partial u}{\partial t} = u_{,t}$.

The equations-of-motion and the Maxwell-Poisson equation [14]-[15] yield

$$\rho u_{z,tt} = T_{rz,r} + \frac{T_{rz}}{r} + T_{zz,z}, \tag{11}$$

$$\rho u_{r,tt} = T_{rr,r} + \frac{T_{rr}}{r} + T_{rz,z} - \frac{T_{\theta\theta}}{r}, \tag{12}$$

$$D_{r,r} + \frac{D_r}{r} + D_{z,z} = 0, \tag{13}$$

where ρ is the density.

Consider (11), (12), and (13) and assume a time harmonic solution of the form $e^{-\jmath\omega t}$. Insertion of the expressions for $T_{rr}, T_{rz}, T_{\theta\theta}$, T_{zz}, D_r, and D_z into the latter three equations yields (14), (15), and (16). These equations are the equations coupling displacement with electrical effects inside a piezoelectric material.

B. Boundary conditions

The boundary conditions needed to solve (14)-(16) at the interface between solid-fluid, boundary B0, and B4 in Fig. 1 are defined as

$$T_{zz} = -n_z \cdot \jmath\omega Z_{fluid} u_z, \tag{17}$$

where Z_{fluid} is the specific acoustic impedance of the fluid given by the product between the fluid density and the thermodynamical speed of sound, $\rho_{fluid} v_{fluid}$, and n_z is the unit normal parallel to the z-axis under investigation i.e $n_z = 1$ at $\partial\Omega^{B0}$ and $n_z = -1$ at $\partial\Omega^{B4}$. This is the impedance method of modeling the coupling between a vibrating solid and a fluid [16].

The boundary conditions at a solid-solid interface have to preserve continuity of stress and displacement. Continuity of stresses at an interface is achieved through the normal of the stresses

$$n \cdot T_{ij}^{\Omega_l} = n \cdot T_{ij}^{\Omega_k} \quad \textit{at} \quad \partial\Omega_{l,k}, \tag{18}$$

where $T_{ij}^{\Omega_l}$ is the stress equation from the solid domain l. $T_{ij}^{\Omega_k}$ is the stress equation from solid domain k at the boundary $\partial\Omega_{l,k}$ and n is the boundary normal vector.

Continuity of displacement requires:

$$u_r^{\Omega_l} = u_r^{\Omega_k}, \tag{19}$$

$$u_z^{\Omega_l} = u_z^{\Omega_k}. \tag{20}$$

The boundaries B1, B2, and B3 in Fig. 1c are considered insulating meaning that there is assumed no flow of current into the silver electrodes and the ring material. However, in principle also the silver electrodes are conductors, but due to their high conductivity they are neglected in this study, where the silver electrodes are considered to be non-conducting acoustic waveguides only. Therefore, the boundaries B1, B2, and B3 are insulating boundaries which mathematically are satisfied by

$$n \cdot D_j = 0. \tag{21}$$

C. Isotropic materials

To model a non-piezoelectric ring around the boundary of the axisymmetric model or matching layers in extension of the poled direction, electrical coupling of the above equations (14)-(15) is to be removed. Equation (16) is not applicable to such materials and can therefore be neglected. The stress coefficients, c^E, for isotropic materials can be found by means of the Young's module, Y, and the Poisson ratio, ν, by [15]:

$$c_{11} = \frac{Y(1-\nu)}{(1+\nu)(1-2\nu)}, \tag{22}$$

$$c_{12} = \frac{Y\nu}{(1+\nu)(1-2\nu)}, \tag{23}$$

$$c_{44} = \frac{Y}{2(1+\nu)}. \tag{24}$$

Notice that the stiffness constants in (14)-(15), when modeling an isotropic material, are related through $c_{11} = c_{22} = c_{33}$, $c_{12} = c_{13} = c_{23}$, $c_{44} = c_{55} = c_{66} = \frac{1}{2}(c_{11} - c_{12})$.

D. Combining the electronic network with the 2D model

The electronic network loading the transducer in Fig. 1 is not accounted for by solving (14)-(21). However, knowledge of the transducer's characteristic electrical impedance can be achieved by solving the above set of equations for the impulse frequency response using a Fourier transform of a voltage impulse, $V_{drive}(\omega)$, where in this study the Fourier transform pair used is

$$V(t) = \frac{1}{\sqrt{2\pi}} \int_{-\infty}^{\infty} V(\omega) e^{-\jmath\omega t} d\omega, \tag{25}$$

$$V(\omega) = \frac{1}{\sqrt{2\pi}} \int_{-\infty}^{\infty} V(t) e^{\jmath\omega t} dt. \tag{26}$$

The impedance is then found from Ohm's law as

$$Z_{piezo} = \frac{V_{drive}}{I}, \tag{27}$$

where I is the current running through the circuit. The displacement current flowing through the piezo material is given by: $I = A\frac{\partial D}{\partial t}$ where A is the cross-sectional

$$\omega^2\rho u_r + (c_{11}u_{r,r} + c_{12}\frac{u_r}{r} + c_{13}u_{z,z} + e_{31}V_{,z})_r + (c_{44}^E(u_{r,z} + u_{z,r}) + e_{15}V_{,r})_z + \frac{(c_{11}^E - c_{12}^E)u_{r,r} + (c_{12}^E - c_{11}^E)\frac{u_r}{r}}{r} = 0, \quad (14)$$

$$\omega^2\rho u_z + (c_{44}^E u_{r,z} + c_{44}^E u_{z,r} + e_{15}V_{,r})_r + (c_{13}^E(u_{r,r} + \frac{u_r}{r}) + c_{33}^E u_{z,z} + e_{33}V_{,z})_z + \frac{c_{44}^E u_{r,z} + c_{44}^E u_{z,r} + e_{15}V_{,r}}{r} = 0, \quad (15)$$

$$(e_{15}u_{r,z} + e_{15}u_{r,z} - \epsilon_{11}^S V_{,r})_r + (e_{31}(u_{r,r} + \frac{u_r}{r}) + e_{33}u_{z,z} - \epsilon_{33}^S V_{,z})_z + \frac{e_{15}u_{r,z} + e_{15}u_{z,r} - \epsilon_{11}^S V_{,r}}{r} = 0. \quad (16)$$

area of the ceramic (equal to (πR^2)). By assuming a time-harmonic solution of the current it may be found as

$$I = -\jmath\omega \int_A n_z \cdot D dA = -\jmath\omega \int_A D_z dA, \quad (28)$$

$$I = -\jmath\omega 2\pi \int_0^R \left(e_{31}\left(\frac{\partial u_r}{\partial r} + \frac{u_r}{r}\right) + e_{33}\frac{\partial u_z}{\partial z} - \epsilon_{33}^S \frac{\partial V}{\partial z}\right) r dr, \quad (29)$$

where R is the radius of the ceramic and n_z is the normal to the boundaries B0 and B4.

The voltage found across the electrodes, when an electronic loading is present, is found by use of Ohm's law:

$$V_{electrodes}(\omega) = V_{drive}(\omega)\frac{Z_{piezo}(\omega)}{Z_{piezo}(\omega) + Z_{external}(\omega)}, \quad (30)$$

where $Z_{external} = Z_{load} + Z_{in}$ and V_{drive} are the external loading impedance and the Fourier transform of the driving pulse, respectively. Hence, the (frequency-dependent) transfer function of the electrical network as

$$H_{electronic}(\omega) = \frac{Z_{piezo}(\omega)}{Z_{piezo}(\omega) + Z_{external}(\omega)}. \quad (31)$$

The voltage-to-surface longitudinal displacement, u_z, of the transducer, when driven with V_{drive}, is then found through

$$u_z = u_{z_{response}} \cdot V_{electrodes}. \quad (32)$$

The value $u_{z_{response}}$ is the frequency response of the surface movement found by solving (14)-(21) at B0 and B4.

The above prescribed method of including the electronic network benefits from the fact that $u_{z_{response}}$ is to be calculated only once for the transducer, whereafter it can be subject to any electrical loading condition.

III. Implementing the 2D equations

In this paper, implementation of (14)-(21) into COMSOL [17] is briefly discussed for the equations of the four domains in Fig. 1. This discussion is chosen because an actual description of the implementation into a finite element program is seldom seen in the literature.

A basic equation set in COMSOL in a two-dimensional general mode reads:

$$-\nabla \cdot (c\nabla\mathbf{u} + \alpha\mathbf{u} - \gamma) + a\mathbf{u} + \beta\nabla\mathbf{u} = f, \quad (33)$$

where the elements $c, \alpha, a, f, \beta, \gamma$ are scalar constants or matrices. The ∇ is in this work defined as $\{\frac{\partial}{\partial r}, \frac{\partial}{\partial z}\}$ and $\mathbf{u}$ is a vector of unknown variables to be solved for. The corresponding mixed boundary conditions to (33) are defined as

$$n \cdot (c\nabla u + \alpha u - \gamma) + qu = g - h^T\lambda, \quad (34)$$

$$hu = r, \quad (35)$$

where λ is a Lagrange multiplier, q and h are coefficient matrices that can be set to any value.

Since the normal of the stresses and the dielectrical effects on a solid's boundaries should satisfy (18) and (21), it is advantageous to make sure that in a piezoelectric domain the mixed boundary conditions becomes $n \cdot (c\nabla u + \alpha u - \gamma) = \{T_{lk}, D_l\}^T$,where $l, k = \{r, z\}$. Ensuring this, the matrix q and g in (34) can be used to define the boundary condition (17). Furthermore, the Direchlet boundary condition, $hu = r$, may be used to ensure continuity of displacements (19) and (20).

The different coefficients for the piezoelectrical material are therefore to be formulated as in (36) by assuming $\mathbf{u} = \{u_r^{piezo}, u_z^{piezo}, V\}^T$. For isotropic domains where the same definitions are to be made with all $e_{i,j}$ and ϵ^S set to zero the implementation is similar. In such domains $\mathbf{u} = \{u_r^{iso}, u_z^{iso}\}^T$, and consequently, (16) is to be left out in this work. However, if it is necessary to model electrical conductivity in the isotropic materials then (16) is to be kept, and $\epsilon^S \neq 0$. The remaining vectors and matrices of (33) is to be set to zero. Then by utilizing the above implementation principle on the

$$c=\begin{bmatrix}\begin{bmatrix}c_{11}^E & 0\\ 0 & c_{44}^E\\ 0 & c_{44}^E\\ c_{13}^E & 0\\ 0 & e_{15}^E\\ e_{31}^E & 0\end{bmatrix} & \begin{bmatrix}0 & c_{13}^E\\ c_{44}^E & 0\\ c_{44}^E & 0\\ 0 & c_{33}^E\\ e_{15}^E & 0\\ 0 & e_{33}^E\end{bmatrix} & \begin{bmatrix}0 & e_{31}^E\\ e_{15}^E & 0\\ e_{15}^E & 0\\ 0 & e_{33}^E\\ -\epsilon_{11}^S & 0\\ 0 & -\epsilon_{33}^S\end{bmatrix}\end{bmatrix}, \quad \alpha=\begin{bmatrix}\begin{bmatrix}c_{12}^E/r\\ 0\\ 0\\ c_{13}^E/r\\ 0\\ e_{31}^E/r\end{bmatrix} & \begin{bmatrix}0\\0\\0\\0\\0\\0\end{bmatrix} & \begin{bmatrix}0\\0\\0\\0\\0\\0\end{bmatrix}\end{bmatrix},$$

$$\beta=\begin{bmatrix}\begin{bmatrix}-(c_{11}^E-c_{12}^E)/r\\ 0\end{bmatrix} & \begin{bmatrix}0\\0\end{bmatrix} & \begin{bmatrix}0\\0\end{bmatrix}\\ \begin{bmatrix}0\\ -c_{44}^E/r\\ 0\\ -e_{15}^E/r\end{bmatrix} & \begin{bmatrix}-c_{44}^E/r\\ 0\\ -e_{15}^E/r\\ 0\end{bmatrix} & \begin{bmatrix}-e_{15}^E/r\\ 0\\ \epsilon_{11}^S\\ 0\end{bmatrix}\end{bmatrix}, \quad a=\begin{bmatrix}\begin{bmatrix}-\rho\omega^2-\frac{(c_{12}^E-c_{11}^E)}{r^2}\end{bmatrix} & \begin{bmatrix}0\end{bmatrix} & \begin{bmatrix}0\end{bmatrix}\\ \begin{bmatrix}0\\0\end{bmatrix} & \begin{bmatrix}-\rho\omega^2\end{bmatrix} & \begin{bmatrix}0\\0\end{bmatrix}\\ & \begin{bmatrix}0\end{bmatrix} & \end{bmatrix}. \quad (36)$$

setup in Fig. 1 nine unknowns are to be solved for each frequency component inside a given bandwidth.

A. The one-dimensional model

The one-dimensional model governing the setup in Fig. 1 is found using the transducer model by Willatzen [13]. This model was investigated earlier in [1], [2], and [3] where it was compared with measurements and good agreement was found. According to the one-dimensional model, the particle velocity and stress obey the expressions:

$$u_{33}(z,t,\omega)=\frac{c_{33}^D S_A}{Z_a}e^{(-\jmath kz-\jmath\omega t)}-\frac{c_{33}^D S_B}{Z_a}e^{(\jmath kz-\jmath\omega t)}, \quad (37)$$

$$T_{33}(z,t,\omega)=c_{33}^D[S_A e^{(-\jmath kz-\jmath\omega t)}+S_B e^{(\jmath kz-\jmath\omega t)}]-h_{33}D, \quad (38)$$

where c_{33}^D and h_{33} are, respectively, the stiffness constant in the longitudinal direction and the piezoelectric constant defined as e_{33}/ϵ_{33}^S. Here e_{33} and ϵ_{33}^S are the piezoelectrical coupling coefficients for stress-charge form and the electrical permitivity. The propagation constant k is defined as ω/v_{33}, where ω is the radial frequency, and v_{33} is the wave velocity defined by $\sqrt{c_{33}^D/\rho}$. Here ρ is the given layer's material density. Furthermore, the acoustical impedance Z_a is defined as $Z_a=v_{33}\rho$. The unknown coefficients S_A and S_B are frequency and layer-dependent coefficients, and D is the frequency-dependent electrical displacement.

The boundary conditions to be fulfilled are continuity of stress and velocity as described in [13] whereby a set of equations is obtained (39)-(47).

The A and B subscripts Ag_1, Ag_2, and p in (39) - (47) refer to the first silver layer, the second silver layer, and the piezoceramic, respectively. This modeling yields nine equations with nine unknowns to be solved in Matlab.

IV. Pressure calculation from the surface vibration

The Field II software is applied for modeling the domain in front of the transducer. The calculation is performed by convolving the transducer dependent spatial impulse response with the time domain surface acceleration of the transducer as

$$p(\bar{r},t)=\rho v(t)\otimes h(\bar{r},t), \quad (48)$$

where h, v, and ρ are the spatial impulse response, the surface acceleration and the density, respectively. The $\otimes$ is the time convolution symbol. The surface acceleration is to be extracted from the solved system of equations of the one-dimensional and the two-dimensional model, which for the one-dimensional case is given by

$$v(t) \;=\; \mathcal{F}^{-1}[-\jmath\,\omega u_{Ag,2}(L_{Ag,2},t,\omega)], \quad (49)$$

where $\mathcal{F}^{-1}$ is the inverse Fourier transform (26), and $u_{Ag,2}$ is defined in consistency with (37) given by

$$u_{Ag,2}(L_{Ag,2},t,\omega)= \frac{c_{Ag,2}^D S_{Ag,2}}{Z_{Ag,2}}e^{(-\jmath k_{Ag,2}L_{Ag,2}-\jmath\omega t)}\ldots -\frac{c_{Ag,2}^D S_{Ag,2}}{Z_{Ag,2}}e^{(\jmath k_{Ag,2}L_{Ag,2}-\jmath\omega t)}. \quad (50)$$

The surface acceleration given from the two-dimensional model is found by

$$v(t,r) \;=\; \mathcal{F}^{-1}[(-\jmath\,\omega)^2\,u_z(r,\omega)] \quad \textit{at} \quad \Omega^{B0}. \quad (51)$$

In (51) it is to be recalled, that the surface movement is not necessarily constant along the radial direction as is assumed in (49).

The latter is a problem in context with the Field II software since this software cannot be brought to account for the radial movement of a transducer surface, which is why only u_z can be considered as a source to the two-dimensional full model and not u_r. Furthermore, to

$$
\begin{aligned}
T_{Back} &= c_{Ag}^{D}\left(A_{Ag,1}+B_{Ag,1}\right), && (39)\\
\frac{T_{Back}}{Z_{Back}} &= \frac{c_{Ag}^{D}}{Z_{Ag}}\left(A_{Ag,1}-B_{Ag,1}\right), && (40)\\
c_{p}^{D}\left(A_{p}+B_{p}\right)-hD &= c_{Ag}^{D}\left(A_{Ag,1}e^{-\jmath k_{Ag}L_{Ag}}+B_{Ag,1}e^{\jmath k_{Ag}L_{Ag}}\right), && (41)\\
\frac{c_{p}^{D}}{Z_{p}}\left(A_{p}-B_{p}\right) &= \frac{c_{Ag}^{D}}{Z_{Ag}}\left(A_{Ag,1}e^{-\jmath k_{Ag}L_{Ag}}-B_{Ag,1}e^{\jmath k_{Ag}L_{Ag}}\right), && (42)\\
c_{Ag}^{D}\left(A_{Ag,2}+B_{Ag,2}\right) &= c_{p}^{D}\left(A_{p}e^{-\jmath k_{p}L_{p}}+B_{p}e^{\jmath k_{p}L_{p}}\right)-hD, && (43)\\
\frac{c_{Ag}^{D}}{Z_{Ag}}\left(A_{Ag,2}-B_{Ag,2}\right) &= \frac{c_{p}^{D}}{Z_{p}}\left(A_{p}e^{-\jmath k_{p}L_{p}}-B_{p}e^{\jmath k_{p}L_{p}}\right), && (44)\\
T_{Front} &= c_{Ag}^{D}\left(A_{Ag,2}e^{-\jmath k_{Ag}L_{Ag}}+B_{Ag,2}e^{\jmath k_{Ag}L_{Ag}}\right), && (45)\\
-\frac{T_{Front}}{Z_{Front}} &= \frac{c_{Ag}^{D}}{Z_{Ag}}\left(A_{Ag,2}e^{-\jmath k_{Ag}L_{Ag}}-B_{Ag,2}e^{\jmath k_{Ag}L_{Ag}}\right), && (46)\\
-\jmath\omega V(\omega) &= -\left(Z_{external}\omega^{2}A+\jmath\omega\frac{L_{p}}{\epsilon^{S}}\right)D-h\frac{c_{p}^{D}}{Z_{p}}\left(A_{p}-B_{p}\right)+h\frac{c_{Ag}^{D}}{Z_{Ag}}\left(A_{Ag,2}-B_{Ag,2}\right), && (47)
\end{aligned}
$$

model the true contribution to a pressure from a discrete set of points along the front surface $B0$ (e.g corresponding to the solved displacements in the grid nodal points) Field II should be set up to model many small individual transducer elements which encloses the circular surface in a grid net. Each small transducer is then assumed to have an impulse response corresponding to the one calculated in the enclosed grid point by the 2D model. The built-in piston model of Field II cannot be used to model the whole circular transducer area because each mathematical element cannot be dedicated a separate impulse response. To model the many small transducer elements is, therefore, a cumbersome procedure.

Therefore, a more reasonable comparison between a two-dimensional and a one-dimensional model is to compare the average surface movement of the two-dimensional surface with the one-dimensional model's prediction. In this way, only a single surface response is obtained and the regular piston models can be used for comparison.

Since the 2D model solves for the surface movement from $r = 0$ to $r = R$ in the region of interest then the average movement may be found as

$$u_{average} = \frac{2\pi}{\pi R^2}\int_0^R u_z(L_{Ag,2}, r)rdr, \qquad (52)$$

where the integration is to be performed along the boundary B0.

V. Simulation test cases

Comparison between the two models is performed using two test cases of the setup in Fig. 1.

2D model of type I : The first case constrains the radial movement at boundary B1 for the two-dimensional model which is enforced by the boundary condition

$$u_r^{piezo} = 0 \quad at \quad \partial\Omega^{B1}. \qquad (53)$$

All other boundary conditions are set up to satisfy (17)-(21).

2D model of type II : The second test case has no radial restriction on B1 but constraints the radial and longitudinal movement at B5 in the ring domain. This is chosen to simulate that the ring is mounted into a rigid fixture prohibiting expansions.

The piezoceramic considered in this work is the Pz27 ceramic from Ferroperm Piezoceramic A/S, Kvistgaard, Denmark, whose database contains the needed simulation parameters. The material parameters describing the silver electrodes and the surrounding ring material (assumed to be polyethylene) are found in [15]. All the simulation parameters are given in Table I.

The thickness of the piezoceramic, L_p, is set to 0.94 mm, and the thickness of the silver electrodes, L_{Ag}, is set to 9 μm. Furthermore, cross sectional dimensions of the polyethylene are set to 2 mm x $(2L_{ag}+L_p)$ mm, and the inner radius of the ring is set to 5 mm. The electronic loading network has a total series impedance of 50 Ω.

Comparison is made firstly by assuming no external electronic loading of the transducer (i.e. $Z_{external} = 0$), secondly comparison is made by loading the transducer with the external circuit. Frequency responses are found using the voltage Fourier transform. This allows Z_{piezo} to be determined as a function of frequency.

Field II is set up to predict the pressure pulses at a distance of 70 mm along the transducer's center axis

TABLE I
MODEL PARAMETERS FOR PZ27, SILVER, POLYETHYLENE, AND WATER.

Constant	Value	Unit
Piezo:		
ρ	7700	$\frac{\text{kg}}{\text{m}^3}$
$c_{11}^E = c_{22}^E$	$1.47{\cdot}10^{11}$	$\frac{\text{N}}{\text{m}^2}$
c_{12}^E	$1.05{\cdot}10^{11}$	$\frac{\text{N}}{\text{m}^2}$
c_{33}^E	$1.13{\cdot}10^{11}$	$\frac{\text{N}}{\text{m}^2}$
c_{44}^E	$2.3{\cdot}10^{10}$	$\frac{\text{N}}{\text{m}^2}$
$c_{31}^E = c_{13}^E$	$9.37{\cdot}10^{10}$	$\frac{\text{N}}{\text{m}^2}$
e_{15}^E	11.64	$\frac{\text{N}}{\text{m}^2}$
e_{33}^E	16	$\frac{\text{N}}{\text{m}^2}$
e_{31}^E	-3.09	$\frac{\text{N}}{\text{m}^2}$
ϵ_{11}^S	$1130 \cdot \epsilon_0$	$\frac{\text{F}}{\text{m}}$
ϵ_{33}^S	$914 \cdot \epsilon_0$	$\frac{\text{F}}{\text{m}}$
ϵ_0	$8.8541 \cdot 10^{-12}$	$\frac{\text{F}}{\text{m}}$
h	$1.98{\cdot}10^9$	$\frac{\text{V}}{\text{m}}$
Silver:		
ρ_{Ag}	10600	$\frac{\text{kg}}{\text{m}^3}$
c_{11}^E	$11.9{\cdot}10^{10}$	$\frac{\text{N}}{\text{m}^2}$
c_{12}^E	$8.94{\cdot}10^{10}$	$\frac{\text{N}}{\text{m}^2}$
c_{44}^E	$4.37{\cdot}10^{10}$	$\frac{\text{N}}{\text{m}^2}$
c_{Ag}^D	$11.9 \cdot 10^{10}$	$\frac{\text{N}}{\text{m}^2}$
Ring material:		
ρ_{ring}	900	$\frac{\text{kg}}{\text{m}^3}$
c_{11}^E	$0.34{\cdot}10^{10}$	$\frac{\text{N}}{\text{m}^2}$
c_{12}^E	$2.88{\cdot}10^9$	$\frac{\text{N}}{\text{m}^2}$
c_{44}^E	$0.026{\cdot}10^{10}$	$\frac{\text{N}}{\text{m}^2}$
Water:		
ρ_{W}	1000	$\frac{\text{kg}}{\text{m}^3}$
c_{W}^D	$2.1904{\cdot}10^9$	$\frac{\text{N}}{\text{m}^2}$

using its piston model with a radius of 5 mm. The Field II setup is chosen to model mathematical elements on the surface with square sizes of 0.1 mm times 0.1 mm and with the inverse Fourier transform of the surface acceleration response (49) and (52) applied as the impulse response.

As driving pulse in the Field II calculation, a 10 cycle tone burst with 2.1 MHz center frequency and an amplitude of 10 V is used. Any tone burst could be applied, however, the choice of a 10 cycle tone burst limits the bandwidth of frequency components needed to be solved for.

VI. RESULTS

Fig. 2 is a comparison between the frequency response of the front surface displacement between the 1D model (1D-M), the 2D model of type I (2D-I), and the 2D model of type II (2D-II). The figure shows that the 1D-M and the 2D-I give almost identical frequency responses and the ceramics longitudinal resonance frequencies around 2.1 MHz and 6.6 MHz are predicted with both models. The 2D-II model is found to have a 2.9 dB lower peak at the 2.1 MHz resonance. For 2D-II simulation energy is seen to be transfered from the lower longitudinal resonance to radial resonances at lower frequencies. Note also that the concentration of the spectrum around the resonance at 2.1 MHz is lower compared to the prediction by 1D-M and 2D-I. The reason is conservation of energy in the system, which limits the energy concentration around the longitudinal resonance while transferring it to the ring- and radial modes.

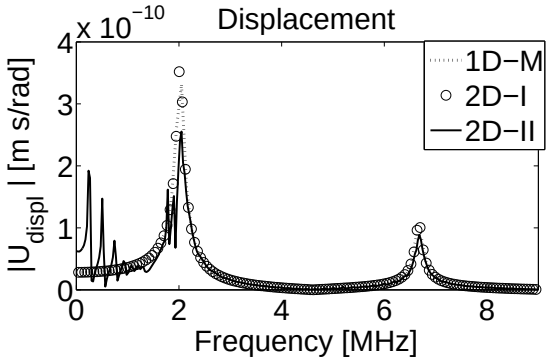

Fig. 2. Absolute value of the frequency response of the surface displacement. Black dotted line is the 1D model. Circles are the 2D-I. Solid line is the 2D-II.

Fig. 3 is a comparison between the different front surface accelerations predicted by each of the three models. The discussion of this comparison is similar to the above where good agreement between all models is obtained. The lower radial modes have been damped significantly compared to the longitudinal resonances which is due to the squared frequency components arising from a twice time derivation of the displacement solution i.e $(-\jmath\omega)^2 u_z$ (see (51)). A twice time differentiation is therefore seen to work as an amplifying filter for the higher frequencies where the lower frequencies are damped. The lower radial resonances are therefore expected to have limited effect on the pressure prediction in (48).

Fig. 4 is a comparison between the electrical impedances. A good consistency between all the models for frequencies above 1 MHz is found, whereas for below 1 MHz the radial resonances are seen to influence the response. Furthermore, for low frequencies an increase toward infinity in the impedance is found, which is in good agreement with theory. The ceramic is a dielectric

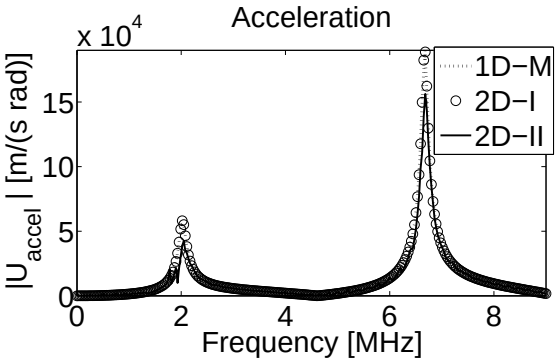

Fig. 3. Absolute value of the surface acceleration frequency response. Black dotted line is the 1D model. Circles are the 2D-I. Solid line is the 2D-II.

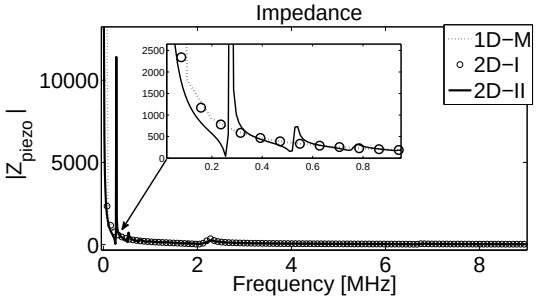

Fig. 4. Absolute electrical impedance frequency comparison between 1D and 2D with and without radial modes. Black dotted line is the 1D model. Circles are the 2D-I. Solid line is the 2D-II.

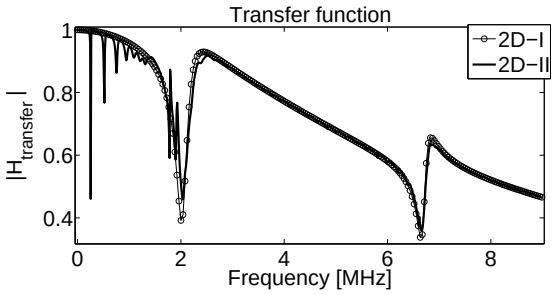

Fig. 6. Electrical transfer function of the loading network for free and restricted radial movement. Circles are the 2D-I. Solid line is the 2D-II.

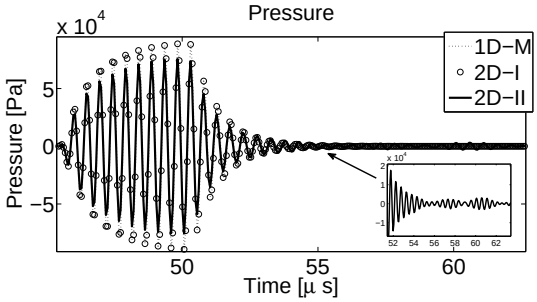

Fig. 7. Pressure comparison with loading network $Z_{external} = 50\ \Omega$. Black dotted line is the 1D model. Circles are the 2D-I. Solid line is the 2D-II.

material, which implies that the current through it has to be zero at its DC value. This also corresponds to an infinite big impedance, which is found in Fig. 4 for $frequency \rightarrow 0$.

Fig. 5a shows a pressure prediction 70 mm away from the transducer surface by using the Field II software. Prediction of the pressure using the 1D-M and the 2D-I is found to be very consistent here as well. They have the same amplitude and the same tail behavior. However, the 2D-II is found to have a 2.0 dB lower maximum amplitude and a faster attenuating tail compared to the two other models. This implies, that the ring material is absorbing energy from the longitudinal resonance, which also can be supported by considering Fig. 3. The smaller and discontinuous amplitude at the lowest longitudinal resonance in Fig. 3 supports this fact. The dashed squares marked A and B in Fig. 5 show the zooming areas for the subplots Fig. 5b and Fig. 5c. Fig. 5b shows a zoom of the three pulses' behavior at the end of the driving force period. From this it is clearly identified how well the 1D-M and the 2D-I are coinciding. Also the lower amplitude of 2D-II is clearly identified. Fig. 5c is a zoom that shows the different tail behavior of the 2D-II model. An extra ringing effect is found on this tail which is not found with the 1D-M and the 2D-I model.

Fig. 6 shows a comparison of the transfer function found in (31). This equation is only valid for the 2D models and it shows the frequency dependent amplification of the system. From this it can be found that the radial resonance frequencies may be amplified, by using proper driving frequencies.

Fig. 7 shows the resultant pressure simulation from applying the loading network on the 2D impulse response. It shows that the 1D-M and the 2D-I give consistent results as expected. However, it also shows that the 2D-II test case leads to a higher pulse amplitude relative to the 1D-M and 2D-I compared to Fig. 5, and the tail of the pulse also has a relatively higher amplitude compared to the two other models. This is different from what was seen in Fig. 5 where the tail of the 2D-II was ringing out relatively faster than the two other models did. The maximum peak pulse amplitude of the 2D-II model undershoots with 1.5 dB. Therefore due to the amplifying behavior of the radial frequencies found in the transfer function plotted in Fig. 6, the radial resonances transfer relatively more energy into the tail's ringing as seen in Fig. 7.

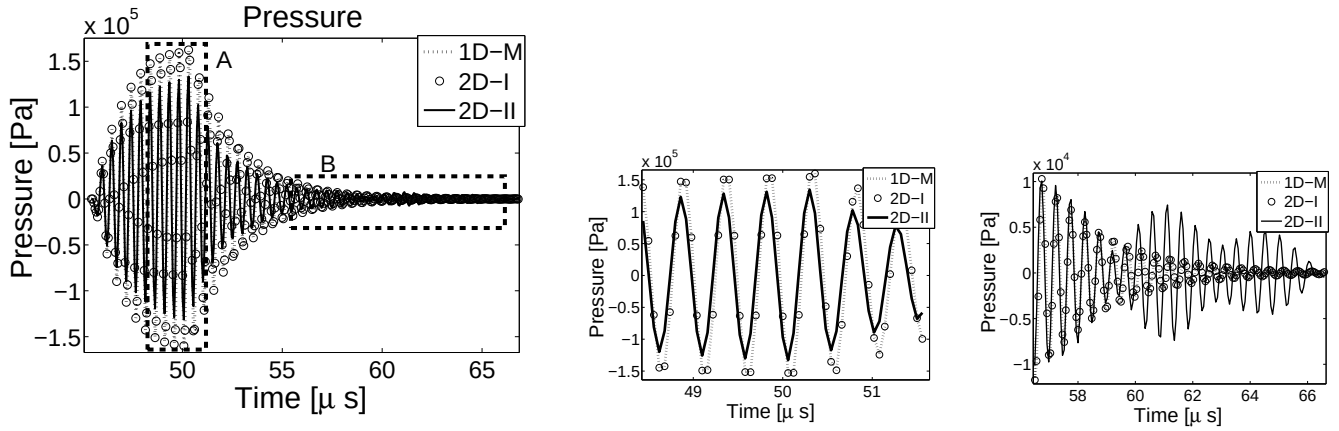

(a) Full view. (b) Zoom of A cut in (a). (c) Zoom of B cut in (a).

Fig. 5. Pressure comparison between 1D prediction, 2D prediction with locked radial boundary and 2D with free boundary. Black dotted line is the 1D model. Circles are the 2D-I. Solid line is the 2D-II. (a) is the full view pressure pulse. The dotted squares are the zoom areas of the subfigures (b) and (c).

VII. Discussion

In the previous section, it was found that the 2D model suggested by Schnabel [14] and the 1D modeling principle suggested by Willatzen [13] agree well in the prediction of the surface acceleration, displacement, and electrical impedance. Also the combination between Field II and the models was shown to give consistent results. This implies that the simple axisymmetrical model has a big potential for implementation into Field II, but it also validates the simple 1D model. An investigation of a proper meshing algorithm and a stable solver would therefore be a natural follow-up project. Clearly the amount of calculations for the 2D model is significant higher than for the 1D model. Each simulation in context with Field II should therefore critically consider whether the radial frequency components are needed. For Field II simulations, where the purpose is to verify the influence of changes in the electronic network on the 2D response, this model comes in handy, which is because the model can calculate the transducer's impedance response once and for all.

VIII. Conclusion

The one-dimensional model is shown to give similar results as compared to a three-dimensional axisymmetrical model when radial movement of the piezoceramic rim is restricted. When no radial restriction is applied a lower amplitude of the pressure pulses is found and the energy is seen transfered to the radial resonance modes. These modes are giving small pulse oscillations at the transducer tails. It has been shown that it is possible to calculate the impulse response of the volt-to-surface acceleration as well as the transducer's electrical impedance. These can next be applied to load the transducer with an electronic network. The obtained impulse responses can be used to investigate the behavior of the physical transducer as well.

References

[1] D. Bæk, J. A. Jensen, and M. Willatzen, "Testing of a one dimensional model for Field II calibration," in *Proc. IEEE Ultrason. Symp.*, Oct. 2008, pp. 1417–1420.

[2] ——, "Calibration of Field II using a convex ultrasound transducer," in *Proc. Int. Cong. on Ultrasonics*, Januar 2009.

[3] ——, "Modeling transducer impulse responses for predicting calibrated pressure pulses with the ultrasound simulation program Field II," *J. Acoust. Soc. Am.* ,vol. 127, no. 5, pp. 2825–2835, May 2009.

[4] J. A. Jensen, "Field: A program for simulating ultrasound systems," *Med. Biol. Eng. Comp.*, vol. 10th Nordic-Baltic Conference on Biomedical Imaging, Vol. 4, Supplement 1, Part 1, pp. 351–353, 1996b.

[5] J. A. Jensen and N. B. Svendsen, "Calculation of pressure fields from arbitrarily shaped, apodized, and excited ultrasound transducers," *IEEE Trans. Ultrason., Ferroelec., Freq. Contr.*, vol. 39, pp. 262–267, 1992.

[6] M. Redwood, "Transient performance of a piezoelectric transducer," *J. Acoust. Soc. Am.*, vol. 33, no. 4, pp. 527–536, April 1960.

[7] R. Krimholtz, D. Leedom, and G. Matthaci, "New equivalent circuits for elementary piezoelectric transducers," *Electr. Lett.*, vol. 6, no. 13, pp. 398–399, June 1970.

[8] Y. Kagawa and T. Yamabuchi, "Finite element simulation of a composite piezoelectric ultrasonic transducer," *IEEE Trans. Son. Ultrason.*, vol. SU-26, no. 2, pp. 81–88, March 1979.

[9] M. Brissaud, "Characterization of piezoceramics," *IEEE Trans. Ultrason., Ferroelec., Freq. Contr.*, vol. 38, no. 6, pp. 603–617, November 1991.

[10] ——, "Rectangular piezoelectric plate loaded on each face: a three dimensional approach," *Ultrasonics*, vol. 34, pp. 87–90, 1996.

[11] P. Marchal, F. Levarssort, L.-P. Tran-Huu-Hue, and M. Lethiecq, "Effects of acoustical properties of a lens on the pulse-echo response of a single element transducer," *IEEE Trans. Ultrason., Ferroelec., Freq. Contr.*, vol. 50th Joint Anniversary Conference, pp. 1651–1654, 2004.

[12] ——, "Lens-focused transducer modeling using an extended klm model," *Ultrasonics*, vol. 46, pp. 155–167, 2007.

[13] M. Willatzen, "Ultrasound transducer modeling - general theory and applications to ultrasound reciprocal systems," *IEEE Trans. Ultrason., Ferroelec., Freq. Contr.*, vol. 48, no. 1, pp. 100–112, January 2001.

[14] P. Schnabel, "Dispersion of thickness vibrations of piezoceramic disk resonators," *IEEE Trans. Son. Ultrason.*, vol. SU-25, no. 1, pp. 16–24, January 1978.

[15] B. A. Auld, *Acoustic Fields and Waves in Solids Volume 1*, 2nd ed. Malabar,Florida: Krieger Publishing Company, 1990.

[16] T. Amby, *Multiphysics Mathematical Modeling of Piezoelectric Transducers*, 2005, vol. Master Thesis, University of Southern Denmark, Sonderborg.

[17] "Comsol multiphysics user's guide, version: Comsol 3.4, comsol ab, 2008."

Paper V

Parameter sensitivity study of a Field II multilayer transducer model on a convex transducer

David Bæk, Morten Willatzen, and Jørgen Arendt Jensen

Proceedings of the IEEE International Ultrasonics Symposium

Presented in Rome, Italy, 2009

10.1109/ULTSYM.2009.0104

Parameter sensitivity study of a Field II multilayer transducer model on a convex transducer

David Bæk*, Jørgen Arendt Jensen*, and Morten Willatzen†
*Center for Fast Ultrasound Imaging, Department of Electrical Engineering, Technical University of Denmark
†Mads Clausen Institute for Product Innovation, University of Southern Denmark, 6400 Sønderborg, Denmark
Email: db@elektro.dtu.dk, jaj@elektro.dtu.dk, willatzen@mci.sdu.dk

***Abstract*—The influence of different model parameters describing a multilayer transducer model is addressed by altering each single simulation parameter within ± 20 % in steps of 2 % and by calculating the pressure and the intensity at a field point located 112 mm from the source. The simulations are compared with a hydrophone measured pressure pulse and intensity from a single element of a 128 element convex medical transducer. Results show that mainly the lens material and the ceramic material are of importance for errors in the pressure pulse prediction. Specifically the thickness, the density, and the stiffness constants are of significance. Among the results it is found that a -4 % change in lens stiffness yields a 6 % relative error change and a -4 % change in ceramic stiffness yields a -1.2 % relative error change. When calculating intensity the piezoceramic and electronic driving circuits are of importance, where a similar change in the lens and the ceramic stiffness shows a -0.1% and a -12% relative error change, respectively.**

I. Introduction

A transducer modeling principle has previously been developed and tested as a supplement to the Field II simulation software [1], [2], [3]. This modeling principle is a step towards calibrated intensity and pressure simulations using Field II [4], [5]. It was shown that the modeling principle is accurate within 0-2 dB for simulations on a simple piston model and a more advanced convex multilayered medical transducer [2], [6]. However, any exact prediction of the amplitude, phase, and attenuation tendency of the pressure pulses from complicated transducers is highly dependent on accurate knowledge of material constants as well as the electronic driving circuits. Such information is most often only known by manufacturers, and these may not even have an accurate estimate. This therefore influences transducer simulations [7], [8]. Also physical dimensions of the transducer, surface roughness, element cross talk, temperature, nonlinearity etc. are influencing the accuracy of the predictions. Previous studies [1], [2], [6] assumed knowledge of exact simulation parameters. However, small deviations in the predictions relative to the measured were found.

In this paper the influence of the different material parameters needed to represent a convex ultrasound transducer using the modeling principle used in [2] and [6] is investigated. The study is made by changing the different parameters of the transducer model within ± 20 % of the values calculated from manufacturer information. The influence is studied as the error of the pressure and the intensity predictions relative to measurements.

II. Theory

The model parameter study in this work is based on a 128 element convex medical transducer from BK Medical Aps. A cross section and a front view drawing in Fig. 1 illustrate how a single element of this transducer is build. A transducer element consists of a backing layer (B), a piezoceramic layer (P), a first matching layer (ML1), a second matching layer (ML2), and a lens (L) as seen in Fig. 1a. The transducer front is assumed to be lowered into water, wherefore the lens is in contact with the water (W). Fig. 1b shows a single element's front view dimensions. The transducer is assumed to be driven with a

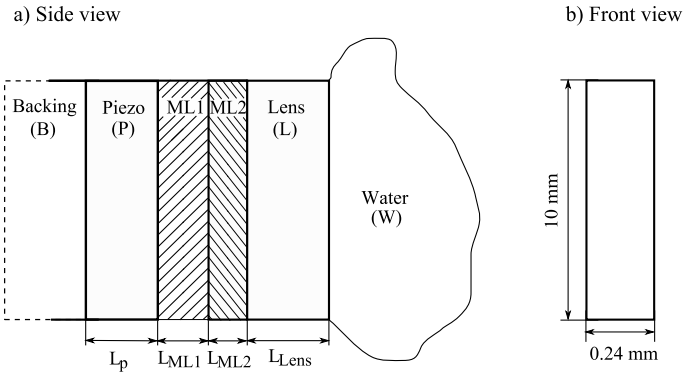

Fig. 1. Sketch of a single transducer element. a) Longitudinal cross section view. b) Front view of a single element.

transmitter unit from BK Medical placed inside our RASMUS [9] research scanner. Fig. 2 is a simplified representation of the driving electronic of such a setup. Clearly the driving circuit represented here is much less complicated than what is found in such scanner. However, by using the above simplification the complexity of the modeling is decreased.

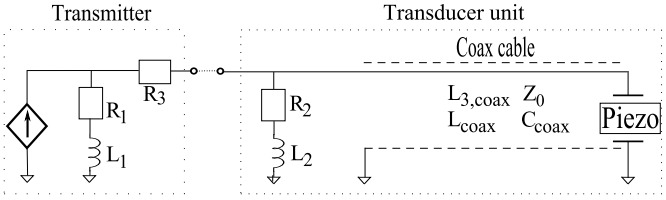

Fig. 2. Approximated electronic loading.

$$T_B = c_p^D (A_p + B_p) - hD, \quad (1)$$

$$\frac{T_B}{Z_B} = \frac{c_p^D}{Z_p} (A_p - B_p), \quad (2)$$

$$c_{ML1}^D (A_{ML1} + B_{ML1}) = c_p^D \left(A_p e^{-\jmath k_p L_p} + B_p e^{\jmath k_p L_p} \right) - hD, \quad (3)$$

$$\frac{c_{ML1}^D}{Z_{ML1}} (A_{ML1} - B_{ML1}) = \frac{c_p^D}{Z_p} \left(A_p e^{-\jmath k_p L_p} - B_p e^{\jmath k_p L_p} \right), \quad (4)$$

$$c_{ML2}^D (A_{ML2} + B_{ML2}) = c_{ML1}^D \left(A_{ML1} e^{-\jmath k_{ML1} L_{ML1}} + B_{ML1} e^{\jmath k_{ML1} L_{ML1}} \right), \quad (5)$$

$$\frac{c_{ML2}^D}{Z_{ML2}} (A_{ML2} - B_{ML2}) = \frac{c_{ML1}^D}{Z_{ML1}} \left(A_{ML1} e^{-\jmath k_{ML1} L_{ML1}} - B_{ML1} e^{\jmath k_{ML1} L_{ML1}} \right), \quad (6)$$

$$c_L^D (A_L + B_L) = c_{ML2}^D \left(A_{ML2} e^{-\jmath k_{ML2} L_{ML2}} + B_{ML2} e^{\jmath k_{ML2} L_{ML2}} \right), \quad (7)$$

$$\frac{c_L^D}{Z_L} (A_L - B_L) = \frac{c_{ML2}^D}{Z_{ML2}} \left(A_{ML2} e^{-\jmath k_{ML2} L_{ML2}} - B_{ML2} e^{\jmath k_{ML2} L_{ML2}} \right), \quad (8)$$

$$T_W = c_L^D \left(A_L e^{-\jmath k_L L_L} + B_L e^{\jmath k_L L_L} \right), \quad (9)$$

$$-\frac{T_W}{Z_W} = \frac{c_L^D}{Z_L} \left(A_L e^{-\jmath k_L L_L} - B_L e^{\jmath k_L L_L} \right), \quad (10)$$

$$-\jmath\omega V_+ + -\jmath\omega V_- = -\jmath\omega \frac{L_p}{\epsilon^S} D - \left[h \frac{c_{ML1}^D}{Z_{ML1}} (A_{ML1} - B_{ML1}) - h \frac{c_p^D}{Z_p} (A_p - B_p) \right], \quad (11)$$

$$-\jmath\omega AD = \frac{1}{Z_0} V_+ - \frac{1}{Z_0} V_-, \quad (12)$$

$$V(\omega) = \left(\frac{Z_g}{Z_0} + \frac{Z_g}{R_2 - \jmath\omega L_2} + 1 \right) V_+ e^{\jmath\gamma L_{coax}} + \left(-\frac{Z_g}{Z_0} + \frac{Z_g}{R_2 - \jmath\omega L_2} + 1 \right) V_- e^{-\jmath\gamma L_{coax}}. \quad (13)$$

Equations (1) to (13) [6] are used to model the transducer setup. The equations are to be solved for the unknown coefficients T_F, T_W, A_p, B_p, A_{ML1}, B_{ML1}, A_{ML2}, B_{ML2}, A_L, B_L, D, V_+, and V_-, by casting the equation system into matrix form and applying Matlab. The model assumes all layers to operate in their thickness modes only, (i.e. the 33 mode). The coefficients Z_B, Z_{ML1}, Z_{ML2}, Z_L, and Z_F are the acoustic impedances given by $Z_i = \rho_i \mathbf{v}_i$, where ρ and $\mathbf{v}$ are the material layer density and the speed of sound in complex form [3], respectively. The mechanical stiffness coefficients c_B^D, c_P^D, c_{ML1}^D, c_{ML2}^D, c_L^D, and c_W^D are used to calculate the real valued form of the speed of sound as $v_i^r = \sqrt{c_i^D / \rho_i}$. The complex valued form of the velocity is $v_i^r / (1 + \frac{\jmath\alpha_i v_i^r}{\omega})$, where α_i is the attenuation constant of the material [3]. The wave propagation constants k_P, k_{ML1}, k_{ML2}, and k_L account for attenuation and are given by $k_i = \omega / \mathbf{v}_i$, where ω is the angular frequency. The four layers P, $ML1$, $ML2$, and L have the thicknesses L_P, L_{ML1}, L_{ML2}, and L_L, respectively. Special constants for the ceramic are the piezoelectric coefficient h and the permittivity ϵ^S. The latter is accounting for dielectric losses through $\epsilon^S = \epsilon_r^S + \jmath\epsilon_r^S \tan(\delta)$, where ϵ_r^S is the real valued permittivity and $\tan(\delta)$ is the tangential loss factor [3]. The electronic network is represented with the coax cable having length L_{coax}, characteristic impedance Z_0. γ is the propagation constant defined as $\omega \sqrt{L_{3,coax} C_{coax}}$, where $L_{3,coax}$ and C_{coax} are the cable series inductance per unit length and the shunt capacitance per unit length. The impedance Z_g is given by $Z_g = R_1 + R_3 - \jmath\omega L_1$, where R_1, R_3, and L_1 are resistances and an inductance. R_2 and L_2 are a resistance and an inductance. The front cross sectional area, A, is given by the dimensions shown in Fig. 1b.

III. Measurements

The measurements of the pressure field from a single transmitting element is performed by submerging the transducer into a water bath and placing a needle hydrophone in front of it at a distance of approximately 112 mm. An Agilent MSO6014A oscilloscope was used to sample the measured pressure, and the transducer was driven at 4.0 MHz using the RASMUS system.

IV. Simulation

The Field II software was set up to represent the convex transducer using the command *xdc_convex_focused_array*. The sampling frequency was set to 400 MHz. The simulations in our previous works [2], [6] used a fixed parameter set calculated from manufacturer supplied informations. The latter parameters are used as the zero reference (ZR). All 35 parameters are altered in steps of 2 % within a limit of ± 20 % around their ZR value. When altering one parameter, the remaining parameters are held at the ZR. For each altering the root mean square (RMS) error is calcualted for the pressure and the intensity relative to the measured value. The pressure pulses are fixed in time, meaning that the cross correlation time that yields the lowest RMS error when using the ZR for simulation is aplied to all the pressure pulses where parameters differ from the ZR. To compare intensities the spatial peak pulse average is used.

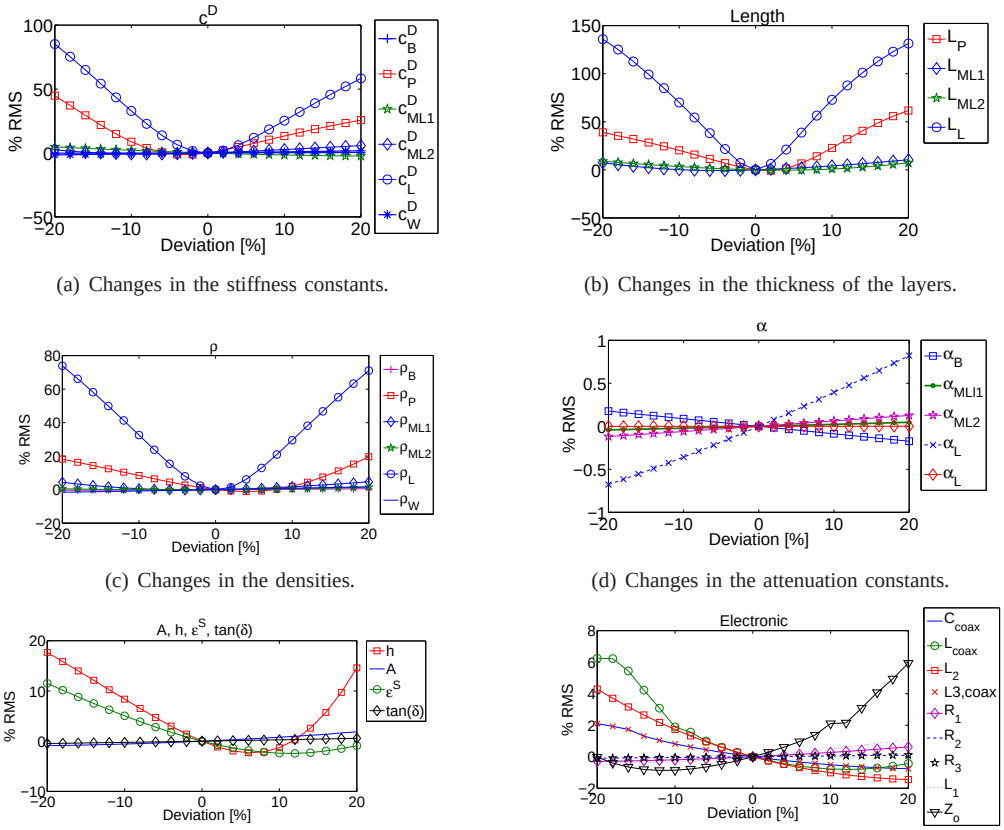

(a) Changes in the stiffness constants.

(b) Changes in the thickness of the layers.

(c) Changes in the densities.

(d) Changes in the attenuation constants.

(e) Changes in the element area, e^S, h and $tan(\delta)$.

(f) Changes in the electronic components.

Fig. 3. RMS errors when simulated pressure pulses are compared with measurements.

V. Results

Fig. 3a to 3d show the relative RMS errors in percent when subtracting simulated and measured pressure pulses from each other. The errors seen in the figures are all subtracted a $32.9\ \%$ RMS error being the RMS error when using the ZR model values. This results initially in a $0\ \%$ RMS for a $0\ \%$ altering of the parameters as shown in the figures. From the figures it is clearly identified that the model is mainly sensitive to the lens (subscript L) and the ceramic (subscript P) parameters. All other components have a relatively neglectibly small affect on the error. Additionally it can be concluded, that the stiffness, c_i^D, the length, L_i, and the density, ρ_i, are the important parameters of the materials. Obviously these three constants affect the phase of the simulated pulse through the propagation constants k_i. The attenuation constant is seen to affect the model linearly, however, the affect is small as shown in Fig. 3d.

Fig. 3e shows the RMS error of the pressure pulse comparison when changes to A, h, ϵ^S, and $\tan(\delta)$ are performed. From these results it is identified that the main factors are h and ϵ^S which both exhibit a non linear affect on the equations. Notice that the RMS error can even be lowered by $2.3-2.5\ \%$ RMS by increasing the values of these two parameters with $6-8\ \%$. Changes to the area, A, and the ceramics electrical damping are only of slight effect. Notice, however, that for the area, A, only the area in (12), and not the area set by defining the geometry in the Field II software, is altered. This is done because this study investigates the sensitivity of the transducer model describing the impulse response and not the Field II surface model and/or changes in the geometry. Clearly, the error would change if the area of the Field II elements where changed as well.

The errors in Fig. 3f indicate that changes in the electronic loading have an affect. However, the error is small compared to changes in the lens and the ceramic, and the affect on the model has a non linear tendency for most of the electronic parameters.

The last six plots, Fig. 4a to 4f, show the RMS intensity errors (IE). For IEs the exact phase requirements are not necessarily needed. The influencing factor is the energy of the pulse itself.

Fig. 4a to Fig. 4c reveal that the piezoceramic is affecting the error more than the lens material, which is different from the pressure pulse study. Also notice that the error is not more sensitive to lens parameters as compared to other transducer material parameters. The attenuation constant in Fig. 4d is an exception albeit the influence of errors in that parameter is relatively small. Fig. 4e shows the same tendency as Fig. 3e hence conclusions are the same. Fig. 4f shows that the

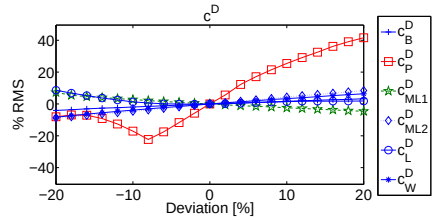

(a) Changes in the stiffness components and the intensity error.

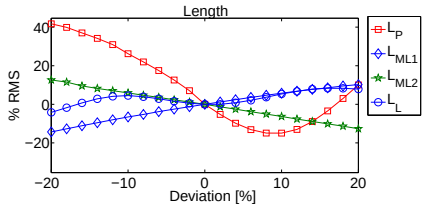

(b) Changes in the length components and the intensity error.

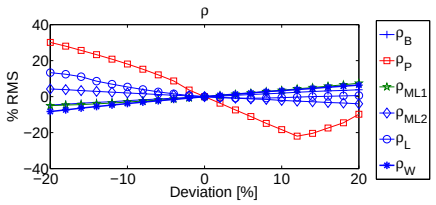

(c) Changes in the density components and the intensity error.

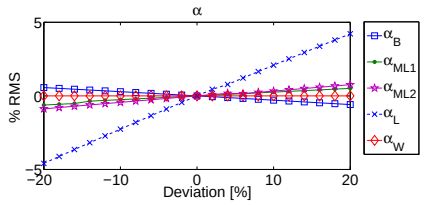

(d) Changes in the attenuation components and the intensity error.

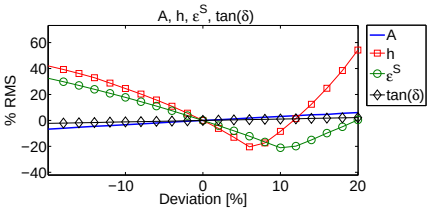

(e) Changes in the piezoelectric components and the intensity error.

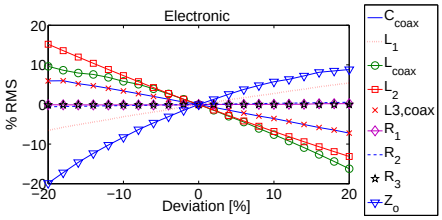

(f) Changes in the electronic components and the intensity error.

Fig. 4. RMS errors of the intensity when comparing simulation and measurements.

electronic components have increased their influences. The reason for this can be explained by the fact that the loading electronic mainly determines the clamped voltage across the piezoceramic more than influencing the phase of the pulse. This is also why it theoretically is possible to generate a zero error for the intensity with these parameters. By studying the figures quantitatively it can be found that a RMS PPE of approximately 6 % for -4 % stiffness change of the c_L^D and a PPE of approximately -1.2 % for a -4 % change c_P^D are found. A slight error improvement is therefore achieved by changing c_P^D. The same study for the RMS IE is -0.1 % and -12 % for c_L^D and c_P^D, respectively. Note also c_P^D in Fig. 4a, where a -8 % change improves the IE by -22.3 %. Similar tendencies are found for L_P and ρ_P in Fig. 4b-c. This indicates that it is possible to approach the measured energy by changing these parameters. However, this may result in an increasing PPE.

VI. Conclusion

By altering the different model parameters one at a time it is determined that for PPE calculations of simulated pressure relative to the measured the model exhibits highest sensitivity to the piezoceramic and the lens parameters. Mainly the stiffness, the thickness, and the density of these two layers are of importance. The remaining parameters were seen to have much less influence on the PPE. When comparing the RMS IE the lens became of less significance but the piezoceramic is still influential. Also the electronic network has a significant influence on the IE.

References

[1] D. Bæk, J. A. Jensen, and M. Willatzen, "Testing of a one dimensional model for Field II calibration," in *Proc. IEEE Ultrason. Symp.*, Oct. 2008, pp. 1417–1420.

[2] D. Bæk, J. A. Jensen, and M. Willatzen, "Calibration of Field II using a convex ultrasound transducer," in *Proc. Int. Cong. on Ultrasonics*, 2009, p. Under review.

[3] M. Willatzen, "Ultrasound transducer modeling - general theory and applications to ultrasound reciprocal systems," *IEEE Trans. Ultrason., Ferroelec., Freq. Contr.*, vol. 48, no. 1, pp. 100–112, January 2001.

[4] J. A. Jensen, "Field: A program for simulating ultrasound systems," *Med. Biol. Eng. Comp.*, vol. 10th Nordic-Baltic Conference on Biomedical Imaging, Vol. 4, Supplement 1, Part 1, pp. 351–353, 1996b.

[5] J. A. Jensen and N. B. Svendsen, "Calculation of pressure fields from arbitrarily shaped, apodized, and excited ultrasound transducers," *IEEE Trans. Ultrason., Ferroelec., Freq. Contr.*, vol. 39, pp. 262–267, 1992.

[6] D. Bæk, J. A. Jensen, and M. Willatzen, "Modeling transducer impulse responses for predicting calibrated pressure pulses with the ultrasound simulation program Field II," *J. Acoust. Soc. Am.*, p. Submitted, 2009.

[7] M. Brissaud, "Characterization of Piezoceramics," in *IEEE Trans. Ultrason., Ferroelec., Freq. Contr.*, vol. 38, 1991, pp. 603-617.

[8] A. Ruz, A. Ramos, and J.L. San Emeterio, "Estimation of some transducer parameters in a broadband piezoelectric transmitter by using an artificial intelligence technique," in *Ultrasonics*, vol. 40, 2004, pp. 459-463.

[9] J. A. Jensen, O. Holm, L. J. Jensen, H. Bendsen, H. M. Pedersen, K. Salomonsen, J. Hansen, and S. Nikolov, "Experimental ultrasound system for real-time synthetic imaging," in *Proc. IEEE Ultrason. Symp.*, vol. 2, 1999, pp. 1595–1599.

Paper VI

Testing of a one dimensional model for Field II calibration

David Bæk, Morten Willatzen, and Jørgen Arendt Jensen

Proceedings of the IEEE International Ultrasonics Symposium

Presented in Beijing, China, 2008

Digital Object Identifier: 10.1109/ULTSYM.2008.0344

Testing of a one dimensional model for Field II calibration

David Bæk*, Jørgen Arendt Jensen*, and Morten Willatzen†
*Center for Fast Ultrasound Imaging, Department of Electrical Engineering, Technical University of Denmark
†Mads Clausen Institute for Product Innovation, University of Southern Denmark, 6400 Sønderborg, Denmark,
Email: db@elektro.dtu.dk, jaj@elektro.dtu.dk, willatzen@mci.sdu.dk

***Abstract*—Field II is a program for simulating ultrasound transducer fields. It is capable of calculating the emitted and pulse-echoed fields for both pulsed and continuous wave transducers. To make it fully calibrated a model of the transducer's electro-mechanical impulse response must be included. We examine an adapted one dimensional transducer model originally proposed by Willatzen [9] to calibrate Field II. This model is modified to calculate the required impulse responses needed by Field II for a calibrated field pressure and external circuit current calculation. The testing has been performed with Pz27 piezoceramic discs from Ferroperm Piezoceramics A/S, Kvistgaard, Denmark. The transmitted acoustic pressures from two sets of each five disc samples with 10.08 mm diameters were measured in an automatic water bath needle hydrophone setup together with the current flow through the driving circuit. Resonance frequencies at 2.1 MHz and 4 MHz were applied. Two types of circuits were considered, one circuit with a simple resistance load of $47.5\ \Omega$ and one with an example of a LR tuning circuit typically found in commercial transducers. The measurements were averaged 128 times and afterwards compared to the calibrated Field II program for 1, 4, and 10 cycle excitations. Two parameter sets were applied for modeling, one real valued Pz27 parameter set, manufacturer supplied, and one complex valued parameter set found in literature, Algueró et al. [11]. The latter implicitly accounts for attenuation. Results show that the combination of the model and Field II can calculate the pressure within -15 % to 5 % RMS error for long excitation bursts and 7 % to 23 % for short excitation bursts. Furthermore it is shown that current simulations can be done within 1 % to maximum 33 % RMS error, where best current simulations are found for 4 MHz long burst simulations and worst case is found for 2.1 MHz short bursts. Finally it is shown that maximum pressure deviation for the real parameter set and the complex parameter simulation is 3 % for pressure and 5.3 % for current.**

I. Introduction

The ultrasound simulation program Field II [1], [2] has been developed to calculate the scattered pressure field from inhomogeneous tissue in front of a transducer. The field calculations are based on time convolutions between the transducer's surface acceleration and spatial impulse responses [2]. To predict the actual pressure level from the convolution by Field II, the transducer's 1D electro-mechanical impulse response needs to be either measured or calculated by a mathematical model.

Models for 1D piezoelectric transducers have been presented in early papers such as those by Mason [3], Redwood [4], or Krimholtz et al. [5] and extensively used and expanded in later works. Some later references which employ these electrical equivalent circuits (EEC) models, are papers with emphasis on EEC multilayer transducers [6], [7], [8], which implies that 1D transducer modeling is a standard tool as of today. However, 1D EEC models hide, to some extent, the real electro-acoustics relationship, the time and position dependent stresses, strains and electric field of the transducer and the influence of the real physical quantities such as stiffness and dielectricity are not easily found.

Willatzen [9], [10] has proposed a multilayered 1D model based on the basic equations of electro-acoustics, where the electrical network is included as an impedance loading. The model may be of special interest for transducer development since the real physical state can be found directly as a function of time and position together with the influence of the physical piezoelectric quantities. The model thus has an interesting advantage in calibrating Field II.

This paper investigates the usability of the model for simulating the pressure and current response of a single piezoceramic transducer mounted with silver electrodes and submerged into water by combining it with Field II. We compare the calculated pressure and current with measured values. Two electronic networks are considered for loading, a single $47.5\ \Omega$ resistor in series with the piezoceramic and a LR network typically found in medical transducers. Pz27 ceramic discs from Ferroperm Piezoceramics A/S, Kvistgaard, Denmark, are applied for simulations and measurements because of manufacturer available parameters, which are real valued, and complex valued parameters found by Algueró et al. [11] that implicitly include losses.

II. Theory

By following the method suggested in [9] and by applying circuit analysis as described in Johnson [12] for the circuit diagram in Fig. 1 and the transducer setup in Fig. 2, one obtain (1) - (10).

In these equations subscripts Ag,p denote the silver and ceramic material respectively and it is assumed that the silver thicknesses, L_{Ag}, are identical on each side of the piezoceramic. $c^D_{Ag,p}$ are the stiffness constant, $Z_{Ag,p,Front,Back}$ are the acoustic impedance of the different medias given by $Z = \rho v$, where v is the wave velocity and ρ the density. $k_{Ag,p}$ are the wave propagation constants defined by $k = \frac{\omega}{v}$, and ω is the radial frequency. The piezoelectric constant h is defined as $\frac{e_{33}}{\epsilon^S}$, where e_{33} and ϵ^S are the piezoelectric coupling coefficient

$$
\begin{aligned}
T_{Back} &= c_{Ag}^{D}\left(A_{Ag,1}+B_{Ag,1}\right), && (1)\\
\frac{T_{Back}}{Z_{Back}} &= \frac{c_{Ag}^{D}}{Z_{Ag}}\left(A_{Ag,1}-B_{Ag,1}\right), && (2)\\
c_{p}^{D}\left(A_{p}+B_{p}\right)-hD &= c_{Ag}^{D}\left(A_{Ag,1}e^{-\jmath k_{Ag}L_{Ag}}+B_{Ag,1}e^{\jmath k_{Ag}L_{Ag}}\right), && (3)\\
\frac{c_{p}^{D}}{Z_{p}}\left(A_{p}-B_{p}\right) &= \frac{c_{Ag}^{D}}{Z_{Ag}}\left(A_{Ag,1}e^{-\jmath k_{Ag}L_{Ag}}-B_{Ag,1}e^{\jmath k_{Ag}L_{Ag}}\right), && (4)\\
c_{Ag}^{D}\left(A_{Ag,2}+B_{Ag,2}\right) &= c_{p}^{D}\left(A_{p}e^{-\jmath k_{p}L_{p}}+B_{p}e^{\jmath k_{p}L_{p}}\right)-hD, && (5)\\
\frac{c_{Ag}^{D}}{Z_{Ag}}\left(A_{Ag,2}-B_{Ag,2}\right) &= \frac{c_{p}^{D}}{Z_{p}}\left(A_{p}e^{-\jmath k_{p}L_{p}}-B_{p}e^{\jmath k_{p}L_{p}}\right), && (6)\\
T_{Front} &= c_{Ag}^{D}\left(A_{Ag,2}e^{-\jmath k_{Ag}L_{Ag}}+B_{Ag,2}e^{\jmath k_{Ag}L_{Ag}}\right), && (7)\\
-\frac{T_{Front}}{Z_{Front}} &= \frac{c_{Ag}^{D}}{Z_{Ag}}\left(A_{Ag,2}e^{-\jmath k_{Ag}L_{Ag}}-B_{Ag,2}e^{\jmath k_{Ag}L_{Ag}}\right) && (8)\\
-\jmath\omega V(\omega) &= -\left(z_{e}\omega^{2}A+\jmath\omega z_{x}\frac{L_{p}}{\epsilon^{S}}\right)D+hz_{x}\frac{c_{p}^{D}}{Z_{p}}\left(A_{p}-B_{p}\right)+hz_{x}\frac{c_{Ag}^{D}}{Z_{Ag}}\left(B_{Ag,2}-A_{Ag,2}\right), && (9)\\
z_{e}=\delta(i)\frac{R1R2}{(R3-\jmath wL)} &+ R1+R2 \quad , z_{x}=1+\delta(i)\frac{R1}{(R3-\jmath wL)}. && (10)
\end{aligned}
$$

for stress-charge form and the electrical permitivity under constant strain, respectively. $R1, R2, R3$ are passive resistors, and L is an inductor. The switch d on Fig. (1) is accounted for by the unit delta function δ in (10). d makes it possible to choose between LR tuned circuits and a simple resistor loop.

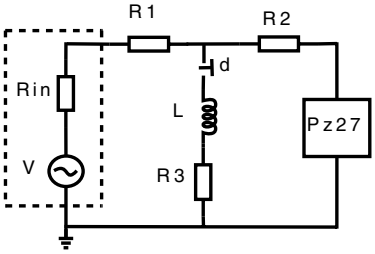

Fig. 1. Electronic circuit systems.

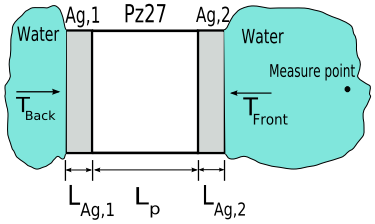

Fig. 2. Model of transducer setup.

As driving source, a Fourier transform of a tone burst, $V(\omega)$, is applied. The unknown T_{Front} and T_{Back} variables are the tensions on the transducers front and back plane respectively, and D is the unknown electric displacement. Furthermore, $A_{Ag,i}$, $B_{Ag,i}$, A_p and B_p are unknown complex coefficients in the general expression for the particle velocity [9]:

$$u(z,t) = \frac{c^{D}}{Z}\left[Ae^{-\jmath kz-\jmath\omega t}-Be^{\jmath kz-\jmath\omega t}\right]. \quad (11)$$

By time differentiating the particle velocity on the front surface of the transducer, the surface acceleration is found, whereby the field pressure can be found through the Field II convolution

$$p(\vec{r},t)=\rho\frac{\partial u}{\partial t}*h(\vec{r},t), \quad (12)$$

where $\vec{r}$ and $h(\vec{r},t)$ are the spatial coordinate and the spatial impulse response, respectively, as defined in Field II [2] .

The nine unknown variables: $A_{Ag,1}$, $B_{Ag,1}$, $A_{Ag,2}$, $B_{Ag,2}$, A_p, B_p, T_{Front}, T_{Back} and D are solved by using MATLAB.

To account for losses in the ceramic we apply two approaches. The first approach is to use complex values for c_p^D, ϵ^S, h found in the article by Algueró et al. [11]. This article lists an experimental estimation of several parameters in complex form which implicitly accounts for acoustic losses. The second approach is to model losses by including a complex propagation constant as suggested in [9]. This is done by deriving a complex speed of sound by converting the propagation constant from real form to complex form as $k \rightarrow \bar{k} = k^r + \jmath\alpha$, where $k^r = \frac{\omega}{v^r}$ and v^r is the real velocity. The attenuation constant α approximates mechanical losses in narrow band transducers [9] and has the units [1/m]. The evaluation of the complex propagation constant can be made by calculating a complex speed of sound

$$\bar{v}=\frac{\omega}{\bar{k}}=\frac{\omega}{k^r+\jmath\alpha}=\frac{v^r}{1+\frac{\jmath\alpha v^r}{\omega}}, \quad (13)$$

and then substituting the propagation constant for each material layer with a complex one $\bar{k}=\frac{\omega}{\bar{v}}$. Dielectric losses in the piezoceramic can be accounted for by substituting the real valued dielectric constant ϵ with the complex one $\epsilon + \jmath\tan\delta$ in (9), where $\tan\delta$ is the dielectric loss factor.

TABLE I

RMS ERROR IN PERCENT FOR THE MODEL AND MEASUREMENTS RELATIVE TO THE MEAN OF THE MEASUREMENTS USING 1,4, AND 10 CYCLE EXCITATIONS AT 2.1 MHZ AND 4 MHZ RESONANCE FREQUENCIES AND EITHER SIMPLE RESISTANCE AS CIRCUIT OR A LR CIRCUIT.

R1 only:	1 cycle excitation			4 cycle excitation			10 cycle excitation		
	Real	Measured	Complex	Real	Measured	Complex	Real	Measured	Complex
Current 2.1 MHz	36.0	3.2	35.5	24.9	4.8	25.4	17.1	3.7	17.9
Current 4 MHz	29.0	12.1	25.3	16.0	9.9	14.3	9.8	7.7	8.6
Pressure 2.1 MHz	37.0	10.0	36.4	24.6	8.5	23.9	15.0	8.5	15.8
Pressure 4 MHz	19.0	25.3	18.0	13.7	24.8	14.1	10.4	25.8	10.7
LR circuit:									
Current 2.1 MHz	49.0	4.5	43.7	34.0	4.0	33.6	21.5	4.3	22.5
Pressure 2.1 MHz	30.1	9.6	33.1	21.1	7.7	19.0	11.5	7.0	12.5

III. NUMERICAL SIMULATION

The numerical simulations are highly dependent on accurate model parameters. Piezoceramic manufacturer supplied parameters and estimated parameters from the paper of Algueró et al. [11] are used. Parameters for the silver electrodes are found by consulting a Ferroperm material database. Table II lists the simulation parameters for the real valued data set simulation and for the complex valued simulation.

TABLE II
MODEL PARAMETERS FOR PZ27.

	Real case	Complex case	
ρ	7700	7700	$\frac{\text{kg}}{\text{m}^3}$
c_{p}^D	$1.44{\cdot}10^{11}$	$[(813.9{+}\jmath 0.113) \pm (0.7{-}\jmath 0.006)]{\cdot}10^{10}$	$\frac{\text{N}}{\text{m}^2}$
h	$1.98{\cdot}10^9$	$[(21.0+\jmath 0.148) \pm (0.4-\jmath 0.004)]{\cdot}10^8$	$\frac{\text{V}}{\text{m}}$
ϵ^S	$9.14{\cdot}10^2\epsilon_0$	$[(822-\jmath 10.3) \pm (12-\jmath 0.4)]\cdot\epsilon_0$	$\frac{\text{F}}{\text{m}}$
$\tan\delta$	0.017	0.017	
ρ_{Ag}	10600	10600	$\frac{\text{kg}}{\text{m}^3}$
c_{Ag}^D	$1.1265{\cdot}10^{11}$	$1.1265{\cdot}10^{11}$	$\frac{\text{N}}{\text{m}^2}$
ρ_{W}	1000	1000	$\frac{\text{kg}}{\text{m}^3}$
c_{W}^D	$2.1904{\cdot}10^9$	$2.1904{\cdot}10^9$	$\frac{\text{N}}{\text{m}^2}$

Velocities and stiffness constants are calculated from $v = \sqrt{\frac{c^D}{\rho}}$. The thickness of a silver layer, L_{Ag}, is estimated by manufacturer to 9 μm, the radius of the discs are estimated to 5.04 mm, and the ceramic thicknesses are 0.94 mm and 0.5 mm giving a 2.1 MHz and a 4 MHz resonance frequency, respectively.

The attenuation constant α for the real valued data set is to be approximated by $\alpha = \frac{\pi}{Q_m \lambda}$ [9], giving $\alpha_{2.1\text{ MHz}} = 19\frac{1}{\text{m}}$ and $\alpha_{4\text{MHz}} = 36\frac{1}{\text{m}}$ when $Q_m = 80$ is the mechanical quality factor and λ is the acoustic wavelength.

The electronic loading for purely resistance loading, i.e $\delta(i \neq 0)$, $R1$ and $R2$ were chosen to be $47.5\ \Omega$ and $0\ \Omega$ respectively, whereas for the LR tuning circuit test, $\delta(i = 0)$, the components were set to $L = 6.1\ \mu H$, $R1 = 47.5\ \Omega$, $R2 = 75.6\ \Omega$, and $R3 = 10.3\ \Omega$. The internal resistance, Rin, of the generator was $50\ \Omega$. All values was chosen in the range of what can be expected in a commercial transducer.

Field II was set up to calculate the point pressure field using its piston model, with mathematical square element sizes of 0.1 mm times 0.1 mm. The sampling frequency was set to 600 MHz and convergence was found for the model in the sense that insignificant amplitude and phase changes were found.

IV. EXPERIMENTAL SETUP

An automatic water tank needle hydrophone setup was set up to measure the field pressure. Current flow through the driving circuit was measured through R1. The ceramics were mounted in a specially made slot that ensured identical mounting position at sample exchange. The acquisitions and excitations were performed with an Agilent MSO6014A oscilloscope and an Agilent 33220A Function Generator that supplied a 10.4 Vpp excitation burst. The measurements were averaged 128 times to minimize measurement noise. Five discs at resonance frequencies of 2.1 and 4 MHz were measured with burst excitations of $1, 4$, and 10 cycles.

V. RESULTS

The mean of five measurements and the corresponding simulations with 1 cycle excitation at 2.1 MHz when the LR-network is applied are plotted in Fig. 3 and Fig. 4 for current and pressure, respectively. These figures show the model's

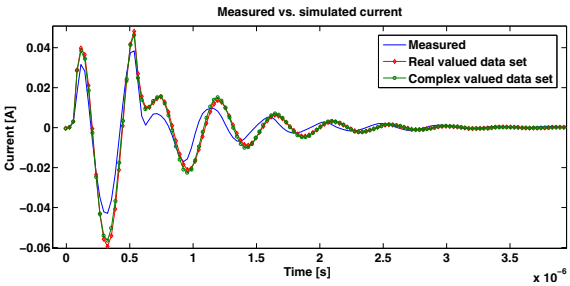

Fig. 3. Simulated and measured current through R1 for 1 cycle excitation.

general ability to predict the waveforms for short bursts. The model exhibits a limited capability in capturing the correct phase on the pulse tails, and it shows an acceptable capability to represent the main excitation period. Also the pressure levels calculated by Field II are seen to be consistent with the mean of the measurements in Fig. 4. However, to account for the hydrophone area we found it necessary to lower the measurements 3.5 dB from what the calibration chart implies, which is a consequence of the Field II's point calculation.

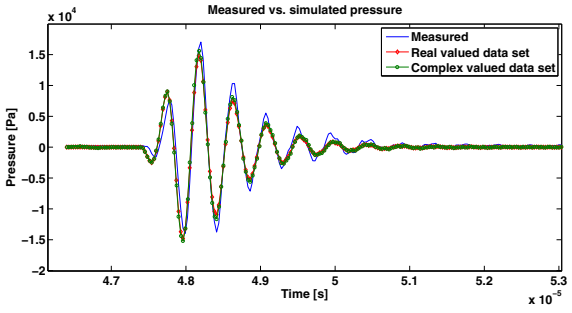

Fig. 4. Calculated and measured pressure at a point 70 mm from the transducer surface.

A quantisation of the model's accuracy when applying the two data sets for the two disc thicknesses, 0.94 mm and 0.5 mm, using one of the two types of electronic circuits is presented in Table I. The table shows the RMS error in percentage of the simulations and measurement samples relative to the mean of the five measurements at 2.1 and 4 MHz respectively. The two data sets for simulation were lowered with 2.5 % in density for both sample types and -0.03 mm in thickness for the 4 MHz samples to achieve the best pulse behaviour. These values are within the manufacturers tolerances and can therefore be considered acceptable.

From Table I it can be concluded that current measurements were performed relatively stable, within $3-12$ % deviation, and pressure measurements were fluctuating significantly more, within $7-26$ %. The latter indicates the difficulty in achieving a consistent point measurement with a needle hydrophone in front of the piezoceramics. Furthermore, the table expresses a clear consistency between simulation with the two parameter sets, found only to differ within $0-8$ %. These results indicate that the estimated values for attenuation, α, may be acceptable ones to use.

It should be noticed that the current simulations are differing relatively more from measurements than the pressure simulations are from corresponding measurements. This is due to pulse tails and transients, which are rapidly changing or drifting for current measurements. An ability that should be considered a model weakness.

The LR circuit simulation is found to exhibit errors at the same level as the simple circuit configuration which demonstrates the validity of the LR circuit model.

Finally, the table reveals that the model performs best in capturing long bursts, which is seen on the increase in error as the pulses get shorter for both current and pressure. The reason is due to generally slight overshoots on transients and pulse tail drifts, which affect the error calculation on short pulses significantly.

It is noticeable that simulation errors can be smaller than measured errors as was the case for the 4 MHz simulation.

VI. Conclusion

The presented research has shown the importance of applying the correct data sets for this one dimensional model. A need to adjust the density constant to "calibrate" the model to the measurement envelope form were found. As a result the model performs best for long burst excitations. The one dimensional model coupled with Field II was found to perform best when calculating the field pressure. Here, simulation errors lower than experimental errors were found. Current measurements, however, were found to exhibit a slightly higher degree of error. Both the complex and the real valued data set were seen to give almost the same simulation results, only differing within 8 %.

Thus, the model is concluded to work well with both parameter sets.

Acknowledgment

The authors would like to thank Dr. Erling Ringgaard, Ferroperm Piezocermics A/S, Kvistgård, Denmark, for delivering the piezoceramic samples and supplying data sets as well as giving support in the discussions.

References

[1] J.A. Jensen, " Field: A program for simulating ultrasound systems, paper presented at the 10th Nordic-Baltic Conference on Biomedical Imaging Published in Medical & Biological Engineering & Computing", pp. 351-353, Volume 34, Supplement 1, Part 1, 1996.

[2] J.A. Jensen and N.B. Svendsen, "Calculation of pressure fields from arbitrarily shaped, apodized, and excited ultrasound transducers", IEEE Trans. Ultrason., Ferroelec., Freq. Contr., 39, pp. 262-267, 1992.

[3] W.P. Mason, "Electromechanical Transducers and Wave Filters", 2nd ed. D. Van Nostrand Company, Inc. 1948, p.205.

[4] M. Redwood, "Transient performance of a piezoelectric transducer", J. Acoust. soc. Amer., vol 33, pp 527-536.

[5] R. Krimholtz, D.A. Leedom, and G.L. Matthaci, "New equivalent circuits for elementary piezoelectric transducers", Electron. Letter., vol 6, pp 398-399, 1970.

[6] M. Castillo, P. Acevedo, and E. Moreno, "KLM model for lossy piezoelectric transducers", Ultrasonics, vol 41, pp 671-679, 2003.

[7] P. Marechal, F. Levassort, L.-P. Tran-Huu-Hue, and M. Lethiecq, "Effect of acoustical properties of a lens on the pulse-echo response of a single element transducer", 2004 IEEE International Ultrasonics, Ferroelectrics, and Frequency Control Joint 50th Anniversary conference

[8] P. Marechal, F. Levassort, L.-P. Tran-Huu-Hue, M. Lethiecq, "Lens-focused transducer modeling using an extended KLM model", Ultrasonics, vol. 46, pp. 155-167, 2007.

[9] M. Willatzen, "Ultrasound transducer modeling-general theory and applications to ultrasound reciprocal systems" IEEE Trans. Ultrason., Ferroelec., Freq. Contr., vol. 48, pp. 100-112, 2001.

[10] M. Willatzen, "Ultrasound transducer modeling-received voltage signals and the use of half-wavelength window layers with acoustic coupling layers", IEEE Trans. Ultrason., Ferroelec., Freq. Contr., vol. 46, No. 5 pp. 1164-1174, 1999.

[11] M. Algueró, C. Alemany, and L. Pardo, "Method for obtaining the full set of linear electric, mechanical and electromechanical coefficients and all related losses of a piezoelectric ceramic", J. Am. Ceram. Soc, 87, pp 209-215, 2004.

[12] D.E. Johnson, J.R. Johnson, J.L. Hilburn, and P. D. Scott, Electric circuit analysis, 3rd ed. John Wiley and Sons, Inc, 1997.

Paper VII

Calibration of Field II using a convex ultrasound transducer

David Bæk, Jørgen Arendt Jensen, and Morten Willatzen

Proceedings of the International Congress on Ultrasonics

Presented in Santiago, Chile, Jan. 2009

Available online at www.sciencedirect.com
ScienceDirect
Physics Procedia 3 (2010) 995–1001
Physics Procedia
www.elsevier.com/locate/procedia

International Congress on Ultrasonics, Universidad de Santiago de Chile, January 2009

Calibration of Field II using a convex ultrasound transducer

David Bæk[a,*], Jørgen Arendt Jensen[a], and Morten Willatzen[b]

[a] *Technical University of Denmark, DTU-Elektro, Ørsteds Plads Build. 349, 2800 Kgs.Lyngby, Denmark*
[b] *University of Southern Denmark, Mads Clausen Institute for Product Innovation, Alsion 2 Alsion, 6400 Sønderborg, Denmark*

Abstract

Field II is an ultrasound simulation program capable of simulating the pressure scattering from inhomogeneous tissue. The simulations are based on a convolution between spatial impulse responses from the field in front of the transducer and the volt-to-surface acceleration impulse response of the transducer. For such simulations to reflect actual measured intensities and pressure levels, the transducer impulse response is to be known. This work presents results of combining a modified form of a 1D linear transducer model originally suggested by Willatzen together with the Field II program to calibrate the pressure and intensity simulations of a 128 element convex medical transducer with elevation focus at 70 mm. The simulations are compared to pressure measurements from a transducer driven at 4.0 MHz using a research scanner with a commercial transducer amplifier from BK Medical (Herlev, Denmark). As input waveform to the Field II model we measured the output voltage of the research amplifier. The peak voltage was limited to 31 V to avoid too high non-linear effects. We measured the hydrophone output from three transducer front elements by averaging 40 shoot sequences on each element using a remotely controlled Agilent MSO6014A oscilloscope. The pressure along the center line in a distance of 33 mm, 72 mm, and 112 mm from each element was measured as well as the intensity in the elevation plane in each depth.
Results show that the 1D modeling of the linear transducer impulse response predicts the pulse waveforms satisfying. We show a root mean square error of approximately 26 % on the pressure prediction and a root mean square error on the intensity prediction from 5.8-16.2 % from 72 mm to 112 mm, and an average of 15.4 % at 33 mm, when a 1.7 dB amplitude correction is made.

Keywords: Field II calibration; calibrated measurement; convex transducer; transducer impulse response

1. Introduction

Field II [1, 2] is a simulation software for simulating the pressure as well as the pulse-echo response in front of a medical ultrasound transducers. The results of a Field II simulation have proven to predict consistent results with measurements [3]. However, to do intensity simulations, non-normalized pressure and pulse-echo simulations with a medical transducer the exact impulse response of each transducer element has to be known on forehand. These impulse responses are most often seen approximated by weighted tone bursts or direct measurements when applied in Field II simulations. Impulse responses are also seen approximated with extensions of one dimensional models

* Corresponding author. Tel.:+45 45-25-39-15.
E-mail address: db@elektro.dtu.dk.

doi:10.1016/j.phpro.2010.01.128

such as those presented in early papers by Mason [4], Redwood [5], or Krimholtz et al. [6], which are all based on electrical equivalent circuit (EEC) models. These models, however, to some extent, hide the time and position dependent stresses, strains, and electric field of the transducer. Furthermore, the influence of the real physical quantities such as stiffness and dielectricity are not easily found.

We have previously shown [3] that a modified version of a 1D transducer modeling principle originally presented by Willatzen [7] works well together with Field II for circular piston models. This model does not rely on equivalent circuits of the acoustics and it can provide displacement, velocity and acceleration to any point in a multi layered transducer assumed operating in longitudinal mode. Simulation of complex medical transducers requires, however, usually full knowledge of transducer material properties as well as the electronic loading network which complicates the modeling of such transducers.

In this paper we investigate the usability of the 1D model we applied for circular pistons [3] together with Field II for simulating the pressure and intensity in front of a 128 element convex array transducer by having knowledge of manufacturer supplied transducer parameters of the acoustic layers and by assuming a simplified version of the electronic transmit network. We compare hydrophone measurements along the center axis of three elements as well as the intensity profile in the elevation plane in front of these elements with simulation results.

2. Theory

Each element of the 128 element convex transducer consists of a backing material, a piezo element, two matching layers and a lens. Furthermore, each transducer element measures 10 mm x 0.24 mm in elevation height and width. Each transducer element area is sub-diced into two columns of 0.1 mm x 0.1 mm smaller elements. The geometrical setup is shown in Fig. 1.

We use our 1D transducer model in the same manner as found in previous works [3, 7], i.e., a set of linear equations which is solved for the unique impulse response of the surface acceleration, v, on a given sub element. This surface acceleration is then applied in the Field II pressure calculation:

$$p(\bar{r},t) = \rho \; v * h(\bar{r},t), \tag{1}$$

where v is the element surface acceleration, $h(\bar{r},t)$ is the spatial impulse response dependent on the spatial coordinate $\bar{r}$. The constant ρ is the density of the propagation media in front of the transducer, and * is the time convolution.

Field II is a field *point* pressure calculator which implies that to achieve proper comparison with hydrophone measurements an average pressure calculation across the hydrophone area should be calculated. For a circular needle hydrophone it is reasonable to consider the received pressure as [7]

$$p_{rec}(t) = \frac{1}{A} \int_A p(\bar{r},t)\, dS, \tag{2}$$

where A is the hydrophone area. This integral can be solved by discretization

$$p_{rec}(t) = \frac{1}{\sum_i^N ds_i} \sum_i^N p_i(\bar{r},t)\, ds_i, \tag{3}$$

where N is the number of sub areas, ds, inside the total hydrophone area, A, and p_i is the calculated point pressure at the center of the sub area ds_i.

The electronic network loading the considered transducer and transmitter can be divided into two parts. The first part is the transmitter part found inside the scanner, the second part is found from the scanner output plug to the transducer ceramic as shown in Fig. 2.

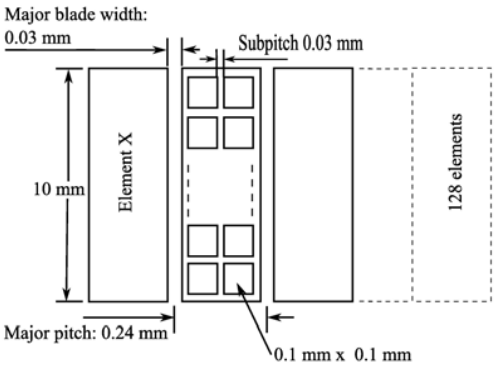

Fig.1 A frontal view of the transducer elements.

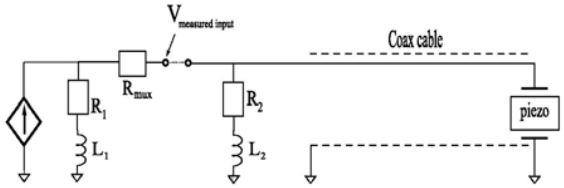

Fig.2 Simplified electronics driving the transducer.

Because we do not model the exact transmitter source the generator output voltage is measured before connecting the two networks for performing pressure measurements. This measured voltage is later applied for simulations as described in the next section.

The coaxial cable is modeled using transmission line theories, by assuming a lossless coaxial cable that terminates into the piezo ceramics and into the components L_1, R_1, L_2, R_2, R_{mux}, which are inductors and resistors used to terminate dc-voltages and drive the transducer.

$$T_{Back} = c_p^D (A_p + B_p) - h D \tag{4}$$

$$\frac{T_{Back}}{Z_{Back}} = \frac{c_p^D}{Z_p}(A_p - B_p) \tag{5}$$

$$c_{ML1}^D (A_{ML1} + B_{ML1}) = c_p^D (A_p e^{-i k_p L_p} + B_p e^{i k_p L_p}) - h D \tag{6}$$

$$\frac{c_{ML1}^D}{Z_{ML1}}(A_{ML1} - B_{ML1}) = \frac{c_p^D}{Z_p}(A_p e^{-i k_p L_p} - B_p e^{i k_p L_p}) \tag{7}$$

$$c_{ML2}^D (A_{ML2} + B_{ML2}) = c_{ML1}^D (A_{ML1} e^{-i k_{ML1} L_{ML1}} + B_{ML1} e^{i k_{ML1} L_{ML1}}) \tag{8}$$

$$\frac{c_{ML2}^D}{Z_{ML2}}(A_{ML2} - B_{ML2}) = \frac{c_{ML1}^D}{Z_{ML1}}(A_{ML1} e^{-i k_{ML1} L_{ML1}} - B_{ML1} e^{i k_{ML1} L_{ML1}}) \tag{9}$$

$$c_{LENS}^D (A_{LENS} + B_{LENS}) = c_{ML2}^D (A_{ML2} e^{-i k_{ML2} L_{ML2}} + B_{ML2} e^{i k_{ML2} L_{ML2}}) \tag{10}$$

$$\frac{c_{LENS}^D}{Z_{LENS}}(A_{LENS} - B_{LENS}) = \frac{c_{ML2}^D}{Z_{ML2}}(A_{ML2} e^{-i k_{ML2} L_{ML2}} - B_{ML2} e^{i k_{ML2} L_{ML2}}) \tag{11}$$

$$T_{Front} = c_{LENS}^D (A_{LENS} e^{-i k_{LENS} L_{LENS}} + B_{LENS} e^{i k_{LENS} L_{LENS}}) \tag{12}$$

$$\frac{T_{Front}}{Z_{Front}} = \frac{c_{LENS}^D}{Z_{LENS}}(A_{LENS} e^{-i k_{LENS} L_{LENS}} - B_{LENS} e^{i k_{LENS} L_{LENS}}) \tag{13}$$

$$-i\omega V_+ - i\omega V_- = -(i\omega \frac{L_p}{\varepsilon_p^S}) D - h\left[\frac{c_{ML1}^D}{Z_{ML1}}(A_{ML1} - B_{ML1}) - \frac{c_p^D}{Z_p}(A_p - B_p)\right] \tag{14}$$

$$-i\omega A D = \frac{1}{Z_0} V_+ - \frac{1}{Z_0} V_- \tag{15}$$

$$V(\omega) = \left(\frac{Z_g}{Z_0} + \frac{Z_g}{R_2 - i\omega L_2} + 1\right) V_+ e^{i\gamma L_{coax}} + \left(-\frac{Z_g}{Z_0} + \frac{Z_g}{R_2 - i\omega L_2} + 1\right) V_- e^{-i\gamma L_{coax}} \tag{16}$$

These assumptions result in a set of equations (4)-(16), where T_{Back}, T_{Front}, Z_{Back} and Z_{Front} are the tension on the transducer's front and backplane as well as the acoustic impedances on the front and backplane of the transducer, respectively. The constants c_p^D, c_{ML1}^D, c_{ML2}^D, and c_{LENS}^D are the stiffness constants for the piezoceramic, matching layer one (ML1), matching layer two (ML2), and the lens respectively. The acoustic impedances are given by $Z = \rho v$, where ρ is the material density and v is the wave velocity. k_p, k_{ML1}, k_{ML2}, and k_{LENS} are the wave propagation constants for the different layers defined by $k = \omega / v$, where ω is the radial frequency. The thickness of each material layer is defined as L_p, L_{ML1}, L_{ML2}, and L_{LENS}. The piezo electric constant h is defined as $h = e_{33} / \varepsilon^S$, where e_{33} and ε^S are the piezo electric coupling coefficient for stress-charge form and the electrical permittivity under constant strain. Z_0 is the characteristic cable impedance, and $\gamma = \omega\sqrt{LC}$ is the propagation constant in the coaxial cable with L and C being the inductance and capacitance per meter. The function V(ω) is the Fourier transform of a unit impulse and Z_g is defined as

$$Zg = R_1 + R_{mux} - i \cdot \omega \cdot L_1 \tag{17}$$

Finally, the coefficients A_p, B_p, A_{ML1}, B_{ML1}, A_{ML2}, B_{ML2}, A_{LENS}, B_{LENS}, T_{Back}, T_{Front},, D, V_+, and V_- are the coefficients to be solved for using Matlab. The coefficients V_+ *and* V_- coefficients are related to the coaxial transmission line.

3. Numerical simulation

The manufacturer of the transducer materials has supplied material parameters corresponding to the different layers. From these values the needed parameter constants are calculated and represented in Table 1.

Table1 Simulation parameters

	Value	Unit
ρ_p	7870	$\frac{kg}{m^3}$
ρ_{ML1}	2140	$\frac{kg}{m^3}$
ρ_{ML2}	1130	$\frac{kg}{m^3}$
ρ_{Lens}	1260	$\frac{kg}{m^3}$
ρ_{Back}	2160	$\frac{kg}{m^3}$
ρ_{Front}	1000	$\frac{kg}{m^3}$
c_p^D	$1.103 \cdot 10^{11}$	$\frac{N}{m^2}$
c_{ML1}^D	$1.750 \cdot 10^{10}$	$\frac{N}{m^2}$
c_{ML2}^D	$4.983 \cdot 10^9$	$\frac{N}{m^2}$
c_{Lens}^D	$1.235 \cdot 10^9$	$\frac{N}{m^2}$
c_{Back}^D	$1.017 \cdot 10^{10}$	$\frac{N}{m^2}$
c_{Front}^D	$2.372 \cdot 10^9$	$\frac{N}{m^2}$
ϵ^S	$11.5 \cdot 10^{-9}$	$\frac{F}{m}$
h	$1.713 \cdot 10^9$	$\frac{V}{m}$
$tan(\delta)$	0.16	□

The electronic components R_1, R_2, R_{mux}, L_1, L_2, Z_0, L and C have the values 100 Ω, 20 Ω, 22 Ω, 3.9 μH, 10 μH, 75 Ω, 3.87 μH/m and 67 pF/m, respectively. The cable length, L_{coax}, is measured to be 2.2 m.

The acoustic losses are accounted for by applying a complex wave velocity defined in (18) [3, 7], with v^r as the real-valued wave velocity defined in (19)

$$v = \frac{v^r}{1 + i\alpha v^r / \omega}, \tag{18}$$

$$v^{r} = \sqrt{c^{D} / \rho}, \tag{19}$$

where ρ in (19) is the material density.

The attenuation constants, α, are calculated from information supplied by the manufacturer and are found to be: {1036, 0, 139, 186, 308, 25e-3} [1/m] for the backing layer, the piezoceramic, ML1, ML2, the lens, and the water, respectively. The dielectric losses are included by changing the dielectric constant to a complex one $\varepsilon' = \varepsilon + i \cdot \tan(\delta)$, [3, 7].

We set up the Field II program to define the surface of the transducer with all its sub elements using the build-in command *xdc_convex_focused_multirow*. The excitation voltage for simulation was measured as shown in Fig. 2 and applied in the Field II setup. We applied a tone burst of 10 cycles and an excitation center frequency of 4.0 MHz. The sampling frequency was set to 400 MHz.

4. Measurements

Pressure measurements were performed with a needle hydrophone in a de-mineralized water bath setup. The transducer was fixed at a known position, and measured data was sampled and they were averaged 40 times using an Agilent MSO6014A oscilloscope. The excitation voltage was limited to approximately 31 volt peak to lower the possibility of non-linear effects. We performed a shooting sequence where one element was excitated at the time using our research scanner [8]. To achieve incident wave fronts normal to the hydrophone we applied three transducer center elements for which the hydrophone could be moved approximately normal to. Due to the transducer's convex nature a measurement normal to all of the 128 elements would require the hydrophone or the transducer head to be rotated which was not possible with our current setup.

5. Results

A comparison between the simulated and measured pressure at the elevation focus of the transducer for a single element is shown in Fig. 3. By performing experiments at three depths we found that approximately a 1.7 dB undershoot on the simulated amplitude was predicted and had to be accounted for in remaining simulations. Furthermore, as it can be identified in Fig. 3 the pulse shape is very well predicted by the model. However, the prediction exhibits a slightly too fast attenuation and oscillation at the pulse tail. A similar tendency was also found in our previous work [3]. This tendency must be followed by the conclusion that the model parameters have a high degree of accuracy, and that the 1D model is capable of predicting the pulse shape during transition and excitation. The tail error may be found in loss mechanisms that we do not model. Furthermore, by assuming the model parameters to be exact then the 1.7 dB adjustment is concluded mainly to be due to the simplified electronic network modeling.

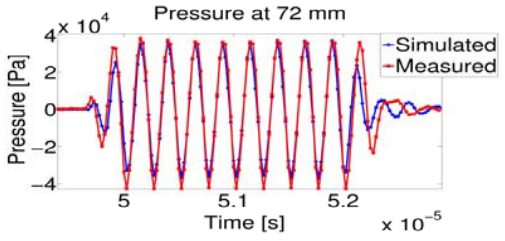

Fig.3 Pressure comparison between measured (red circles) and simulated pressure (blue squares) at 72 mm along the center axis of element 64

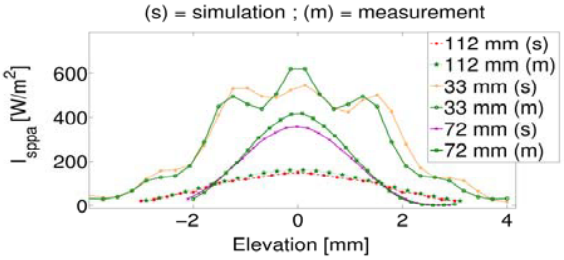

Fig.4 Comparison between measured and simulated spatial peak pulse average intensity

Fig. 4 is a simulation of the spatial peak pulse average intensity for pressure pulses simulated and measured in the elevation plane at the depths 33 mm, 72 mm, and 112 mm along the center axis of element 64. From these plots one clearly identify a nice consistency between simulations and measurements, where best results are found in the "far-field". Experimental measurements at 33 mm having the purpose to map the intensity in a parallel plane to the elements proved a highly complex surface shape, which the Field II surface model does not account for. A comparison between simulation and measurements are therefore expected to be difficult close to the elements as also shown in Fig. 4.

Table 2 is a quantitative study of the comparison between measurements and simulations. It represents the root mean square error (RMS) in percents of the difference between simulation and measurements relative to measurements. It represents the error in the intensity study along the elevation plane of three elements as well as the pressure along the elements center axis in three depths.

Table2. RMS error at three depths

	RMS % Intensity			RMS % Pressure		
Depth [mm]	33	72	112	33	72	112
Element 64	11.5	14.2	5.9	26.2	26.3	27.2
Element 65	19.5	16.2	14.6	25.2	27.1	26.7
Element 66	15.2	7.1	5.8	26.0	26.2	26.1

From the table it can be identified, that the pressure measurements were performed consistently within an RMS error of approximately 26 %. This tendency implies that the physical transducer elements have almost identical performance. For the intensity prediction a higher deviation in the errors are found, which imply that measurements in the elevation plane are more difficult to measure. One may assume that the hydrophone measurements have not been adequately normal to the wave fronts at maximum. Also the non-linear effects and possible small inaccuracies in time measurements may be sources for errors.

6. Conclusion

This paper has shown that a simplified model of the complicated electronic network loading and driving a 128 element convex transducer is possible within an amplitude adjustment of 1.7 dB by measuring the output voltage of our research scanner and using it as input for the Field II program. The study has shown that the linear 1D model predicts the pressure pulse in corporation with Field II within a ~26 % RMS error. We have also found that the simplified modeling can predict the elevation intensity of a 10 cycle 4.0 MHz tone burst excitation within a RMS error of ~5.8-19.5 %, where best results are achieved furthest away from the elements. Errors are mainly found on pulse tails and due to non-linearity. From the study we also conclude, that the presented 1D transducer model works very well in predicting the impulse response of the squared transducer elements. However, an improvement in the electronic network modeling may be needed to achieve proper amplitude simulations with more complicated excitation pulses.

Acknowledgements

The authors would like to thank Sound Technology, Inc. for supplying the transducer information as well as giving support in discussions, and would like to thank BK Medical Aps for giving support in discussions.

References

[1] J.A. Jensen, " Field: A program for simulating ultrasound systems, paper presented at the 10th Nordic-Baltic Conference on Biomedical Imaging Published in Medical & Biological Engineering & Computing", pp. 351-353, Volume 34, Supplement 1, Part 1, 1996.

[2] J.A. Jensen and N.B. Svendsen, "Calculation of pressure fields from arbitrarily shaped, apodized, and excited ultrasound transducers", IEEE Trans. Ultrason., Ferroelec., Freq. Contr., 39, pp. 262-267, 1992.

[3] D. Bæk and J.A. Jensen and M. Willatzen, "Testing of a one dimensional model for Field II calibration", Proc. IEEE Ultrason. Symp. Oct. 2008, pp. 1417-1420.

[4] W.P. Mason, "Electromechanical Transducers and Wave Filters", 2nd ed. D. Van Nostrand Company, Inc. 1948, p.205.

[5] R. Krimholtz, D.A. Leedom, and G.L. Matthaci, "New equivalent circuits for elementary piezoelectric transducers", Electron. Letter., vol 6, pp. 398-399, 1970.

[6] M. Redwood, "Transient performance of a piezoelectric transducer", J.Acoust. Soc. Amer., vol 33, pp. 527-536.

[7] M. Willatzen, "Ultrasound transducer modeling-general theory and applications to ultrasound reciprocal systems" IEEE Trans. Ultrason., Ferroelec., Freq. Contr., vol. 48, pp. 100-112, 2001

[8] J. A. Jensen, O. Holm, L. J. Jensen, H. Bendsen, H. M. Pedersen, K. Salomonsen, J. Hansen, and S. Nikolov, "Experimental ultrasound system for real-time synthetic imaging", in Proc. IEEE Ultrason. Symp., volume 2, 1595–1599 (1999).

.

Abstract I

Testing of a spatial impulse response algorithm for double curved transducers

David Bæk, Jørgen Arendt Jensen, and Morten Willatzen

Abstract to: Proceedings of the IEEE International Ultrasonics Symposium

Accepted for conference in San Diego 2010

Testing of a spatial impulse response algorithm for double curved transducers

David Bæk*, Jørgen Arendt Jensen*, and Morten Willatzen†
**Center for Fast Ultrasound Imaging, Department of Electrical Engineering, Technical University of Denmark*
†Mads Clausen Institute for Product Innovation, University of Southern Denmark, 6400 Sønderborg, Denmark
Email: db@elektro.dtu.dk , jaj@elektro.dtu.dk , willatzen@mci.sdu.dk

Background, Motivation and Objective

The spatial impulse response (SIR) method for solving the Rayleigh integral is a well known method for fast time response simulation of acoustic. Several analytical expressions have been found for simple transducer geometries such as rectangles and discs. However, no analytical solution is found for double curved transducers (DCT), i.e. transducers with both concave and convex radius. To calculate the pressure from such transducers Field II uses a far-field approximation by dividing the surface into smaller flat elements and then do a summation of the response from all the elements using Huygens principle. This calculation method involves several summations, and it relies on exact phase calculation to avoid numerical noise in the response. A stable analytical expression for the SIR would therefore be beneficial to the Field II software as an alternative solver. A semi-analytic algorithm (SAA) has been developed, and it is the objective of this work to validate an analytical approximation of the algorithm as an alternative solver for Field II.

Statement of Contribution/Methods

A semi-analytical algorithm that finds the SIR for DCT has been developed and implemented. An exact solution to this algorithm requires a numerical integrator; however, a part of the algorithm may be approximated by a parabola function to yield a computational efficient analytical expression. This paper investigates the accuracy of the approximation. The root mean square (RMS) error of calculating the SIR using Field II and the approximated algorithm (AA) are calculated relative to the exact solution on a single element transducer with convex and concave radius of 70 mm and 60 mm, respectively. Error calculations are performed at sampling frequencies ranging from 40 MHz to 4.94 GHz in steps of 100 MHz. The transducer width is 250 µm and the height is 10 mm. The exact solution of the semi-analytical solution is solved at 4.94 GHz using MATLAB and used as a reference for the error calculation at point locations {x,y,z}= {-1,0,20}, {-1,10,120}, and {-1,0,20} mm for point P1, P2, and P3, respectively. Field II uses 500x550 mathematical elements to gain high resolution.

Results

A second order polynomial was found suitable for approximating a part of the SAA. As a consequence the SAA could be solved analytically. By comparing the SIR it was found that at 140 MHz the RMS errors at the points P1, P2, and P3 are {12.3,3.3,32.4} **%** and {0.04,0.5,0.09} **%** for Field II and the AA, respectively. At 4.94 GHz the errors are {1.1, 0.8, 10.2} **%** and {0.04, 0.5, 0.07} %.

Discussion and Conclusions

It is found that the AA is accurate within an RMS of 0.5 % at 140 MHz relative to the exact solution, and 0.5 % at 4.94 GHz exhibiting only a very small error fluctuation. Field II is seen to have up to 32.4 % and 10.2 % at 140 MHz and 4.94 GHz. The RMS is very fluctuating. It is concluded that the algorithm has potential for implementation into Field II as an accurate solver. Future development should focus on an implementation in c code.

Abstract II

Simulating CMUTs using Field II

David Bæk, Ömer Oralkan, Mario Kupnik, Morten Willatzen, Butrus T. Khuri-Yakub, and Jørgen Arendt Jensen

Abstract to: Proceedings of the IEEE International Ultrasonics Symposium

Accepted for conference in San Diego 2010

Simulating CMUTs using Field II

David Bæk[1], Ömer Oralkan[2], Mario Kupnik[2], Morten Willatzen[3], Butrus T. Khuri-Yakub[2], Jørgen Arendt Jensen[1]
[1]*Center for Fast Ultrasound Imaging, Department of Electrical Engineering, Technical University of Denmark, Kgs. Lyngby,Denmark,* [2]*Edward L. Ginzton Laboratory, Stanford University, Stanford, CA, USA,* [3]*Mads Clausen Institute for Product Innovation,University of Southern Denmark, Sønderborg, Denmark*

Background, Motivation and Objective

For more than ten years Field II has been a recognized simulation tool for piezo ceramic medical array transducers. It has its strength in doing fast computation of the pulse echo spatial impulse response (PESIR) from array elements by dividing the elements into smaller mathematical elements (ME) from which it then calculates the PESIR far-field responses. The program has predefined models for classical transducer geometries, but currently none for the fast advancing CMUTs. Elements of CMUTs consist of many cells. Each plate of these vacuum sealed cells deflects due to an applied DC bias voltage and ambient pressure. Therefore, modeling each cell with deflection using Field II requires many ME. This paper addresses the error in modeling the PESIR with and without deflection and it investigates the possibility of using area scaling of the PESIR when modeling the whole element area as active.

Statement of Contribution/Methods

A single flat array element of size 190x5700 μm^2 and a corresponding CMUT element with 5x150 cells with 18 μm radii, distributed with a pitch of 38 μm, are modeled. Cases with maximum plate deflections of 0 and 12.1 nm are studied. The difference in the PESIR due to active area is calculated by comparing the model of a flat full area active element (FE) and the model of an element with only the cell areas considered as active. The error is calculated as the ratio of the difference of the two PESIRs to the PESIR of modeling only active cells. The root mean square error (RMS) of the difference in the pulse shapes relative to the PESIR from active cells is also studied. It is furthermore investigated how the errors are affected by scaling the FE's PESIR with the square of the ratio between the active areas of the two element types. The square of the ratio comes into play because the PESIR is a pulse-echo signal. The calculations are made at distances of 1, 10, and 100 mm along the elements' center axis and at a sampling frequency of 200 MHz. Finally, a study of the number of mathematical elements needed for modeling deflecting plates is studied.

Results

With a 0 deflection the un-scaled PESIR of the FE yields an area error ranging from 91-98 %, whereas the scaled PESIR of the FE yields 1.2-4.7 % relative error. For a 12.1 nm center deflection the errors range from 90-97 % and 1.7-6.8 % for the un-scaled and scaled FE area, respectively. The RMS errors range from 91-99 % and 1.2-6.8 % for the un-scaled and scaled PESIR, respectively. Best results are found at 100 mm distance. The number of ME across the radius, needed to resolve the cells, is found to be 5, which gives a 2.6 % RMS error of the pulse shape. For higher resolution the area error oscillates within 0-5 % and the solution time increases exponentially.

Discussion and Conclusions

In conclusion PESIR modeling at 200 MHz does not benefit from modeling each cell deflection. Energy of the PESIR pulse can be well preserved by area scaling of a PESIR modeled from elements that models the in-between cell inactive area as active

_____

Bibliography

[1] J. A. Jensen and N. B. Svendsen, "Calculation of pressure fields from arbitrarily shaped, apodized, and excited ultrasound transducers," *IEEE Trans. Ultrason., Ferroelec., Freq. Contr.*, vol. 39, pp. 262–267, 1992.

[2] J. A. Jensen, "A new calculation procedure for spatial impulse responses in ultrasound," *J. Acoust. Soc. Am.*, vol. 105, no. 6, pp. 3266–3274, 1999.

[3] ——, "A model for the propagation and scattering of ultrasound in tissue," *J. Acoust. Soc. Am.*, vol. 89, pp. 182–191, 1991a.

[4] ——, "Ultrasound fields from triangular apertures," *J. Acoust. Soc. Am.*, vol. 100(4), pp. 2049–2056, 1996a.

[5] M. Willatzen, "Ultrasound transducer modeling - general theory and applications to ultrasound reciprocal systems," *IEEE Trans. Ultrason., Ferroelec., Freq. Contr.*, vol. 48, no. 1, pp. 100–112, January 2001.

[6] L. Rayleigh, *The theory of sound*. Dover, 1945.

[7] H. T. O'Neil, "Theory of focusing radiators," *J. Acoust. Soc. Am.*, vol. 21-5, pp. 516–526, 1949.

[8] F. Oberhettinger, "On transient solutions of the baffled piston problem," *Journal of research of the National Bureau of Standards-B, Mathematics and Mathematical Physics*, vol. 65B-1, pp. 1–6, 1961.

[9] A. Freedman, "Transient fields of acoustic radiators," *J. Acoust. Soc. Am.*, vol. 48, pp. 135–138, 1970a.

[10] G. R. Harris, "Review of transient field theory for a baffled planar piston," *J. Acoust. Soc. Am.*, vol. 70, pp. 10–20, 1981.

[11] G. E. Tupholme, "Generation of acoustic pulses by baffled plane pistons," *Mathematika*, vol. 16, pp. 209–224, 1969.

[12] P. R. Stepanishen, "An approach to compute time-dependent interaction forces and mutual radiation impedances between pistons in a rigid planar baffle," *J. Acoust. Soc. Am.*, vol. 49, pp. 283–292, 1971.

[13] ——, "The time-dependent force and radiation impedance on a piston in a rigid infinite planar baffle," *J. Acoust. Soc. Am.*, vol. 49, pp. 841–849, 1971.

[14] ——, "Transient radiation from pistons in an infinite planar baffle," *J. Acoust. Soc. Am.*, vol. 49, pp. 1629–1638, 1971.

[15] J. C. Lockwood and J. G. Willette, "High-speed method for computing the exact solution for the pressure variations in the nearfield of a baffled piston," *J. Acoust. Soc. Am.*, vol. 53, pp. 735–741, 1973.

[16] A. Neild and D. A. Hutchins, "The calculation of radiated pressure fields from irregular multi-sided polygons," *J. Acoust. Soc. Am.*, vol. 115-5, pp. 2021–2031, 2004.

[17] A. Penttinen and M. Luukkala, "The impulse response and nearfield of a curved ultrasonic radiator," *J. Phys. D: Appl. Phys.*, vol. 9, pp. 1547–1557, 1976.

[18] M. Arditi, F. S. Forster, and J. Hunt, "Transient fields of concave annular arrays," *Ultrason. Imaging*, vol. 3, pp. 37–61, 1981.

[19] J. N. Tjøtta and S. Tjøtta, "Nearfield and farfield of pulsed acoustic radiators," *J. Acoust. Soc. Am.*, vol. 71, pp. 824–834, 1982.

[20] B. Piwakowski and K. Sbai, "A new approach to calculate the field radiated from arbitrarily structured transducer arrays." *IEEE Trans. Ultrason., Ferroelec., Freq. Contr.*, vol. 46-2, pp. 422–440, 1999.

[21] B. Piwakowski and B. Delannoy, "Method for computing spatial pulse response: Time-domain approach," *J. Acoust. Soc. Am.*, vol. 86-6, pp. 2422–2432, 1989.

[22] F. Lingvall, "User manual for the DREAM toolbox- an ultrasound simulation software for use with MATLAB and GNU OCTAVE," 2009.

[23] P. Faure, D. Cathignol, and J. Y. Chapelon, "On the pressure field of a transducer in the form of a curved strip," *J. Acoust. Soc. Am.*, vol. 95-2, pp. 628–637, 1994.

[24] J. F. Theumann, M. Arditi, J.-J. Meister, and E. Jaques, "Acoustic fields of concave cylindrical transducers," *J. Acoust. Soc. Am.*, vol. 88-2, pp. 1160–1169, 1990.

[25] P. Wu and T. Stepinski, "Spatial impulse response method for predicting pulse-echo fields from a linear array with cylindrically concave surface," *IEEE Trans. Ultrason., Ferroelec., Freq. Contr.*, vol. 46-5, pp. 1283–1297, 1999.

[26] S. Holm, "Ultrasim - a toolbox for ultrasound field simulation," *University of Oslo*, 2001.

[27] M. A. Ellis, D. Guenther, and W. F. Walker, "Spline-based approach for computing spatial impulse responses," *IEEE Trans. Ultrason., Ferroelec., Freq. Contr.*, vol. 54-5, pp. 1045–1054, 2007.

[28] L. E. Kinsler, A. U. Fray, A. B. Coppens, and J. V. Sanders, *Fundamentals of Acoustics*, 3rd ed. New-York: New-York: John Wiley and Sons, Inc., 1982.

[29] W. Mason, *Electromechanical Transducers and Wave Filters*, 2nd ed. D. Van Nostrand Company, Inc., 1948.

[30] M. Redwood, "Transient performance of a piezoelectric transducer," *J. Acoust. Soc. Am.*, vol. 33, no. 4, pp. 527–536, April 1960.

[31] R. Krimholtz, D. Leedom, and G. Matthaci, "New equivalent circuits for elementary piezoelectric transducers," *Electr. Lett.*, vol. 6, no. 13, pp. 398–399, June 1970.

[32] B. A. Auld, *Acoustic Fields and Waves in Solids Volume 1*, 2nd ed. Malabar,Florida: Krieger Publishing Company, 1990.

[33] A. Arnau, *Piezoelectric Transducers and Applications*, 1st ed. Berlin Heidelberg: Springer-Verlag Berlin Heidelberg, 2004.

[34] M. Willatzen, "Ultrasound transducer modeling - received voltage signals and the use of half-wavelength window layers with acoustic coupling layers," *IEEE Trans. Ultrason., Ferroelec., Freq. Contr.*, vol. 46, no. 5, pp. 1164–1174, September 1999.

[35] P. Maréchal, F. Levassort, L.-P. Tran-Huu-Hue, and M. Lethiecq, "Lens-focused transducer modeling using an extended KLM model," *Ultrasonics*, vol. 46, pp. 155–167, 2007.

[36] P. Schnabel, "Dispersion of thickness vibrations of piezoceramic disk resonators," *IEEE Trans. Son. Ultrason.*, vol. SU-25, no. 1, pp. 16–24, January 1978.

[37] M. Algueró, C. Alemany, , and L. Pardo, "Method for obtaining the full set of linear electric, mechanical and electromechanical coefficients and all related losses of a piezoelectric ceramic," *J. Acoust. Soc. Am.*, vol. 87, pp. 209–215, 2004.

[38] T. Amby, *Multiphysics Mathematical Modeling of Piezoelectric Transducers*, 2005, vol. Master Thesis, University of Southern Denmark, Sonderborg.

[39] "Comsol multiphysics user's guide, version: Comsol 3.4, comsol ab, 2008."

[40] O. A. Sapozhnikov, A. V. Morozov, and D. Cathignol, "Piezoelectric transducer surface vibration characterization using acoustic holography and laser vibrometry," in *Proc. IEEE Ultrason. Symp.*, 2004, pp. 161–164.

[41] O. A. Sapozhnikov, A. E. Ponomarev, and M. A. Smagin, "Transient acoustic holography for reconstructing the particle velocity of the surface of an acoustic transducer," *Acoustical Physics*, vol. 52-3, pp. 324–330, 2006.

[42] B. Bayram, Ö. Oralkan, A. S. Ergun, E. Hæggström, G. G. Yaralioglu, and B. T. Khuri-Yakub, "Capacitive micromachined ultrasonic transducer design for high power transmission," *IEEE Trans. Ultrason., Ferroelec., Freq. Contr.*, vol. 52-2, pp. 326–339, 2005.

[43] Y. Huang, E. Hæggström, B. Bayram, X. Zhuang, A. S. Ergun, C.-H. Cheng, and B. T. Khuri-Yakub, "Comparison of conventional and collapsed region operation of capacitive micromachined ultrasonic transducers," *IEEE Trans. Ultrason., Ferroelec., Freq. Contr.*, vol. 53-10, pp. 1918–1933, 2006.

[44] Y. Huang, X. Zhuang, E. O. H. ggström, A. S. Ergun, C.-H. Cheng, and B. T. Khuri-Yakub, "Capacitive micromachined ultrasonic transducers with piston-shaped membranes: Fabrication and experimental characterization," *IEEE Trans. Ultrason., Ferroelec., Freq. Contr.*, vol. 56-1, pp. 136–145, 2009.

[45] A. Lohfink, *Untersuchung und Optimierung der akustischen Eigenschaften kapazitiver mikromechanischer Ultraschallwandler am Beispiel der medizinischen Diagnostik*. Ph.D. Thesis, Universität Bremen, 2005.

[46] X. Zhuang, A. S. Ergun, Y. Huang, I. O. Wygant, Ö. Oralkan, and B. T. Khuri-Yakub, "Integration of trench-isolated through wafer interconnects with 2d capacitive micromachined ultrasonic transducer arrays," *Sensors and Actuators A*, vol. 138, pp. 221–229, 2007.

[47] A. S. Ergun, Y. Huang, X. Zhuang, Ö. Oralkan, G. G. Yaralioglu, and B. Khuri-Yakub, "Capacitive micromachined ultrasonic transducers: Fabrication technology," *IEEE Trans. Ultrason., Ferroelec., Freq. Contr.*, vol. 52-12, pp. 2242–2258, 2005.

[48] X. Zhuang, I. O. Wygant, D.-S. Lin, M. Kupnik, Ö. Oralkan, and B. T. Khuri-Yakub, "Wafer-bonded 2-d cmut arrays incorporating through-wafer trench-isolated interconnects with a supporting frame," *IEEE Trans. Ultrason., Ferroelec., Freq. Contr.*, vol. 56-1, pp. 182–192, 2009.

[49] Ö. Oralkan, A. S. Ergun, J. A. Johnson, M. Karaman, U. Demirci, K. K. ad T. H. Lee, and B. T. Khuri-Yakub, "Capacitive micromachined ultrasonic transducers: Next-generation arrays for acoustic imaging?" *IEEE Trans. Ultrason., Ferroelec., Freq. Contr.*, vol. 49-11, pp. 1596–1610, 2002.

[50] B. Bayram, G. G. Yaralioglu, A. S. Ergun, Ö. Oralkan, and B. T. Khuri-Yakub, "Dynamic fem analysis of multiple cmut cells in immersion," *Proc. IEEE Ultrason. Symp.*, vol. 2004, pp. 252–255, 2004.

[51] B. Bayram, G. G. Yaralioglu, M. Kupnik, A. S. Ergun, Ö. Oralkan, A. Nikoozadeh, and B. T. Khuri-Yakub, "Dynamic analysis of capacitive micromachined ultrasonic transducers," *IEEE Trans. Ultrason., Ferroelec., Freq. Contr.*, vol. 52-12, pp. 2270–2275, 2005.

[52] B. Bayram, M. Kupnik, G. G. Yaralioglu, Ö. Oralkan, A. S. Ergun, D. Lin, S. H. Wong, and B. Khuri-Yakub, "Finite-element modeling and experimental characterization of crosstalk in 1d cmut arrays," *IEEE Trans. Ultrason., Ferroelec., Freq. Contr.*, vol. 54-2, pp. 418–430, 2007.

[53] W. Zhou, T. Yu, and F. Yu, "Calculation of equivalent parameters in cmut 1-d theoretical model," *Proc. IEEE Ultrason. Symp.*, vol. 2008, pp. 491–495, 2008.

[54] A. Lohfink and P.-C. Eccardt, "Linear and nonlinear equivalent circuit modeling of cmuts," *IEEE Trans. Ultrason., Ferroelec., Freq. Contr.*, vol. 52-12, pp. 2163–2172, 2005.

[55] I. O. Wygant, *Three-dimensional ultrasound imaging using custom integrated electronics combined with capacitive micro machined ultrasonic transducers*. Phd Thesis at the Department of Electrical Engineering, Stanford University, California, 2008.

[56] I. O. Wygant, M. Kupnik, and B. T. Khuri-Yakub, "Analytically calculating membrane displacement and the equivalent circuit model of a circular cmut cell," *Proc. IEEE Ultrason. Symp.*, vol. 2008, pp. 2111–2114, 2008.

APPENDIX

A

Derivations and the physics of piezoelectric transducer equations

The following derivation note is based on findings in Auld [32] and Willatzen [5]. It gathers the most important equations needed for arriving at a set of solvable equations.

When an external force is applied to a piezoelectric material, its shape will be linearly deformed. This deformation will result in internal stresses and heating due to the atoms' internal bindings.

Because of the atoms relative displacements the internal deformation results in an internal work, δW. The work will be followed by internal heating due to both viscosity and friction. External heating, dQ, can also occur. This type of heating is contributing to the internal energy by increasing the energy of the electrons. The crystal can also experience a change in stored energy by means of an applied magnetic field, B.

The total amount of stored energy, due to external forces such as pressure forces, electric forces and magnetic forces, can be written as:

$$\delta U = \delta W + \delta Q, \tag{A.1}$$

where δW is representing the internal work done by external forces, and δQ represents the internal heating [32] due to external heat supply. The work is a contribution of mechanical forces $T_I dS_I$, electrical forces $E_i dD_i$ and magnetic forces $H_i dB_i$. The subscript to cover a full dimensional analysis follows $i, k = 1, 2, 3$ or $i, k = x, y, z$. The heat contribution dQ can be defined as $\tau d\sigma$, where

τ is the temperature and $d\sigma$ is the differential of the entropy. Finally, the stored energy can be written as a summation of the above energies:

$$dU = T_{ik}dS_{ik} + E_i dD_i + H_i dB_i + \tau d\sigma. \tag{A.2}$$

T_{ik} is the tension, S_{ik} the strain, E_i is the electric field, D_i the electric displacement, H_i and B_i are magnetic field quantities, τ is the temperature and σ is the entropy [32].

The above definitions can be written as matrices in the following manner:

$$T_{ik} = \begin{bmatrix} T_{xx}T_{yx}T_{zx} \\ T_{xy}T_{yy}T_{zy} \\ T_{xz}T_{yz}T_{zz} \end{bmatrix}, \quad S_{ik} = \begin{bmatrix} S_{xx}S_{yx}S_{zx} \\ S_{xy}S_{yy}S_{zy} \\ S_{xz}S_{yz}S_{zz} \end{bmatrix}. \tag{A.3}$$

The above matrices can be alternatively written as [32]

$$T_I = \begin{bmatrix} T_1 \\ T_2 \\ T_3 \\ T_4 \\ T_5 \\ T_6 \end{bmatrix} = \begin{bmatrix} T_{xx} \\ T_{yy} \\ T_{zz} \\ T_{yz} \\ T_{xz} \\ T_{xy} \end{bmatrix}, \quad S_I = \begin{bmatrix} S_1 \\ S_2 \\ S_3 \\ S_4 \\ S_5 \\ S_6 \end{bmatrix} = S_I = \begin{bmatrix} \frac{\partial u_x}{\partial x} \\ \frac{\partial u_y}{\partial y} \\ \frac{\partial u_z}{\partial z} \\ \frac{\partial u_y}{\partial z} + \frac{\partial u_z}{\partial y} \\ \frac{\partial u_x}{\partial z} + \frac{\partial u_z}{\partial x} \\ \frac{\partial u_y}{\partial x} + \frac{\partial u_x}{\partial y} \end{bmatrix}. \tag{A.4}$$

This notation form is in general given in the litterature [32]. The remaining matrices are given by

$$E_i = \begin{bmatrix} E_x \\ E_y \\ E_z \end{bmatrix}, \quad D_i = \begin{bmatrix} D_x \\ D_y \\ D_z \end{bmatrix}, \quad B_i = \begin{bmatrix} B_x \\ B_y \\ B_z \end{bmatrix}, \quad H_i = \begin{bmatrix} H_x \\ H_y \\ H_z \end{bmatrix}. \tag{A.5}$$

Consider (A.2). If the stored energy is to be represented as a set of state variables, the function $U(S, D, B, \sigma)$ can be established. This implies that one can introduce the chain rule formulation as

$$dU = \frac{\partial U}{\partial S}dS + \frac{\partial U}{\partial B}dB + \frac{\partial U}{\partial D}dD + \frac{\partial U}{\partial \sigma}d\sigma, \tag{A.6}$$

where

$$T = \frac{\partial U}{\partial S}, \qquad E = \frac{\partial U}{\partial D}, \qquad \tau = \frac{\partial U}{\partial \sigma}, \qquad H = \frac{\partial U}{\partial B}. \tag{A.7}$$

Most piezoelectric transducer modeling is independent of the piezomagnetic contribution, because it is found to be negligibly small and thus can be discarded [32]. Furthermore, it is a good presumption that the piezo material

is isentropic, i.e. adiabatic and reversible. This implies that one can leave out the temperature dependence τ because of the assumption $d\sigma = 0$. This simplifies (A.6) to

$$dU = \frac{\partial U}{\partial S} dS + \frac{\partial U}{\partial D} dD. \tag{A.8}$$

All processes can be expressed in terms of their enthalpy. The enthalpy is an expression of the useful work which can be obtained from a closed system. For a piezoelectric crystal one can write the total enthalpy as a contribution of the following terms

$$H_e = U - E_i D_i - T_{ik} S_{ik}. \tag{A.9}$$

When neglecting the electrical contribution in (A.9), the Helmholtz free energy function is found. It is typically denoted by A. Similarly, the enthalpy associated with the electrical effects can be found when neglecting the tension. The latter is presented with $\bar{A}$. These functions are then written as

$$A = U - T_{ik} S_{ik}, \qquad \bar{A} = U - E_i D_i. \tag{A.10}$$

Applying the method suggested in (A.8) one can write the following useful expressions for H_e:

$$\begin{aligned} dH_e &= dU - d(E_i D_i) - d(T_{ik} S_{ik}) = T_{ik} dS_{ik} + E_i dD_i - E_i dD_i - \\ &\quad T_{ik} dS_{ik} - S_{ik} dT_{ik} - D_i dE_i \end{aligned} \tag{A.11}$$

$$dH_e = -D_i dE_i - S_{ik} dT_{ik}. \tag{A.12}$$

The same method applied on A and $\bar{A}$ yields

$$dA = E_i dD_i - S_{ik} T_{ik} \qquad d\bar{A} = -D_i dE_i + T_{ik} S_{ik}. \tag{A.13}$$

Applying the chain rule to (A.6), (A.12) and (A.13) yields several expressions for constants which are commonly found in the piezoelectric world [5, 32]. These can be defined as

$$h_{ikl} = -\left(\frac{\partial E_i}{\partial S_{kl}}\right)_D = \left(\frac{\partial^2 U}{\partial S_{kl} \partial D_i}\right) = -\left(\frac{\partial T_{kl}}{\partial D_i}\right)_S, \tag{A.14}$$

$$d_{ikl} = \left(\frac{\partial D_i}{\partial T_{kl}}\right)_E, \tag{A.15}$$

$$g_{ikl} = -\left(\frac{\partial E_i}{\partial T_{kl}}\right)_D, \tag{A.16}$$

$$e_{ikl} = \left(\frac{\partial D_i}{\partial S_{kl}}\right)_E. \tag{A.17}$$

Many more combinations can be derived by assuming that the order of differentiation is of no significance. Similarly, the permitivity tensor can be found as

$$\epsilon_{ik}^{T} = \left(\frac{\partial D_i}{\partial E_k}\right)_T, \qquad \epsilon_{ik}^{S} = \left(\frac{\partial D_i}{\partial E_k}\right)_S. \tag{A.18}$$

The inverse permitivity is given as

$$\beta_{ik}^{T} = \left(\frac{\partial E_i}{\partial D_k}\right)_T, \qquad \beta_{ik}^{S} = \left(\frac{\partial E_i}{\partial D_k}\right)_S. \tag{A.19}$$

Compliance and stiffness tensors are defined as

$$s_{iklm}^{D} = \left(\frac{\partial S_{ik}}{\partial T_{lm}}\right)_D, \qquad s_{iklm}^{E} = \left(\frac{\partial S_{ik}}{\partial T_{lm}}\right)_E, \tag{A.20}$$

$$c_{iklm}^{D} = \left(\frac{\partial T_{ik}}{\partial S_{lm}}\right)_D, \qquad c_{iklm}^{E} = \left(\frac{\partial T_{ik}}{\partial S_{lm}}\right)_E. \tag{A.21}$$

The permitivity is an expression for the solids capacitance behavior, and the stiffness tensor expresses how stiff the solid is in its constraints. c is to be compared to the well known proportionality constant found in Hooks law for linear stress-strain. The compliance tensor, s, is the inverse of c.

Piezoelectric constitutive equations

Combination of the above expressions gives several piezoelectric equations [5]:

$$D_i = \epsilon_{ik}^{T} E_k + d_{ikl} T_{kl}, \tag{A.22}$$

$$E_k = \beta_{ik}^{T} D_i + g_{klm} T_{lm}, \tag{A.23}$$

$$D_i = \epsilon_{ik}^{S} E_k + e_{ikl} S_{kl}, \tag{A.24}$$

$$E_k = \beta_{ik}^{S} D_i + h_{klm} S_{lm}, \tag{A.25}$$

$$S_{kl} = d_{ikl} E_i + s_{klmn}^{E} T_{mn}, \tag{A.26}$$

$$T_{kl} = -e_{ikl} E_i + C_{klmn}^{E} S_{mn}, \tag{A.27}$$

$$S_{kl} = g_{ikl} D_i + s_{klmn}^{D} T_{mn}, \tag{A.28}$$

$$T_{kl} = -h_{ikl} D_i + c_{klmn}^{D} S_{mn}. \tag{A.29}$$

These expressions are the ones usually applied in piezoelectric formulations. Note that it is sufficient to apply only two equations, e.g. (A.25) and (A.29) to

find the unknowns. It also implies that many possible combinations can be made dependent on the given application.

Consider (A.29) and write it out in the form of (A.4). Furthermore, restrict the consideration to the material PZT- 5H. This material has a hexagonal atomic structure [32]

$$\begin{bmatrix} T_1 \\ T_2 \\ T_3 \\ T_4 \\ T_5 \\ T_6 \end{bmatrix} = \begin{bmatrix} c_{11}^D & c_{12}^D & c_{13}^D & 0 & 0 & 0 \\ c_{12}^D & c_{11}^D & c_{13}^D & 0 & 0 & 0 \\ c_{13}^D & c_{13}^D & c_{33}^D & 0 & 0 & 0 \\ 0 & 0 & 0 & c_{44}^D & 0 & 0 \\ 0 & 0 & 0 & 0 & c_{44}^D & 0 \\ 0 & 0 & 0 & 0 & 0 & c_{66}^D \end{bmatrix} \cdot \begin{bmatrix} S_1 \\ S_2 \\ S_3 \\ S_4 \\ S_5 \\ S_6 \end{bmatrix} - \begin{bmatrix} 0 & 0 & h_{z1} \\ 0 & 0 & h_{z2} \\ 0 & 0 & h_{z3} \\ 0 & h_{x5} & 0 \\ h_{x5} & 0 & 0 \\ 0 & 0 & 0 \end{bmatrix} \cdot \begin{bmatrix} D_x \\ D_y \\ D_z \end{bmatrix}. \tag{A.30}$$

Consider also the second possible set of equations, which account for the electrical affects given by (A.25).

$$\begin{bmatrix} E_x \\ E_y \\ E_z \end{bmatrix} = \begin{bmatrix} 0 & 0 & 0 & 0 & h_{x5} & 0 \\ 0 & 0 & 0 & h_{x5} & 0 & 0 \\ h_{z1} & h_{z1} & h_{z_3} & 0 & 0 & 0 \end{bmatrix} \cdot \begin{bmatrix} S_1 \\ S_2 \\ S_3 \\ S_4 \\ S_5 \\ S_6 \end{bmatrix} - \begin{bmatrix} \beta_{xx}^S & 0 & 0 \\ 0 & \beta_{yy}^S & 0 \\ 0 & 0 & \beta_{zz}^S \end{bmatrix} \cdot \begin{bmatrix} D_x \\ D_y \\ D_z \end{bmatrix}. \tag{A.31}$$

Introducing the electrical potential yields an alternative way of representing the electric field

$$\bar{E} = -\nabla\phi. \tag{A.32}$$

This modifies the above equation set to the following form

$$\begin{bmatrix} -\frac{\partial\phi}{\partial x} \\ -\frac{\partial\phi}{\partial y} \\ -\frac{\partial\phi}{\partial z} \end{bmatrix} = \begin{bmatrix} 0 & 0 & 0 & 0 & h_{x5} & 0 \\ 0 & 0 & 0 & h_{x5} & 0 & 0 \\ h_{z1} & h_{z1} & h_{z_3} & 0 & 0 & 0 \end{bmatrix} \cdot \begin{bmatrix} S_1 \\ S_2 \\ S_3 \\ S_4 \\ S_5 \\ S_6 \end{bmatrix} - \begin{bmatrix} \beta_{xx}^S & 0 & 0 \\ 0 & \beta_{yy}^S & 0 \\ 0 & 0 & \beta_{zz}^S \end{bmatrix} \cdot \begin{bmatrix} D_x \\ D_y \\ D_z \end{bmatrix}. \tag{A.33}$$

These equations constitute the piezoelectric equations in a full dimensional analysis. However, to solve the acoustic field inside the piezo element one

has to introduce Newton's second law of force

$$\nabla \cdot \mathbf{T} = \rho \frac{\partial^2 \mathbf{u}}{\partial t^2} - \mathbf{F}, \tag{A.34}$$

where $\mathbf{u}$ is the particle displacement and $\mathbf{F}$ is the external force. This force accounts for all forces and their reaction acting on an infinite volume element inside the crystal. Using the abbreviated subscripts presented in (A.4) and Auld [32], the gradient operator takes the following form

$$\nabla \cdot \rightarrow \begin{bmatrix} \frac{\partial}{\partial x} & 0 & 0 & 0 & \frac{\partial}{\partial z} & \frac{\partial}{\partial y} \\ 0 & \frac{\partial}{\partial y} & 0 & \frac{\partial}{\partial z} & 0 & \frac{\partial}{\partial x} \\ 0 & 0 & \frac{\partial}{\partial z} & \frac{\partial}{\partial y} & \frac{\partial}{\partial x} & 0 \end{bmatrix} \tag{A.35}$$

Written out in full (A.34) yields

$$\begin{aligned} \frac{\partial T_1}{\partial x} + \frac{\partial T_5}{\partial z} + \frac{\partial T_6}{\partial y} &= \rho \frac{\partial^2 u_x}{\partial t^2} - F_x, \\ \frac{\partial T_2}{\partial y} + \frac{\partial T_4}{\partial z} + \frac{\partial T_6}{\partial x} &= \rho \frac{\partial^2 u_y}{\partial t^2} - F_y, \\ \frac{\partial T_3}{\partial z} + \frac{\partial T_4}{\partial y} + \frac{\partial T_5}{\partial x} &= \rho \frac{\partial^2 u_z}{\partial t^2} - F_z. \end{aligned} \tag{A.36}$$

The above yields 13 unknown variables and 12 equations. To solve this combination of equations in their full form an equation introducing the electric circuit driving the crystal can be applied. The crystal will generally be mounted with two electrodes on two parallel sides. Between these two sides an electrical potential may be formulated e.g.

$$V(t) = I Z_e + \int_{r0}^{rL} E_i dr_i, \tag{A.37}$$

where I is the current in the external circuits, Z_e is the electrical impedance of the external circuit, and $V(t)$ is the applied source voltage. Written with the potential function (A.37) becomes

$$V(t) = A \frac{\partial D_i}{\partial t} Z_e + \int_{r0}^{rL} -\frac{\partial \phi}{\partial r_i} dr_i, \tag{A.38}$$

where the following relation between current and electrical displacement was applied

$$I_i = A \frac{\partial D_i}{\partial t}. \tag{A.39}$$

13 equations has then been presented with 13 unknowns.

For other equation combinations of (A.22) to (A.29) it may be helpful to introduce the conservation of charge statement as well. This equation state

$$\nabla \cdot D = \rho_{free}. \tag{A.40}$$

Since one can assume that there is no source generator inside the material $\rho_{free} = 0$.

Non-piezoelectric solid materials

The constitutive equations for non-piezoelectric materials are simpler than those for piezoelectric materials since one do not have the coupling between mechanical displacement and electric fields. These two phenomenas can be considered separately. However, in the context of transducer modeling it is only interesting to consider the mechanical behavior.

The relation between stress-strain is

$$\mathbf{T} = c : \mathbf{S}, \tag{A.41}$$

$$\mathbf{S} = s : \mathbf{T}. \tag{A.42}$$

The stiffness matrix for an isotropic medium yields [32]

$$c = \begin{bmatrix} c_{11} & c_{12} & c_{12} & 0 & 0 & 0 \\ c_{12} & c_{11} & c_{12} & 0 & 0 & 0 \\ c_{12} & c_{12} & c_{11} & 0 & 0 & 0 \\ 0 & 0 & 0 & c_{44} & 0 & 0 \\ 0 & 0 & 0 & 0 & c_{44} & 0 \\ 0 & 0 & 0 & 0 & 0 & c_{44} \end{bmatrix}. \tag{A.43}$$

The compliance matrix s is the inverse of the stiffness matrix coefficients.

The constants c_{11}, c_{12}, c_{44} are in literature shown to be formulated by means of Young's modulus and the Poisson ratio as:

$$c_{11} = \frac{Y(1-\nu)}{(1+\nu)(1-2\nu)}, \quad c_{12} = \frac{Y\nu}{(1+\nu)(1-2\nu)}, \quad c_{44} = \frac{Y(1-2\nu)}{(1+\nu)(1-2\nu)}, \tag{A.44}$$

where Y is the Young's modulus and ν is the Poisson ratio.

Newton's second law, (A.34), is also applicable in non-piezoelectric materials.

One-dimensional equations

The above full dimensional modeling is a very computational heavy way of modeling. To approximate the above in a simple manner one can consider the one dimensional case. Assume a transducer to operate in its thickness mode only. It is poled and only allowed to operate in one dimension. Furthermore, one assumes that the operation is performed in the third direction, i.e. the z-direction. This implies that one can consider the $33, zz$ operation mode only. This simplifies the above equation sets.

For Equation (A.30) one then finds

$$T_3 = c_{33}^D S_3 - h_{z3} D_z \tag{A.45}$$

or (A.46)

$$T_{zz} = c_{33}^D \frac{\partial u_z}{\partial z} - h_{z3} D_z. \tag{A.47}$$

Equation (A.33) is simplified to

$$-\frac{\partial \phi}{\partial z} = h_{z3} \frac{\partial u_z}{\partial z} - \beta_{zz}^s D_z. \tag{A.48}$$

Also Equation (A.49) is applicable in the following form

$$V(t) = A \frac{\partial D_z}{\partial t} Z_e + \int_{r0}^{rL} -\frac{\partial \phi}{\partial z} dz. \tag{A.49}$$

APPENDIX

B

Description of a model for a deflecting CMUT plate

The following description is based on the reference [55].

The external forces deflecting down the top plate of a circular axissymetric CMUT are a combination between the surrounding pressure and the electrostatic force pulling the plate down towards the pull-in point. This force can be written as a pressure

$$P_0 = P_{atm} + \frac{F_e}{\pi a^2}, \tag{B.1}$$

where $a = r_{cell}$ is the effective radius of the CMUT cell, P_{atm} is the surrounding pressure, and F_e is the electrostatic force.

The plate takes on a form that for a circular membrane may be calculated from classical membrane theory by solving a fourth order equation set [28] or by applying a polynomial of the following type [56]:

$$w(r) = \frac{P_0 a^4}{64D}\left(1 + \frac{r^2}{a^2}\right)^2. \tag{B.2}$$

Here r is the radial coordinate, and D is the flexural rigidity. The latter is given from

$$D = \frac{Et^3}{12(1-\nu^2)}, \tag{B.3}$$

where t is the membrane thickness, ν is the poison ratio, and E is the Young's module.

The maximum deflection, w_{pk} is found when $r = 0$

$$w_{pk} = \frac{P_0 a^4}{64D}. \tag{B.4}$$

An integration of the shape function (B.2) in polar coordinates shows that the average plate deflection is related to the peak deflection:

$$w_{avg} = \frac{w_{pk}}{3}. \tag{B.5}$$

The CMUT is a capacitor with a vacuum sealed air gap. The capacitance of the CMUT is then found to be

$$C = \frac{\epsilon_0 \pi a^2 \arctan \sqrt{\frac{w_{pk}}{g_0}}}{\sqrt{g_0 w_{pk}}}, \tag{B.6}$$

where ϵ_0 is the free permittivity constant, and g_0 is the effective air gap height. See e.g. Fig. 4.1 for terminology.

The average displacement for small displacements of the plate relatively to its thickness can be described with the linear Hooke's law and can be used to express the mechanical force at the center deflection point

$$F_m = \frac{P_0 a^2}{192\pi D} w_{avg} = k_1 w_{avg}. \tag{B.7}$$

To find the average deflection one must solve the equality

$$F_m(w_{avg}) - F_e(w_{avg}) = 0. \tag{B.8}$$

This yields the average static deflection of the membrane to a given applied DC bias. F_e is the electrostatic force and is given by

$$F_e = \frac{1}{2} V^2 \frac{\partial C}{\partial w_{avg}}, \tag{B.9}$$

where V is the applied voltage. Notice that the initial displacement when $V = 0$ is different from zero because of the sealed vacuum cavity.

The above is valid for small deflections. An extra term may be introduced as suggested in [55] or [56] which can account for larger displacement and weak non-linear behavior of the plate. In [55] a k_3 term is introduced for the non-linear part

$$k_3 = \frac{18 c_v k_1}{t^2}. \tag{B.10}$$

The constant c_v is a material constant dependent on the material being used.

To calculate the average displacement with the non-linear term the mechanical force should be introduced as

$$F_m = k_1(w_{awg} - w_{atm}) + k_3(w_{awg} - w_{atm})^3, \tag{B.11}$$

where w_{atm} is the displacement when no electrical forces occur. The displacement is found by solving

$$F_m(w_{avg}) - F_e(w_{avg}) = 0. \tag{B.12}$$